A Novel Method of Sensing and Classifying Terrain for Autonomous Unmanned Ground Vehicles

A thesis submitted to Middlesex University in partial fulfilment of the requirements for the degree of Doctor of Philosophy

Siddharth Odedra

School of Engineering and Information Sciences
Middlesex University

September 2014

ABSTRACT

Unmanned Ground Vehicles (UGVs) play a vital role in preserving human life during hostile military operations and extend our reach by exploring extraterrestrial worlds during space missions. These systems generally have to operate in unstructured environments which contain dynamic variables and unpredictable obstacles, making the seemingly simple task of traversing from A-B extremely difficult.

Terrain is one of the biggest obstacles within these environments as it could potentially cause a vehicle to become stuck and render it useless, therefore autonomous systems must possess the ability to directly sense terrain conditions. Current autonomous vehicles use look-ahead vision systems and passive laser scanners to navigate a safe path around obstacles; however these methods lack detail when considering terrain as they make predictions using estimations of the terrain's appearance alone.

This study establishes a more accurate method of measuring, classifying and monitoring terrain in real-time. A novel instrument for measuring direct terrain features at the wheel-terrain contact interface is presented in the form of the Force Sensing Wheel (FSW). Additionally a classification method using unique parameters of the wheel-terrain interaction is used to identify and monitor terrain conditions in real-time. The combination of both the FSW and real-time classification method facilitates better traversal decisions, creating a more Terrain Capable system.

ACKNOWLEDGEMENTS

First and foremost I would like to thank my Director of Studies Professor Mehmet Karamanoglu for always supporting and believing in me, the road was long and sometimes rough but we got there in the end.

I would like to extend my gratitude to my supervisor Dr Stephen Prior for his guidance and even though we didn't always agree, I will always respect your opinion and be grateful for the opportunities you have given me over the years.

I would also like to acknowledge the facilities and technicians at Middlesex University without which the extensive developments within this study wouldn't have been possible.

On a personal note, I am ever grateful to my mother Mira for being a guiding light and my grandfather Rana for inspiring the engineer in me. Thank you to my brother Adarsh and sister Shradha for being supportive throughout. I owe the deepest gratitude to my father Hamir who has raised us showing drive and determination no matter the circumstance, which has given me the belief that everything is possible.

Last but definitely not least Rebecca, words cannot even begin to express my love and gratitude for everything you do. You have been there to share the stress when things didn't quite work and elation when they did. Thank you for coming into my life, this would have been impossible without you but nothing ever will be now that you are in my life.

CONTENTS

Chapter 8 – Conclusions and Further Work

LIST OF FIGURES

LIST OF TABLES

NOMENCLATURE

A	contact surface area
B	exponential relationship parameter
b	wheel width / smaller dimension of pressure plate
C	exponential relationship parameter
c	cohesion
c_1, c_2	soil cohesion coefficients
DP	drawbar pull
e	Euler's number
F	force
F_p	peak force
H	horizontal thrust
i	slip
k	modulus of soil deformation
k_c	cohesive modulus
k_φ	frictional modulus
L_v	lateral pressure variation
n	exponent of deformation
p	normal pressure
R	resistance
R^2	coefficient of determination
r	wheel radius
T	torque
V	linear velocity
v	voltage
W	vertical load
x	sensor radial/longitudinal position
y	sensor lateral position
z	sinkage (depth)

θ	contact angle
θ_1	front contact region
θ_2	rear contact region
θ_m	location of maximum pressure
μ	degree of membership
σ	normal stress
σ_1	front stress region
σ_2	rear stress region
τ	shear stress
φ	internal friction angle
ω	angular velocity

CHAPTER 1
INTRODUCTION

1.1 Background

In the early 20th century Czech writer Karel Čapek first used the word 'Robot' to describe the mechanical beings in his play Rossum's Universal Robots (Capek, Playfair et al. 1920). Following that, science fiction author Isaac Asimov (1950) wrote about a future where humans would coexist with intelligent robots that would follow set laws. Later in 1965 Intel co-founder Gordon E. Moore predicted that the capability of computing systems will grow exponentially (Moore 1965). This prediction, which later became known as Moore's Law, led to a technological revolution at the turn of millennium and could be seen as one of the most significant factors in making advanced robotic systems possible. Today robots are omnipresent, used to carry out a variety of tasks from assembling components on the factory floor to cleaning the floors in our homes.

Robots are generally used to carry out tasks where humans are either unwilling or unable to safely function. P.W Singer (2009) better describes this as the "three 'D's - Dull, Dirty and Dangerous". Robots will happily do the dull repetitive tasks that we dislike without complaint and operate for extended periods of time in dirty and dangerous environments without losing concentration and needing rest.

Modern systems have evolved to become highly capable and many industries have invested in robotic solutions because in some cases they are more accurate, productive and efficient than a human doing the same task (Miller, Atkinson 2013). Two industries standout at the forefront of advancing robotic technologies mainly because the systems they operate have more critical roles: the Unmanned Systems used to preserve human life during military operations and the Space Rovers used to explore unreachable worlds.

1.1.1 Unmanned Systems

Robots are an integral part of 21st century military operations worldwide, better known as unmanned systems they are used to assist soldiers in their mission in order to keep them alive by informing them of any potential dangers before arriving at hostile areas, as well as keeping them away from perils on the battlefield when they arrive.

There are a range of unmanned systems deployed by the military: Unmanned Aerial Vehicles (UAVs) provide aerial reconnaissance, Unmanned Ground Vehicles (UGVs) drive forward ground operations, Unmanned Underwater Vehicles (UUVs) monitor the seas and Unmanned Surface Vehicles (USVs) patrol the shores. These systems serve as an extension of the soldier's capability on the battlefield and carry out many critical missions because if a robot can replace a soldier in one of the most hostile environments on the planet and becomes damaged or destroyed, then it is a far smaller price to pay than to risk human life. This was greatly realised during the recent conflicts in Iraq and Afghanistan where insurgents targeted coalition forces with small homemade bombs that could be hidden easily (usually by the roadside) and be detonated either remotely or by proximity; known as Improvised Explosive Devices (IEDs) they became the insurgents' primary weapon and quickly became the single biggest killer of coalition troops (Schmitt 2004) accounting for 2,545 U.S. service member deaths since 2001 as reported by The Washington Post (2014).

A typical tour in Iraq would see each team going on more than six hundred IED calls, diffusing two a day (Singer 2009). This would be done by skilled Explosive Ordnance Disposal (EOD) teams whom quickly became critical in the fight against IEDs. These valuable soldiers would get extremely close to volatile explosives that could detonate without warning and with zero chance of survival at that proximity if they didn't succeed it would be fatal. There was a need for a better solution and in 2004 to counter these attacks, 150 iRobot Packbot UGVs (Figure 1.1) were deployed in Iraq to help EOD operations (Schmitt 2004).

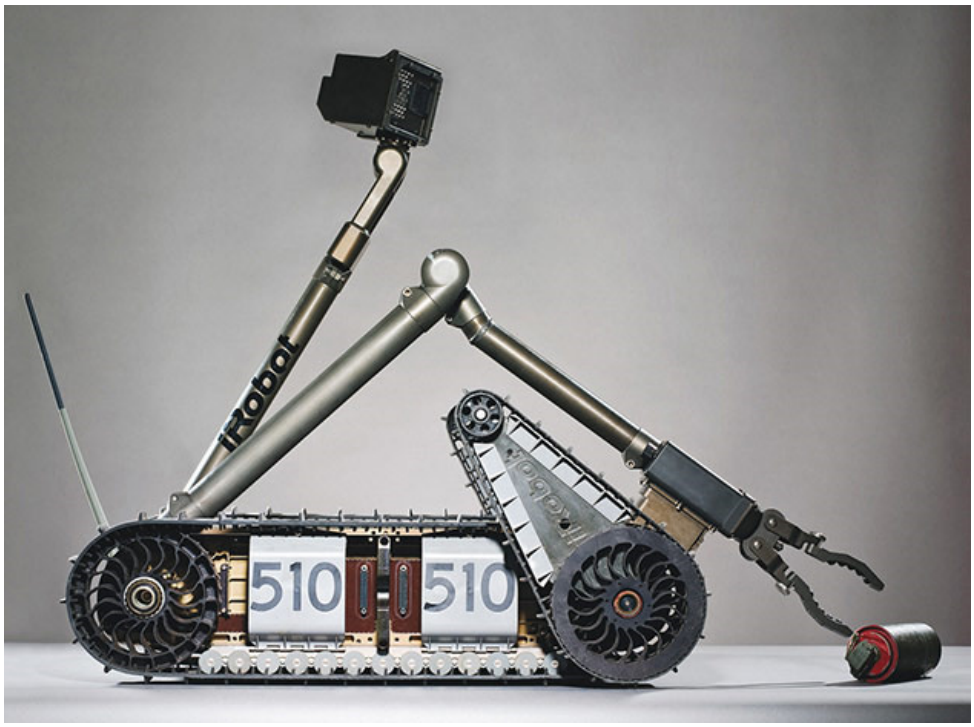

Figure 1.1 – iRobot Packbot 510 UGV used for Explosive Ordnance Disposal. This robot soldier keeps its EOD operator at a safe distance from IEDs (iRobot 2014).

This capable robotic companion was well received as it allowed EOD soldiers to operate at a safer distance while diffusing harmful devices, potentially saving dozens of lives in the process; and if it failed its mission then it meant that the (replaceable) machine got damaged or destroyed rather than the soldier getting killed (Figure 1.2).

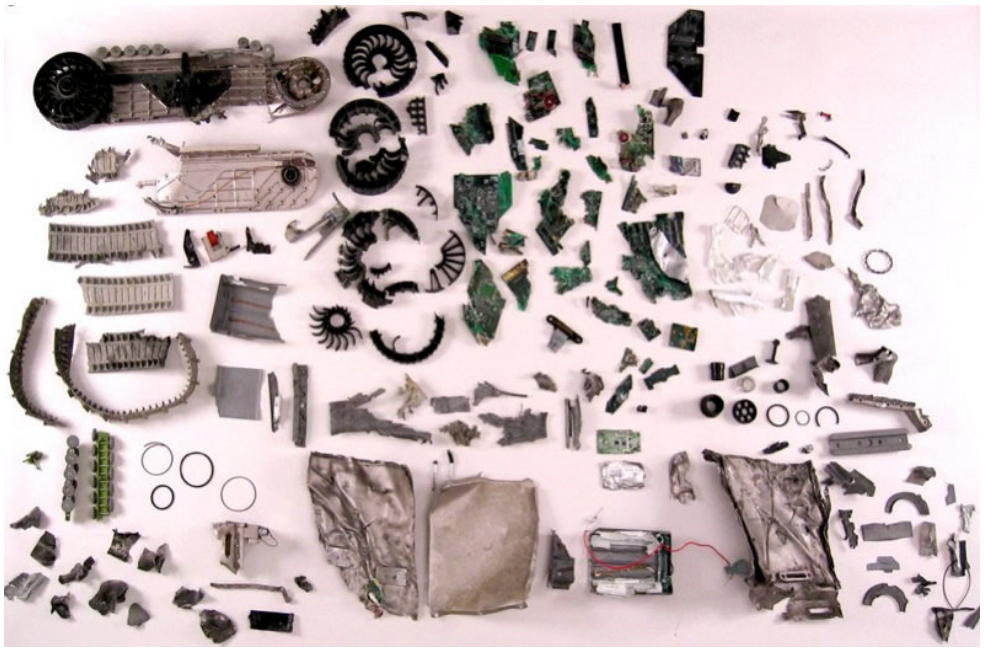

Figure 1.2 – Packbot #129 killed in action on April 8th 2004. Far better a robot gets destroyed than the loss of a human life (Matson 2010).

It was quickly realised that robots were helping to save multiple human lives which led to the number of robotic systems deployed on the ground in Iraq going from zero in 2003, to 12,000 by the end of 2008 (Singer 2009). This countermeasure helped neutralize the lethal threat and as seen in Figure 1.3 the number of fatalities caused by IEDs began to fall.

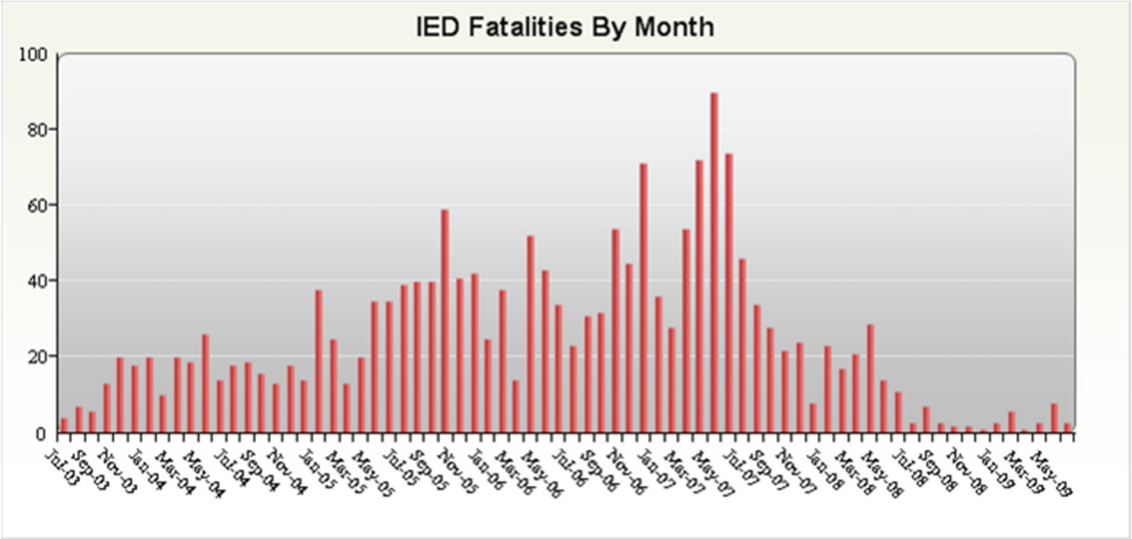

Figure 1.3 – IED Fatalities during the conflict in Iraq. IEDs were eventually neutralised with the introduction of more advanced counter measures including robots (iCasualties 2009).

1.1.2 Space Rovers

The late 20th century Space Race saw the launch of the first satellite, the first person in space and land a man on the moon, giving belief to the possibility of reaching new worlds. Today with the advancement of technology there are many Earth orbiting satellites, probes roaming outer space and a habitable International Space Station (ISS); however it is still beyond our reach to safely send a manned mission to another planet. Even though this hasn't happened yet, we already possess a wealth of knowledge about the surface of our neighbouring planet Mars thanks to numerous robotic missions.

The National Aeronautics and Space Agency (NASA) in collaboration with the Jet Propulsion Laboratory (JPL) have spearheaded robotic missions to search for signs of life on Mars. On July 4th 1997 after travelling 309 million miles, the Pathfinder spacecraft successfully landed on Mars and opened to deploy a small Space rover named *Sojourner* (Figure 1.4). Initially planned to operate for between a week to a month, Sojourner surpassed expectations and spent the next three months traversing

across 328ft of Martian terrain while conducting 15 chemical analyses of rocks and soil using special on-board instruments (Wilcox, Nguyen 1998). This mission provided invaluable data about the Martian environment and with an excess of 16,500 images sent back, offered a never before seen view of the red planet.

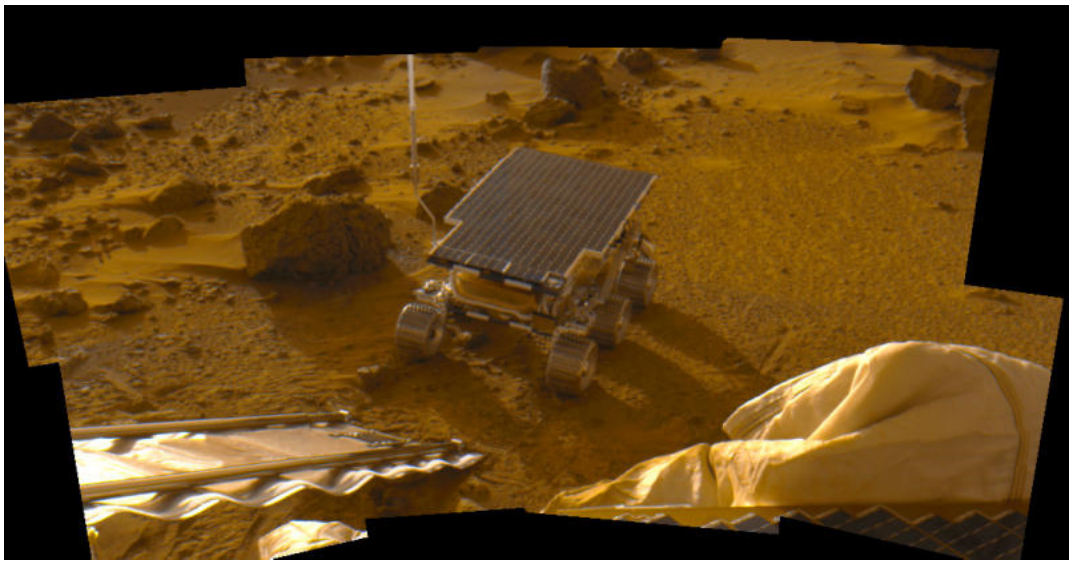

Figure 1.4 – Sojourner drives onto the Martian surface for the first time. This demonstrated that robotic systems can help extend our reach (NASA/JPL 1999).

The Pathfinder mission was a success and after analysing the data that was collected, Mars was seen as having once been more Earth-like than previously imagined. Images showed deep valleys within the craters, symbolizing that there could have once been a presence of water and therefore sustained life (Stoker 1998). NASA/JPL made plans to send better equipped rovers to carry out more advanced geological experiments to search for solid evidence that there is, or once was water on Mars (Squyres 2005).

In 2003 NASA/JPL launched two identical Mars Exploration Rovers (MER) to opposite sides of the planet and on January 3rd 2004 *Spirit* successfully landed followed on January 24th 2004 by its twin *Opportunity*. Larger and more capable than their predecessor, they carried out more advanced experiments and sent back some of the highest resolution colour images ever seen of another planet, showing an immensely clear view of the Martian landscape. Figure 1.5 shows one such image which was described as “one of the most important findings by either rover” as it carried with it evidence that there once was water on Mars (Webster 2011). The white layer seen beneath the Martian surface in the image was exposed by Spirit’s wheel tracks and with

further scientific investigation using on-board instruments it was confirmed that the substance was nearly pure Silica usually found in hot springs and its formation would have involved a volcanic environment and water which could have provided favourable conditions for microbial life (Smith, Onstott 2011). Both rovers continued to gather further evidence while impressively exceeding their planned three month mission with Spirit operating for more than six years before going quiet and Opportunity still operating today over ten years later.

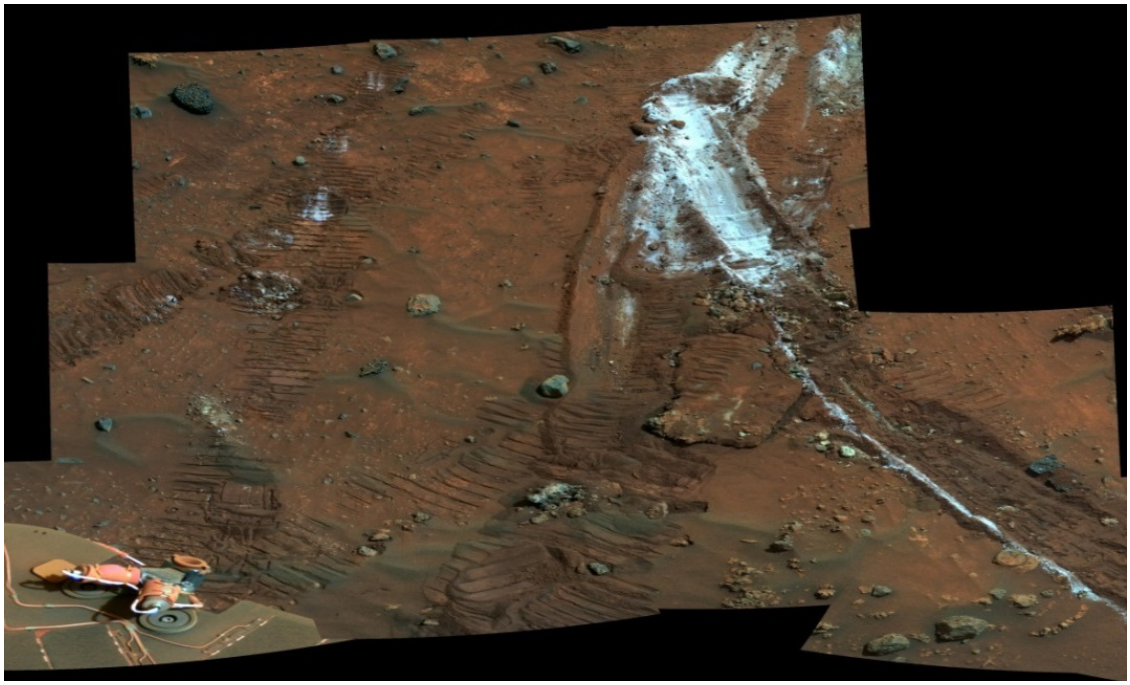

Figure 1.5 – White Martian soil uncovered by Spirit. The rover's wheel tracks expose proof that there once was water present on Mars (NASA/JPL 2009).

With the discovery made by Spirit (Figure 1.5) it became apparent that there would be more valuable information about the history of Mars under the surface and so nearly a decade after the launch of the previous mission and with greater advancements in technology, NASA/JPL were preparing to launch the Mars Science Laboratory (MSL); a veritable giant compared to previous Mars missions as seen in Figure 1.6. The larger rover named *Curiosity* would include a scientific payload nine times heavier than carried by each of the twin rovers and be able to see better with a host of cameras for scientific analysis and navigation (Baker 2013). Most significantly, Curiosity was equipped with drill and laser systems to be able to examine geological features under the top layer.

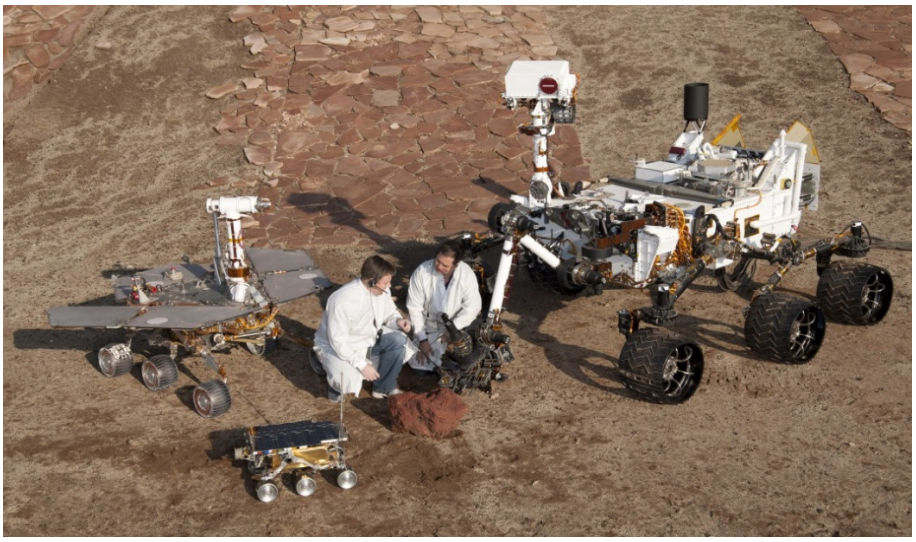

Figure 1.6 – Three generations of Mars rovers. Engineers sit with (clockwise from bottom left) Sojourner, Spirit/Opportunity and Curiosity (NASA/JPL 2012).

Curiosity successfully landed on Mars on August 5th 2012 and set out to carry out more detailed environmental experiments than before. After roaming the planet for six months Curiosity finally carried out its first sample drilling on a rock situated in the middle of what looked like a valley that would have once flowed with water. A sample of powdered rock was transferred from the drill to the rover's scoop where it was delivered to on-board chemistry and mineralogy laboratories to be analysed (Figure 1.7), the results of which confirmed evidence of an ancient lake. Curiosity is still operational today and has since found all the essential elements required for habitability to be present on Mars (Amos 2013).

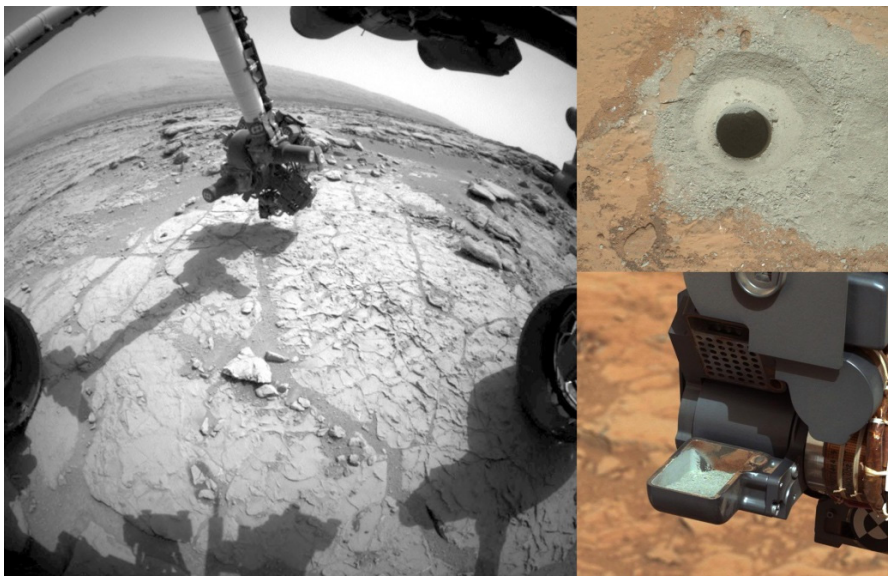

Figure 1.7 – Curiosity's first sample drilling on Mars. The drill first penetrates the Martian surface before samples are collected and analysed (NASA/JPL 2013).

1.2 Motivation

Robots have helped to save a countless number of lives in the battle against terror and searched for evidence of alien life on a distant planet; albeit great accomplishments they still require comprehensive commands in order to function and therefore need dedicated resources. This can be costly not only financially but more importantly to mission success because certain situations will require immediate decisions that cannot be made from a distance by an uninformed operator. Systems have to become more knowledgeable about their environment (increased situational awareness), be able to make immediate decisions accordingly (more autonomy) and possess the ability to cope with critical conditions (advanced configurations).

This is primarily the case when having to identify and avoid (or overcome) perilous environmental obstacles that could cause the vehicle in question to fail; aerial systems will be affected by strong wind speeds and waterborne vehicles have extreme sea conditions to deal with, however UGVs have the hardest task of navigating their environment due to the range of terrain types within sometimes unknown and generally unstructured environments, that could include dynamic variables and unpredictable obstacles. This makes the seemingly simple task of traversing from A-B on the ground extremely difficult and a lack of information in an environment littered with potential pitfalls can be terminal.

Figure 1.8 – Spirit embeds itself in soft Martian soil. The rover unknowingly drove into a sand trap ending the mission (NASA/JPL 2009).

This was the case for the Mars rover Spirit when it unknowingly became stuck in soft terrain where it stayed for the next eight months while engineers tried to extricate it (Figure 1.8). After numerous attempts to free it, they decided it was irrecoverable and three months later Spirit stopped communicating, ending the mission (Webster 2011).

Another example can be seen during the first 'Grand Challenge' set by the Defense Advanced Research Projects Agency (DARPA) in 2004 to accelerate the development of autonomous UGVs for potential military exploitation. The challenge was to create a vehicle capable of autonomously traversing across 142 miles of the Mojave Desert and even though 15 teams made it to the start line, none finished the course with many teams becoming stuck in unforgiving terrain as seen in Figure 1.9 (Hooper 2004).

Figure 1.9 – DARPA Grand Challenge UGVs getting stuck in rough terrain. Autonomous vehicles get into trouble due to a lack of real-time information regarding ground conditions (DARPA 2014).

1.2.1 UGV Perception

Over the past decade there have been a number of advancements in creating more perceptive UGVs. DARPA's subsequent 2005 and 2007 Grand Challenges have helped develop advanced algorithms and navigation sensors, such as look-ahead vision systems and passive laser scanners, giving autonomous platforms the ability to map their environments and carry out on-board image processing to search for the safest path.

While these are great innovations, the 'safe path' determined by these systems might not be ideal in a military context because "the best route for covert missions will most likely not coincide with the easiest mobility route and timely mission accomplishment cannot be achieved if the platform has to spend its time searching for an easy path" (Rose 2002: 76). The U.S. Department of Defense (DoD) state that "the ability of a UGV to navigate autonomously is largely dependent on the accuracy and robustness of its perception system" (Winnefeld, Kendall 2013, p87). This highlights the fact that current systems, albeit sophisticated, become ineffective when coping with adverse terrain conditions because they use passive look-ahead sensors to make decisions on terrain traversability based on the appearance and measurements of the top layer alone, which is fine when navigating a safe path across flat structured ground; however many military and space exploration scenarios (where these systems need to operate) include unchartered territories featuring unstructured terrain that could change without warning, exposing potential pitfalls under the surface. The DoD acknowledges that "current state-of-the-art UGVs are designed from the ground up to operate within assumed environments. If these assumptions are valid, the UGV often operates effectively, however when circumstances are different from assumed, the UGV will fail to operate as intended" (Winnefeld, Kendall 2013, p87). This could cause systems to use up (power) resources either by trying to drive through unfriendly terrain, or by looking for a safe path, potentially leading one of two terminal mission outcomes: becoming stuck or running out of power. This makes terrain the principal obstacle for UGVs and coping with it is paramount to mission success, emphasizing the requirement for a more comprehensive approach to measuring and coping with terrain conditions.

1.2.2 Improving the Terrain Capability of UGVs

This study is motivated by a broader research program aiming to create a more 'Terrain Capable' system that can directly measure the terrain, classify it and then choose the best configuration to traverse it, all in real-time; lowering the limitations on where the vehicle can go and increasing the system's operational range (Figure 1.10). This is supported again by the DoD who state that "it is desirable to have a perception system that can adapt to various environments. To be able to adapt, the UGV must understand the context of its environment and recognize when that context changes" (Winnefeld, Kendall 2013, p87).

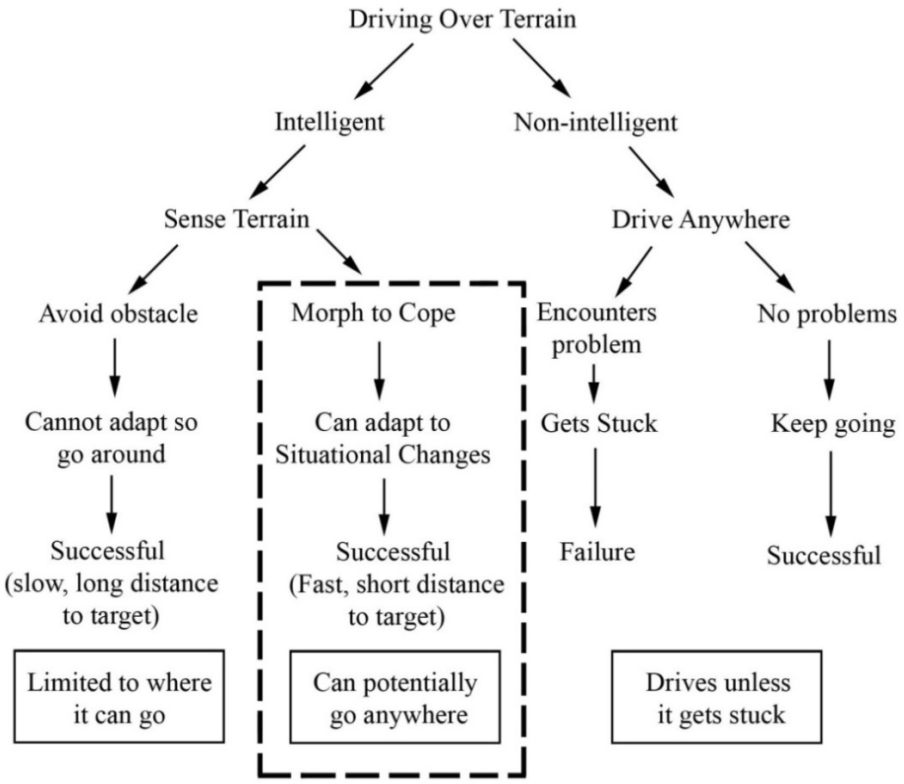

Figure 1.10 – The different ways in which to cope with terrain. Intelligent systems with advanced configurations can potentially go anywhere (Odedra, Prior et al. 2007).

The development towards creating a more Terrain Capable system is split into two phases each with a hardware and software component, as seen in Table 1.1. This study focuses on Phase 1 by aiming to increase the system's perception of the terrain and creating a unique method of classifying it in real-time. This approach aligns with the DoD's Roadmap on Robotic Evolution (Figure 1.11) where Situational Awareness and Feature Identification are currently at the forefront of robotic developments; relating in this study to Terrain Perception and Terrain Classification respectively.

Table 1.1 – Development phases required to create more Terrain Capable systems. Each of the two phases has hardware and software components that need further development.

Phase 1	Hardware	Increased Perception: greater sense of environmental conditions.
	Software	Enhanced Autonomy (part 1): on-line terrain classification.
Phase 2	Hardware	Advanced Mobility: better choice of configuration options.
	Software	Enhanced Autonomy (part 2): real- time configuration selection.

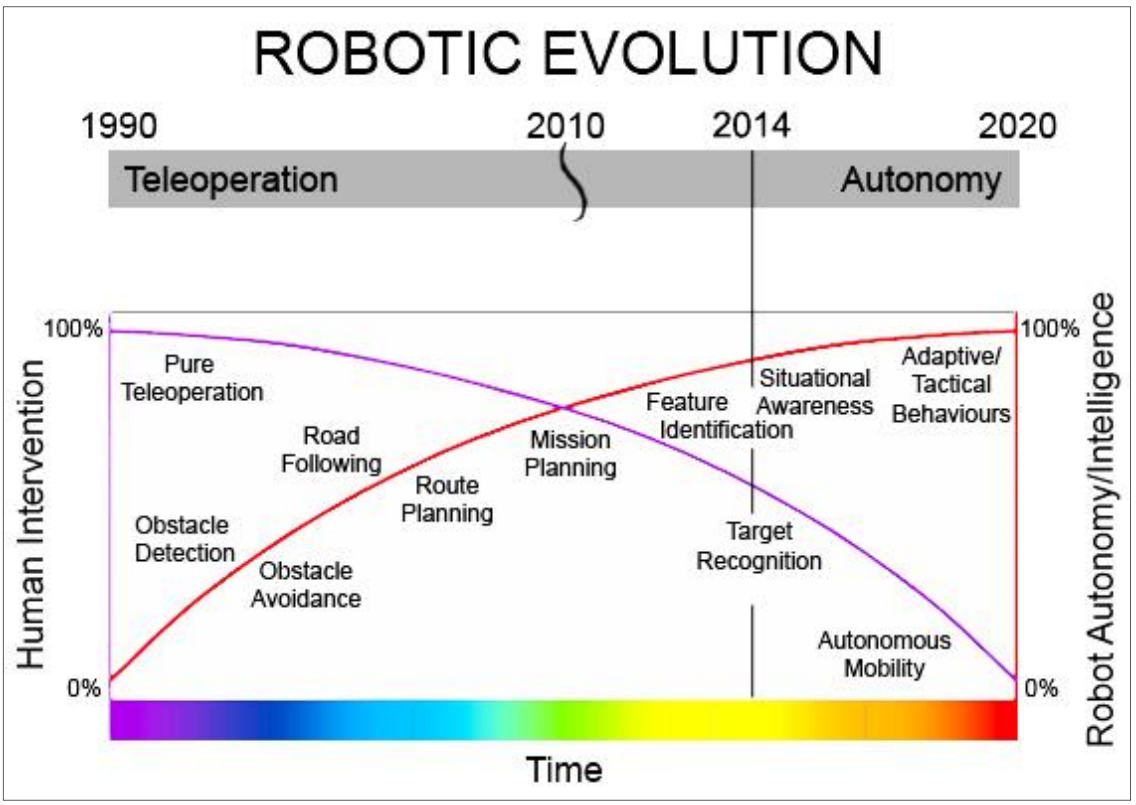

Figure 1.11 – DoD Robotic Evolution Roadmap. This highlights the development steps required to create autonomous systems and where we currently stand (Cambone, Krieg et al. 2005).

1.3 Problem Statement

In summary, current autonomous UGVs navigate their environments using passive look-ahead sensors for obstacle avoidance and path planning. These sensors however, are also used to (indirectly) sense the terrain and predictions on traversability are made using these inaccurate measurements. There are two problems with this, firstly the system has no way of validating initial terrain estimations and traversability predictions, and therefore the system has no way of evaluating accuracy in order to improve future predictions. Secondly the system lacks the ability to monitor immediate terrain conditions in real-time, meaning that if earlier predictions were wrong or terrain conditions suddenly change, the (uninformed) system will continue without warning, potentially causing it to become stuck.

1.4 Research Objectives

The scope of this research was to establish a more accurate method of measuring, classifying and monitoring terrain in real-time. The aim was to develop a novel terrain sensing method to increase terrain perception by using a unique classification method to identify and monitor terrain in real-time.

1.4.1 Research Questions and Hypothesis

The hypothesis for this study is as follows:

Data gathered from performance measurements of the vehicle's reaction to the terrain (the interaction) can be used as a unique method of classifying terrain in real-time.

The study was driven by the following research questions:

1. What sensory modes have been utilised to identify terrain?
2. What are the significant parameters during wheel-terrain interaction?
3. How could new sensor technologies/methods be used to better identify terrain?
4. What parameters can be utilised to classify terrain in real-time?

1.4.2 Contribution to Knowledge

This research proposes a new method of sensing and classifying terrain in real-time. The principle contributions to knowledge are summarised as:

- A novel sensing method capable of directly measuring pressure distribution across the contact interface during wheel-terrain interaction.

- An on-line terrain classification algorithm that uses unique parameters of the wheel-terrain contact interface to accurately identify terrain features in real-time.

- A number of contributions made towards international research papers (listed in the Publications Section).

1.4.3 Boundaries and Assumptions

The following boundaries and assumptions were considered for this study:

a) The vehicle class is a small UGV < 50kg.
b) The vehicle is wheeled.
c) The wheels are rigid.
d) The terrain is deformable.
e) Single wheel-terrain model considered (not vehicle model).
f) No heating and wearing factors are considered.
g) No turning moments are considered.
h) No slip or shear stresses are considered

1.5 Thesis Outline

Chapter 1: Introduction (this chapter) - introduces the topic area and discusses the motivation behind the study. The research objectives and contributions are outlined and the boundaries of the study are stated.

Chapter 2: Terrain Sensing – is the initial literature review looking at elements of terrain and previous work carried out by various research institutions in the area of terrain sensing.

Chapter 3: Proprioceptive Sensing – describes early empirical work carried out to identify terrain properties using internal measurements of vehicle parameters in reaction to terrain conditions. The chapter includes sensor research and an additional review into terrain properties, followed by the initial experiment. Finally the test results are discussed and conclusions drawn.

Chapter 4: Methodology – discusses the research methods that were utilised to complete the main part of the study. The quantitative research methods, chosen experimental approach and variables of the study are highlighted.

Chapter 5: Terramechanics – is an additional review investigating the fundamentals of terrain mechanics and complex quantitative parameters of the interaction between the wheel and terrain.

Chapter 6: Measuring the Wheel-terrain Interface – discusses the novel Force Sensing Wheel developed to measure the radial pressure distribution across the 3D contact patch of the wheel-terrain interface in real-time.

Chapter 7: Terrain Sensing and Classification – presents the main empirical study, which was designed to determine potential relationships between terrain properties and features of the contact interface. The results are analysed and used to create the unique classification technique, which is outlined and tested.

Chapter 8: Conclusions and Further Work – concludes the study by discussing the outcomes of the research, developments and experiment. The contributions to knowledge are highlighted and ideas for further work are presented.

CHAPTER 2
TERRAIN SENSING

2.1 Terrain

Terrain has a great deal of unpredictability especially in unchartered areas. It is therefore vital for autonomous UGVs to be able to measure, classify and monitor ground conditions to avoid potential pitfalls. To fulfil the research objective and to create a novel method of sensing and classifying terrain, a deeper understanding of it was required.

Terrain can be split into three types: solid, granular and liquid. Manufactured hard and flat roads made from materials such as concrete or tarmac are the best example of solid terrain. They have extremely good frictional properties and virtually no deformation, making them easily traversable. Granular terrain types, better known as soil, are those generally found off-road. These are classed as granular because the composition of natural soil contains percentages of three different types of solid grains: sand, silt and clay (Coleman, Crossley Jr 2004). The percentage of each grain type that a soil contains affects its textural properties and is used in geology to classify it, which is usually displayed in a *Soil Triangle* (Figure 2.1).

Grain type will determine the soil's textural properties, however the size of the grains have a greater bearing on the soil's mechanical characteristics. This makes grain size more important from an engineering perspective and thus it is the main characteristic used by the International Organization for Standardization (ISO) to classify soil, which is shown in Table 2.1.

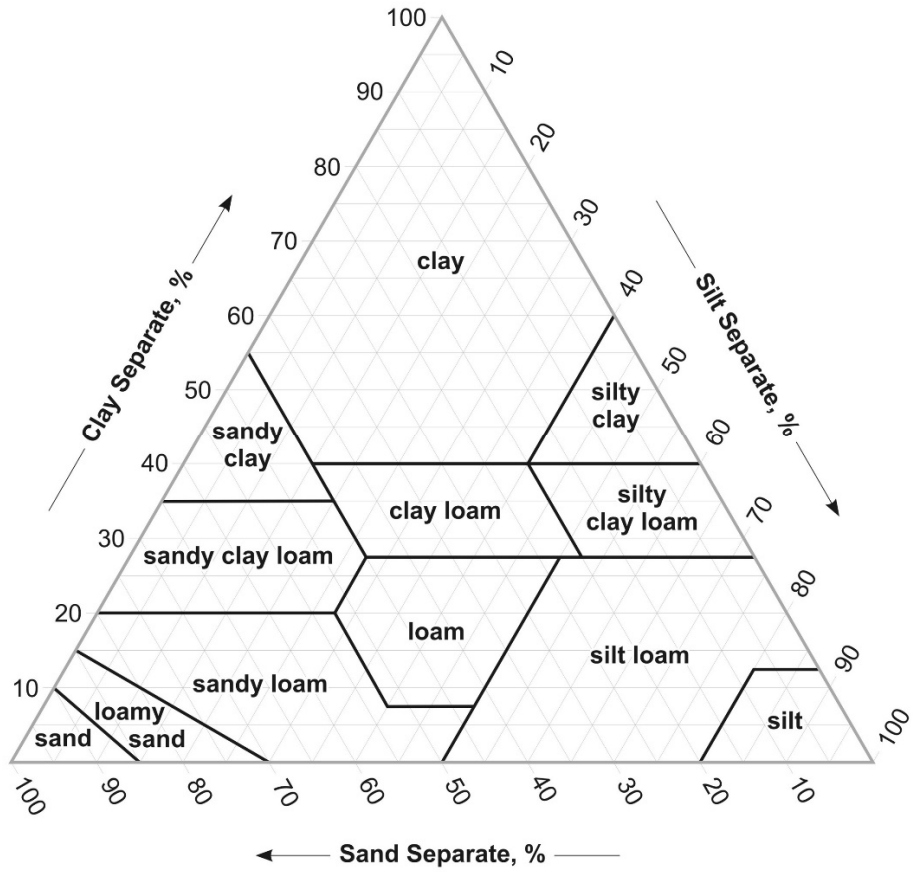

Figure 2.1 – Soil textural triangle. Soil texture is determined by the percentage of sand, silt and clay within it (Coleman, Crossley Jr 2004).

Table 2.1 – Soil classification table from ISO 14688-1:2002 *Geotechnical investigation and testing - Identification and classification of soil - Part 1: Identification and description* (ISO 2002).

Soil Fractions		Sub-Fractions	Symbols	Grain Size (mm)
Very coarse soil		Large boulder	LBo	>630
		Boulder	Bo	>200 - 630
		Cobble	Co	>63 - 200
Coarse Soil	Gravel (Gr)	Coarse gravel	CGr	>20 - 63
		Medium gravel	MGr	>6.3 - 20
		Fine gravel	FGr	>2 - 6.3
	Sand (Sa)	Coarse sand	CSa	>0.63 - 2
		Medium sand	MSa	>0.2 - 0.63
		Fine sand	FSa	>0.063 - 0.2
Fine Soil	Silt (Si)	Coarse silt	CSi	>0.02 - 0.063
		Medium silt	MSi	>0.0063 - 0.02
		Fine silt	FSi	>0.002 - 0.0063
	Clay		Cl	≤0.002

With a number of grain types and sizes, a natural soil's overall structure will typically contain void spaces that will be filled by air or water (Figure 2.2). The volume of air between particles and/or the amount of water retained by the soil (better known as moisture content) will adversely affect the terrain's physical properties and therefore its behaviour, especially from a traversability perspective. These elements cause off-road terrain to possess 'plastic' properties that deforms when under load, impacting on the terrain's ability to support a vehicle; known as Trafficability (Muro, O'Brien 2004).

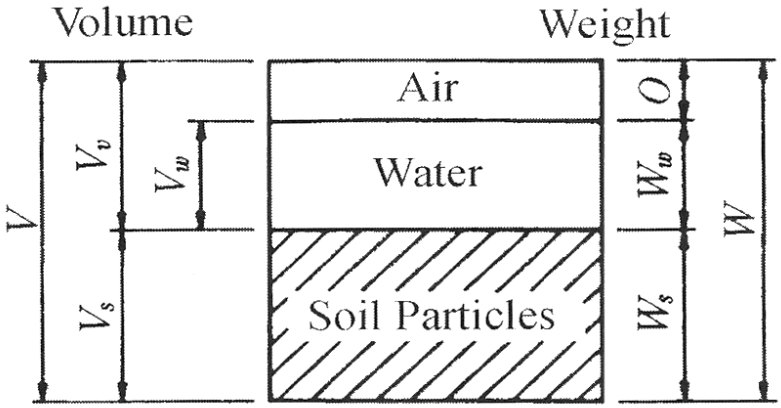

Figure 2.2 – Typical soil structure. Void spaces between particles are filled with air or water, which will affect the soil's physical properties (Muro, O'Brien 2004).

If the soil structure contains more than 23.2% water content then the terrain is classed as being in "a liquid state" (Bekker 1969), the third terrain type mentioned earlier. This viscous terrain has extremely poor traversability/trafficability characteristics because of its liquid behaviour.

Other factors that will affect the terrain's properties are climatic conditions such as weather. Rain for example can saturate the soil in water, instantly changing its properties and therefore its traversability characteristics. Terrain will therefore act differently during various weather conditions as seen in Table 2.2, where sixteen terrain types could be in up to forty-eight different states during three different weather conditions. This demonstrates that terrain characteristics can suddenly change without warning, highlighting the unpredictability of unstructured terrain. Other environmental factors that will affect terrain traversability are the gradient or slope of the land, and positive and negative obstacles. Positive obstacles include vegetation, rocks, fences and hills; negative obstacles include cliffs and valleys.

Table 2.2 – Table of terrain types and their properties. Terrain can be affected by climatic conditions such as weather, changing its traversability characteristics (Odedra, Prior et al. 2007).

			Effect of weather		
	Terrain type	**General surface properties**	**Sun**	**Rain**	**Snow/ice**
Harder >>	Sand	sinkage, slippage	hot	hydrocolloid	n/a
	Mud	sinkage, slippage	soft	liquefaction	hard
	Clay	slippage, sinkage	hard	liquefaction	slippage
	Rocks	uneven, hard	dry, hot	slippage	slippage
	Forest	long grass, foliage,	dazzle	marsh	hard
	Short grass	can get tangled	$\mu = 0.35$	$\mu = 0.2$	$\mu = 0.15$
	Gravel	loose, uneven, slippage	dry, hot	slippage	slippage
	Dirt track	dusty, level	dry	liquefaction	slippage
	Paved road	gaps, flat, high friction	$\mu = 0.7$	$\mu = 0.5$	$\mu = 0.08$
<< Easier	Asphalt	flat, high friction	$\mu = 0.8$	$\mu = 0.4$	$\mu = 0.06$
	Concrete	flat, high friction	$\mu = 0.7$	$\mu = 0.5$	$\mu = 0.08$

2.2 Terrain Sensing

UGVs must have a high level of perception regarding terrain conditions to facilitate autonomous operation. Previous work has been done in the area of terrain sensing, which can also be known as terrain classification, terrain trafficability or terrain traversability. Discussed here are some examples of work carried out in this area which is by no means a complete catalogue of all the work completed in the field, but a selection of works related to this study.

2.2.1 Vision-based Sensing

Research into terrain sensing can be seen as early as 1962 in the technical report *Feasibility Study of Terrain Sensors and Terrain Sensing* carried out by Emerson Electric for the U.S. Army. The objective of the report was to find an appropriate method of sensing terrain to provide information for the actuation of an active vehicle suspension system, in order to allow ordnance military vehicles to maintain greatly increased speeds over cross-country terrain (Gilmore, Ramsey et al. 1962). The study elects to use a passive optical ranging technique to measure the profile and consistency

of the terrain ahead of a cross-country military vehicle. Analysis is carried out on the feasibility of such a system and "its effectiveness in determining terrain contour and consistency under various climatic, tactical and terrain conditions" (Gilmore, Ramsey et al. 1962, p2). The report concludes by saying that this method does meet tactical and environmental requirements but highlights that lighting conditions such as time of day and atmospheric conditions such as fog, haze, dust, rain or snow can degrade the performance of optical instruments.

With the advancement of optical technology and image processing techniques, vision based sensing has been refined over the years. Systems were developed to use stereo cameras and triangulation to create three-dimensional images, used to measure their environments for path planning and navigation. Work done by Lacroix et al (1994) shows an example of a system that looks at the path ahead and segments the images into simple cells based on three–dimensional image data. These cells are labelled into four categories: flat, uneven, obstacle and unknown; using certain terrain characteristics such as point density, altitude, and mean vector. This classification method is then used to make navigational decisions.

A similar approach was taken by Gennery (1999) who also suggested using the analysis of a three-dimensional data produced by a stereo vision system to plan a path for a vehicle. The aim of this study was to produce more robust results from data classed as "sparse and of varying accuracy" generally expected from this type of sensing method. This was done by producing estimates for slope and roughness of each data point at equally spaced grid points to compute the (power) cost of driving over each grid point. A parallel search algorithm was then used to find the path of minimum cost.

Seraji and Howard (2002) also use a vision-based system to decide on the best route but use a novel measure of terrain traversability. They create a traversability index using fuzzy rules to detect terrain using four key elements: roughness, slope, discontinuity and hardness. Roughness indicates coarseness and surface irregularity; slope looks at the surfaces incline/decline; discontinuity looks at the end of the surface such as cliffs; and the surface hardness is measured to see how it affects traction. The rules for each set are simple, for example roughness is either smooth, rough or rocky and slope is classified as

flat, sloped or steep. The system uses this information to detect the terrain's traversability and identifies it simply as a low, medium or high risk.

These examples show that for vision-based sensing the algorithms used for image processing are vital. This has led to systems utilising more complex processing methods to classify terrain. Shirkhodaie (2007) work in this area is a good example of this, where a number of images are taken from different poses and are fused together with data from range sensors and environmental landmarks. The terrain is then classified using a fusion of three different techniques: a rule-based terrain classifier, a neural network based terrain classifier and a fuzzy-logic terrain classifier. Each terrain classifier divides a region of natural terrain within the image into finite sub-terrain regions, and then it classifies the terrain conditions exclusively within each sub-terrain region based on terrain visual clues.

2.2.2 Developments from the DARPA Grand Challenge

The winner of DARPA's second Grand Challenge in 2005 was *Stanley,* a modified Volkswagen Touareg from the University of Stanford, who crossed the line in the fastest time after traversing the rugged off-road course in a little less than seven hours (Orenstein 2005). Terrain sensing was a vital part of the systems successful traversal of the 132-mile course. Stanley was equipped with five single-scan laser range finders mounted on the roof, tilted downward to scan the road ahead for short and medium range obstacle avoidance, illustrated in Figure 2.3.

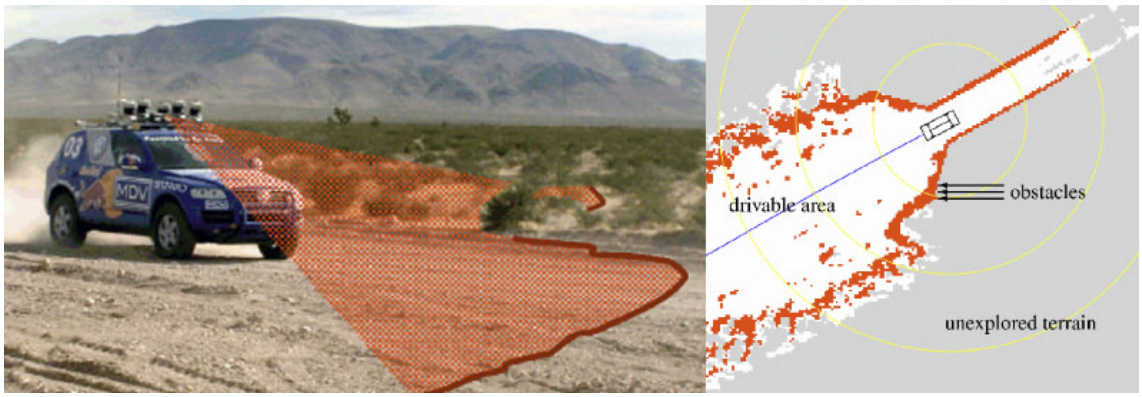

Figure 2.3 – Stanford's Stanley scanning the road ahead. Laser scanners mounted on the roof of the vehicle scan the environment to detect obstacles and adverse terrain (Thrun, Montemerlo et al. 2006).

The point cloud data acquired by all the different sensors is then positioned into the "global coordinate frame according to the estimated pose of the vehicle" (Thrun, Montemerlo et al. 2006, p669) resulting in a 3D map of the surrounding environment as seen in Figure 2.4. This data is also organized into a 2D surface grid where each point is given one of three possible values: occupied, free, and unknown. The information is then used to decide on traversability by creating a "final drivability map that is provided to the vehicle's navigation engine" (Thrun, Montemerlo et al. 2006, p669).

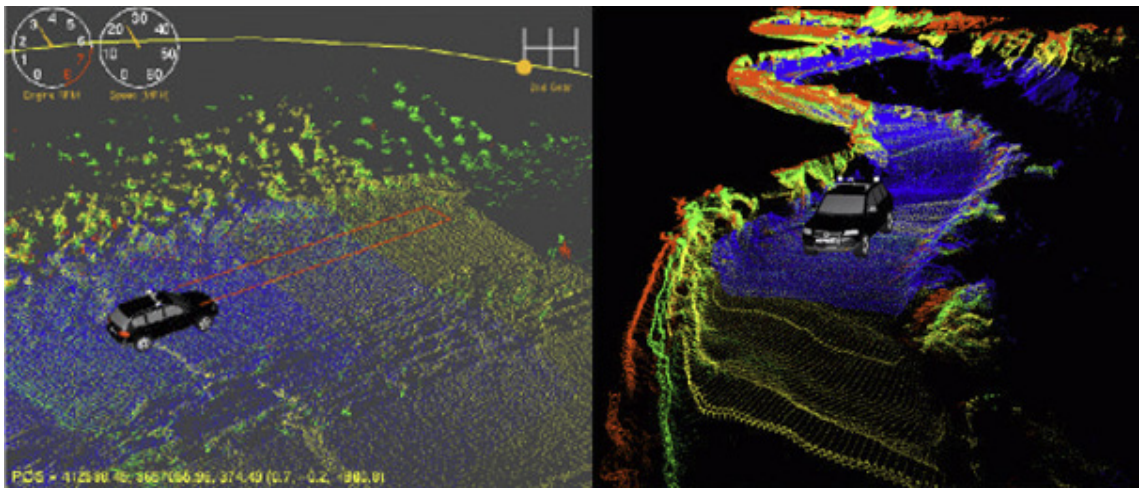

Figure 2.4 – 3D map of the area surrounding the vehicle. Data gathered from various sensors is overlaid to create an accurate three-dimensional model of the environment (Thrun, Montemerlo et al. 2006).

In addition to the laser scanners, stereo cameras are used to look beyond the laser range to make predictions on features further afield; however these camera images alone are not reliable enough for robot navigation. To combat this, point cloud data from the laser scanner is overlaid and the system uses machine learning algorithms to validate decisions and grow with experience. With adequate training then more accurate predictions are made regarding the area beyond the laser range so that the vehicle can travel and operate at a greater velocity.

2.2.3 Extraterrestrial Systems

Terrain sensing is crucial to extraterrestrial planet exploration because systems have to roam unknown environments containing benign terrain, and with communication limited to twice a day then the rover has to have the ability to cope with situational changes.

Early work by Volpe, Estlin et al (2000) from the Jet Propulsion Lab (JPL) looked to employ stereo imagery techniques similar to those previously discussed, to give the system some on-board decision making capabilities; alleviating the burden on ground controllers found during the previous Pathfinder mission. Long range navigation planning is done by ground operators however while traversing along this path the system only has an envelope of 20 metres (at best resolution) of the immediate environment in front of the rover. The rover breaks down the overall goal by processing the stereo imagery within that range to form a partial panorama and elevation map of the terrain in the desired direction (Figure 2.4), it then "selects a path through the terrain to the edge of the effective stereo range, and repeats the process until the goal is achieved" (Volpe, Estlin et al. 2000, p1). This method was successfully deployed and used on the 2004 Spirit and Opportunity Mars rovers.

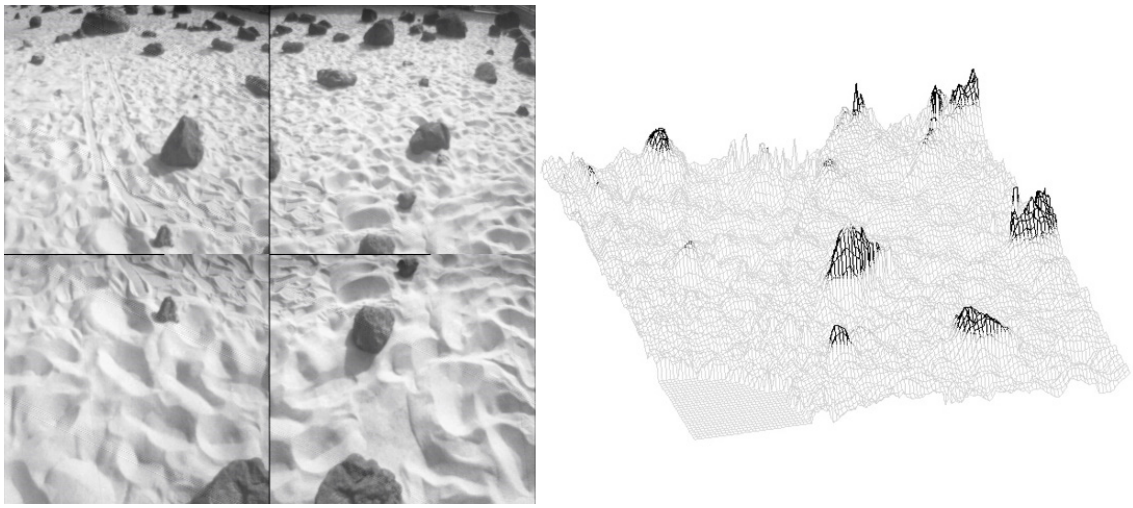

Figure 2.4 – Partial panorama and terrain elevation map. A terrain elevation map is created from stereo imagery and used for short range path planning (Volpe, Estlin et al. 2000).

Further work towards terrain sensing for planetary exploration has been carried out by Iagnemma, Shilby and Dubowsky (2002) from the Massachusetts Institute of Technology (MIT) who look at terrain classification, taking into account vehicle capabilities such as mobility. They propose a novel approach of 'estimating' parameters of the terrain on which the rover is currently traversing, by measuring rover-based properties such as torque and wheel angular velocity. Simplified forms of equations from the study of terrain mechanics, known as *Terramechanics,* is used to predict terrain properties such as cohesion and internal friction angle. This method not only

helps characterise terrain and predict traversability, but also enhances the understanding of planetary surface composition.

2.2.4 Reaction-based Sensing

The work discussed above demonstrates that using measurements of the vehicle's reaction to terrain conditions is a more accurate method of classifying the terrain, especially for traversability calculations. Sadhukhan (2004) also takes this approach by using internal sensors to classify terrain. A novel algorithm is proposed that uses the vehicle's internal sensors to measure vibration and noise to categorize the terrain type being traversed.

Leppanen et al (2008) propose that terrain slope and roughness are the main characteristics that express the geometry of the terrain. They emphasise that touch is a better method of sensing the terrain surface because this could potentially be hidden under snow or vegetation and other methods would fail to accurately measure it. They use a hybrid wheel-leg robot to determine the quality of terrain by measuring the vertical, horizontal and rotational strain forces affecting its wheels or feet. The measured parameters are then used for mapping, path planning or to select the best mode of locomotion.

Brooks and Iagnemma (2007) use a combination of visual and vibration-based sensing at the wheel-terrain interaction to classify the terrain. A belly-mounted camera looks at the point where the wheel and terrain interact and classifies the terrain based on the image alone which proved to be inaccurate. Vibration data is then used to supply 'training data' for the visual classifier, which increased the accuracy of classification predictions. They state that stereo vision is a good method of remotely detecting environmental (geometric) hazards such as large rocks but "little research has addressed remote sensing of non-geometric hazards, such as the loose drift material in which the Mars Exploration Rover Spirit became entrenched in" (Brooks, Iagnemma 2007, p1).

2.3 Discussions

As discussed, off-road terrain generally contains granular elements which include a number of variables that determine the terrain's physical properties. The large number of different soil types, each with very different characteristics, are ever-changing with climatic conditions; meaning that the terrain's ability to support a vehicle could suddenly change without warning, demonstrating the highly unpredictable nature of terrain. This highlights the need for autonomous systems to be able measure the terrain and monitor for situational changes.

The review of previous work shows that vision and radar systems are predominantly used for terrain sensing, which look ahead at the terrain and 'estimate' terrain conditions to make traversability decisions. This method takes into account larger geometric obstacles within the environment and broader terrain features for path planning and navigation; however more detailed terrain parameters that affect traversability are overlooked.

Work on reaction-based sensing of the vehicles internal conditions, also known as *Proprioceptive* sensing, take into account direct terrain parameters during interaction. This is far more valuable when classifying terrain from a traversability perspective because a vehicle can manoeuvre better over a surface that it has more knowledge about. More direct terrain measurements can also be used to 'train' learning algorithms to validate earlier estimations made by look-ahead sensors, creating a system that will make more accurate predictions with experience.

CHAPTER 3
PROPRIOCEPTIVE SENSING

3.1 Additional Research

3.1.1 Sensor Review

A sensor review was completed in order to get an insight into technologies that could be exploited to directly sense terrain and its elements. This helped to recognise the range of current sensor technologies available; however it was realised that finding the right sensor requires knowledge of what elements need to be sensed. This led to a further study into what terrain parameters could be measured, which is discussed later. This helped focus the initial sensor list which contained 150 sensors down to 10 sensors that could potentially be utilised to sense terrain, as seen in Table 3.1 below.

Table 3.1 – Table of the Top 10 sensors that could be utilised to sense terrain parameters.

Sensor type	Used to measure	How it could be used to sense terrain
Tilt/Gyro	Angle	Could measure the slope or gradient of the terrain.
Contact	Contact	Used to measure the contact between the vehicle and terrain.
Strain Gauge	Force/moment	Measuring the force between vehicle and terrain.
Hygrometer	Humidity	The difference in humidity could help define terrain type.
Contact Image (Scanner)	Contact image	Could be utilised to scan an image of the contact area.
Impedance	Moisture	Measuring the terrains moisture could help differentiate its type.
Laser Rangefinder (LADAR)	Proximity/distance (3d scanner)	Used to build up 3D image of the terrain.
Acoustic	Sound	Measure the sound difference across various terrain types.
Piezoelectric accelerometer	Vibration	The vibration feedback could define the surface roughness.
Stereo camera	3d image	A stereo image could be used to build an accurate 3d image of the terrain.

Further work was done to analyse the suitability of these sensors by looking at attributes such as their size, weight, cost, availability and whether they are contact or non-contact as well as their range and resolution. From this analysis, certain sensors were chosen for the initial experiment, discussed later in this chapter.

3.1.2 Terrain Parameters

Unstructured off-road terrain contains many different elements (as presented in the previous chapter) which required further investigation. Soil properties, test methods and even different terminologies used across many industries were looked into and a large number of measurable properties and test methods were discovered (listed in Appendix A). This list was condensed to a top 20 list of measurable properties and possible test methods that could potentially be used to support the research, seen in Table 3.2. This investigation informed the sensor research discussed earlier by highlighting what terrain parameters could be sensed.

3.1.3 Testing Methods

In addition to looking at sensor technologies and terrain parameters, research was carried out into what tests are done on off-road vehicles to validate them. *Millbrook Proving Ground* is the main U.K centre that carries out these tests using specialist vehicle test and development facilities to approve off-road vehicle capabilities. They use specific test specifications including environmental obstacles such as hills and ditches, as well as tough terrain types such as sand and gravel. This research was initially done to search for any existing terrain classification lists; however the main outcome of the study was the understanding that certain (environmental) conditions such as slope and gradient of the ground or positive/negative obstacles such as hills and ditches, are just as important to vehicle performance.

Table 3.2 – Table showing the Top 20 soil properties and test methods.

Soil Property	**Description**
Friction Angle	resistance due to roughness of surfaces.
Permeability	rate of seepage - linked to hydraulic conductivity.
Porosity	a measure of the void spaces in materials.
Dielectric permittivity	relating to a materials ability to transmit (or permit) an electric field.
Density	the ratio of the amount of matter in an object compared to its volume (mass per unit volume).
Bulk density	a property of particulate materials relating to the mass of many particles of the material divided by the volume they occupy.
Reynolds' dilatancy	is the observed tendency of a compacted granular material to dilate (expand in volume) as it is sheared.
Deformation	relating to the shear, sliding, distortion and compression under load.
Shear Strength	maximum strength of soil at which point significant plastic deformation (or yielding) occurs due to stress.
Plasticity	the point at which the material changes or deforms.
Moisture content	the percentage of liquid water.
Triaxial shear	measurement of the mechanical properties of many deformable soils.
Test method/equipment	**Description**
Hydrometer	an instrument used to measure the specific gravity (or relative density) of liquids.
Standard penetration test	used to determine the geotechnical engineering properties of soil.
Cone penetration test	test method consisting of pushing an instrument cone tip into the ground at a controlled rate.
California Bearing Ratio (CBR)	another penetration test measuring pressure required to penetrate soil with a standard sized plunger.
Atterberg limits	used to measure nature of soil; soil is defined by its moisture content for which there are 4 states -solid, semi-solid, plastic and liquid.
Atterberg limits - shrinkage limit	relating to water content where the loss of moisture results in the reduction of volume.
Atterberg limits - plastic limit	when soil starts to exhibit plastic behaviour.
Atterberg limits - liquid limit	relating to water content where a soil changes from plastic to liquid behaviour.

3.2 Experimental Design

3.2.1 Rationale

The objective of this experiment was to identify the relationship between terrain and vehicle performance. A data collection instrument in the form of a sensor rich vehicle platform was used to measure variables of the vehicle-terrain interaction with the aim to use the data gathered from the elements relating to vehicle performance during various terrain scenarios to search for a unique method of terrain classification.

3.2.2 Variables

Since this experiment related to the effect the terrain has on the vehicle, the terrain was the independent variable with the elements pertaining to vehicle performance being the dependant variables. The independent variables were the terrain's slope, gradient, surface roughness and surface continuity (also known as topology). The dependant variables were those affected by the independent variables, which in this case were the vehicle's power consumption (or rolling resistance), ride quality (or vibration), and orientation (or tilt angle). These variables were measured using proprioceptive sensing; Table 3.3 shows how the measured vehicle properties relate to the terrain variables.

Table 3.3 – Selected properties of the interaction and how they are measured.

Property to be measured	Method
Rolling Resistance	The vehicles power consumption is affected by the rolling resistance which can be identified by measuring the current draw (Taking slope/gradient into consideration).
Slope	Vehicle tilt angle (Around the x-axis).
Gradient	Vehicle tilt angle (Around the y-axis).
Surface Roughness	Measured by the frequency of suspension travel (Rate of vibration).
Topology	Measured by the suspension stroke (Amount of travel).

Rolling resistance will greatly affect vehicle performance because it will cause an increase in the vehicles power consumption. This was measured using a current sensor. Linear potentiometers at each wheel were used to measure the frequency of the suspension to measure the roughness of the surface, and the suspension stroke used to measure its topology. Alongside these measurements, the vehicles orientation was measured using tilt sensors in order to monitor the terrain's slope/gradient. Further information on the selected suite of sensors that were used on the vehicle platform can be seen Appendix B.

3.2.3 Control Variables

In order to keep the tests fair, other variables were controlled. The control variables were those of the vehicle that influenced vehicle performance, which were the vehicle's mass, power input, distance travelled, suspension properties (spring rate/stroke length), centre of gravity, wheel size, and tyre deflection. Note that speed and time are variables that weren't controlled; this is because controlling them would have affected the results pertaining to power consumption. Instead the power input and the distance travelled was controlled, and the speed/time was dictated by how hard the vehicle was working. This gave a better measure of vehicle performance.

3.2.4 Sampling (Site Selection)

For comparability this experiment involved a test being carried out to gather a (datum) set of results in order to compare to the results of the other tests. The datum set of results were gathered by driving the platform across an indoor sports hall with a laminated floor. This was selected as the controlled test because it is flat and level and had the least effect on vehicle performance, making it ideal to compare to other terrain test results.

For the main experiment, terrain types were chosen that each represent one of three main divisions: hard, soft and loose terrain. Site selection included a tarmac road (hard terrain), a grassy bank (soft terrain) and gravel (loose terrain). These were chosen to ensure equal representation of the three main divisions of terrain to give comparable results.

3.2.5 Sample Size

The sample size was kept to three runs for every test. This can be considered as a low sample size, however it was sufficient for this experiment because the aim at this stage was to recognise and measure the effect terrain has on vehicle performance and therefore the degree of accuracy of these experiments didn't need to be high. The choice of three runs can also be justified by the outcome of initial tests which have shown that by the third run there was a low degree of variance between results, which can be classed as the saturation point. Finally the sample size needed to be kept low in order to limit intervening variables, yet to be discussed.

The distance of each run was set to 5 metres to provide a regulated sample. This helped to cap the amount of data being gathered, which was necessary because only enough data needed to be obtained to identify the terrain type and too much data would have overwhelmed data processing and analysis. Additionally the available length of regular terrain at some of the test sites was limited.

3.2.6 Experiment Instrumentation/ Test-Rig

The instrument used in this experiment was a sensor rich vehicle platform. An off-the-shelf vehicle was selected as the test-platform that would represent the size and weight of the UGV class this study is focused on. This was in the form of the TRAXXAS E-Maxx (Figure 3.1), a highly capable 1/10 scale radio controlled off-road vehicle which was selected because it was affordable and sufficient to house the relevant sensors.

3.2.7 Hardware Developments

The platform was equipped with a suite of sensors used to measure various states of the vehicles reaction to the terrain conditions. Modifications were carried out in order to integrate these sensors (Figure 3.2), linkages and support brackets to connect the linear potentiometers to the suspension were added, tilt sensors were correctly positioned, and a flat panel was added to house the electronics and hold the additional power source for the sensors.

Figure 3.1 – The TRAXXAS E-Maxx off-road vehicle. This highly capable platform has been selected for the initial terrain interaction experiment (TRAXXAS 2014).

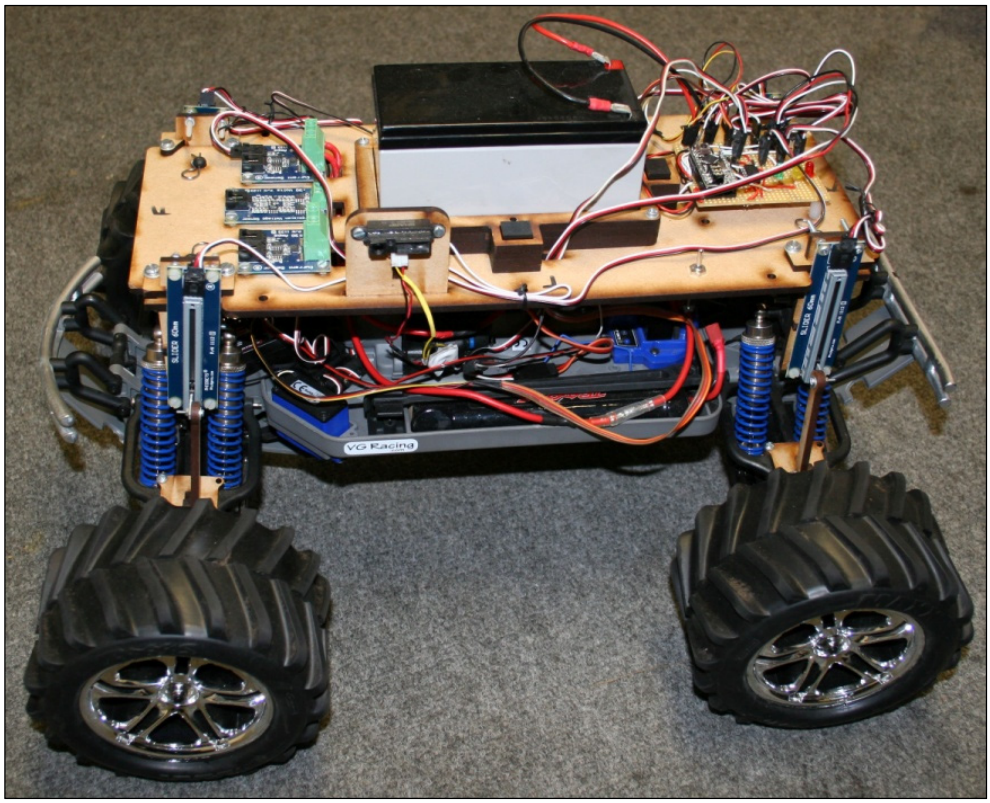

Figure 3.2 – Final modified test-rig/platform. Modifications have been made to the original chassis in order to house all the sensors, electronics and additional power source.

With the addition of this extra mass, the standard suspension was found to be insufficient, therefore a new set of dampers and springs were sourced and installed, which gave better feedback. A method of indicating when to start and stop logging data was also added to the platform, which needed to be done accurately and kept the same throughout the experiment in order to eliminate inaccuracies. This was done using an Infrared (IR) sensor which was placed on one side of the platform. This sensor looked for vertical markers at the start and finish placed exactly 5 metres apart, which told the system when to start and stop logging the data. The full range of all these developments can be seen in Appendix C.

3.2.8 Gathering/Storing Data

The system needed to be able to manage the sensors, gather data and then store it on-board to be analysed off-line; for which the PICAXE microcontroller and an EEPROM chip were selected. The PICAXE microcontroller was programmed in order to manage the sensors and read data at the correct time, as well as send the data to the EEPROM for storage. An EEPROM memory chip was used to store the data so it could be accessed offline as well as act as a failsafe in case of a power failure. The power source for all the electronics was kept separate from the drive system's power source. This was because the drive system has a greater current draw which would not only drain the power source quicker, but could potentially affect the sensors performance and create false data. Each of the sensors were wired directly into the PICAXE which supplied them with the correct (regulated) voltage, and the data read from them was stored on the EEPROM.

3.2.9 Constraints and Limitations

Weather is an intervening variable that could affect the characteristics of the terrain and consequently the vehicle's performance. It has already been discussed that sample size was kept low to help limit differences within the same patch of terrain. Additionally tests over the same type of terrain were carried out successively during the same day at the same time.

Another constraint within the experiment was with the capabilities of the test equipment. The first was the limitations of the sensors such as their resolution and reliability. Secondly, the range of the vehicle in terms of battery capacity because as it dissipated the power input would also drop, affecting the speed and time taken during the tests. This also limited the window in which successive tests could be carried out and is another reason why sample size was low.

The final and most significant constraint was with the PICAXE microcontroller which was selected as an affordable option that could be easily integrated, however its capabilities are limited in terms of sampling rate with a maximum clock speed of 64MHz, therefore it cannot control and monitor many complex situations; making its reliability and repeatability questionable.

3.2.10 Calibration Test (error elimination)

Once integrated, the sensors needed to be tested and calibrated to eliminate any errors and help find the relationship between raw data and actual values to assist in the data processing stage. To do this a test runway was developed with an obstacle of known dimensions (seen in Figure 3.3). The platform was driven over the obstacle and data was successfully logged and processed off-line. The raw data gathered from these calibration tests have been used to calculate actual measurements and create a set of formulas that are used to process data gathered from the main experiment. The results from this calibration test are displayed in Appendix D.

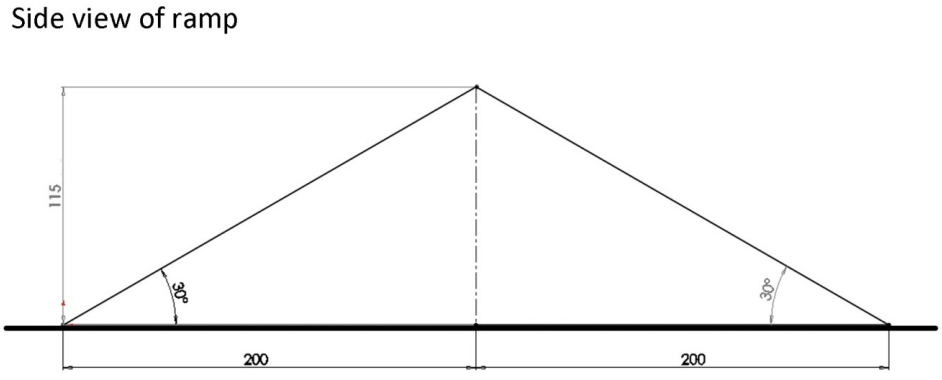

Figure 3.3 – Obstacle used for calibration tests. A ramp of known dimensions was used to calibrate the sensors and help convert raw data into meaningful measurements.

3.2.11 Experiment Procedure/Protocol

The test procedure consisted of the vehicle platform being set-off 1m before the start marker (to account for acceleration); it then drove 5m in a straight line and in a single direction across the selected terrain while logging the sensor data. Once it reached the finish marker the logging of data automatically stopped and the vehicle drove another metre before stopping (to account for deceleration). This procedure was carried out three times in succession over all sites before the data was downloaded for review, processing and analysis.

3.2.12 Displaying the Results

After all the tests were completed, the data received was downloaded and organised for processing. The raw sensor values were then converted to actual data, calculated using the formulas previously conceived from the calibration tests. The average of the data received from the three runs of each terrain test was taken and arranged graphically for comparisons to be made. The information displayed on these graphs includes the sensor data (performance) versus the time taken to traverse the 5m site. For each test there are two graphs, the first includes the suspension data, and the second includes the current and tilt angle data. This culminated in a graph comparing the data gathered from all terrain types using the same data set.

3.3 Results and Analysis

The full range of results from these experiments is also displayed in Appendix D. They validate the hypothesis that performance measurements (in this case using proprioceptive sensing) can be used to classify some terrain conditions. Data obtained from suspension stroke can be used to determine the surface roughness (topology) of the terrain (Figure 3.4). The frequency of the stroke is used to measures the vibration reaction (or turbulence) caused by crossing the terrain, which helps determine surface roughness. Additionally the variance of the suspension stroke can be used to determine how uneven the surface is; for example the stroke variance across a flat tarmac road was ±2mm, compared to gravel which showed a variance of ±6mm.

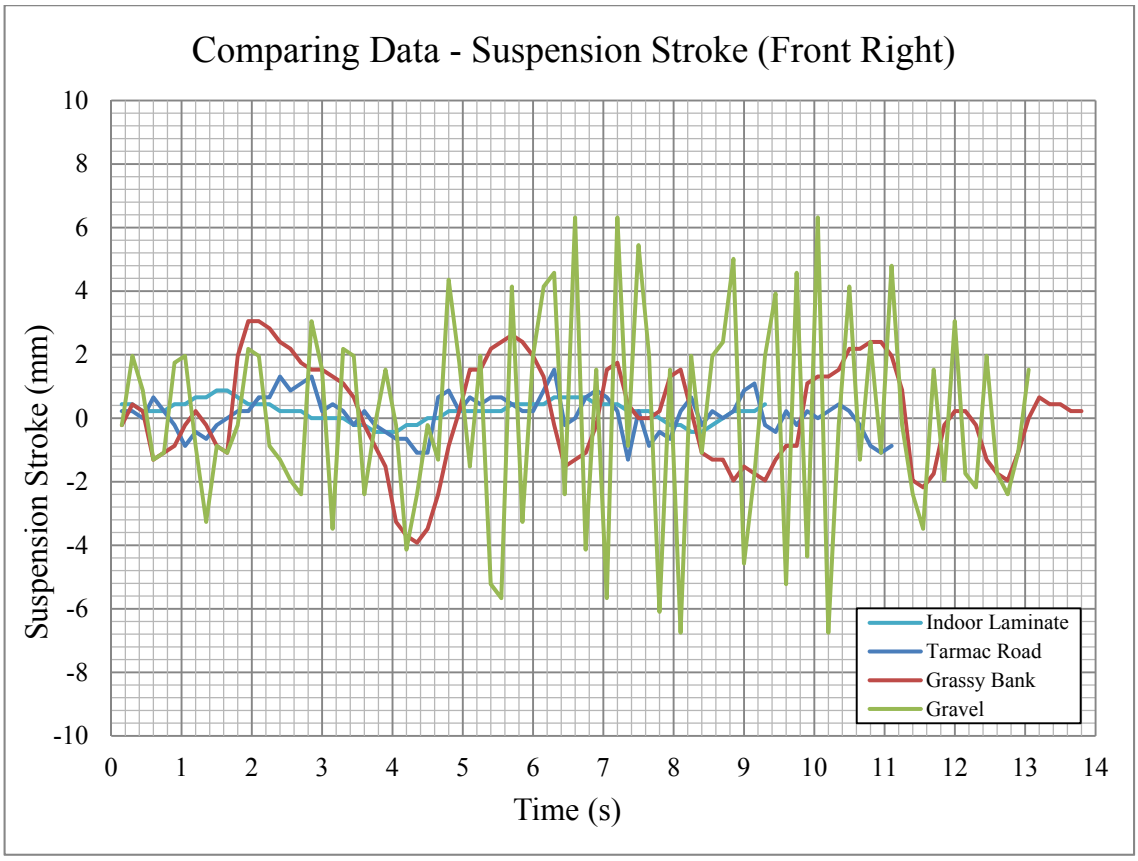

Figure 3.4 – Graph comparing suspension stroke data. The results show that suspension stroke measurements can be used to classify terrain surface properties (Odedra 2011).

In addition to suspension stroke measurements there were also current draw and tilt angle results. The current draw displays how hard the vehicle had to work in order to cross the terrain, and the tilt angle informs of the vehicles orientation due to the slope/gradient of the terrain. The current draw results not only display the affect the terrain had on the vehicle but are used to determine power consumption which is used for efficiency and range calculations. The results from the current draw measurements demonstrated that various terrain types affect the vehicle's performance at different rates and can therefore be used to classify terrain types using a 'difficulty rating'. Current draw will ultimately tell you how hard the vehicle had to work to cross the terrain and therefore is the ultimate measure of performance; however a rise in current draw could also be caused by environmental conditions such as the slope/gradient, which do need to be accounted for but aren't direct terrain properties. Tilt angle was therefore used to measure the vehicle's orientation which would be affected by slope and gradient. This was then used to distinguish whether a rise/fall in current draw was due to terrain properties or environmental conditions.

In summary, the state of the surface can be recognized in terms of how level it is and its roughness by using the suspension stroke data; and the measurement of the vehicles power consumption can help to detect the affect the terrain has on the vehicle, taking external factors into consideration such as slope/gradient that affected vehicle orientation. To conclude, this method of detecting the vehicle's reaction to terrain properties can be used to determine terrain types and classify them using a difficulty rating using the two key parameters discussed: the surface type and the rate at which it affects the vehicle.

3.4 Discussions

The additional research highlighted the measurable terrain conditions and what sensor technologies could be exploited to measure them. The previous review of terrain sensing and the subsequent research into testing methods has shown that the conditions which affect vehicle performance can be used to classify terrain. It was proposed that these parameters could be measured by monitoring the vehicle's performance while it is traversing the terrain, which was confirmed through experimentation. The results gathered from the tests carried out using the test-rig/platform was extremely useful in validating the theory that the interaction will cause a reaction to the vehicle and it's performance, which can be measured and used to identify the properties of the terrain and environment. The results were scrutinised off-line and the differences across various terrain types were identified, which helped classify the terrain type.

This initial experiment validated the possibility of using performance data from the vehicle-terrain interaction to classify terrain; however using proprioceptive sensing lacks accuracy, reliability and the ability to measure direct elements of the terrain. This area required further exploration with greater rigor in order to help develop a novel method of directly measuring terrain conditions. A further investigation was carried out into the area of terramechanics (Chapter 5) to better understand the complex parameters of the direct wheel-terrain interaction to find a unique method of gathering more direct quantitative data (Chapter 6). Additionally more scientific methods and tools are utilised to process and analyse collected data, and used to create a unique algorithm capable of more accurately classifying terrain (discussed in Chapter 7).

CHAPTER 4
METHODOLOGY

"Quantitative research is explaining phenomena by collecting numerical data that are analysed using mathematically based methods" (Aliaga, Gunderson 1999).

The primary aim of this study was to develop a novel method of measuring and classifying terrain in order to increase UGV system's perception and understanding of terrain conditions. This was done using quantitative research methods and an experimental approach, discussed further in this chapter.

4.1 Formulating a Research Problem

An extensive research study was carried out into the topic area in order to formulate a definitive research problem. The initial literature review helped to understand the topic area as well as highlight opportunities to contribute new knowledge. This focused the study towards a specific problem within the field of UGV development; identified as a UGV's ability to cope with terrain. Following the review, a better understanding of the problem allowed the main concept of the study to be derived, a hypothesis to be formulated and specific research questions to be generated; bringing clarity to the research problem.

In order to have a deeper understanding of the research problem and to further help answer the research questions, a second more in-depth review into the area of terramechanics was carried out. The aim of this additional study was to further focus the study on specific aspects of the research problem by gaining a better understanding of the properties pertaining to the wheel-terrain interaction; in particular the measureable variables within the interface which led to the construction of a research design that was used to validate the hypothesis (Kumar 2005).

4.2 Conceptualising a Research Design

There were two main functions of the research design, the first was to help identify the relevant methods and operational procedures in order to complete the study and the second was to help ensure the quality and validity of these procedures in order to accurately answer the research questions.

4.2.1 Variables

Before selecting the correct research design method, the variables within the study needed to be recognised. Creswell (2003) discusses how there are two main types of variables to consider: independent variables which influence or affect outcomes, and dependant variables which depend on, and are influenced by the independent variables. Additionally the control variables need to be taken into account, which are those that are constrained and kept the same throughout the study to ensure accuracy. Kumar (2005) best summarises this by stating that during the study the independent variable(s) need to be allowed to have the maximum effect on the dependant variable(s), while the effect of extraneous and chance variables are minimised.

The preliminary experiment discussed in Chapter 3 focused on variables of the vehicle-terrain interaction. For the main study however the independent, dependant and control variables were derived from properties of the wheel-terrain interaction; and the measure of their relationship was paramount to the outcome of the study.

4.2.2 Research Design Method

With the existence of quantitative variables and due to the scientific nature of the investigation, the type of research design method this project relates to is experimental. There are many types of experimental design methods which all involve data being gathered during a series of experiments. This study employed the matched-control method where one experiment was considered as a controlled test and the others experimental. This type of method was selected because it is systematic in manipulating and controlling one or more of the variables in order to measure the change in others

and then relating the results to those from the controlled case. This was ideal for measuring the difference between terrain experiments in this study.

This method is sometimes classed as challenging because of the difficulty in selecting a suitable variable as the basis for matching when more than one variable has to be manipulated. The selection of this method was justified however because the increased complexity of the variables formed the basis of the unique method of terrain classification, the principal aim of this study.

4.3 Constructing an Instrument for Data Collection

"There are two major approaches to gathering information about a situation, person, problem or phenomenon. Sometimes, information required is already available and need only be extracted. However, there are times when the information must be collected" (Kumar 2005, p118).

This approach lends itself to two types of data: primary and secondary. Primary sources of information are 'extracted' by interrogating or observing the subject, whereas secondary sources of data collection are in the literature of previously collected data. Secondary data from previously documented work is generally easier to obtain however its validity and reliability is always questionable and with the fast pace of technological developments within the field of robotics, secondary data can quickly become dated and obsolete; highlighting the need for collecting new (primary) data within this project. There are three primary data collection sources: observation, interviewing and questionnaires; however due to this project not including a human element, the only way to gather new data was with the observation method. The observation in this study was of the terrain, which could have been made under two main conditions: natural which requires observing the subject in its natural operation/environment, and controlled which includes introducing a 'stimulus' for the subject to react to and observing the reaction. With the primary focus of this study being on the wheel-terrain interaction then the controlled method was deployed where the vehicle was introduced as the stimulus and the measure of the terrain at the wheel-terrain interaction was scrutinised to help classify the terrain.

4.3.1 Recording the Data

During the experiment ‘observations’ needed to be recorded, which in this study were of the parameters pertaining to the wheel-terrain interaction. There are a number of different observation recording methods including the narrative method where the observation is merely described, the scaling method which allows the observer to rate various aspects of the interaction; however for this study the best method of recording data was using data capturing equipment/instruments.

This method was ideal for this study firstly because it is a more accurate way of measuring quantitative variables and secondly it allows more complex variables to be measured that could not be done any other way. Another advantage of using this method is the ability to revisit and examine the data long after the experiment has been completed (off-line analysis), which means that the process of data analysis can be more thorough.

4.3.2 Constraints

The final elements that needed to be considered when constructing the instrument for data collection were the constraints, such as the limitations of test equipment and facilities. The limitations were dictated in this case by the availability of certain terrain types and the capabilities of the test equipment such as accuracy, reliability and resolution to name but a few. All these elements established the validity and reliability of the data collection method and quality of results and therefore they needed to be identified and limited/controlled (if possible).

4.4 Selecting a sample

In this study (as in many studies) it was not possible to measure all the individual elements/variables that make up the study; therefore the concept of sampling had to be employed. Sampling includes selecting a sample which represents the total ‘population’ where the average of the data collected becomes an estimation of the overall outcome. Sampling is usually employed to make the study feasible as it saves time and resources.

There are three categories of sampling strategies: random/probability sampling, non-random/non-probability sampling, and finally mixed sampling. Selecting the correct sampling type is very important as it will form the strategy of the study and will help to achieve maximum precision in the estimates, however all selections must be justified and made rationally, avoiding bias (Creswell 2003).

For this study non-random/non-probability sampling was selected where a particular terrain type was selected for the experiments and variations within that type represented a change in terrain conditions. This method of non-random/non-probability sampling is called judgemental or purposive sampling for which the primary selection is judged by the researcher who selects the elements that are likely to provide the best information. Kumar (2005) states that this type of sampling is extremely useful when you want to develop something about which only little is known; which in this case was to help discover more about terrain.

4.4.1 Sample Size

Alongside selecting the sampling type, the required amount of (gathered) data needed to be to be decided upon. Better known as the sample size, this determines the accuracy of the results. In this study enough data needed to be gathered to have a greater level of confidence in the results, however in the pursuit of increasing the degree of accuracy in the results there was a risk of gathering too much data, causing problems in sorting and processing the data.

The key was to select a sample size depending on the level of accuracy required and limit it to the point where no new data was being acquired, known as the saturation point. An important consideration that needed to be taken into account when deciding the sample size in this study was the number of times tests could be repeated before terrain conditions dramatically changed.

4.5 Research Proposal

The write up of the research proposal preceded the experiment. The proposal included the framework of the study, discussing the findings and highlighting the total intended research process. It informed of what was going to be done (research questions), how it was going to be done (research methods/tools) and why certain methods were selected (justification). The key part of the proposal was in the discussion of the experimental design, which highlighted the main rationale of the experiment and detailed all the elements of the study/experiment.

4.6 Collecting Data

Once the research design and experimental design stages were completed, collecting the data became procedural. The independent and dependant variables needed to be measured, the relevant control variables needed to be fixed and monitored, and tests were carried out in such a way to limit any external interference (such as environmental conditions that could affect the terrain). The emphasis was on accuracy, repeatability and reliability within the constraints and limitations of the experiment previously discussed.

4.7 Processing Data

Once the experiment was successfully completed and the data gathered, it needed to be sorted and processed for analysis. The first stage was to sort the gathered data to check for errors and inconsistencies and convert the raw data into a logical format that was then displayed it in a readable format (e.g. in a table or graph), which made it easier to make sense of the information. Subsequently for this study, statistical analysis was used to interrogate the quantitative data to create a unique classification method. All these stages of data processing were done with the assistance of computer software, which helped to convert, display and analyse the data quickly and accurately. Advanced software programs were also used to handle more complex statistical and mathematical procedures to develop a unique algorithm capable of terrain analysis and classification.

4.8 Research Report

The final step of the research process was to compile a scientific research report. Discussed in this report are the details of the study, the research process, the experiment details and the results. After displaying and analysing the results of the experiment, discussions are made and conclusions drawn where the research questions and hypothesis is revisited to measure the outcome of the study. Finally ideas for further work are presented.

4.9 Discussions

In this chapter the research methods used to complete the study are discussed. The research problem was formulated through a thorough research review which helped develop the research questions and create a hypothesis. With the study including numerous quantitative variables and the generally scientific nature of the investigation, an experimental approach was employed to prove (or disproved) the hypothesis.

The selection of the different variables within the experiment was vital to the outcome of the study. The independent and dependant variables were chosen from the parameters of the wheel-terrain interaction (discussed in later chapters), while the extraneous and chance variables that needed to be controlled and limited were those of the environment, equipment and facilities. With such a large range of terrain types in existence, not all of them could be used and therefore a sample was used to represent a terrain class with specific (measurable) conditions. A relevant sample size was also selected to gather the correct amount of data before the saturation point, giving confidence in the results.

Finally the (novel) data collection instrument was used to gather raw data. This went through a number of processes to organise, sort and convert into a more logical format. The results were not only graphically displayed to highlight the outcomes, but more significantly used to create a unique classification algorithm.

CHAPTER 5
TERRAMECHANICS

An additional review investigating the fundamentals of terrain mechanics and complex quantitative parameters of the wheel-terrain interaction was carried out for this study; the findings of which are discussed further in this chapter.

"Terramechanics is a field study that deals with the physical mechanics of land locomotion; it concerns itself with the interaction problems that occur between terrain and various kinds of mobile plant" (Muro, O'Brien 2004). This area has stimulated a great deal of interest in the study of vehicle mobility over unprepared terrain within a number of industries such as construction, agriculture, cross-country transport and even the military. The aim of terramechanics is to "provide guiding principles for the rational development, design, and evaluation of off-road vehicles and terrain-working machinery" (Wong 2010). Established mathematical models for vehicle-terrain systems have enabled engineers to "evaluate, on a rational basis, a wide range of options and to select the appropriate vehicle configuration for a given mission and environment" (Wong 2010).

5.1 Measuring Terrain Values

The discipline of terramechanics has been said to be 'invented' by Dr Mieczyslaw Gregory Bekker during his study on land locomotion mechanics (Muro, O'Brien 2004). Bekker wrote extensively on the subject over a period of approximately 20 years from 1950-70 with his pioneering work presented across three published books: *Theory of Land Locomotion* (1956), *Off-the-road Locomotion* (1960), and *Introduction to Terrain-vehicle Systems* (1969). This work famously led to the development of the Lunar Rover (Figure 5.1) used during the 1971-2 Apollo missions to the Moon. One of the most significant outcomes of this work, however, was the development of the Bevameter technique which has become widely used in terramechanics to measure terrain values.

Figure 5.1 – Ferenc Pavlics, Mieczyslaw Bekker & Sam Romano with the Lunar Buggy. Dr Bekker's pioneering work in the area of terramechanics led to the development of wire mesh tyres that could efficiently traverse the surface of the Moon (BME Omikk 2000).

5.1.1 Bevameter

The 'Bekker Value Meter' better known as the bevameter technique, is based on the "premise that terrain properties pertinent to vehicle mobility can best be measured under loading conditions similar to those exerted by an off-road vehicle" (Wong 2010, p68). Mechanical properties of soils, like properties of any other solid, are defined by stress-strain relationships. Vehicles traveling across terrain produce horizontal loads balanced by soil thrust and vertical loads indirectly balanced by motion resistance, therefore "any empirical approach to the measurement of soil properties must entail the determination of both the horizontal and vertical stress-strain relationships" (Bekker 1969, p5). The bevameter technique therefore comprises of two separate tests to simulate vertical and horizontal loads to derive mechanical terrain values.

The horizontal load is better categorized as the tangential or shear stress. The shear tests involve pressing a treaded circular plate or 'shear ring' into the soil at different normal loads, rotating it and measuring the resulting torque and angular displacement. The results are used to derive the shear stress-strain relationship which is based on the Mohr-Coulomb's Equation (1) where shear stress τ is related to two soil parameters: cohesion c and internal friction φ through normal stress σ at the loading area (Bekker 1969).

$$\tau = c + \sigma \tan\varphi \tag{1}$$

Cohesion is defined as the bond that cements particles of the terrain together regardless of the normal stress between the particles; however the internal friction angle is also significant because 'frictional' particles can only be held together when a normal stress is present (Wong 2001). The calculated shear stress - shear displacement relationship is then used to estimate the tractive-effort slip characteristics and in turn the maximum traction of a vehicle.

To simulate the normal (vertical) pressure distribution on the vehicle-terrain interface, a plate comparable to the contact area of a vehicle wheel (or track) is penetrated into the terrain a number of times and the results are plotted. The resulting empirical curves $p(z)$ are fitted with sinkage Equation (2) where z is the sinkage depth, p is the normal pressure, k is a modulus of soil deformation and n is an exponent of deformation.

$$p = kz^n \tag{2}$$

$$p = \left[(k_c/b) + k_\varphi\right]z^n \tag{3}$$

Bekker (1969) later stated that the k-value in Equation (2) was very sensitive to the form of the test plate greatly affecting the results, which he classed as 'unacceptable' in characterising soil parameters. Further work led to the Bernstein-Goriatchkin Equation (3) being utilised where k_c and k_φ are 'cohesive' and 'frictional' moduli of deformation, and b is the smaller dimension of the rectangular loading plate (or the radius of a circular plate). Two tests with different sized plates are carried out to create redundancy and the overall results are used to obtain the pressure-sinkage relationship of the given soil, from which vehicle sinkage and motion resistance can be predicted.

The results from both the shear strength and plate penetration tests are combined and fitted into mathematical models where the soil is characterised and its overall mobility performance is predicted, completing the bevameter technique.

5.1.2 Cone Penetrometer

The Cone Penetrometer technique developed during the Second World War is another empirical method used to measure and characterise terrain. The Waterways Experiment Station (WES) of the U.S. Army Corps of Engineers developed this method to provide military intelligence and reconnaissance personnel with a simple field device for assessing terrain trafficability on a 'go/no go' basis, taking vehicle mobility into account (WES 1948).

The instrument used for this technique comprises of a 1.59cm diameter rod with a 30-degree circular cone and a 3.23cm² base area. The technique requires the cone to be penetrated into the soil at 3cm/s and force measurements displayed on a dial are taken at intervals throughout the experiment. A dimensionless parameter known as 'cone index' (CI) is then derived using the force per unit of the cone's base area, which represents both the shear strength and deformation characteristics of the terrain.

This simple method was suitable for its original purpose of making 'go/no go' decisions during the "emergencies of World War II" (WES 1948); however Wong (2010) states that "this method alone is not sufficient for adequately defining the mechanical properties of the terrain that are pertinent to vehicle mobility".

5.2 Ground Pressure

In the measurement techniques discussed, terrain values and mobility characteristics are derived by using instruments to apply vertical and horizontal loads. These loads are used to simulate the pressure exerted on the terrain by a vehicle, known as ground pressure. Ground pressure (denoted p) is a vehicular parameter measured in Pascals (Pa) defined as the force per unit area. This can be calculated by using the standard pressure Equation (4) where and F is the force acting on the contact surface area A.

$$p = F/A \tag{4}$$

Ground pressure is important to vehicle mobility (especially in soft terrain) because it defines the amount of pressure that will be exerted by the vehicle on the ground, affecting sinkage and increasing motion resistance. The normal force exerted by a vehicle is relative to its weight; however the contact surface area (or contact patch) is dependent on the interaction between the drive system and terrain, making it vital to ground pressure. An early test using a passenger vehicle was carried out to demonstrate the effect contact surface area has on ground pressure. During the experiment the tyre pressure was adjusted to change the contact surface area (Figure 5.2), which had a great effect on the ground pressure (Figure 5.3).

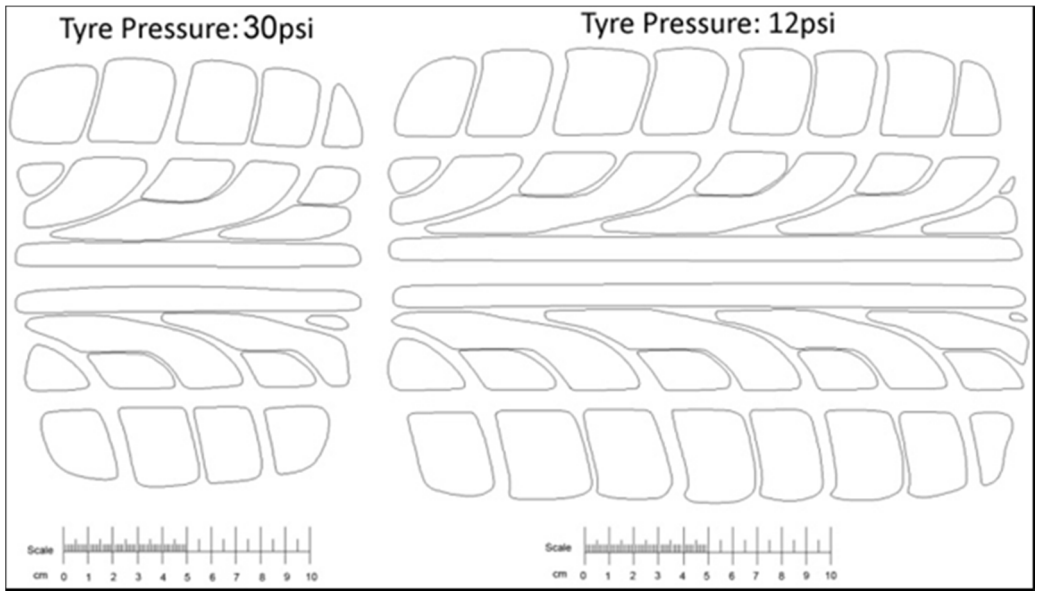

Figure 5.2 – Two tyre footprints with different contact surface areas. This experiment demonstrates that contact surface area affects ground pressure (Odedra, Prior et al. 2009).

5.2.1 Defence Standards

"One of the most demanding features hoped for modern military wheeled tactical vehicles is to achieve a high degree of mobility" (Kaczmarek 1984). To better understand this, an extensive review was carried out looking at the specifications of a large range of worldwide military vehicles including DARPA Grand Challenge entrants. This study led to the discovery of strict military standards that vehicles have to adhere to in order to operate in the field.

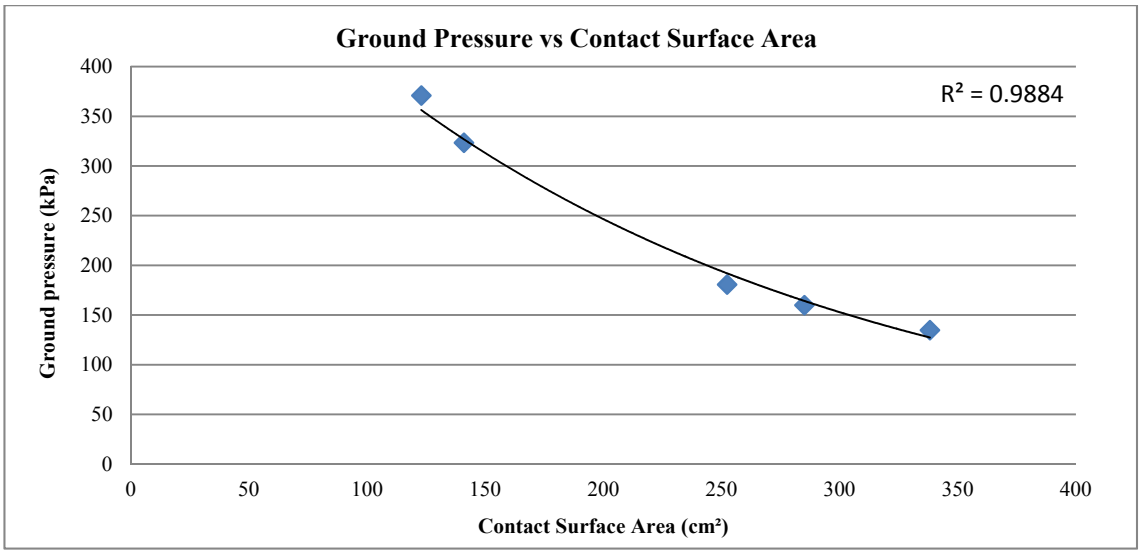

Figure 5.3 – Graph displaying results from the ground pressure experiment. The results show the relationship between contact surface area and ground pressure (Odedra, Prior et al. 2009).

The U.K. Ministry of Defence (MoD) require all operational vehicles to meet Defence Standard (DEF-STAN) 23-06. Within the specifications there are five mobility classes ranging from Low Mobility Load Carrier (LMLC) to High Mobility Load carrier (HMLC) for which ground pressure is a key criterion alongside ground clearance and tilt angle stability (Ministry of Defence 2000). Figure 5.4 displays the ground pressure limits set by the MoD for vehicles weighing less than 4 tonnes, highlighting the relationship between ground pressure and mobility.

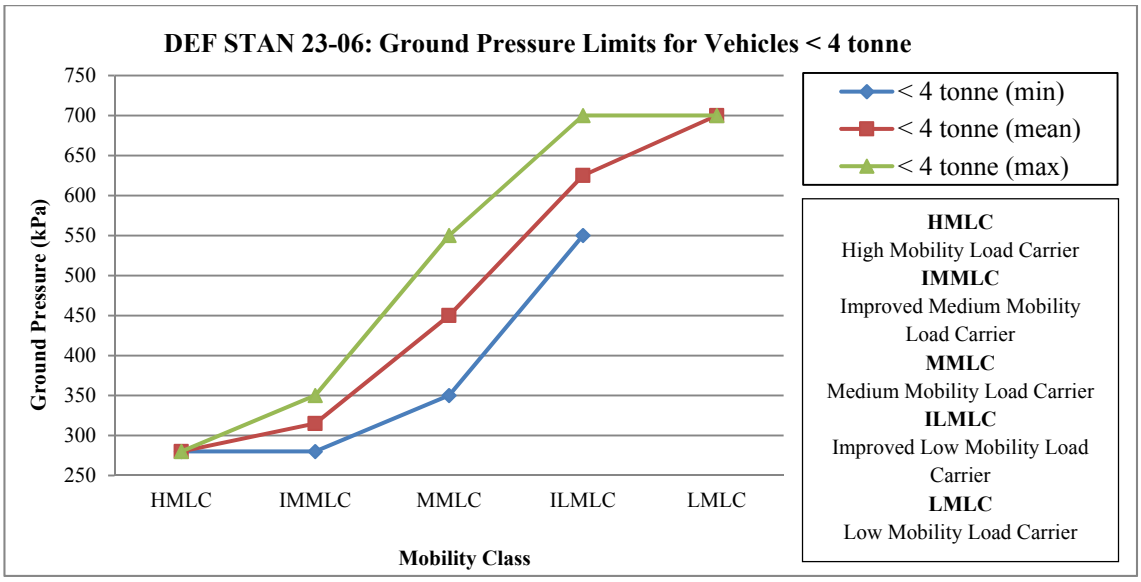

Figure 5.4 – Graph showing ground pressure limits for military vehicles. This emphasises the importance of ground pressure on mobility (Odedra, Prior et al. 2009).

5.2.2 Central Tire Inflation System

The earlier experiment that involved adjusting a passenger vehicle's tyre pressure, established the relationship between contact surface area and ground pressure (Figures 5.2 & 5.3). With ground pressure being vital to mobility then the idea of being able to adjust the vehicle's ground pressure (and mobility characteristics) by varying the tyre pressures greatly interested military organisations worldwide; therefore after the Second World War, both the U.S. and Soviet Union experimented with a system that "permitted the vehicle tyre pressures to be regulated by the vehicle driver/crew from within the vehicle cab, while on the move" (Kaczmarek 1984, p1255). This system is now widely used in off-road military vehicles and is known as the Central Tire Inflation System (CTIS), which gives the driver the ability to inflate/deflate the tyres with the press of a button, maximizing the vehicle's mobility by dynamically controlling the vehicle's ground pressure.

5.3 Wheel-Terrain Interaction

"A vehicle of adequate power moves across country if the strength of the ground is sufficient to support its weight without much resistance to motion and to provide the thrust required for propulsion" (Bekker 1960, p25).

Terramechanics at its core is focused on better understanding this physical relationship, with a fundamental emphasis on the interaction between the wheel and terrain. This is a complex problem and extensive work has been done to explore the mechanics of the wheel-terrain interaction.

There are four possible wheel-terrain scenarios (Figure 5.5) defined by the "mechanical properties of the materials involved in the construction of both the wheel and the road" (Bekker 1956, p186):

a) A rigid wheel travelling over deformable terrain
b) A rigid wheel travelling over rigid terrain
c) A deformable wheel travelling over rigid terrain
d) A deformable wheel travelling over deformable terrain

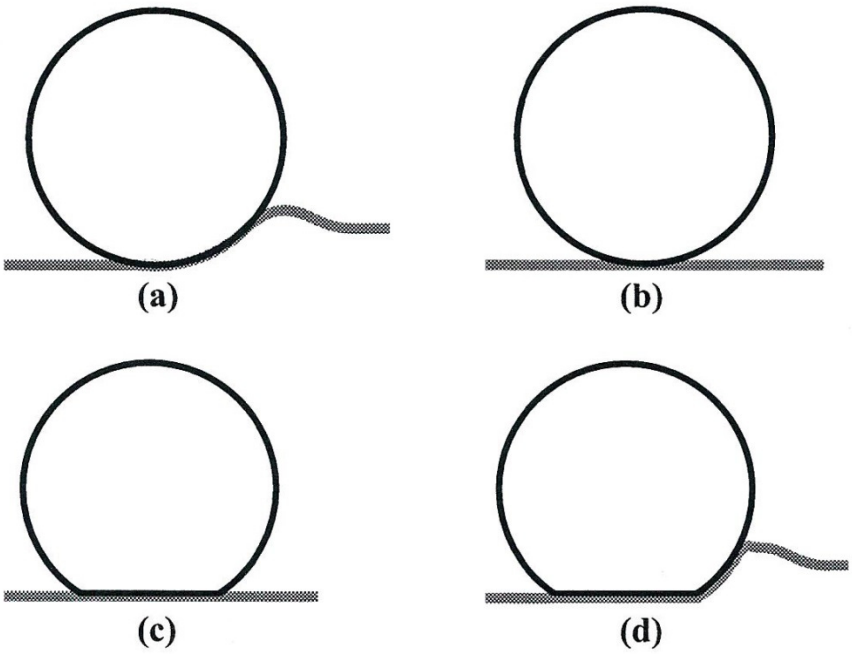

Figure 5.5 – The four possible wheel-terrain interaction scenarios. a) rigid wheel travelling over deformable terrain, b) rigid wheel travelling over rigid terrain, c) deformable wheel travelling over rigid terrain, d) deformable wheel travelling over deformable terrain (Iagnemma, Dubowsky 2004).

The scenario of a rigid wheel travelling over deformable terrain (a) has been the principal focus of many terramechanics investigations. This is because deformable terrain will greatly affect a vehicle's mobility performance and even pneumatic tyres can behave like a rigid rim if the inflation pressure is sufficiently high and the terrain is soft enough (Bekker 1969). This scenario is also significant to this study because military and space UGVs (the vehicle type this study is motivated by) predominantly possess rigid wheels and have to operate in unstructured environments consisting of deformable terrain.

5.3.1 Analytical Model

Bekker (1956) set out to simplify the problem and proposed an analytical model of the interaction between a rigid wheel and deformable terrain. This model is used to calculate the significant parameters of the interaction during soil deformation and now forms the basis of most equations within the field of terramechanics to help predict vehicle performance. Figure 5.6 shows a simplified version of this model by Wong and Reece (1967), which displays the significant parameters and stresses that occur at the wheel-terrain interface.

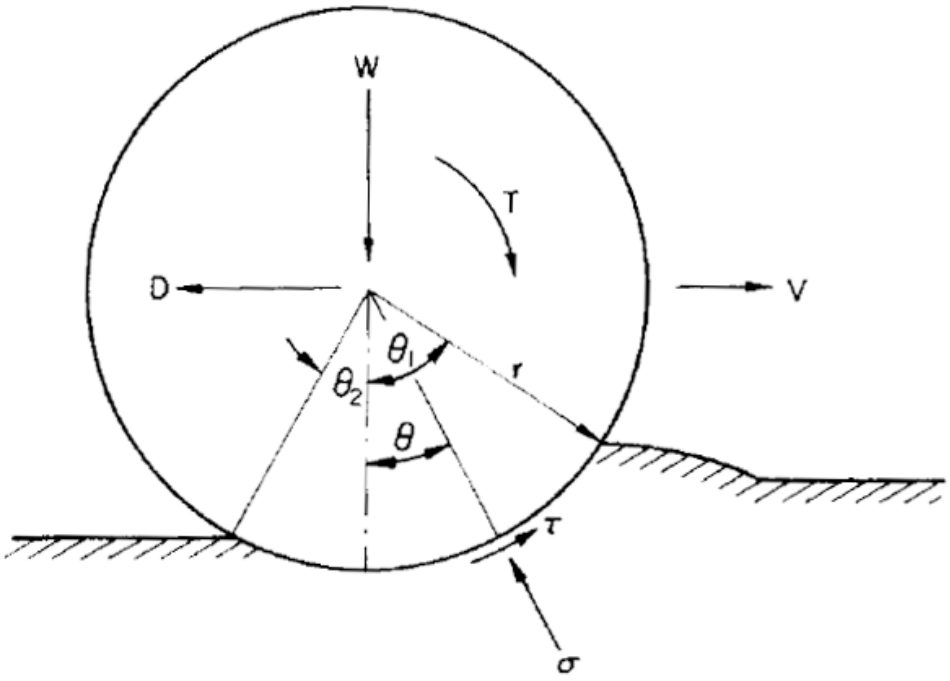

Figure 5.6 – Analytical model of a driven rigid wheel on deformable terrain. This model displays the parameters and stresses involved during the wheel-terrain interaction (Wong, Reece 1967).

The wheel-terrain interaction model displayed above in Figure 5.6 shows a rigid wheel of radius *r* and width *b* driving through deformable terrain. The wheel has a vertical load *W* and a horizontal force *D* more commonly categorized as drawbar pull[1] and denoted *DP*. An actuator (motor) applies torque *T* to the wheel's rotation axis, giving the wheel centre a linear velocity *V*.

At the wheel-terrain contact interface, θ represents an arbitrary angle from the vertical axis. The angle from where the wheel first makes contact with the terrain to the vertical axis is denoted as θ_1 (also known as the front region). Likewise the angle from the vertical to where the wheel loses contact with the terrain is denoted θ_2 (also known as the rear region); the entire contact region is therefore defined as $\theta_1 + \theta_2$. There is radial stress across the contact interface acting normal to the wheel denoted as σ and shear stress acting tangentially denoted as τ.

[1] Drawbar pull is the net traction force which is described further in Section 5.3.3

The equilibrium of a driven rigid wheel travelling across the ground is well known by Equations (5-7), which highlight that it is necessary to determine the relationships between radial/tangential stresses and other parameters in order to predict wheel performance (Wong, Reece 1967).

$$W = rb\left[\int_{\theta_2}^{\theta_1} \sigma(\theta)\cos\theta\, d\theta + \int_{\theta_2}^{\theta_1} \tau(\theta)\sin\theta\, d\theta\right] \tag{5}$$

$$DP = rb\left[\int_{\theta_2}^{\theta_1} \tau(\theta)\cos\theta\, d\theta - \int_{\theta_2}^{\theta_1} \sigma(\theta)\sin\theta\, d\theta\right] \tag{6}$$

$$T = r^2 b\int_{\theta_2}^{\theta_1} \tau(\theta)\, d\theta \tag{7}$$

5.3.2 Pressure Distribution

Bekker (1956) predicted that the soil's reaction to a (rigid) wheel rim was the same as beneath a plate penetrated to the same depth as per bevameter tests, assuming that the distribution of pressure is situated 'bottom dead centre' under the wheel. However further investigation by Wong and Reece (1967) found that the location of maximum normal radial pressure (denoted θ_m) is located further forward and situated within the front region θ_1, shown in Figure 5.7 below.

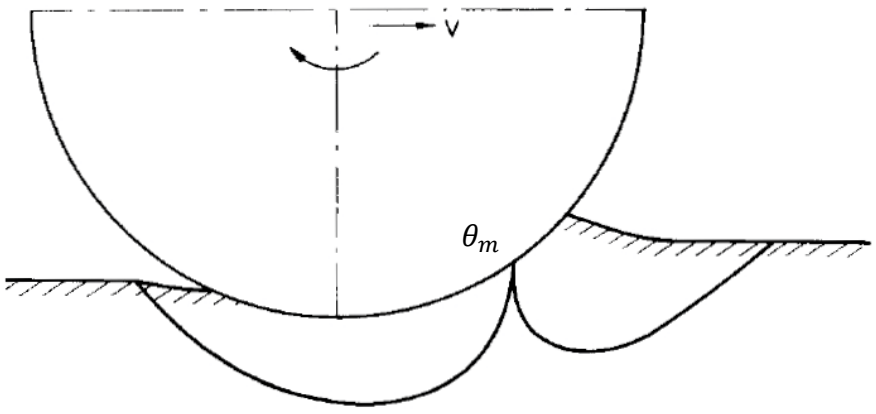

Figure 5.7 – Diagram showing the location of maximum pressure on the contact interface. The location of maximum pressure is further forward than results from plate penetration tests (Wong, Reece 1967).

Deformation occurs during wheel-terrain interaction due to soil failure. There are two soil failure zones located either side of θ_m illustrated in Figure 5.7 by the two flow curves. Figure 5.8 shows a free body diagram of the wheel-terrain interface developed by Iagnemma and Dubowsky (2004) where θ_m is the (angular) location of maximum pressure from the vertical axis, with the two stress regions σ_1 and σ_2 situated either side. (Additional parameters include sinkage depth *z* and angular velocity ω).

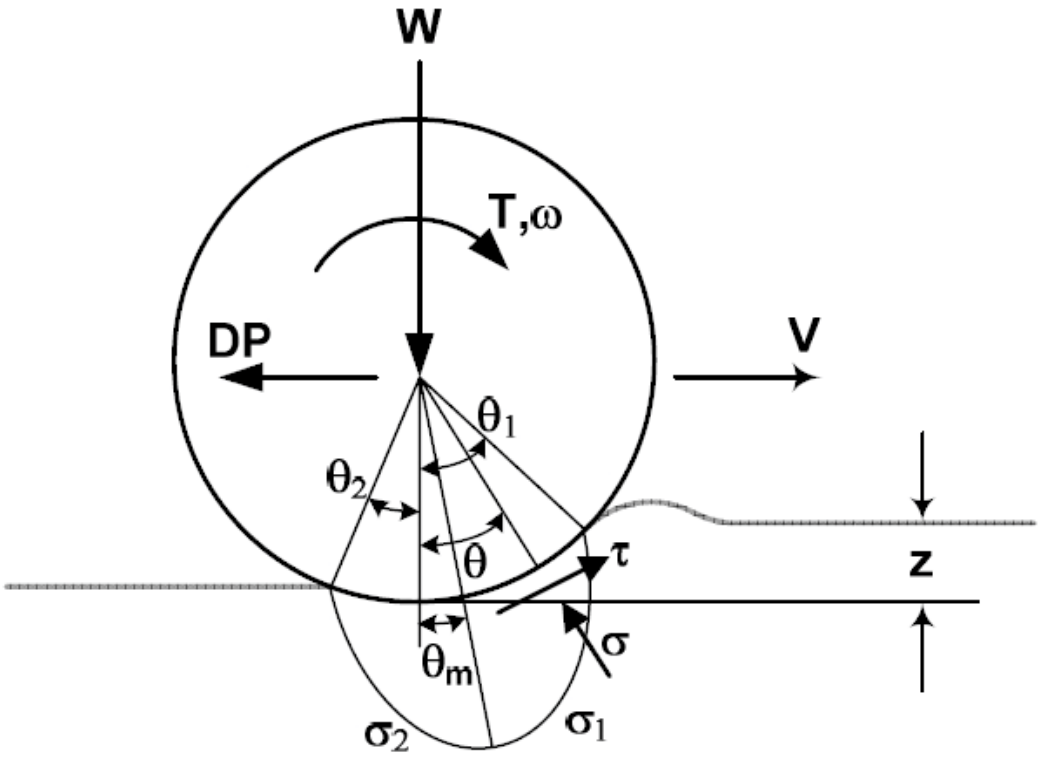

Figure 5.8 – Free-body diagram of a rigid wheel on deformable terrain. This diagram highlights the stress distribution under a rigid wheel at the contact interface (Iagnemma, Dubowsky 2004).

Wong and Reece (1967) carried out a number of experiments to verify their earlier claims, which not only verified that θ_m is situated in region θ_1 but also indicated that its position is related to slip and shifts forward with increasing slip (Figure 5.9). Slip *i* can either be negative or positive and is calculated using wheel angular velocity and wheel linear velocity as seen in Equation (8) below (Senatore, Iagnemma 2014):

$$i = 1 - \frac{V}{\omega r} \tag{8}$$

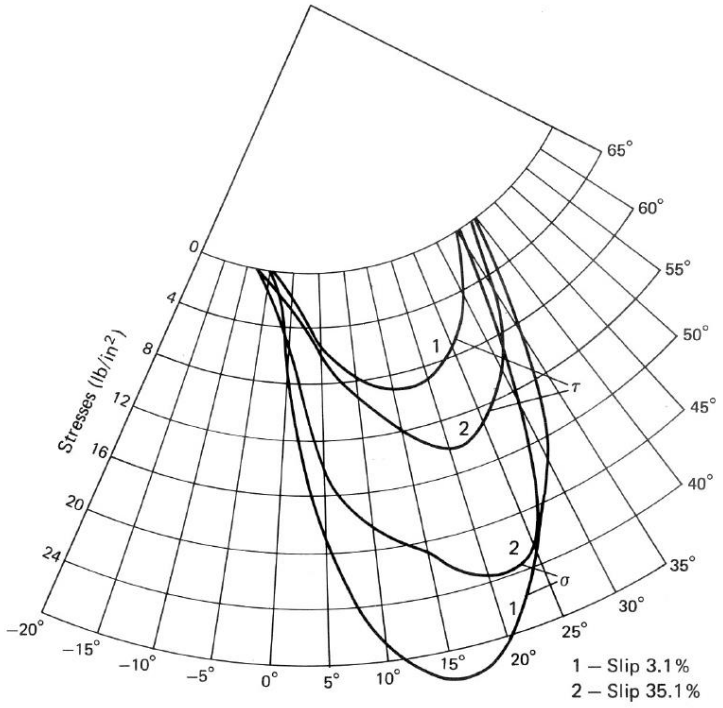

Figure 5.9 – Measured normal and shear stress on the contact patch. The position of the maximum stress is related to slip as it shifts forward with increasing slip percentage (Wong, Reece 1967).

The results of Wong and Reece's experiments, seen in Figure 5.9 above, display a significant change in the location of normal and shear stress distribution during tests of varying slip amounts. This relationship can be expressed by Equation (9) where c_1 and c_2 are coefficients related to soil conditions:

$$\theta_m = (c_1 + c_2\, i)\, \theta_1 \tag{9}$$

These results verify that θ_m is further forward than 'bottom dead centre' and relates to slip. This study also indicated that θ_m depends on the compressibility of the terrain, represented by the coefficients in Equation (9). These results also show a relationship in the rate of change of normal and shear stress distribution. Shilby, Iagnemma et al. (2005) carried out experiments taking normal and shear stress distribution measurements around a driven rigid wheel while it travelled across a diverse range of terrain types. The results seen in Figure 5.10 verify that an (approximate) linear relationship does exist between normal and shear stress distribution regardless of terrain type and therefore normal stress measurements could be used to estimate shear stress values.

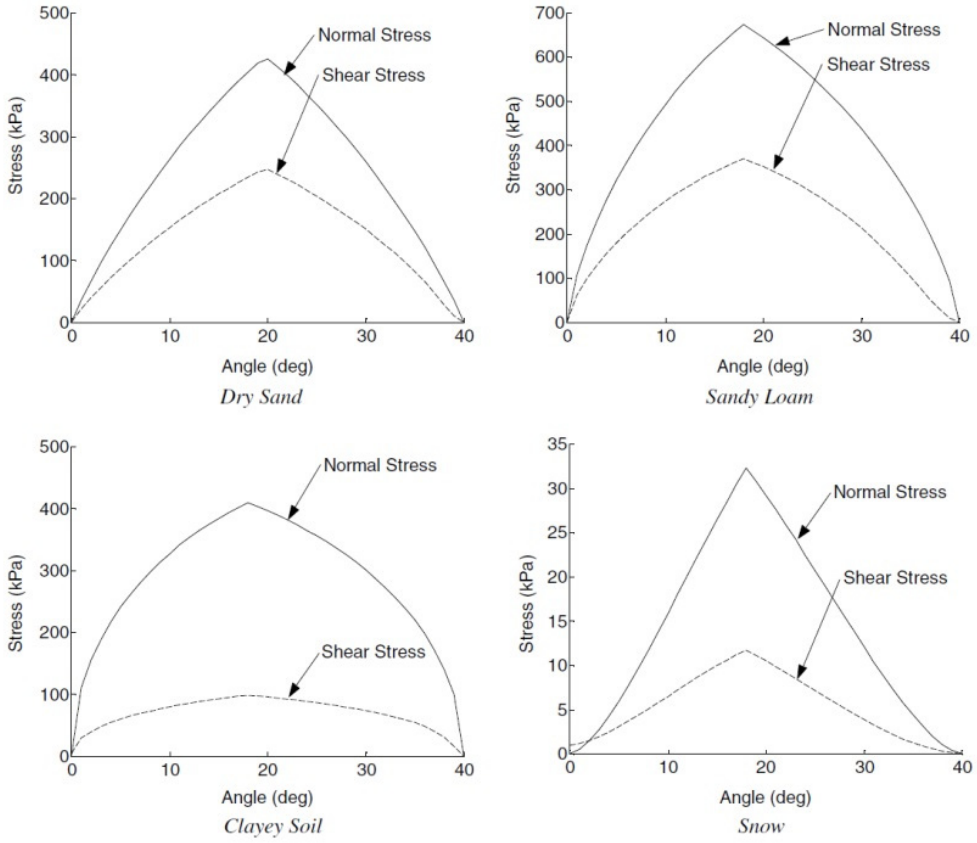

Figure 5.10 – Normal & shear stress distribution results across various terrain types. These results show the linear relationship between normal and shear stress (Shibly, Iagnemma et al. 2005).

5.3.3 Thrust and Drawbar Pull

The maximum thrust a vehicle possesses will determine its (traversing) performance; however this becomes affected by resistance due to environmental conditions which in this case is due to parameters of the wheel-terrain interaction. A vehicle's horizontal thrust H (or tractive effort) is developed through its shearing action on the terrain surface and therefore can be estimated using Equation (1). If the wheel-terrain contact area is known and the pressure distribution on the contact patch is uniform, then the maximum thrust (across a known terrain) can be predicted using Equation (10)[2] where A is the contact area of the wheel and W is the load on the wheel (Wong 2010):

$$H = \tau A = (c + \sigma \tan \varphi)A = Ac + W \tan \varphi \tag{10}$$

[2] The equation is dependent on soil properties cohesion c and internal friction angle φ.

Drawbar pull (which was mentioned earlier) is therefore defined as the net traction force, calculated as the difference between thrust and the sum of all the resisting forces $\sum R$ acting on the vehicle:

$$DP = H - \sum R \tag{11}$$

5.3.4 Wheel Diameter

Bekker's early theories have successfully been used for decades to model large vehicle mobility performance; however the accuracy of these theories are called into question when dealing with smaller vehicles. Bekker (1956) himself stated that his theories "become less accurate" when dealing with wheels smaller than 50cm in diameter, but during that time smaller wheels were not as common so didn't need to be considered. Today's modern UGVs however, possess smaller diameter wheels and therefore wheel-terrain interaction models are needed to be modified to account for this. Extensive work has been done in this area, for example Senatore and Iagnemma (2014) have developed vehicle interaction models for small lightweight vehicles; and Meirion-Griffith, Nie and Spenko (2014) have modified Bekker's original pressure-sinkage models to include wheel diameter and width, enabling more accurate mobility predictions for smaller vehicles. This investigation also found that smaller diameter wheels act significantly different from flat plate approximations due to the increased curvature of the wheel-soil interface.

5.4 Discussions

This additional review into the area of terramechanics highlighted the parameters involved during wheel-terrain interaction, which was greatly valuable to this study. Bekker's early works proposed the bevameter technique used to measure and classify terrain. The tractive (shear) capabilities of the terrain are calculated using the Mohr-Coulomb Equation (1) and deformation calculated using Bekker's pressure-sinkage Equation (3). These models have been used to successfully predict vehicle performance, however they require prior knowledge of terrain parameters such as cohesion and internal friction properties and therefore cannot easily be utilised for real-time classification while traversing unknown terrain.

The simplified analytical model of the wheel-terrain interaction was greatly insightful and highlighted the importance of stresses across the contact interface in relation to equilibrium Equations (5-7). Work by Wong and Reece took this further and proved that maximum radial pressure at the contact interface between a rigid wheel and deformable terrain is not situated 'bottom dead centre' as per plate penetration tests. Their findings expressed a relationship between the location of maximum stress and slip illustrated in Equation (9); however this calculation is dependent on terrain compressibility as represented by coefficients c_1 and c_2 and therefore prior knowledge of terrain conditions are again required.

The analytical models of the wheel-terrain interaction discussed (as well as many others not mentioned) have been used by many to predict mobility performance; however they present the interaction problem as two dimensional (2D) and calculate stress across the three dimensional (3D) contact patch through simply multiplying stress values by the wheel width b. These models therefore assume that the distribution of pressure exerted by the wheel across the width of the contact interface is uniform, which is known from contact mechanics not to be true (Meirion-Griffith, Spenko 2010). Nagatani et al. (2009) validated this through experimentation by measuring radial pressure at four points across the wheel width during wheel-terrain interaction. The results showed that θ_m was different in all measurements, confirming that the distribution of pressure along the wheel width is not uniform.

As mentioned, stress values are important to mobility performance calculations as per balance Equations (5-7); however inaccuracies can occur due to the assumption that pressure is equally distributed across the width of the wheel as discussed above. This required further exploration for which a novel instrument needed to be developed, capable of measuring the radial pressure distribution across the 3D contact patch of the wheel-terrain interface.

CHAPTER 6
MEASURING THE WHEEL-TERRAIN INTERFACE

6.1 Context

Earlier experiments discussed in Chapter 3 demonstrated that vehicle performance measurements could be used to (approximately) detect terrain properties; however these related to environmental conditions rather than direct terrain parameters. A further investigation highlighted the basic properties of the interaction between a vehicle and the terrain (Figure 6.1) which are more significant to the study because they consist of elements that are "far more measurable" (Bekker 1969).

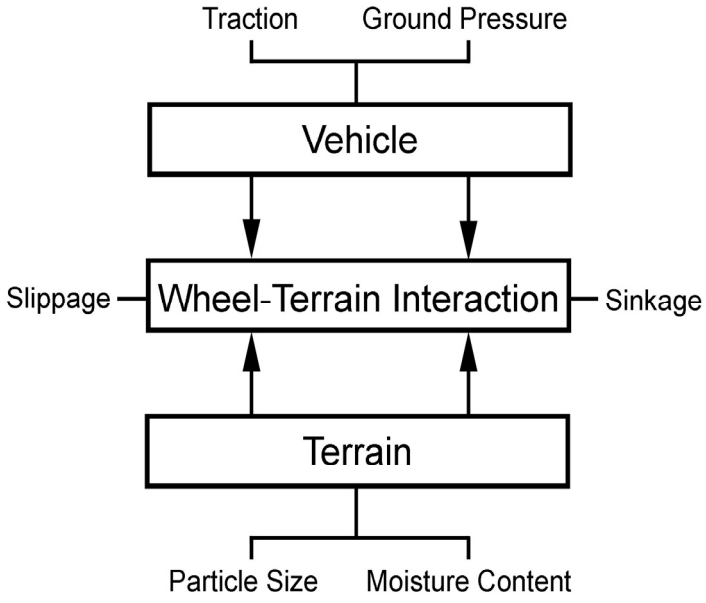

Figure 6.1 – Diagram displaying key elements of the wheel-terrain interaction. The basic vehicle and terrain properties that determine interaction parameters slip and sinkage are shown (Odedra 2011).

A more comprehensive study into the area of terramechanics (discussed in the previous chapter) uncovered the quantitative parameters that exist during the interaction between the wheel and terrain (Figure 6.2), which relate to the two main conditions that will affect mobility performance: sinkage and slippage.

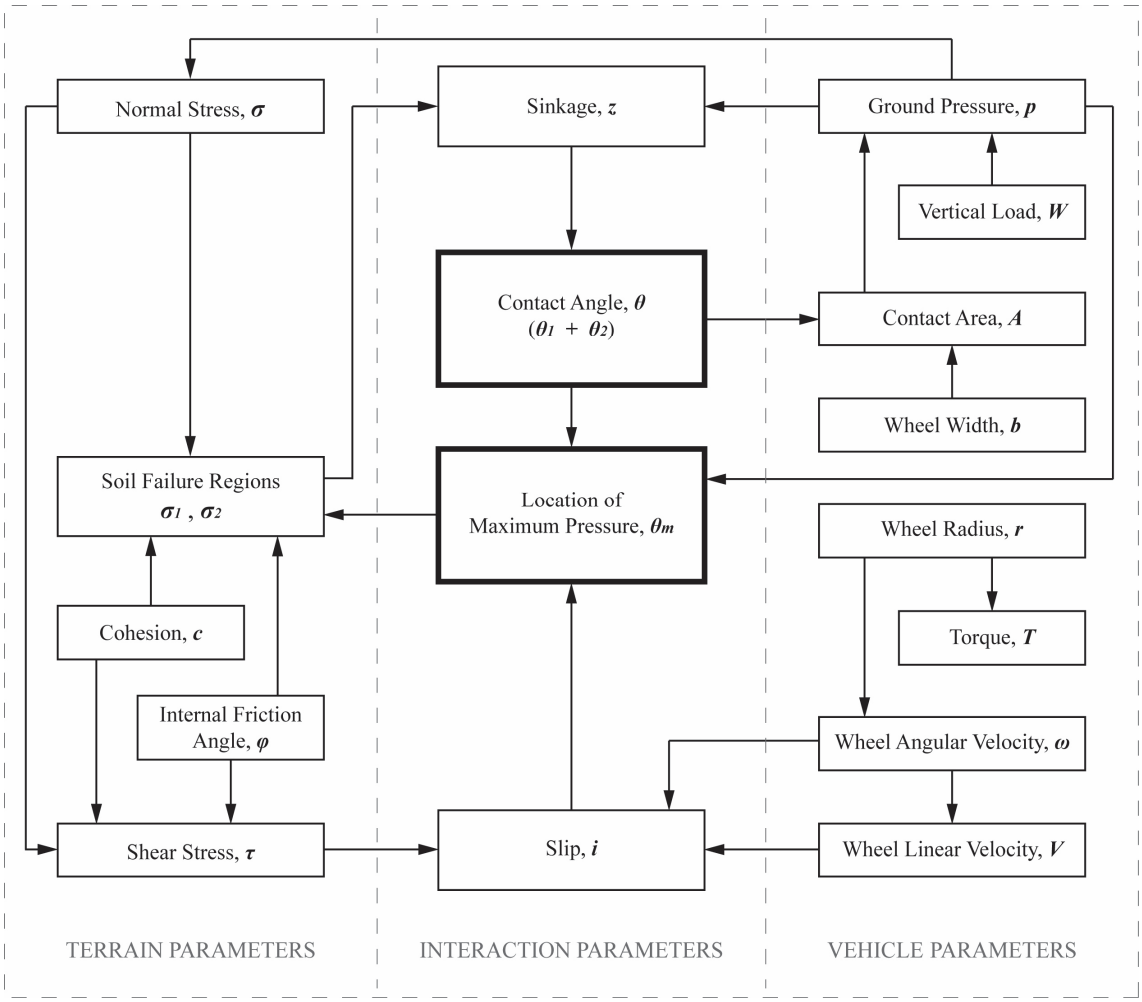

Figure 6.2 – The key quantitative parameters of the wheel-terrain interaction. This diagram shows the links between parameters derived from terramechanics, with those most significant to this study in bold.

The diagram in Figure 6.2 above, derived from terramechanics, presents the key parameters of the wheel-terrain interaction and displays relationships that exist between them. Terrain based parameters can be seen on the left, with vehicle based parameters on the right and the parameters that exist due to the interaction in the centre. This highlights that slip and sinkage are determined by conditions of the terrain and are related to pressure distribution across the wheel-terrain interface produced by vehicle parameters.

The contact angle θ and the location of maximum pressure θ_m (shown in bold at the centre of Figure 6.2) are those most significant to this study because a system capable of directly measuring (and monitoring) them during wheel-terrain interaction, could potentially classify terrain conditions in real-time.

6.2 Force Sensing Wheel Construction

6.2.1 Concept

The objective of the main experiment was to determine the contact angle θ, pressure distribution and the location of maximum pressure θ_m during wheel-terrain interaction. In order to do this a wheel embedded with an array of exteroceptive force sensors across its entire surface was developed to actively measure pressure distribution on the (3D) contact patch at the wheel-terrain interface. The self-contained unit known as the Force Sensing Wheel (FSW) includes embedded electronics capable of taking real-time force measurements and communicating them wirelessly to the Main System Controller to be stored and/or analysed.

6.2.2 Sensor Exploration

A suitable tactile sensor capable of measuring force needed to be selected for the FSW. A review of existing sensors led to the discovery of a material known as Quantum Tunnelling Composite (QTC). QTC is a flexible polymer that exhibits an extraordinary electrical property as a result of applied mechanical pressure; when compressed the material changes from an insulator to a conductor with resistance decreasing exponentially with force. This material was an ideal choice for the FSW because of its electrical properties, size, cost, availability and durability.

These sensors required testing to verify their capabilities and to find the best way of mounting and integrating them onto the surface of the wheel. A number of tests were carried out where the QTC sensors were placed on various circuit board configurations (Figure 6.3) and the voltage (V) relative to force (N) was measured using a simple LabVIEW test program as seen in Figure 6.4. These tests verified that the QTC sensors exhibit an exponential relationship between force and voltage and can therefore be utilised for the Force Sensing Wheel.

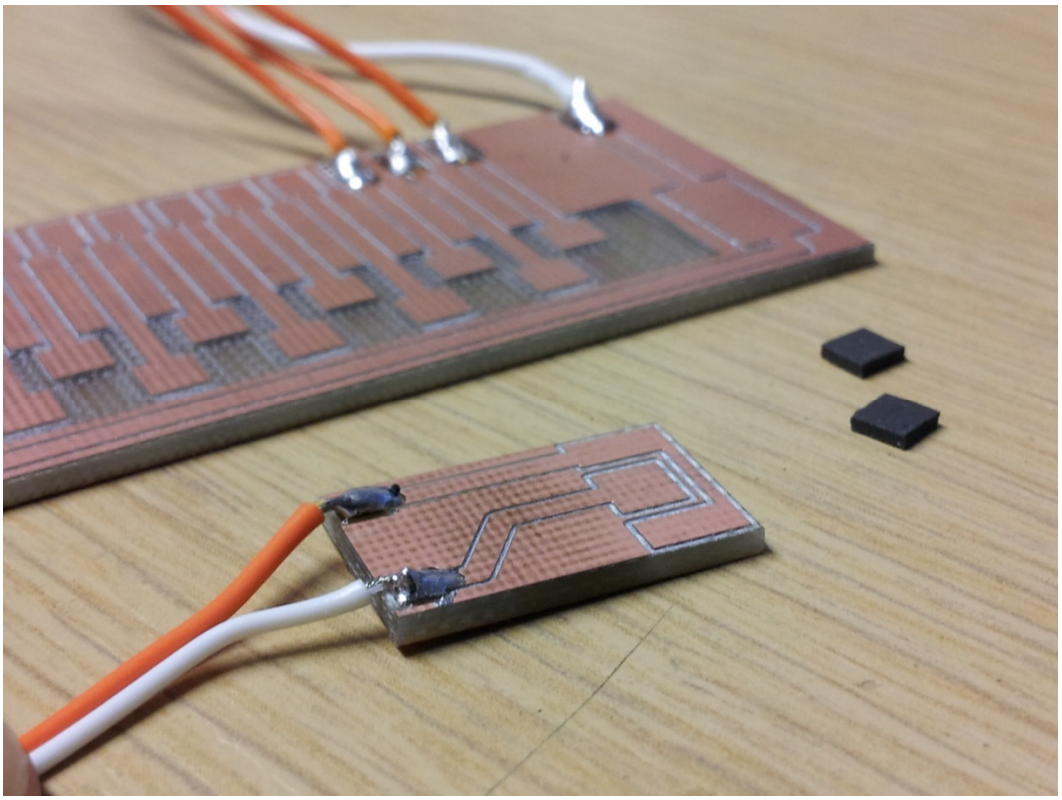

Figure 6.3 – QTC sensors and various circuit board configurations. Different configurations were tested to find the best method of mounting these sensors onto the Force Sensing Wheel.

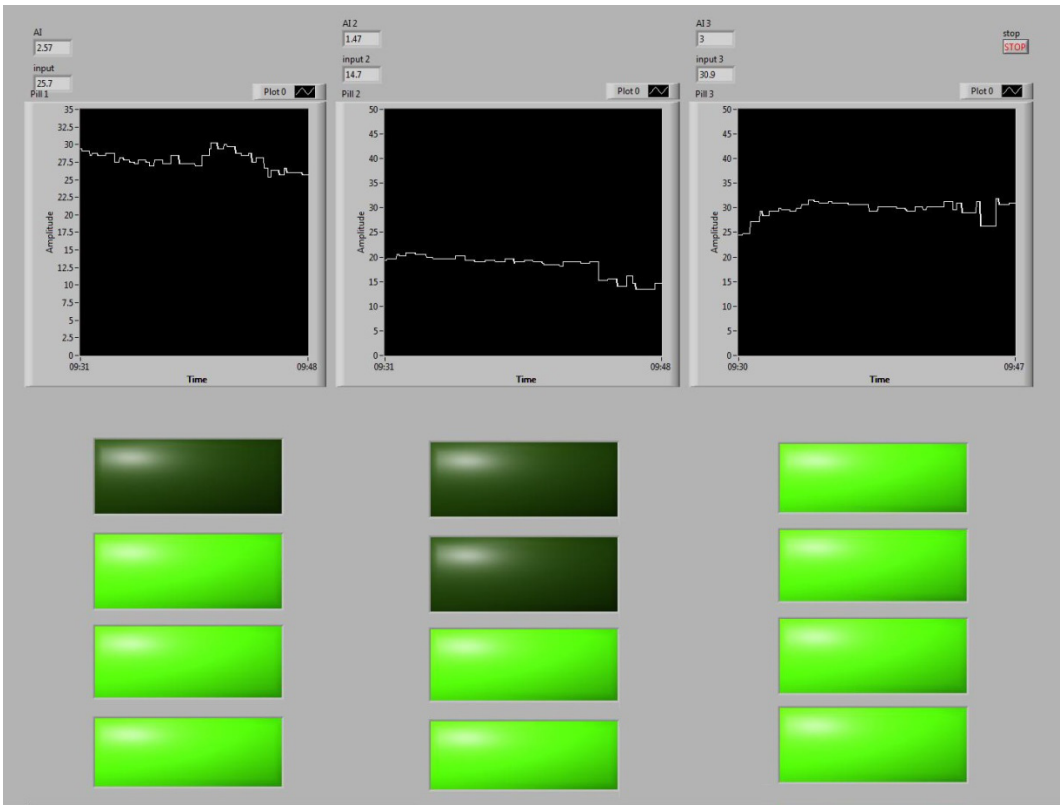

Figure 6.4 – LabVIEW test program for QTC sensor validation. The test program measured voltage relative to force with QTC pills mounted in different configurations.

To measure the 3D contact patch at the wheel-terrain interface the QTC sensors needed to be mounted across the both the circumference and width of the entire wheel, meaning a large sensor array was required. In order to physically measure and manage this large quantity of individual analogue sensors in real-time multiplexers were used.

The Texas Instruments CD74HC4067 multiplexer was selected for the system, which comprises of 16 input channels that can be electrically switched to connect to one common output within nanoseconds (ns). This meant that 16 sensors could almost simultaneously be measured using only one input.

A breakout board for the selected multiplexer was sourced to test the component's compatibility with the QTC sensors, which was carried out using an embedded development board as seen in Figure 6.5 below. This test successfully demonstrated that the multiplexer can manage data from a number of QTC sensors and was therefore a good choice for the FSW system.

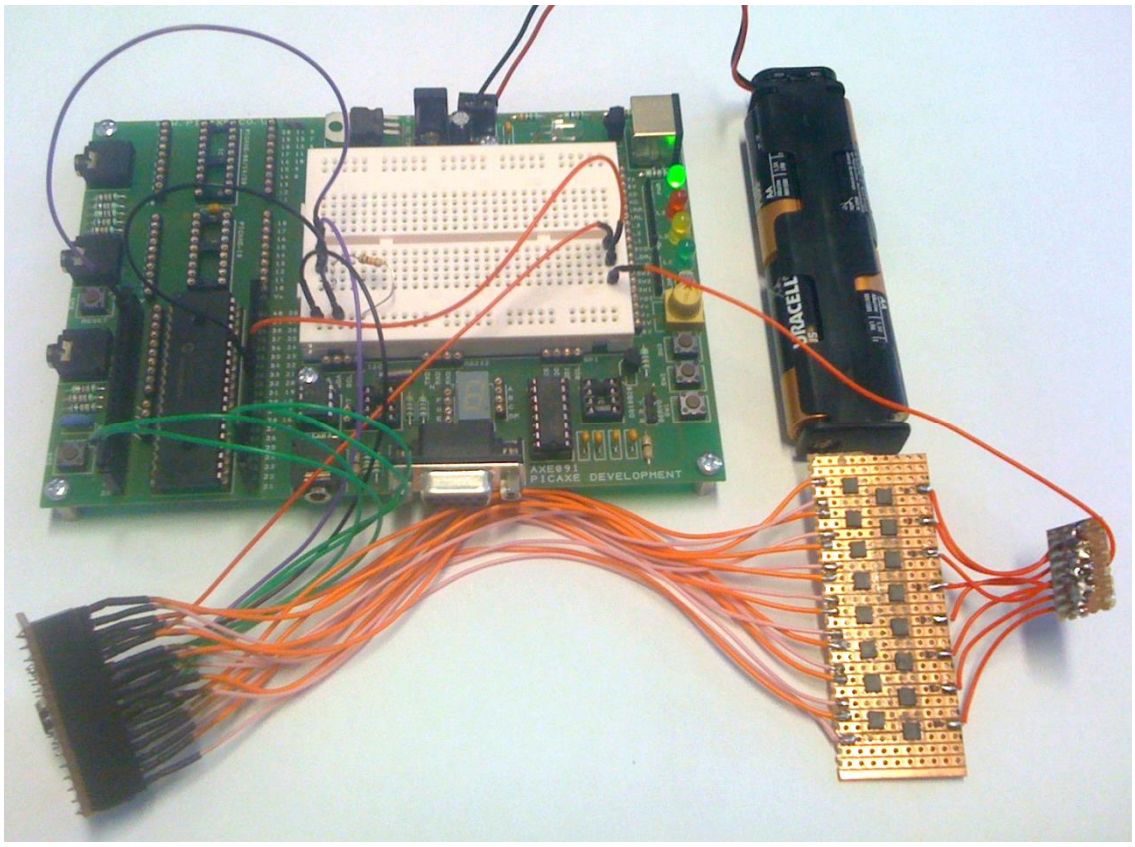

Figure 6.5 – QTC array tested with a 16-channel multiplexer. This test was done to check component compatibility between the multiplexer and QTC sensors using an embedded development board.

A bespoke Printed Circuit Board (PCB) was designed to mount the QTC sensors onto the surface of the wheel. With the successful multiplexer tests, it was decided that 16 sensors would be mounted on a single PCB to be managed by a single multiplexer. Known as a Sensor Board, they would be placed radially on the wheel to cover the entire wheel surface.

The layout of the Sensor Board was designed to hold 16 QTC sensors arranged in two alternating rows of eight (Figure 6.6). This pattern was chosen as it proved to be the optimum array, allowing 16 sensors to be mounted in close proximity while covering a greater surface area across the width as well as the (arc) length of the contact interface.

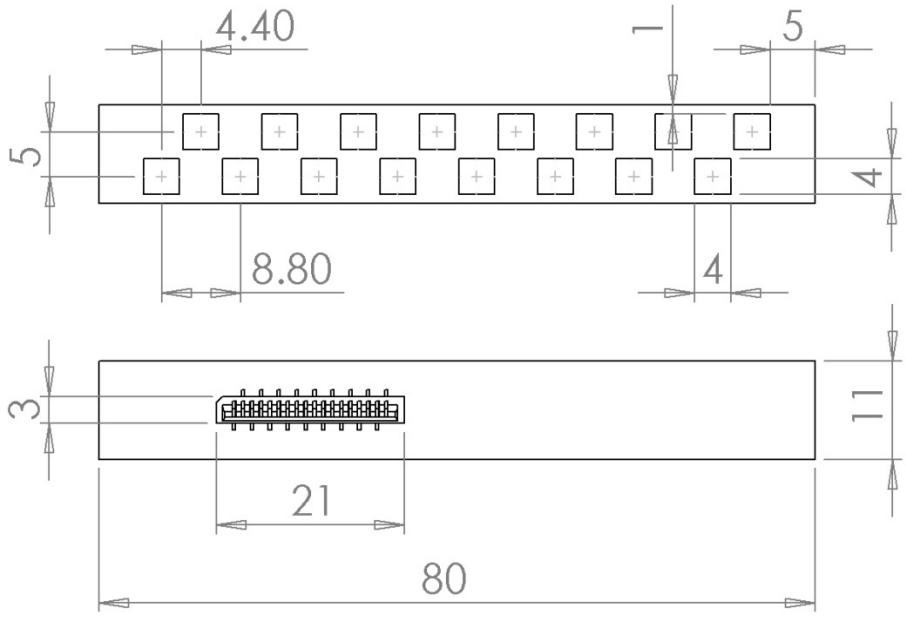

Figure 6.6 – Sensor Board layout. This custom PCB holds 16 sensors arranged in 2 alternating rows of 8 in order to cover an optimum surface area of the wheel.

The Sensor Board design was developed through a number of iterations until the final design was reached as seen in Figure 6.7. The final design includes an 18-pin surface mount connector to accept an 18-way Flexible Flat Cable (FFC), connecting each Sensor Board to other parts of the system where they are managed by multiplexers (to be discussed later). FFCs were chosen for this system to save space, make cable management easier and allow easy 'plug and play' between the system's various elements.

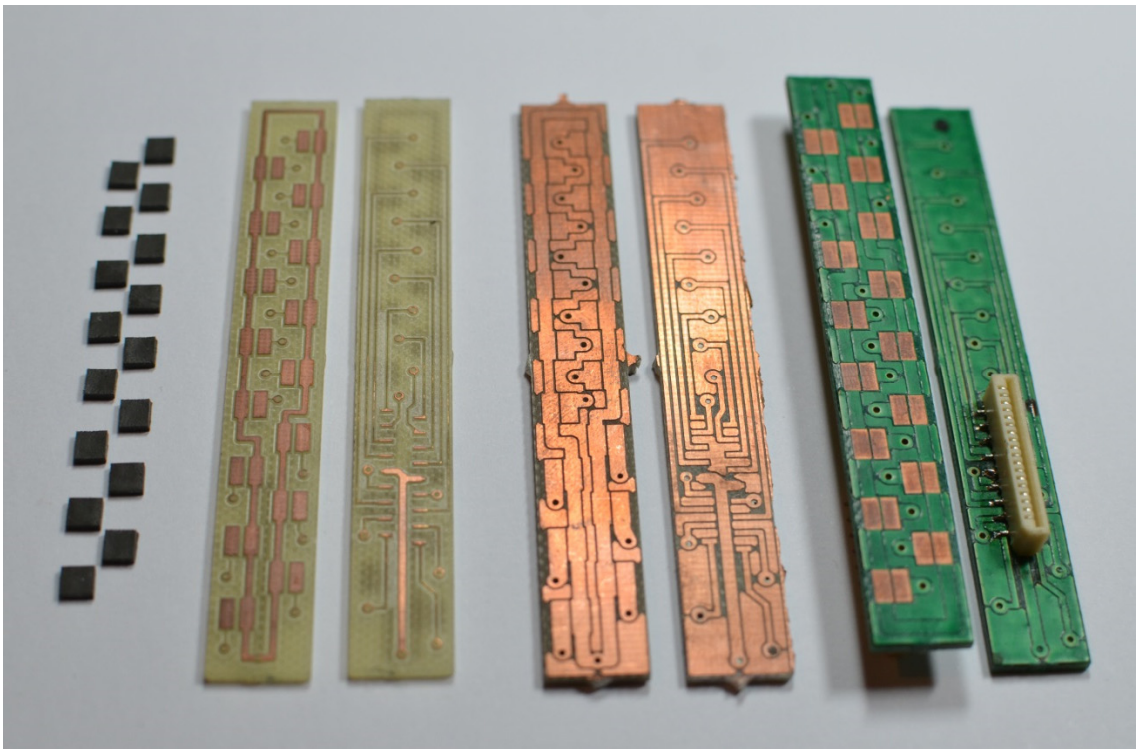

Figure 6.7 – Sensor Board design iterations. Each Sensor Board holds 16 QTC sensors in an optimised array and includes an 18-pin surface mount connector to connect to other parts of the system.

6.2.3 Wheel Structure

With the design of the Sensor Boards complete then the next task was to mount them on a wheel structure. To start with Computer Aided Design (CAD) software was used to precisely calculate the best pattern in which to create an optimal sensing array. The compact size of the Sensor Boards meant that 48 boards could be placed radially, spaced 7.5 degrees apart, creating a 70mm wide sensing area with an alternating resolution pattern of 5mm around the entire 360 degree wheel circumference (Figure 6.8). The resulting wheel diameter of 190mm by 80mm width was ideal as it is comparable to wheels on existing small UGVs while still being proportionate to the vehicle chassis.

The initial concept for mounting the Sensor Boards in this radially pattern on the FSW was to use a number of structural elements, each one housing a single Sensor Board (Figure 6.9), which would slot together to make up a complete wheel rim (Figure 6.10). The idea behind this modular system was to enable the integration of the many custom electronic components in addition to making installation and maintenance easier.

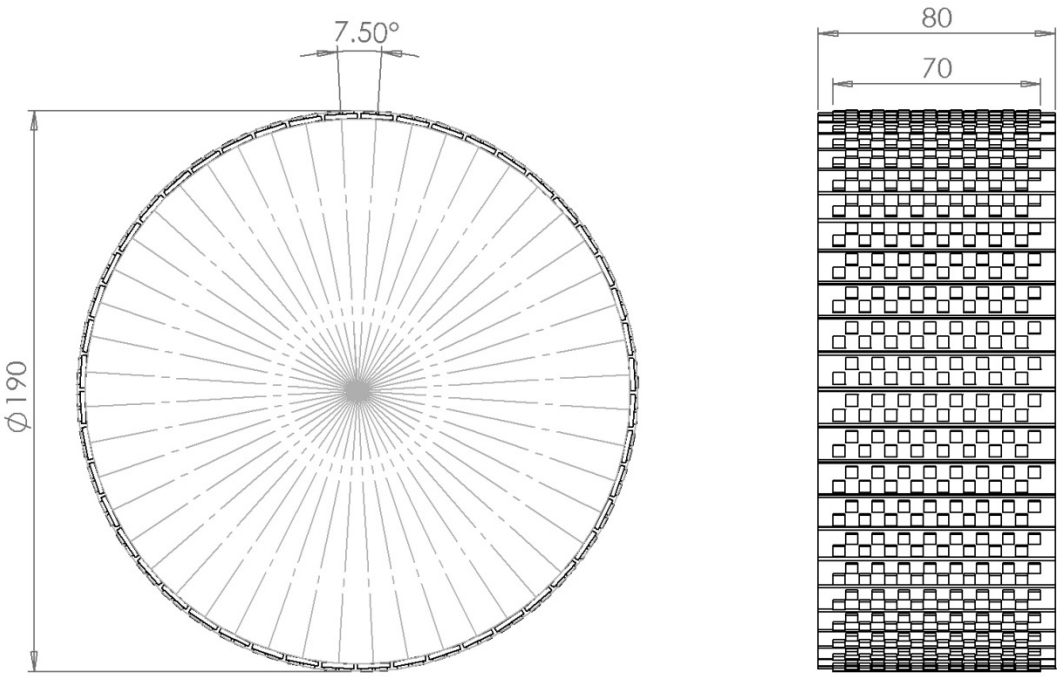

Figure 6.8 – Sensor Board radial array. This shows that 48 boards could be placed around the wheel resulting in a large radial sensing area and an ideal wheel diameter comparable to other small UGVs.

The structural element concept was designed using CAD software and quickly validated using rapid prototyping tools to create 3D printed models as seen in Figure 6.9 below. The initial concept was to create a complete wheel by slotting together eight of these elements to create a 'Wheel Segment' of which six are needed to make a complete wheel as seen in Figure 6.10.

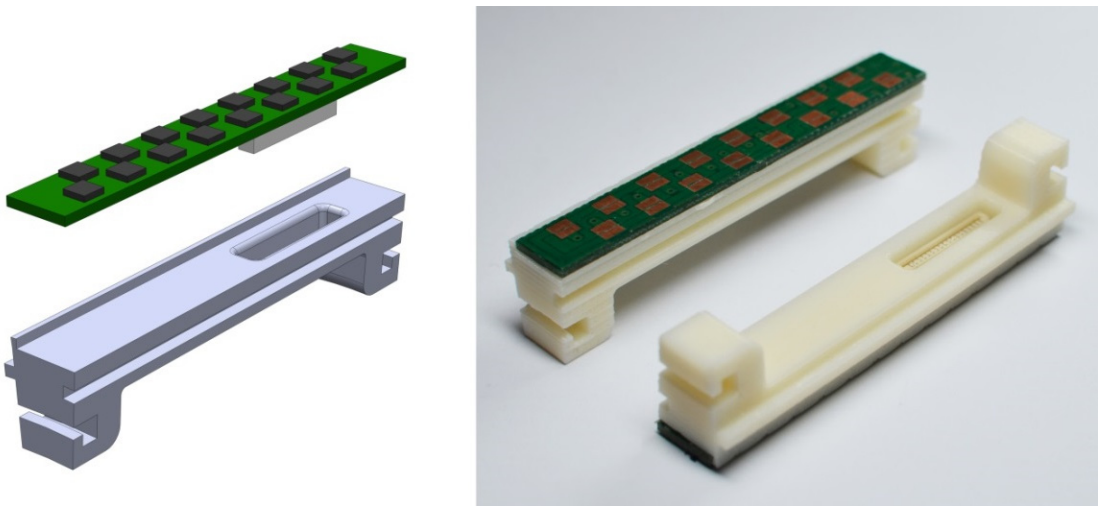

Figure 6.9 – Individual Sensor Board structural element. The image on the left shows the CAD design of a Sensor Board element and the image on the right displays the 3D printed prototype.

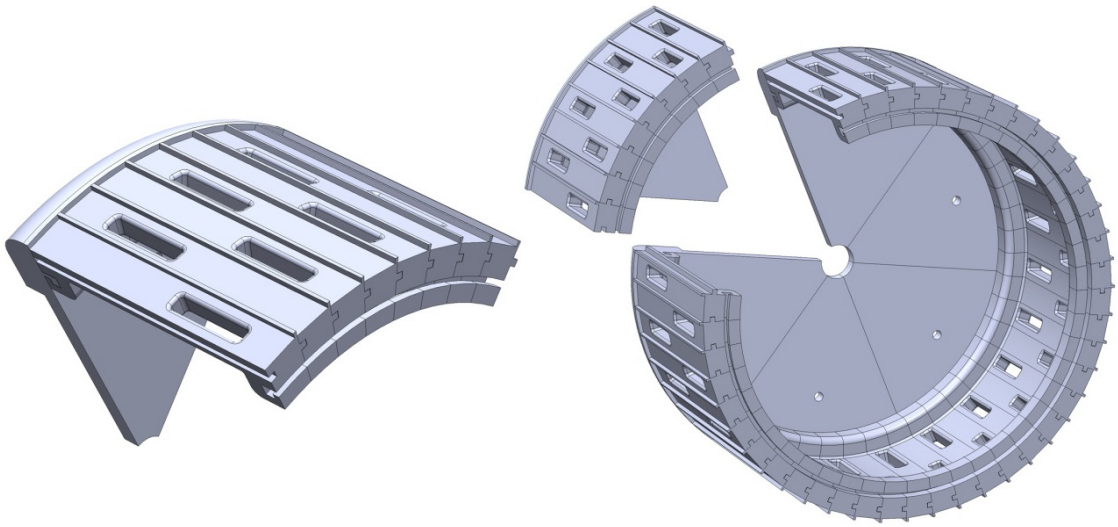

Figure 6.10 – Structural slotted wheel rim concept. The left image shows 8 elements slotted together to make a wheel segment, of which 6 are needed to make up a complete wheel rim as seen on the right.

This initial concept was tested and it was found that having a large number of individual Sensor Board elements only weakened the overall wheel structure and added unnecessary complexity. After a number of design developments the concept was improved to house eight sensor boards on one complete Wheel Segment as seen in Figure 6.11. This simplified the design and strengthened the wheel structure while retaining enough modularity for the integration and maintenance of embedded electronics.

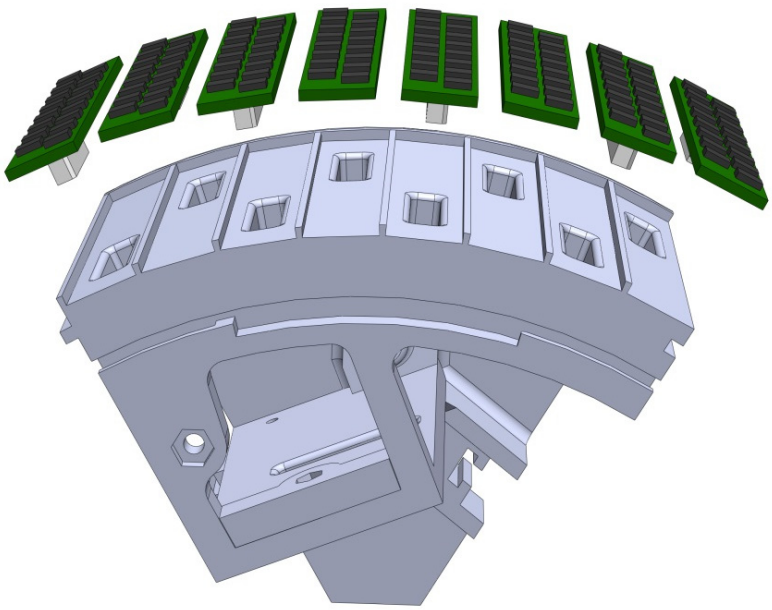

Figure 6.11 – Final Wheel Segment design. Each Wheel Segment houses 8 Sensor Boards, strengthening and simplifying the design while retaining enough modularity for easy integration of electronics.

The final design was produced using 3D printing tools as it enabled rapid manufacture while maintaining the accuracy and intricacy of the CAD model. Figure 6.12 below displays the final manufactured Wheel Segment complete with 8 Sensor Boards. This final design also needed to accommodate another bespoke PCB known as a 'Segment Board' which manages the sensor data within each segment (discussed later), seen mounted in the bottom image of Figure 6.12.

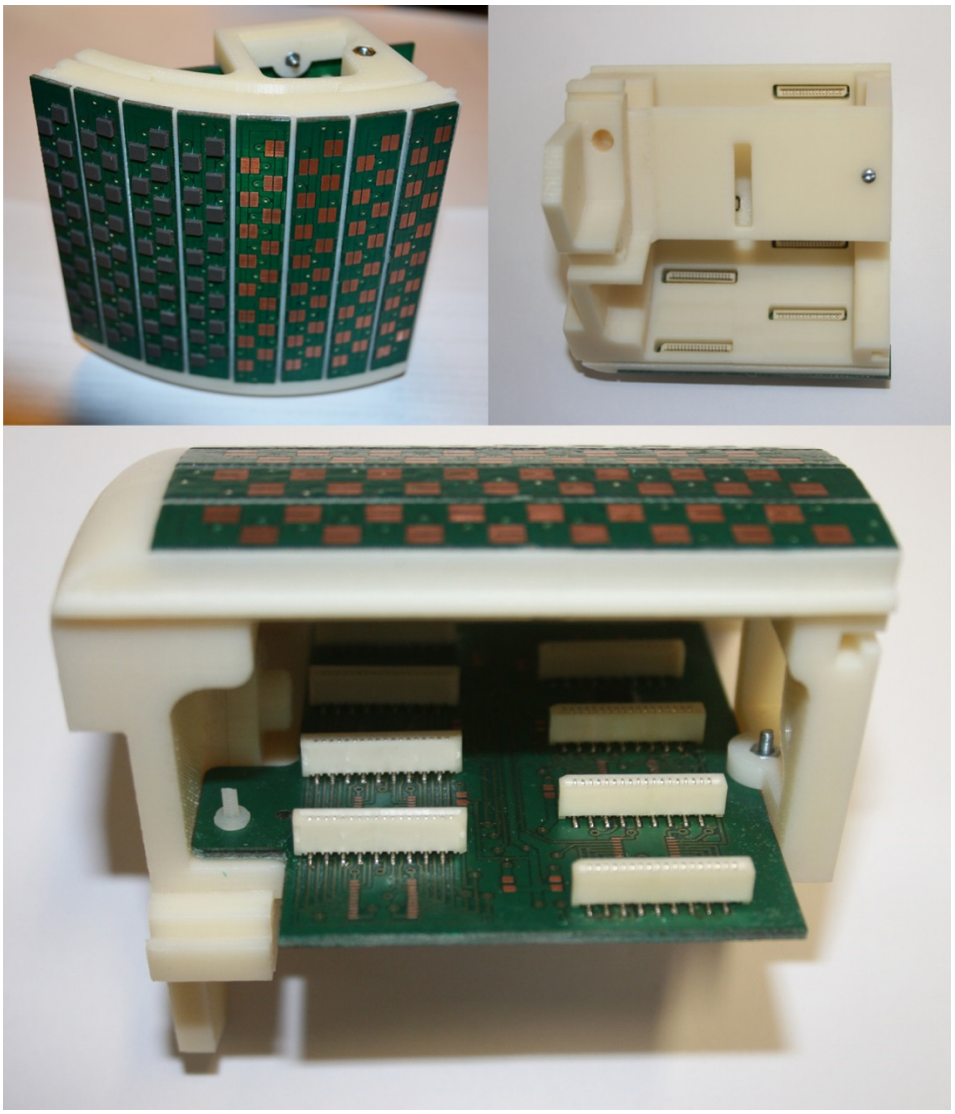

Figure 6.12 – Assembled 3D printed Wheel Segment. Each Wheel Segment was manufactured using 3D printing to keep the accuracy and intricacy of the CAD model.

The Wheel Segment was also designed to slot together with 5 other segments to create a full wheel structure as seen in Figure 6.13. The full wheel structure is then mounted onto an aluminium 'Wheel Disc' (Figure 6.14) which is used to attach the assembled wheel to the chassis while strengthening the structure by holding it all together.

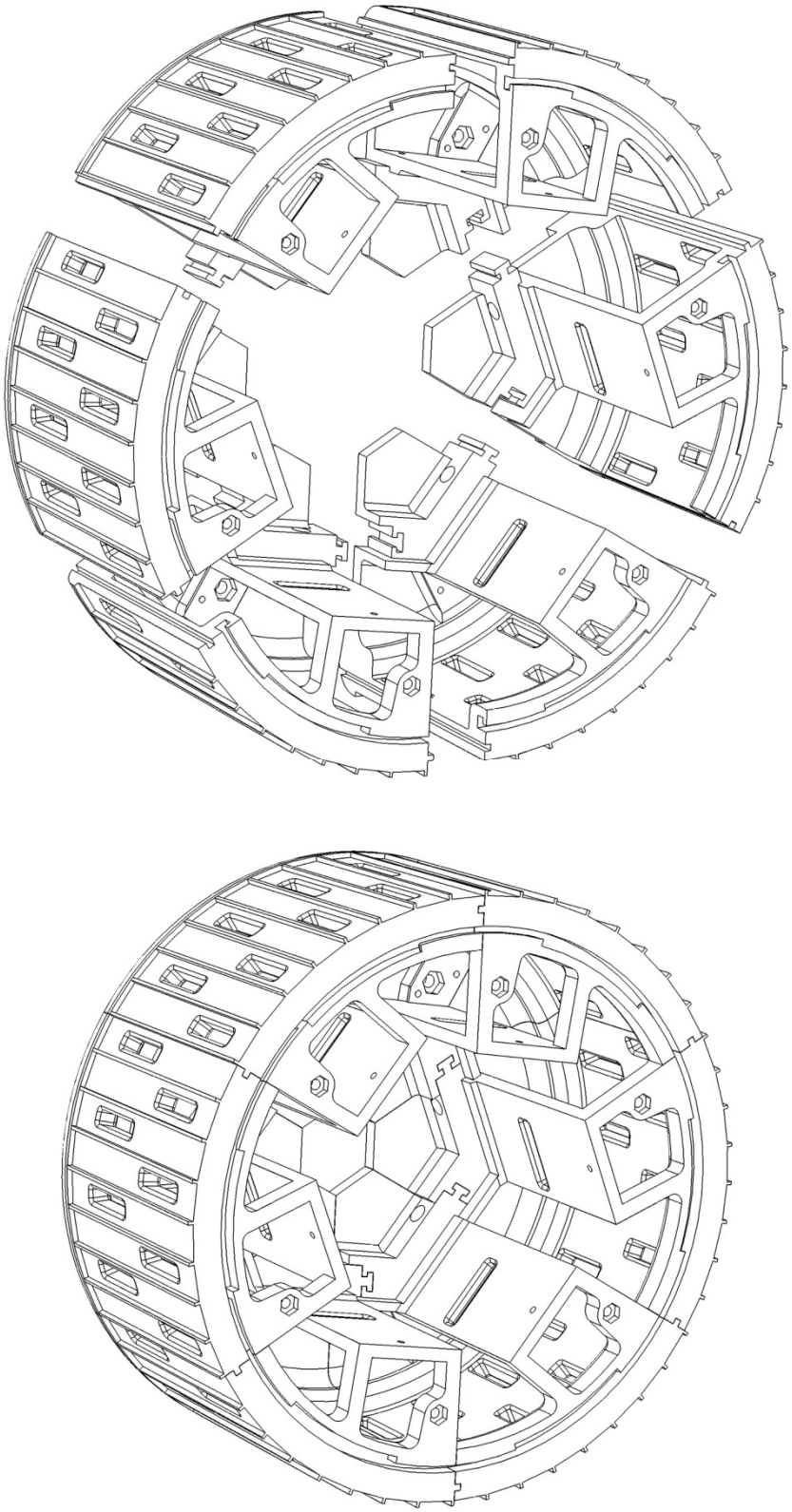

Figure 6.13 – Complete wheel structure comprising of 6 Wheel Segments. The Wheel Segments were designed to slot together, with 6 required to make a complete wheel.

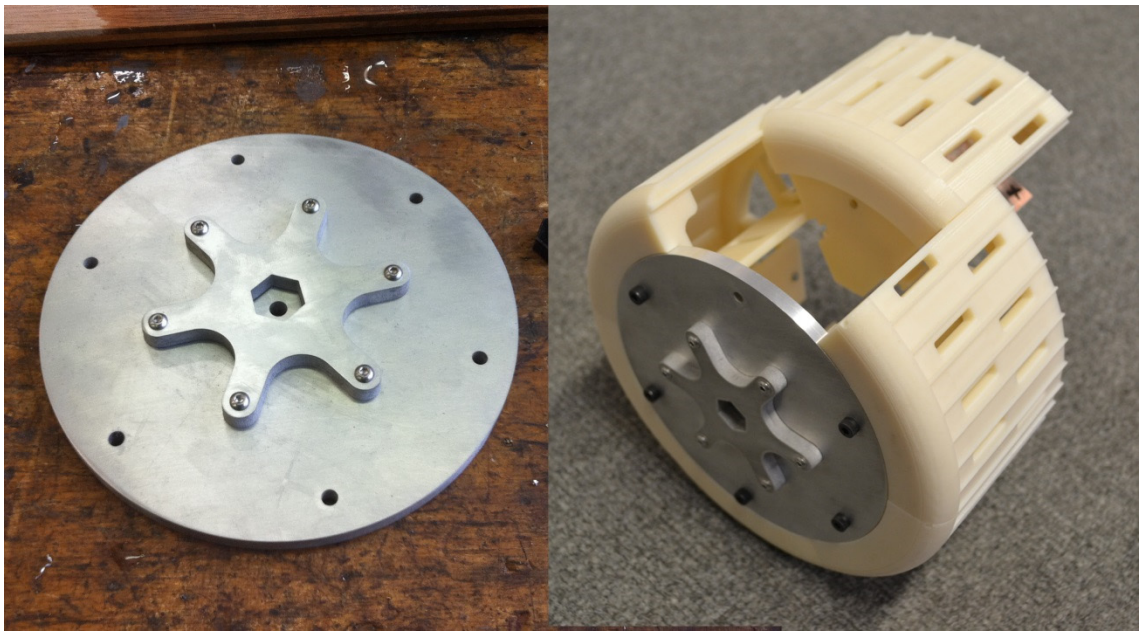

Figure 6.14 – Wheel Disc used for holding together the wheel structure. An aluminium disc is used to mount the assembled wheel to the chassis as well as giving strength to the wheel structure.

The final integral part of the FSW is known as the 'Core' which has a number of functions. This star shaped cage houses the system's power supply and microcontroller (discussed later) and slots into the centre of the wheel structure (Figure 6.15) providing structural integrity while also holding in the 'Junction Board' yet to be discussed.

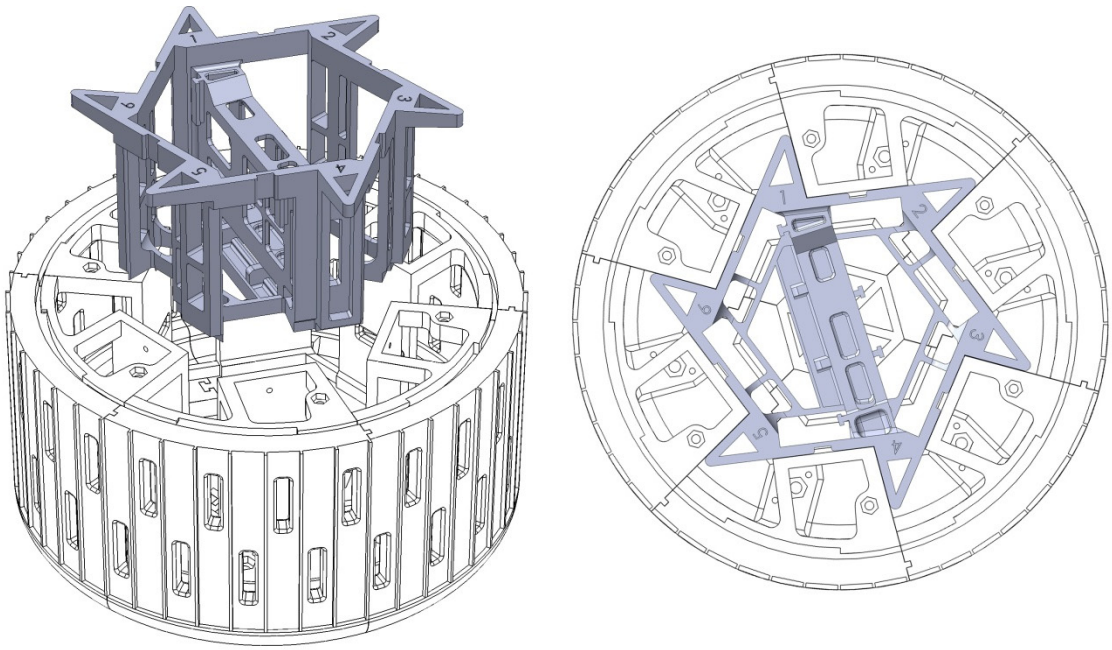

Figure 6.15 – The FSW's integral star-shaped Core. The Core houses important components and slots into the centre of the wheel providing structural integrity to the entire assembly.

As discussed, the inside wheel rim is securely held together by the aluminium Wheel Disc; to secure the outside rim a component known as the ‘Lock Rim’ is used. The Lock Rim slots onto the front of the wheel assembly and is rotated clockwise (Figure 6.16) securing the outer rim of the Wheel Segments in addition to locking the Core in place. Finally, the closed position of the Lock Rim aligns the mounting holes for the Wheel Lid, which is the final structural component of the wheel assembly seen in Figure 6.17.

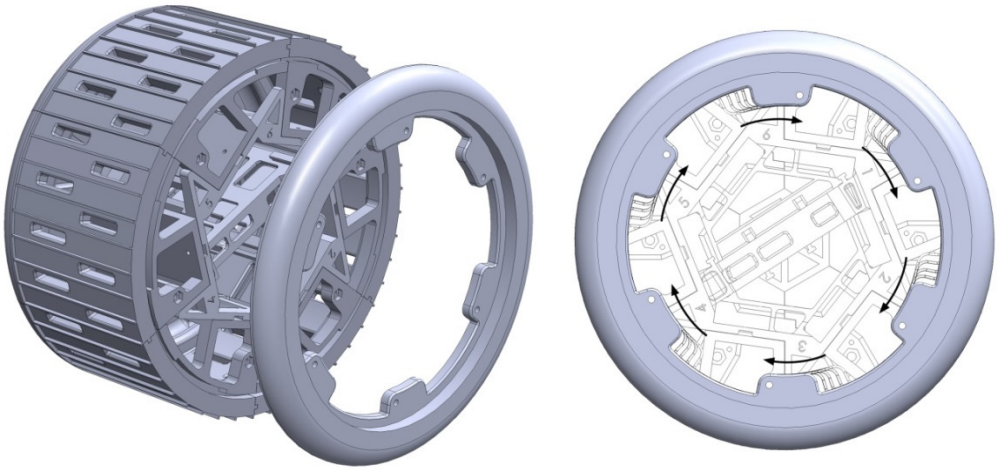

Figure 6.16 – The wheel’s outer Lock Rim. The Lock Rim is slotted in place and rotated clockwise to secure the Core as well as lock the outer rim of the Wheel Segments together.

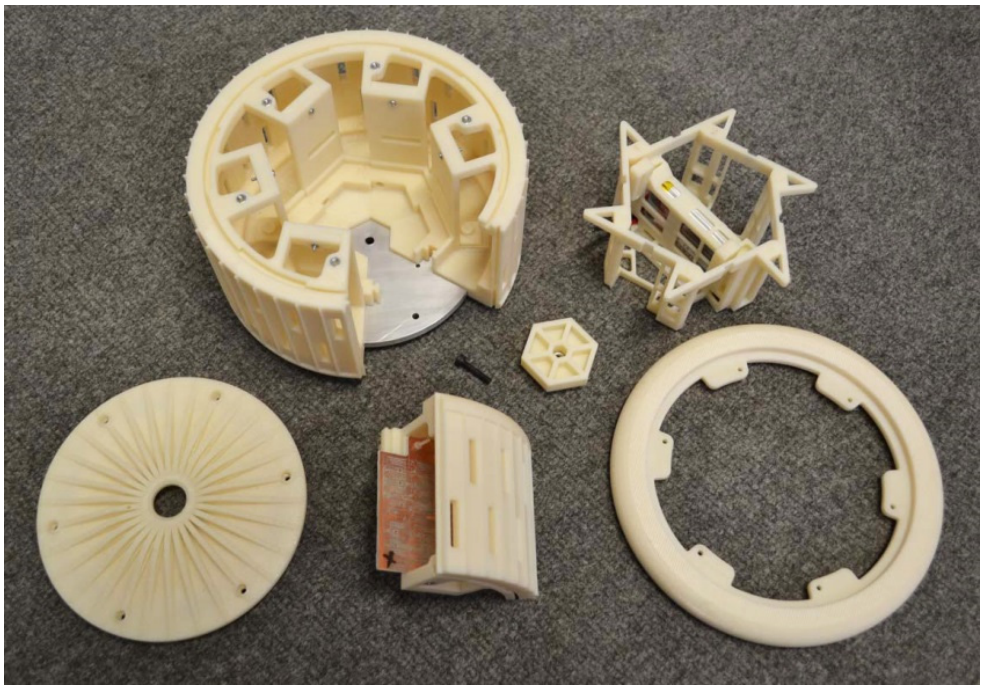

Figure 6.17 – All the structural components of the FSW. This image displays all the wheel components: Wheel Segments on the Wheel Disc, Core, Lock Rim and Wheel Lid.

6.2.4 Electronic Design

The central electronic component embedded in the Force Sensing Wheel is the microcontroller (MCU) which is based on the mbed development platform. The mbed suite was chosen because it offers a professional environment while offering flexibility for rapid prototyping and off-the-shelf development boards are readily available. Additionally supporting development tools including modular software libraries and a C/C++ compiler are easily accessible online.

The selected development board is based on the NXP LPC1768 microcontroller, a highly capable 32-bit ARM Cortex M3 processor, which boasts an impressive CPU frequency of up to 100MHz and includes 512KB of Flash memory and 64KB of data memory (RAM). This low power MCU offers several communication interfaces with plug and play peripherals and a number of digital and analogue Inputs/Outputs (I/O). This powerful board offers high level integration within a small form factor of 54mm x 26mm on a convenient 40-pin dual in-line (DIP) package as seen in Figure 6.18 below.

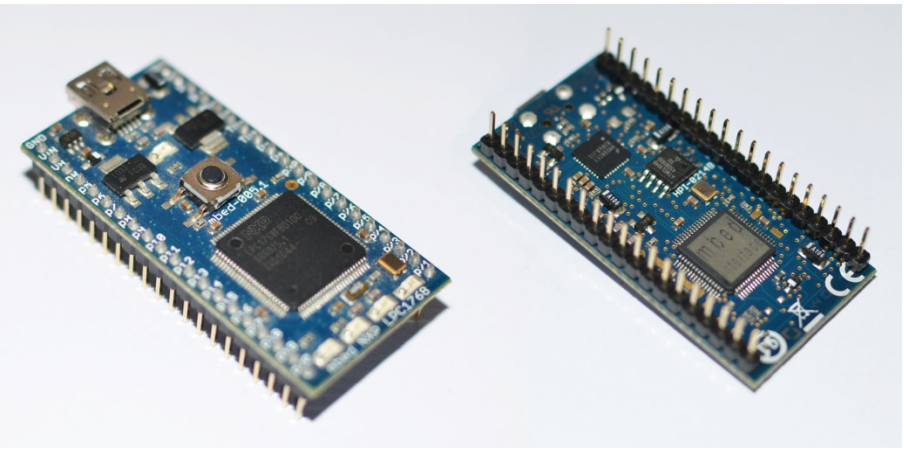

Figure 6.18 – 32-bit ARM mbed development board. The mbed offers a powerful ARM M3 core which has impressive specifications all within a small form factor.

The mbed was ideal for the FSW as its small form factor meant it could easily be embedded into the wheel while offering powerful capabilities and development flexibility. The main function of the mbed was to control data flow and manage sensor data from a large array of sensors; however only six analogue inputs are available out of the many I/O pins on the development board, hence an intelligent use of multiplexers was required.

As discussed the FSW system comprises of 48 Sensor Boards each containing 16 sensors, meaning that the number of individual sensors across the wheel surface totals to 768. With such a large array of analogue sensors and only six inputs, a novel approach was needed to manage and control data flow in real-time.

The problem was simplified by controlling data flow from the eight Sensor Boards on each of the 6 Wheel Segments through a central control point and into each of the six analogue inputs on the MCU. This was made possible by using multiplexers, enabling all 768 sensors to be read into six analogue inputs within nanoseconds. A simplified diagram of the system architecture can be seen in Figure 6.19 below where each Segment Board labelled 1-6 manages its eight Sensor Boards labelled A-H and connects to the (hexagonal) Junction Board, which centralises data flow to the mbed MCU.

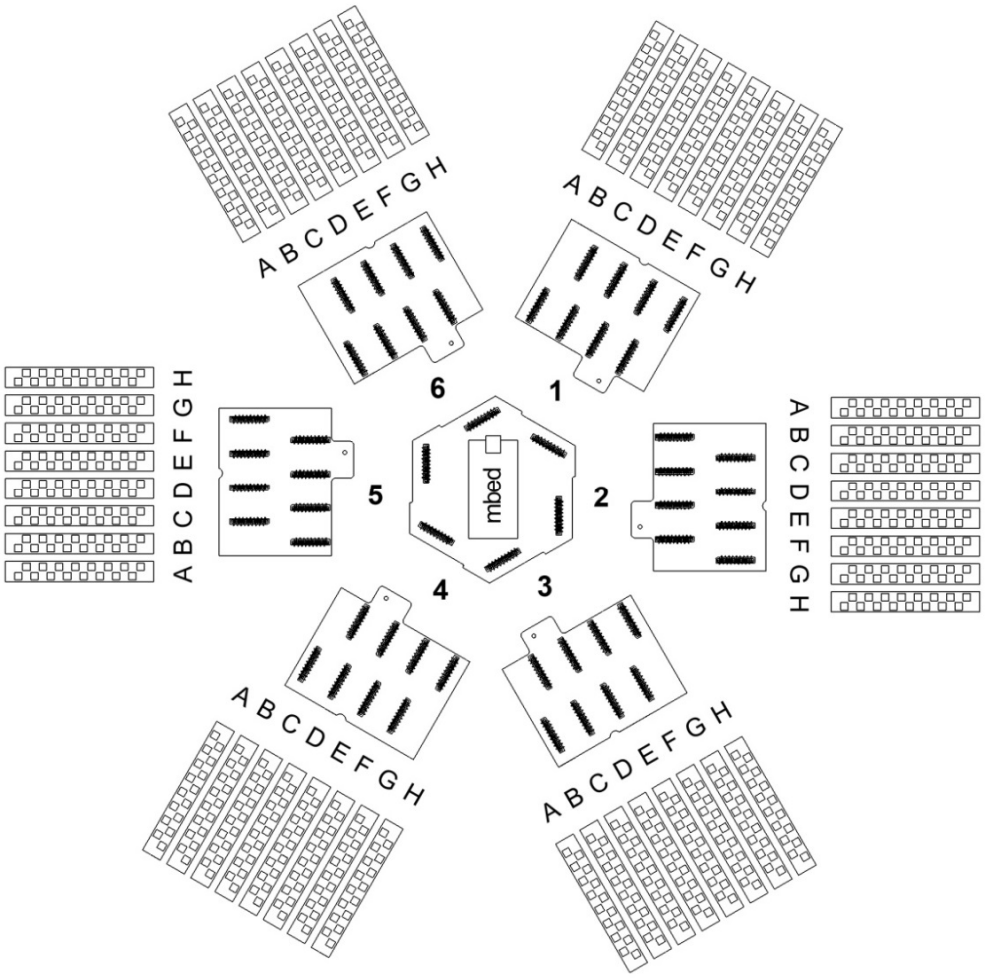

Figure 6.19 – Simple diagram of the FSW system architecture. With 768 analogue sensors the problem had to be broken down in order to control and manage sensor data in real-time.

The Segment Boards situated within each segment are integral to controlling data flow. Their main task is to multiplex the sensors integrated onto their segment so that data from 128 sensors can be read into a single analogue input on the MCU. To enable this, these bespoke PCBs include eight multiplexer ICs which are each wired to an FFC connector, that are spaced accordingly to connect to eight Sensor Boards. A single FFC connector is located on the reverse to connect to the MCU via the Junction Board. The Segment Board was prototyped to test and validate the electrical design (Figure 6.20), check connector alignment and to make sure the board physically fit into the segment structure. Once verified the final Segment Boards were professionally manufactured and assembled ready for installation into the wheel structure (Figure 6.21).

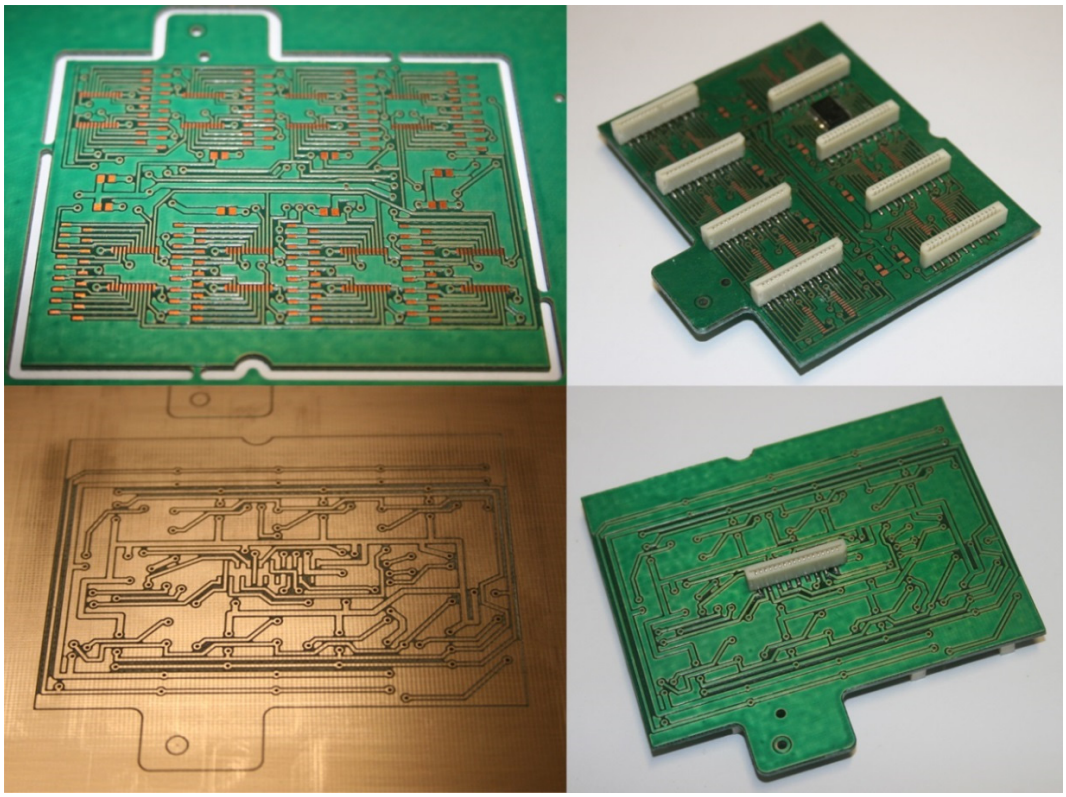

Figure 6.20 – Segment Board prototypes. The Segment Board design was prototyped using rapid prototyping tools to verify the electrical layout and check for physical fit into the Wheel Segment.

As mentioned, data is sent back to the MCU from the Segment Boards via a central PCB known as the Junction Board. The hexagonal shaped Junction Board sits in the middle of the assembled wheel structure and centralises data flow from the Segment Boards through six FFC connectors (Figure 6.22). The Junction Board also includes a 2-pin connector for power input to distribute power to the Segment Boards and a central FFC connector passes data to and from the MCU by connecting to the ‘Main Board’.

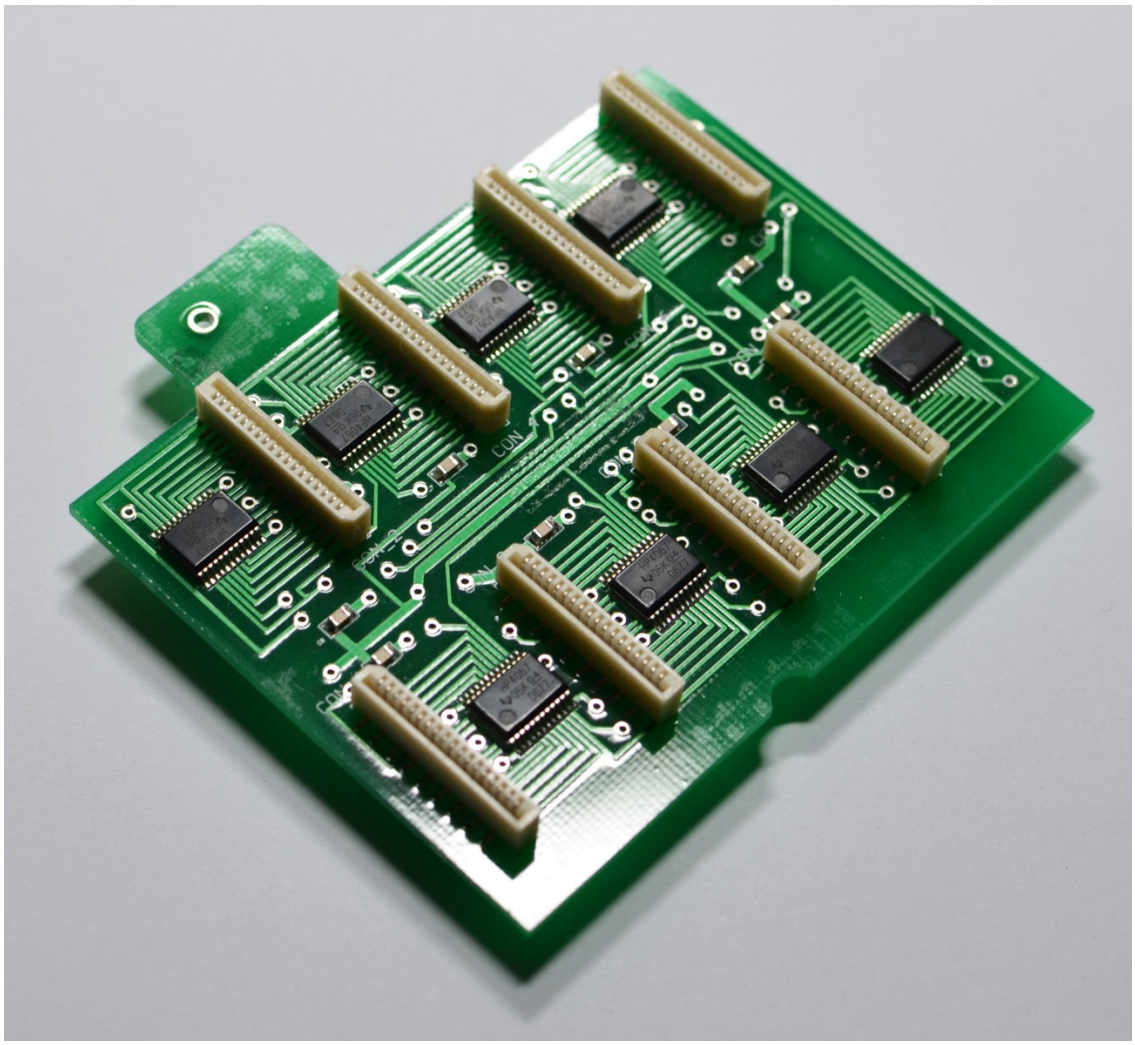

Figure 6.21 – Final manufactured Segment Board. Each Wheel Segment houses a Segment Board which controls the data flow of 128 sensors into a single analogue input on the MCU within nanoseconds.

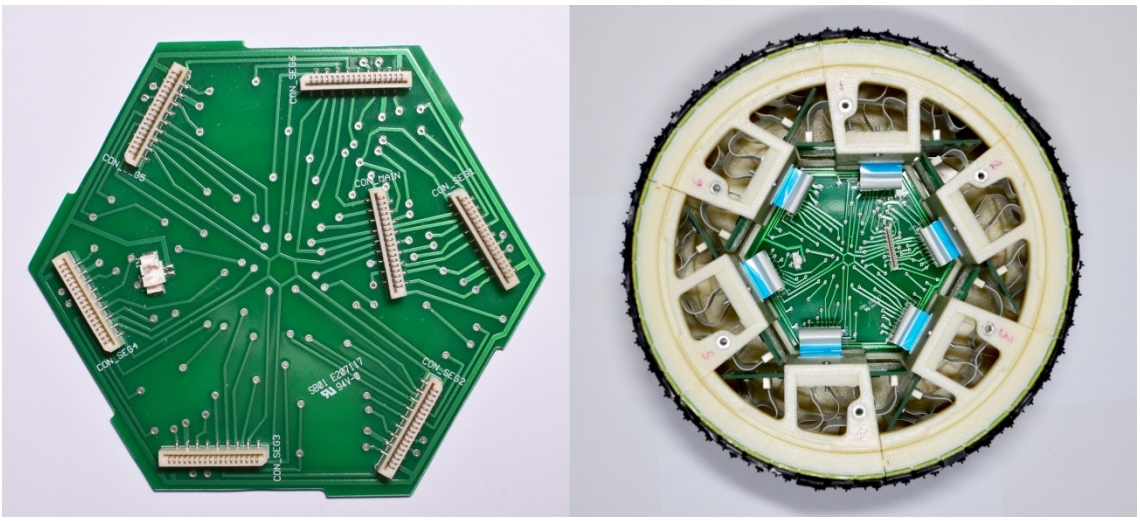

Figure 6.22 – Junction Board centrally located. The Segment Boards all connect to the hexagonal Junction Board which distributes power and centralises data flow to and from the MCU.

The Main Board is housed inside the Core (Figure 6.23) and includes the mbed MCU and a Bluetooth module for wireless data transfer to the Main System Controller. The selected Bluetooth module is Roving Networks RN42, a fully certified (class 2) low power Bluetooth radio that offers data transfer rates of up to 3Mbps. The 'postage stamp sized' module includes an on-board trace antenna and communicates with the MCU using serial communication protocols.

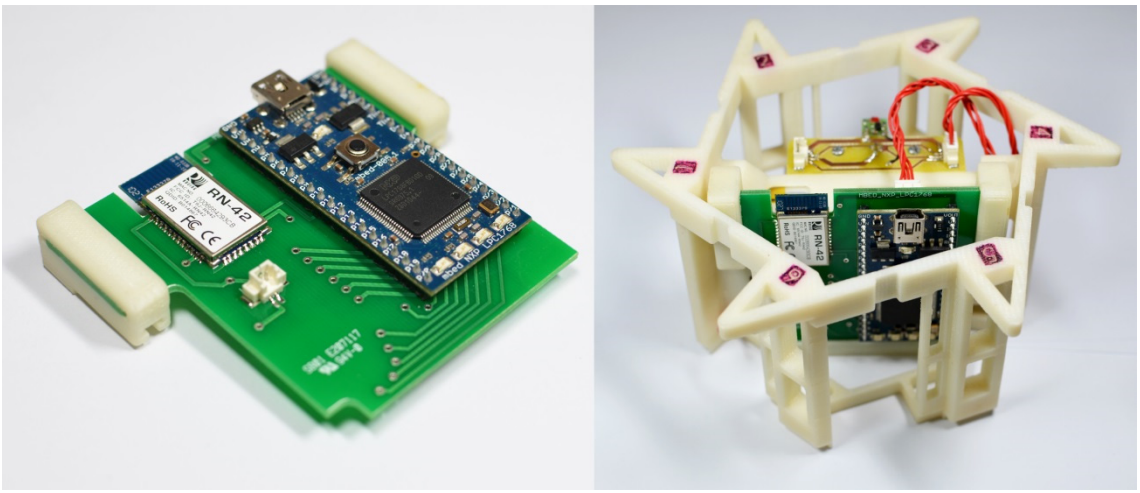

Figure 6.23 – Main Board housed in the Core. The Main Board includes the mbed MCU and RN42 Bluetooth module and connects to the Junction board to supply power and control data flow.

The Master Board connects to the Junction Board to supply power through a 2-pin connector and for data transfer/control via a single FFC connector on the reverse. A 4-pin connector (also on the reverse) supplies power to the Main Board from the 'Power Board' in addition to connecting the MCU to the status LED integrated into the main on/off switch (situated on the lid). This LED notifies different states of the system by using various blinking patterns to show when the system is reading and/or sending data.

The Power Board situated on top of the Core (left image in Figure 6.24) is where the main power is supplied from. It also includes a small off-the-shelf circuit which indicates when the power supply is low via a small red LED. Finally the power supplied to the entire system is in the form of a rechargeable 850mAh, 7.4V Lithium-ion Polymer (Li-Po) battery also housed in the Core (right image in Figure 6.24). The battery slots into the middle of the Core; placed centrally to keep weight distribution equal within the Force Sensing Wheel.

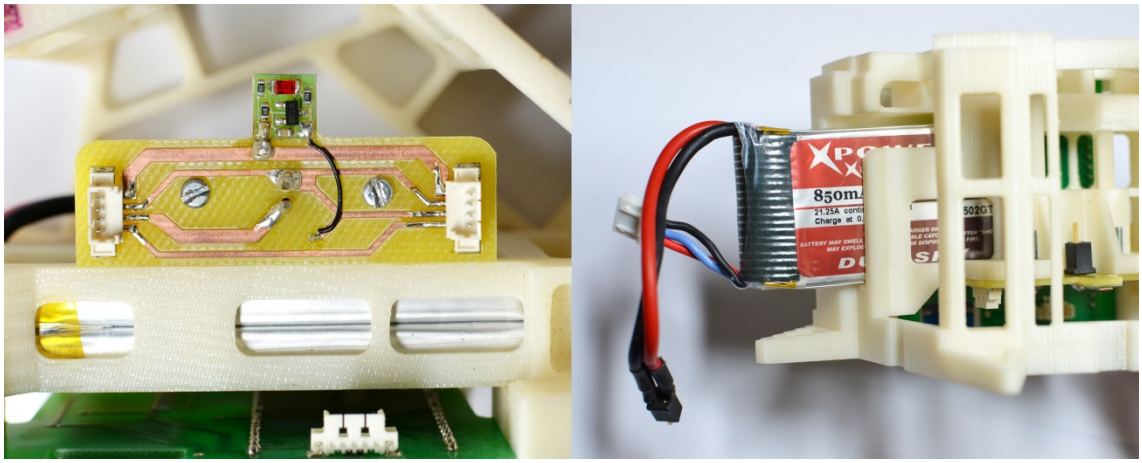

Figure 6.24 – Power Board and power source. A compact LiPo battery is housed centrally in the core and supplies power to the entire system through the Power Board which includes a low-power indicator.

6.2.5 Sensor Development

The QTC Sensors were installed onto the Sensor Boards using a special conductive adhesive supplied by 3M; however this method produced mixed results during testing. The sensitivity of the sensors varied across boards and it was discovered that this was because the uncoated copper pads where the sensors are mounted became tarnished over time, affecting conductivity (Figure 6.25). This also affected the strength of the adhesive meaning that without any external protection the QTC sensors became prone to peeling off, especially when interacting with the rough surface of certain terrain.

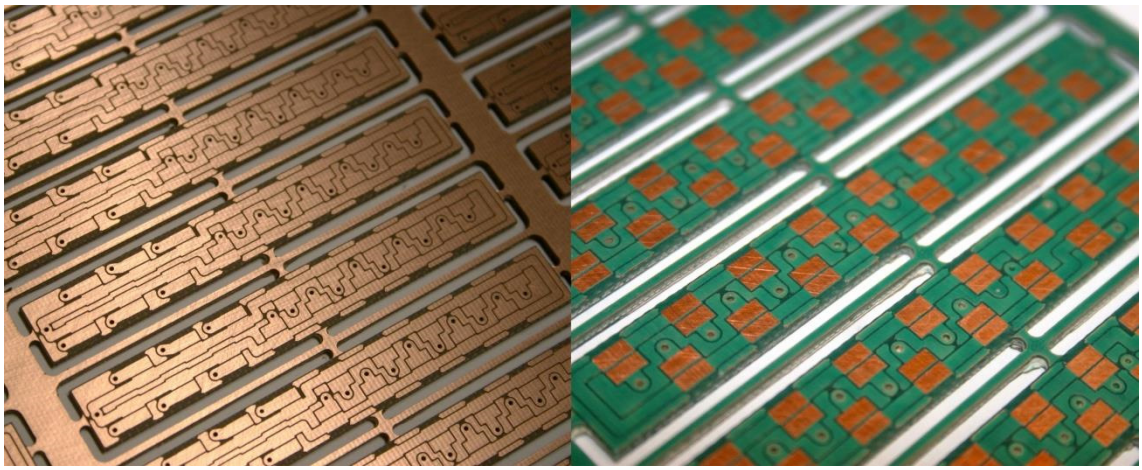

Figure 6.25 – Tarnishing of uncoated copper pads. The bare copper pads on the Sensors Boards became tarnished over time, affecting conductivity and in turn sensor sensitivity and the strength of the adhesive.

The first solution was to coat the pads on the Sensor Boards to stop them tarnishing. This was professionally done using an electroplating process to gold plate the pads, giving consistency to their conductivity (Figure 6.26). The second solution was not as easy as the QTC sensors needed to be protected from excessive external forces while retaining their ability to measure force.

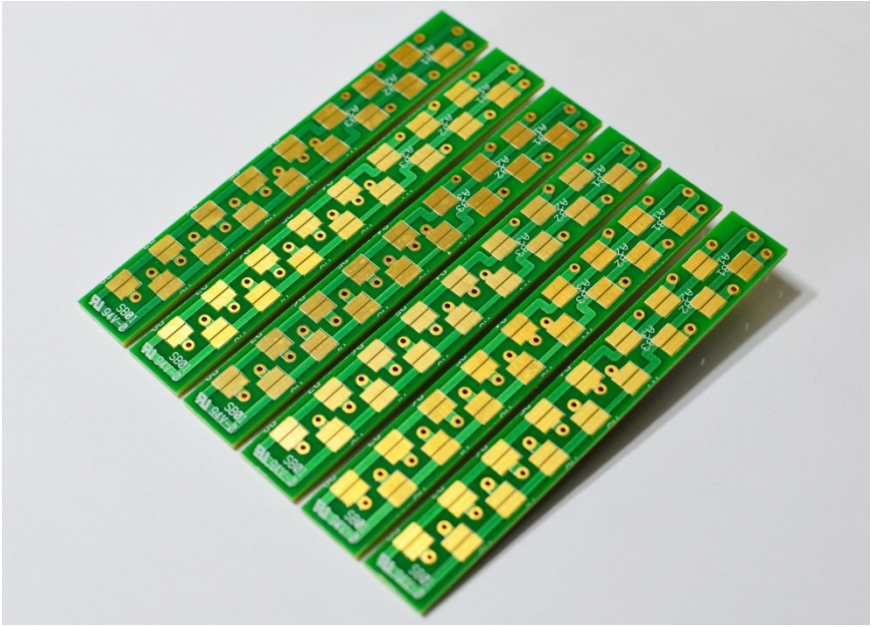

Figure 6.26 – Gold plated sensor pads. The pads on the Sensor Boards where the sensors are mounted were gold plated to stop them tarnishing.

To protect the QTC sensors the initial concept was to cover them with a rubber casing. This was prototyped using CAD and 3D printing to create simple rubber moulds from which silicone covers were cast (Figure 6.27). After testing the initial design it was found that the rubber casing affected sensor performance by dampening the majority of forces acting on the wheel surface; therefore the design needed improvements.

Figure 6.27 – Casting protective rubber casings. These casings were designed to protect the QTC sensors.

Firstly a harder rubber was used to eliminate some of the dampening and secondly the casing design was modified to include a number of peaks intended to focus any applied force onto the surface of the QTC sensors inserted under them (Figure 6.28). The test results showed an improvement from previous tests; however there were problems with this design. The inclusion of the peaks meant that the size of the area used to detect normal force was now considerably smaller and the slopes on the peaks meant that side forces were easily transferred onto the QTC sensors giving false results. This led to the conclusion that this method would not suffice for the FSW.

Figure 6.28 – Developed QTC sensor casing. The design of the protective casing was modified to include peaks to focus applied force onto the QTC sensors situated below.

The next approach was to move away from the QTC sensors and create a more rugged 'rubber sensor' that could be moulded into a single strip, capable of measuring force across its entire surface. This was be done by developing a custom conductive rubber compound that would exhibit similar behaviours to QTC material. A number of different compounds were developed and cast into moulds to create sensor strips (Figure 6.29). These sensor strips were tested and they all displayed a relationship between voltage and force; however their consistency was hugely unreliable even within the same unit. This was found to be because uniform conductivity could not be guaranteed during the construction of the compound, therefore it was not a viable option for the Force Sensing Wheel.

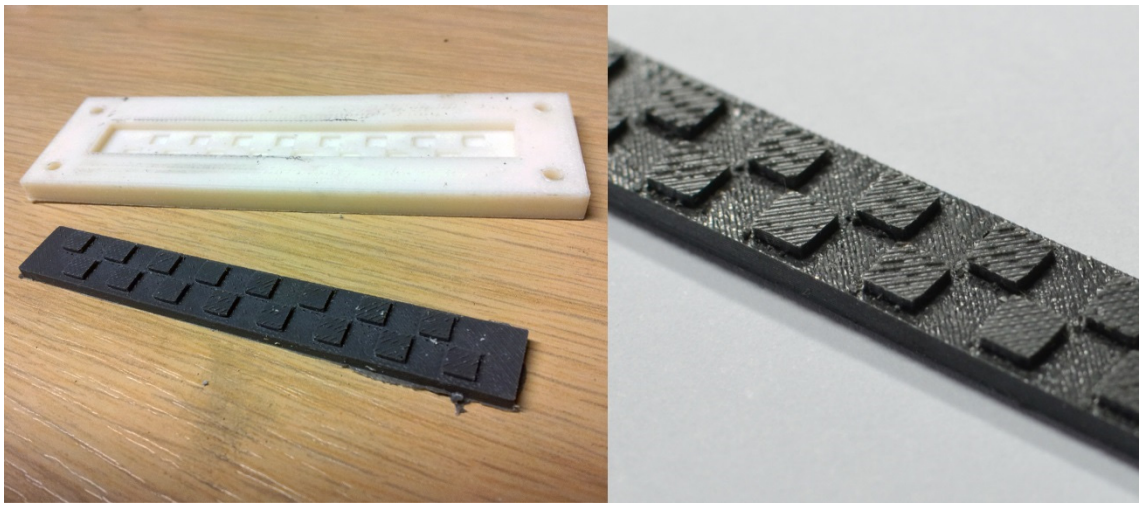

Figure 6.29 – Creating a customisable force-sensing compound. A conductive compound was developed to create a more rugged 'rubber sensor' capable of exhibiting similar behaviour to QTC material.

The developments discussed led to the realisation that QTC sensors were not right for the FSW as they could not easily be protected without affecting sensor performance. Furthermore a bespoke material-based solution was not possible within the constraints of the study, therefore another method of measuring (normal) force was required.

The solution to this problem was found in the tried-and-tested method found in existing Human Interface Devices (HID) such as silicone keypads, which use conductive carbon pills as tactile electrical switches. This method was ideal for the FSW because it offers a mechanical-based solution where the contact area of a domed-shaped carbon pill across PCB traces, increases with applied force causing a change in resistance. Additionally, carbon pills (generally) need to be pressed in the normal direction of the pill meaning they are less susceptive to side forces. Finally they are usually moulded with a silicone outer layer which acts as a good insulator and adds strength and durability while the carbon pill situated below retains sensitivity. Moulds were created for the new design of a silicone 'Sensor Unit' where 8 carbon pills, arranged in the same pattern as before, were inserted ready to be bonded into place by a two-part silicone mix (Figure 6.30). Before the silicone mix was injected into the moulds it was put into a vacuum degasser to remove any air introduced during the mixing process, which would affect sensor performance. Additionally a number of air bleed holes/slots were included in the mould design to allow air to disperse when the rubber mix was inserted. The mould design also included 'pill pockets' that surround the carbon pills to create a flexible membrane, allowing them to return to their normal position (Figure 6.31).

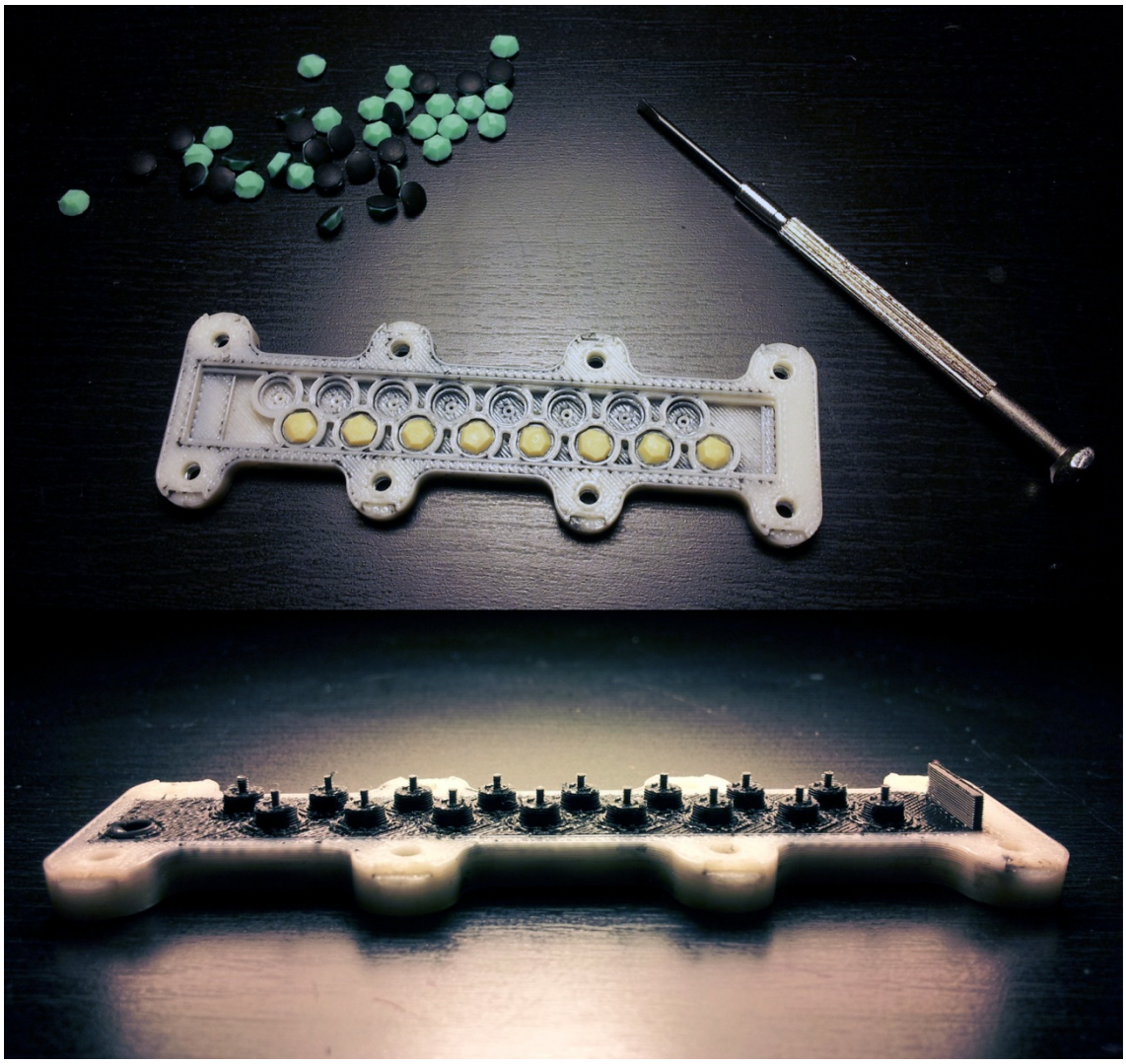

Figure 6.30 – Sensor Unit mould with carbon pills. The mould design included bleed holes to stop any air getting trapped. The carbon pills were carefully inserted before silicone was injected.

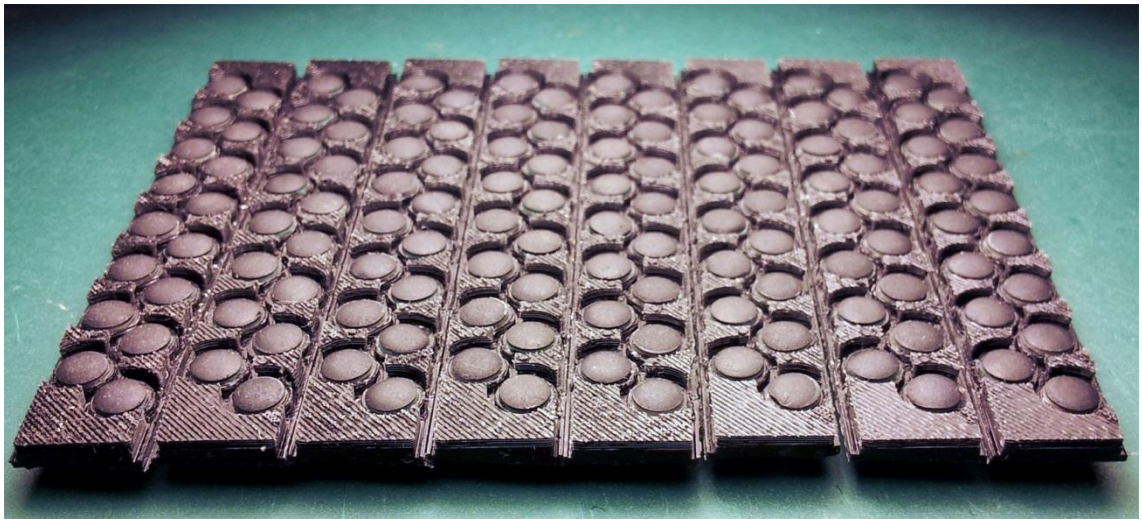

Figure 6.31 – Carbon pills moulded into Sensor Units. The carbon pills were placed in the same pattern as before. The flat surrounding area is the surface where the units are bonded onto the Sensor Boards.

These Sensor Units were designed to easily attach to the Sensor Boards, adding simplicity to the installation process (Figure 6.32). Once removed from their moulds and cleaned up they were bonded to the Sensor Boards using the flat sections surrounding the carbon pills as seen in Figure 6.31. This gave a greater bonding surface area while not affecting the carbon pills or sensor pads. The top part of the Sensor Unit includes a number of raised 'tread' which help to depress the carbon pills located below, increasing sensor sensitivity (Figures 6.32 and 6.33). The Sensor Units were tested for performance and produced good results. They exhibited an exponential relationship between force and voltage with a good level of sensitivity and minimal variance across different sensors; making them the ideal choice for the FSW.

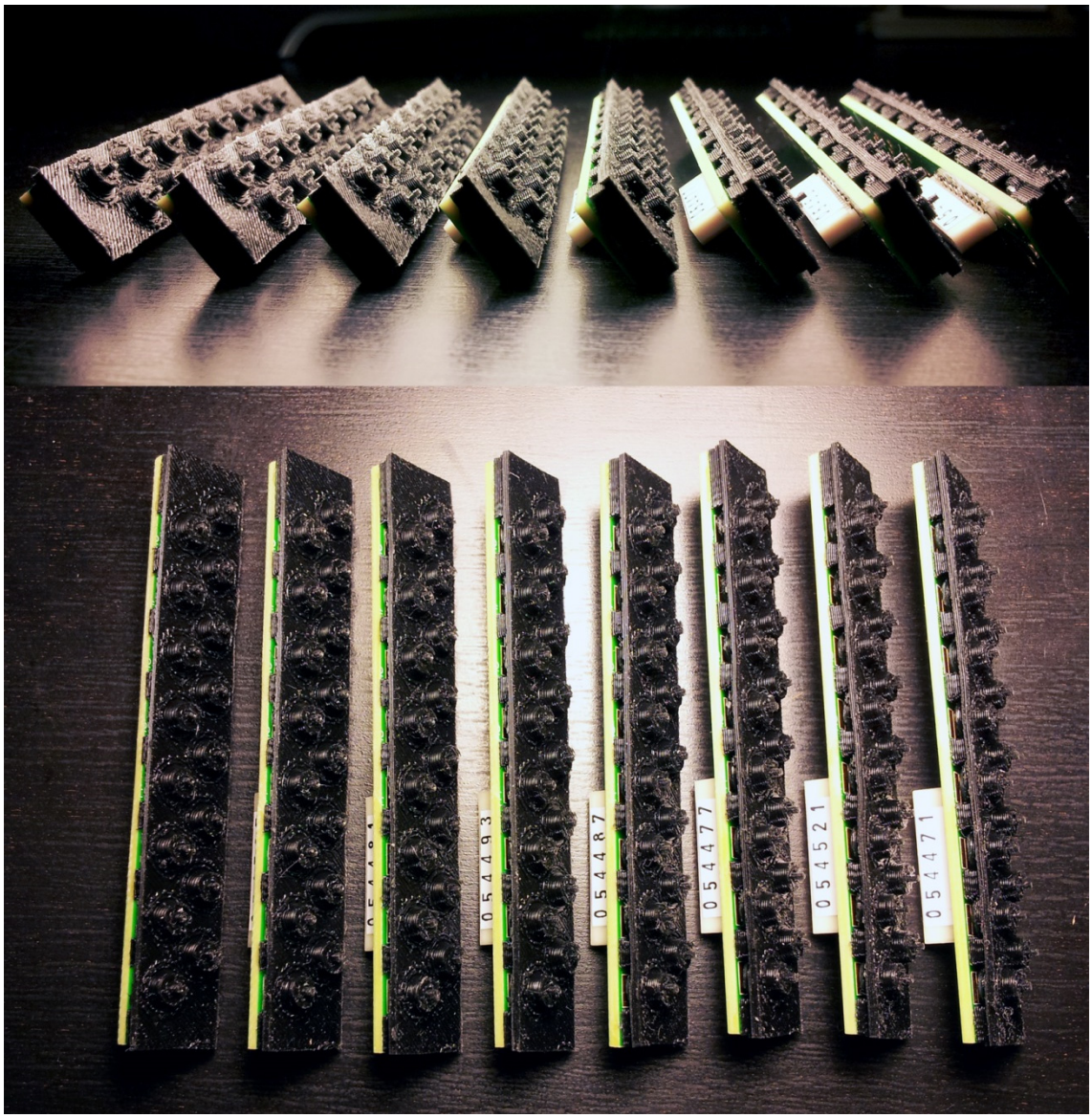

Figure 6.32 – Final Sensor Unit / Sensor Board installation. These images show the final installed Sensor Units which include raised tread, making them more sensitive while offering protection.

Figure 6.33 – Sensor Unit tread. The raised rubber tread helps depress the carbon pills situated below.

6.2.6 Wheel Assembly

Wheel assembly started with each Wheel Segment where the Segment Board was installed and secured in place with a small locator clamp (Figure 6.34). The FFC cables were plugged in and fed through their respective slots for the Sensor Boards to plug into. The Sensor Boards with preinstalled Sensor Units were plugged in and attached to the wheel surface using another special adhesive supplied by 3M. Each segment was then slotted together, located using the tongue and grove slots as seen in the right image of Figure 6.35. The Wheel Segments were then bolted to the Wheel Disc together.

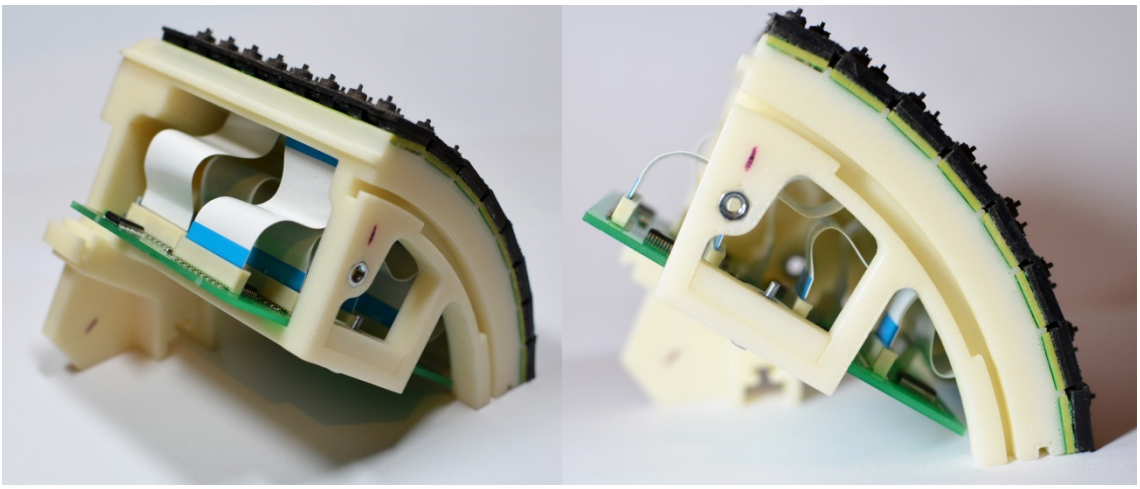

Figure 6.34 – Assembled Wheel Segment. Each Wheel Segment was assembled with a Segment Board which plugged into 8 Sensor Boards / Sensor Units, attached to the surface using adhesive.

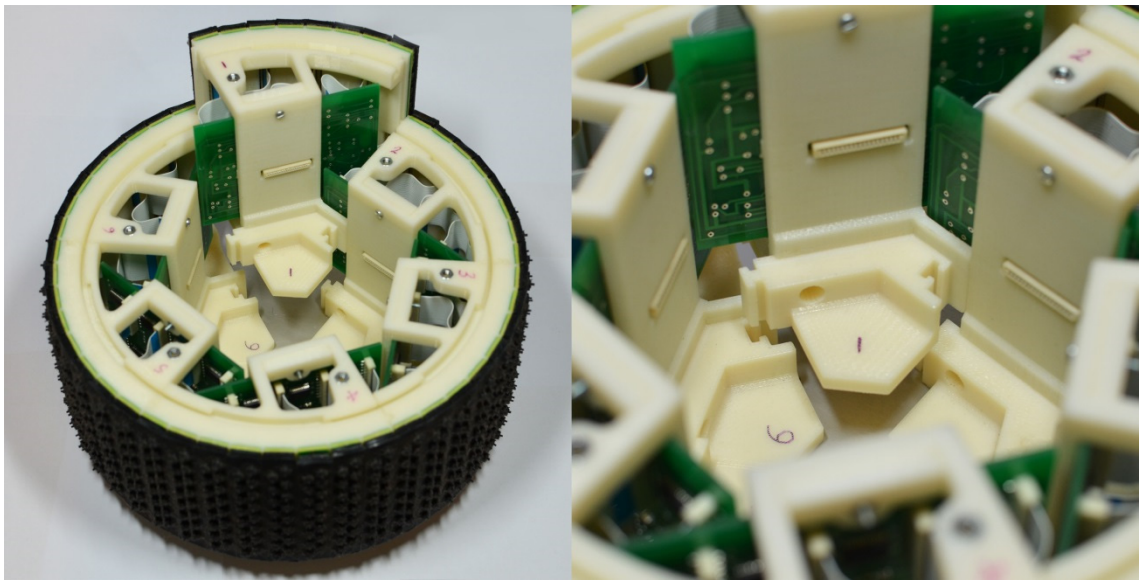

Figure 6.35 – Wheel Segments slotting together. The 6 assembled Wheel Segments were slotted together, located using the tongue and grove slots seen close-up in the image on the right.

The next component to be installed was the Junction Board, however before this could be placed into the wheel a small hexagonal block needed to be inserted into the centre of the wheel structure as seen in the left image of Figure 6.36. This block created a level base for the Junction Board in addition to locating the wheel onto the wheel shaft. Once the block and Junction Board were installed, the six FFC cables were plugged into each Segment Board. The preassembled Core was plugged into the Junction Board via a single FFC and 2-way cable to supply power and then slotted into the centre of the wheel structure, holding the Junction Board in place (Figure 6.37).

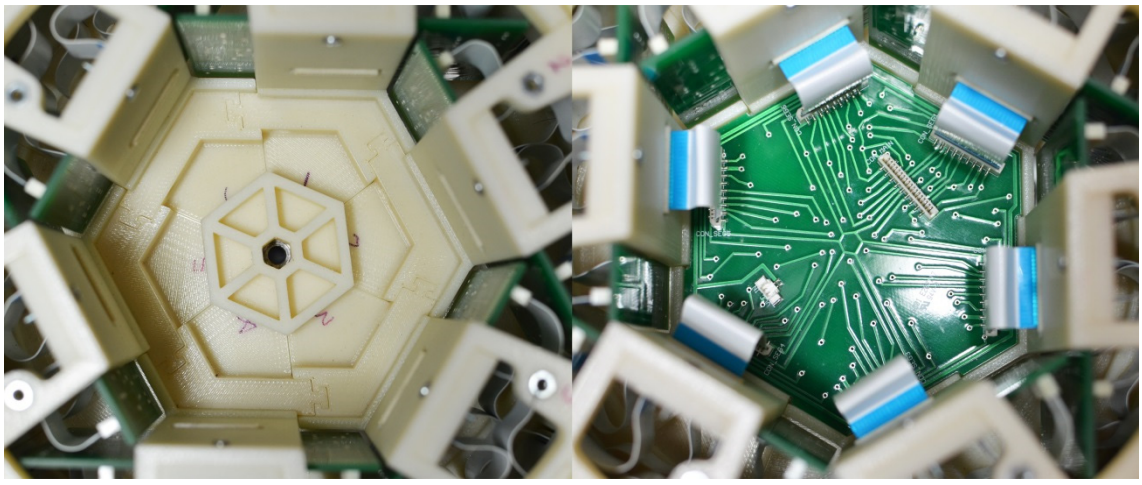

Figure 6.36 – Hexagonal block and Junction Board. The hexagonal block needed to be installed as a level base for the Junction Board which was slotted in and plugged into all 6 Segment Boards via FFC cables.

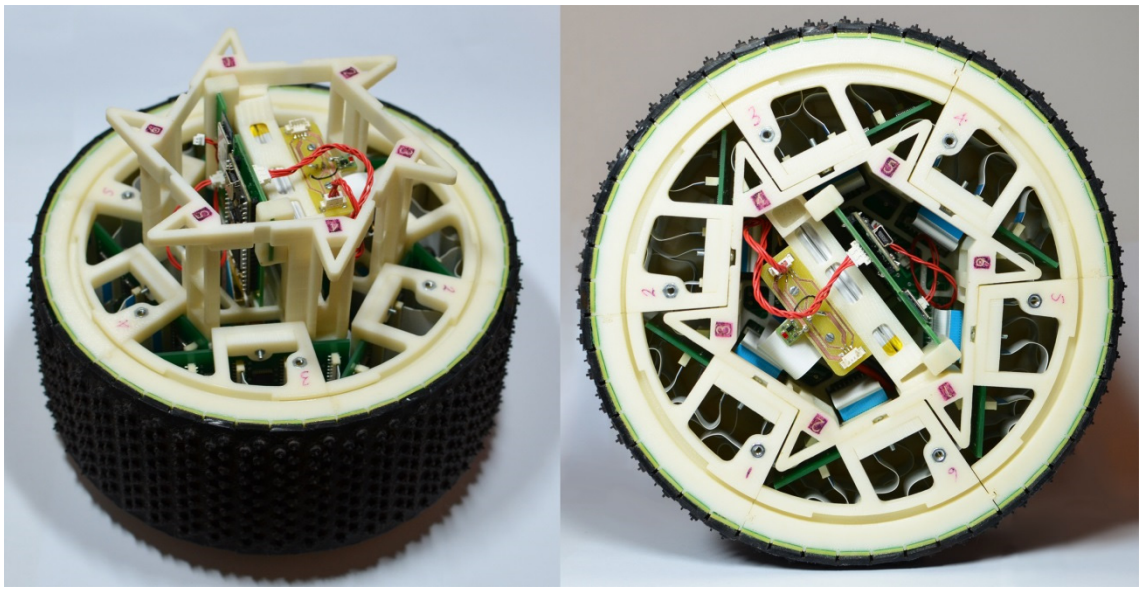

Figure 6.37 – Inserting the Core into the wheel structure. The Core was slotted into the middle of the wheel after plugging into the Junction Board via a single FFC cable and a 2-way cable to supply power.

Finally the Lock Rim was located in the circular groove on the front face and rotated to lock in the Core and the outer rim of the six Wheel Segments. The clear lid, with the on/off button, was plugged into the Power Board and located and bolted into place. The Force Sensing Wheel was now fully assembled as seen in Figure 6.38 below.

Figure 6.38 – Fully assembled Force Sensing Wheel. Once the Lock Rim was installed the Lid could be plugged in and bolted in place, completing the assembly of the FSW.

6.3 Sensor Calibration

The limitations of available facilities and variables involved during sensor manufacture led to minor differences in sensitivity across the custom-made sensors; therefore the sensors needed to be calibrated to have confidence in the accuracy of measurements. The calibration tests involved applying a range of (normal) forces onto individual sensors and measuring the relative voltage, so that each sensor's (exponential) relationship between voltage and force could be calculated and used to accurately convert raw sensor data to actual force values.

Specialist test equipment was required to apply exact amounts of force onto individual sensors; therefore an industrial force gauge test stand was sourced, which is capable of applying and measuring forces of up to 25N with a resolution of 0.01N. To complete the calibration test-rig a custom clamp was built to attach to the stand and hold the FSW in position. A number of settings on the clamp allowed the wheel to be fixed in various positions radially and across the wheel width, so that every one of 768 sensors could be accurately aligned normal to the force gauge probe (Figure 6.39).

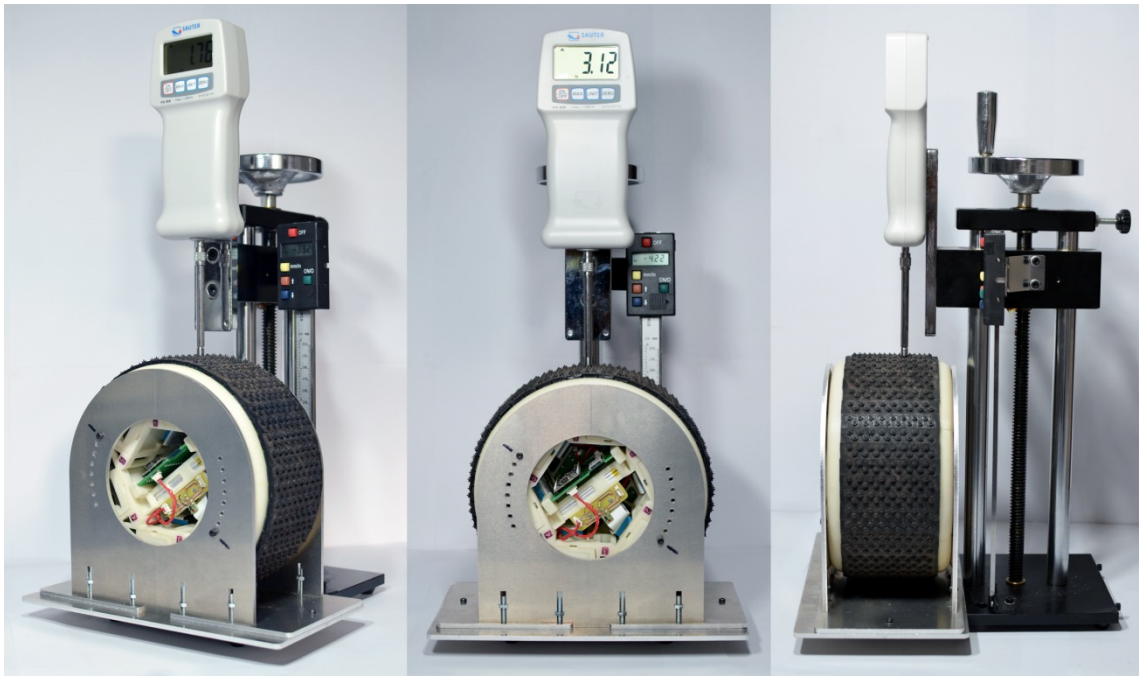

Figure 6.39 – Calibration test-rig. The calibration test-rig incorporated an industrial 25N force gauge test stand and custom made clamp to hold the FSW so that every sensor could be aligned to the gauge probe.

The test procedure involved fixing the FSW into the clamp to align a particular sensor to the force gauge probe which was then lowered to apply specific forces to the sensor as seen in Figure 6.40. Initial tests saw the sensors exhibit a larger range (higher sensitivity) for forces <1N and a smaller range (lower sensitivity) for forces >1N. This is believed to be because forces up to 1N will generate initial contact between the carbon pill and the PCB traces, causing a greater change in resistance. To account for this, the forces applied onto the sensors during the calibration tests ranged from 0.2-10N in two different phases: every 0.2N between 0-1N and then every 1N between 1-10N. This range was sufficient for the tests as the total distributed force expected across the entire wheel-terrain contact interface was approximately 20N.

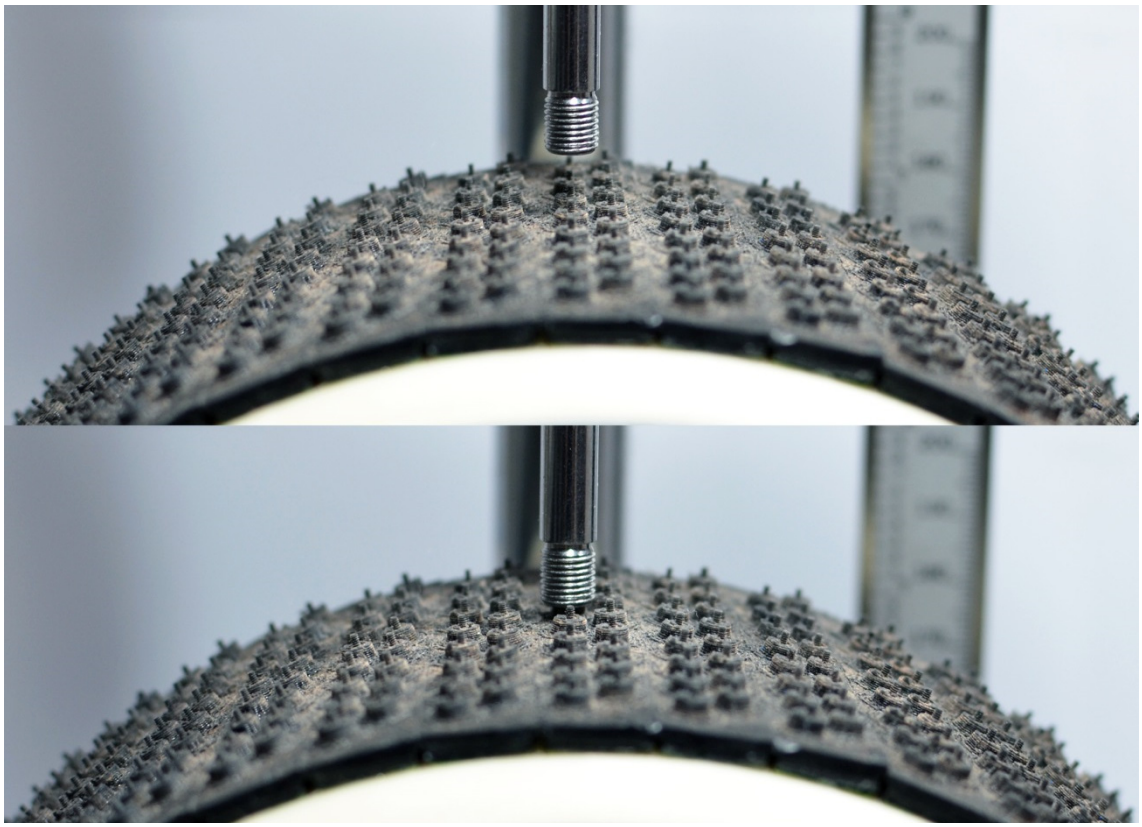

Figure 6.40 – Force gauge probing a sensor. The calibration test involved the force gauge being lowered onto a specific sensor by exact forces, while sensor data was streamed to LabVIEW where it was logged.

A simple program was created in LabVIEW to log the real-time data streamed from the FSW. This raw data was converted to voltage figures and arranged in a table alongside corresponding force values to generate a graph. A selection of results from the calibration tests can be seen in Appendix E with Figure 6.41 showing an example of one of these graphs where exponential curves are accurately fitted to logged sensor values.

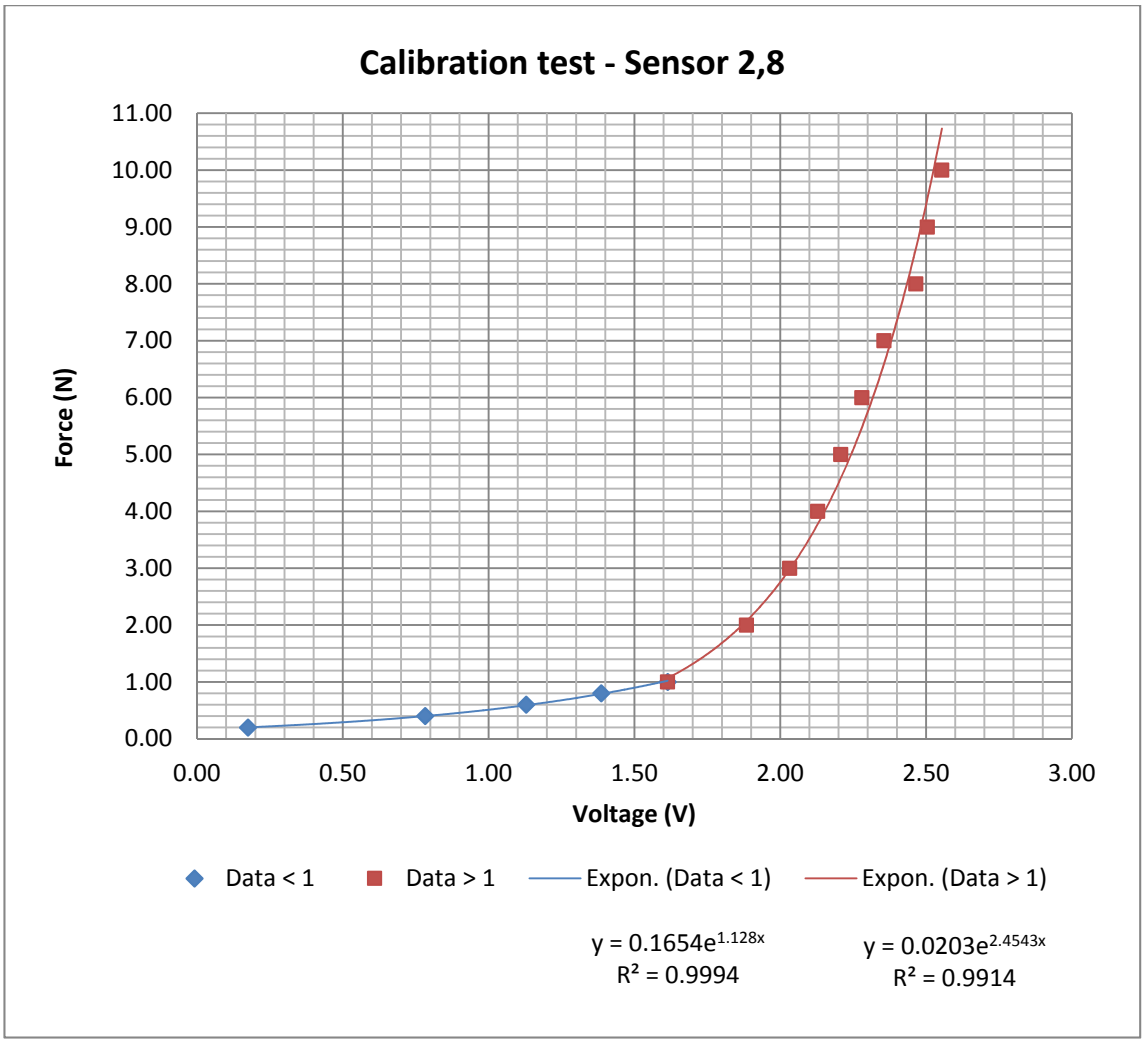

Figure 6.41 – Graph showing a set of calibration test results. The logged data was arranged in tables alongside corresponding force values to create graphs where exponential curves were fitted.

The results of the calibration tests as seen in the example above (Figure 6.41) gave two exponential relationships: one for force values <1N and one for values >1N, due to the reasons discussed earlier. This gave a more accurate fit as demonstrated by the extremely high coefficient of determination (denoted R^2), giving confidence in the accuracy of future measurements.

The values relating to the exponential relationships of the fitted curves can be seen in the formulas at the bottom of Figure 6.41. These formula values relate to each sensor's sensitivity and are needed to accurately calculate force values from raw sensor data; therefore the unique values for all 768 sensors were calculated and stored, ready to be used during the data processing procedure (discussed later).

6.4 Platform Developments

The platform used for the main experiment was based on the same vehicle chassis from the earlier experiment; however modifications needed to be made to mount the Force Sensing Wheel and a new suite of electronic components. To start with all the unnecessary components were removed, leaving only the essential mechanical parts of the chassis and the encoder mounted on the gearbox as seen in Figure 6.42 below.

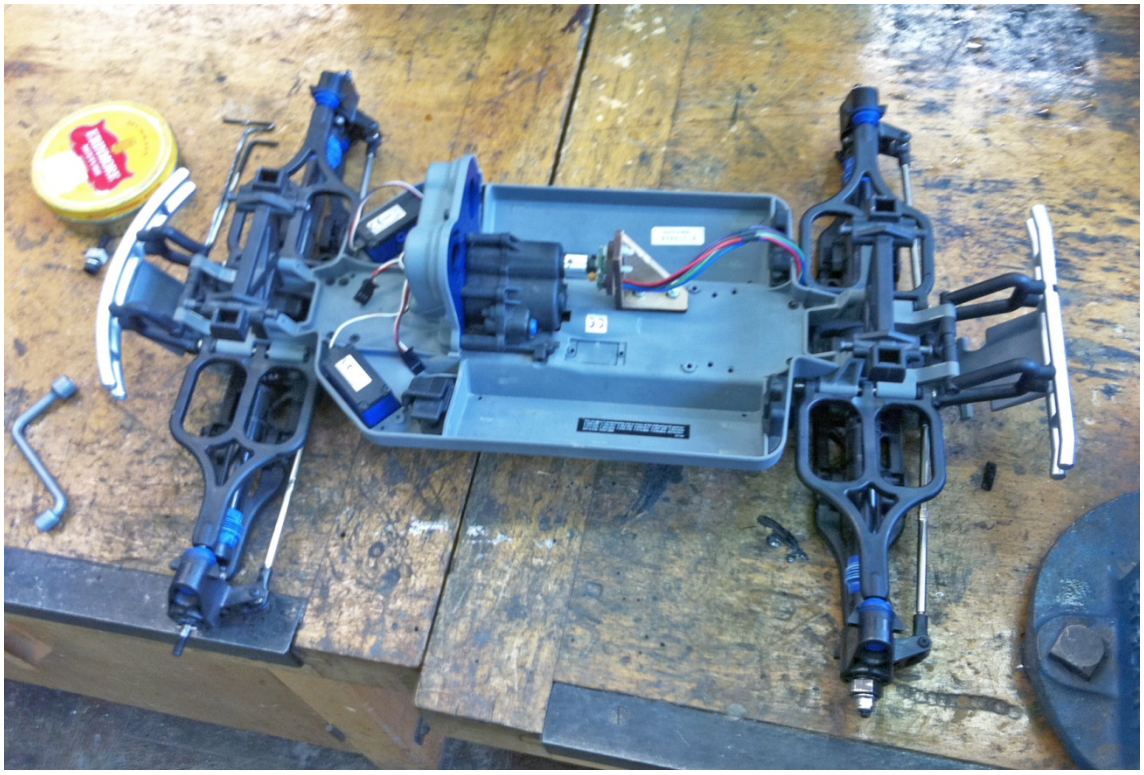

Figure 6.42 – Stripped down vehicle chassis. The original vehicle chassis from the earlier experiment was stripped down to the essential mechanical parts ready to house the new platform components.

6.4.1 Chassis Modifications

The first modification to the original chassis was the installation of off-the-shelf differential locks. This was to stop unequal torque distribution caused by individual wheel slip which would lead to false wheel angular velocity values with the encoder being mounted on the gearbox. The next task was to lock the suspension to stop it affecting the (normal) force exerted on the wheel-terrain interface. Custom designed parts were cut from 5mm aluminium sheet using water-jet cutting technology and installed using the original suspension mounts (Figure 6.43).

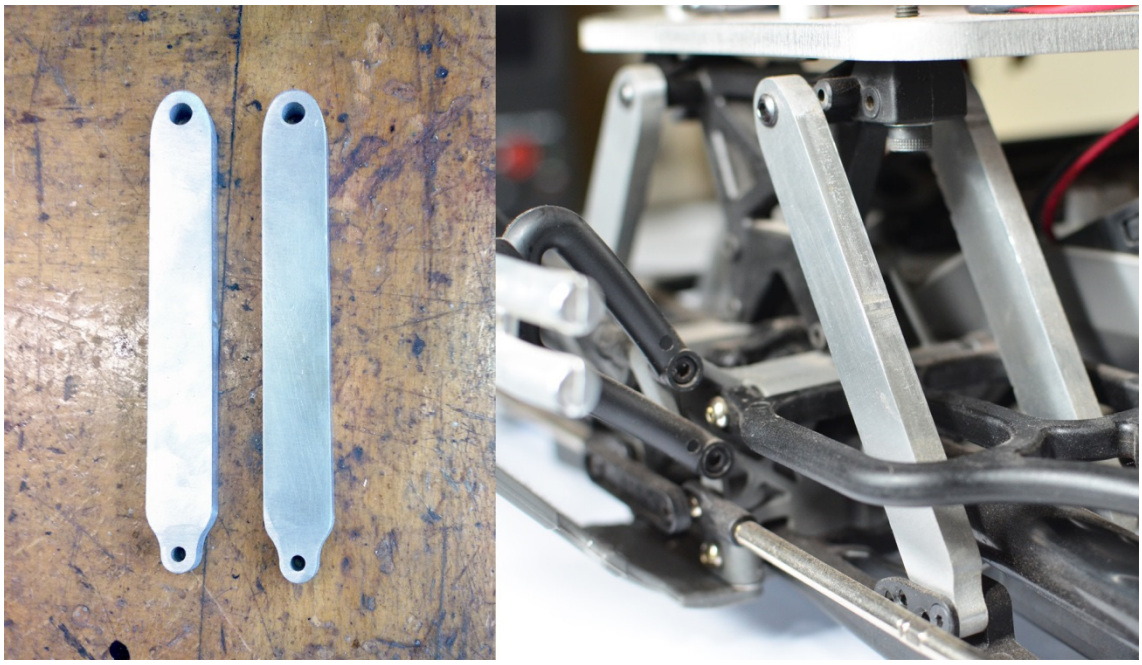

Figure 6.43 – Custom suspension locks. These aluminium parts were designed using CAD software and manufactured using water-jet cutting technology before being installed on the original mounts.

Also cut from the 5mm aluminium sheet were the parts for the Wheel Discs mentioned earlier. This component consists of two parts, the round outer disc which the FSW mounts to using six bolts and the inner star shaped part which attaches and aligns the entire wheel assembly to the existing hub (Figure 6.44). The final aluminium part was a large plate attached on top of the main chassis mounts as seen in Figure 6.45. This plate was installed to strengthen the chassis and mount the Main System Controller.

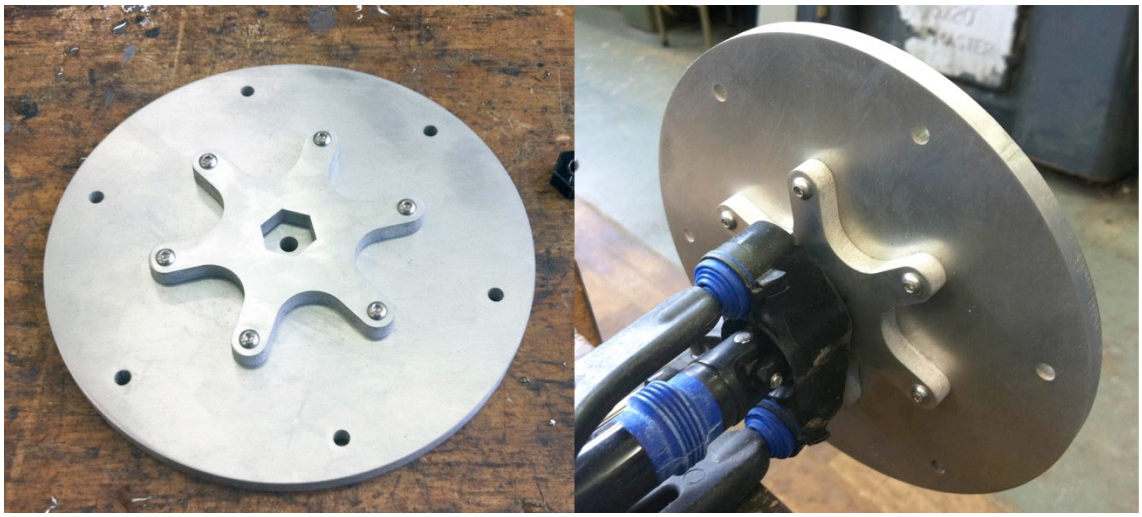

Figure 6.44 – Assembled Wheel Disc components. The two wheel disc parts were also manufactured from aluminium and are used to attach the FSW to the original wheel hub on the chassis.

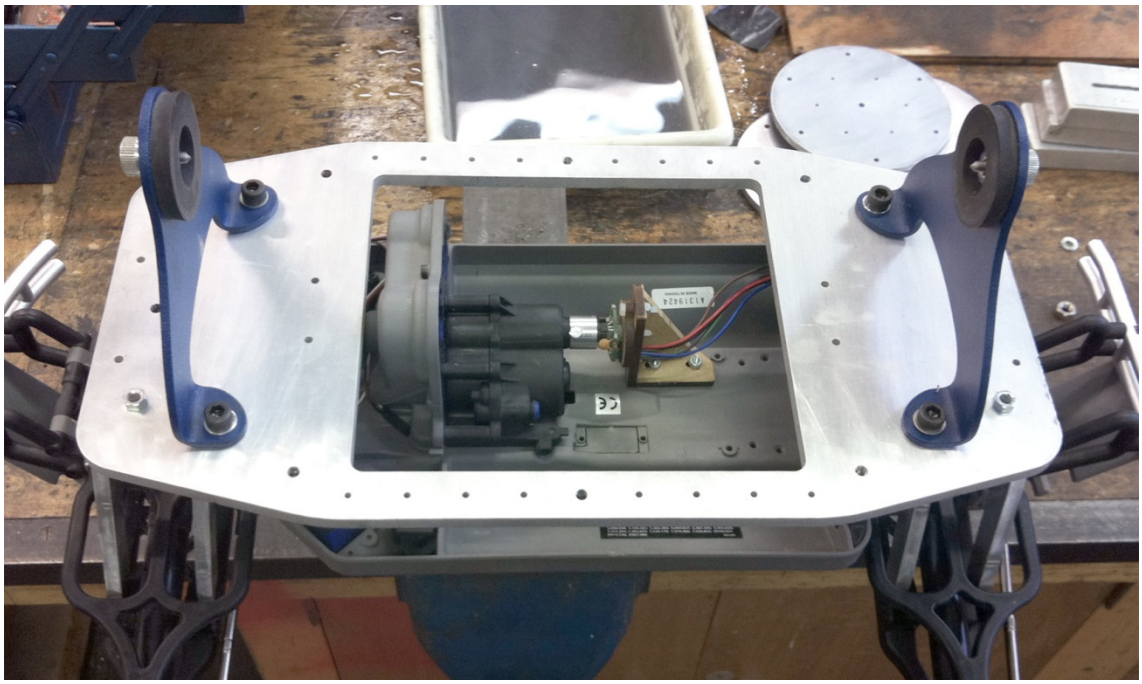

Figure 6.45 – Aluminium mounting plate. A large aluminium plate was designed and installed to add strength to the original chassis and accommodate the mounts for the Main System Controller.

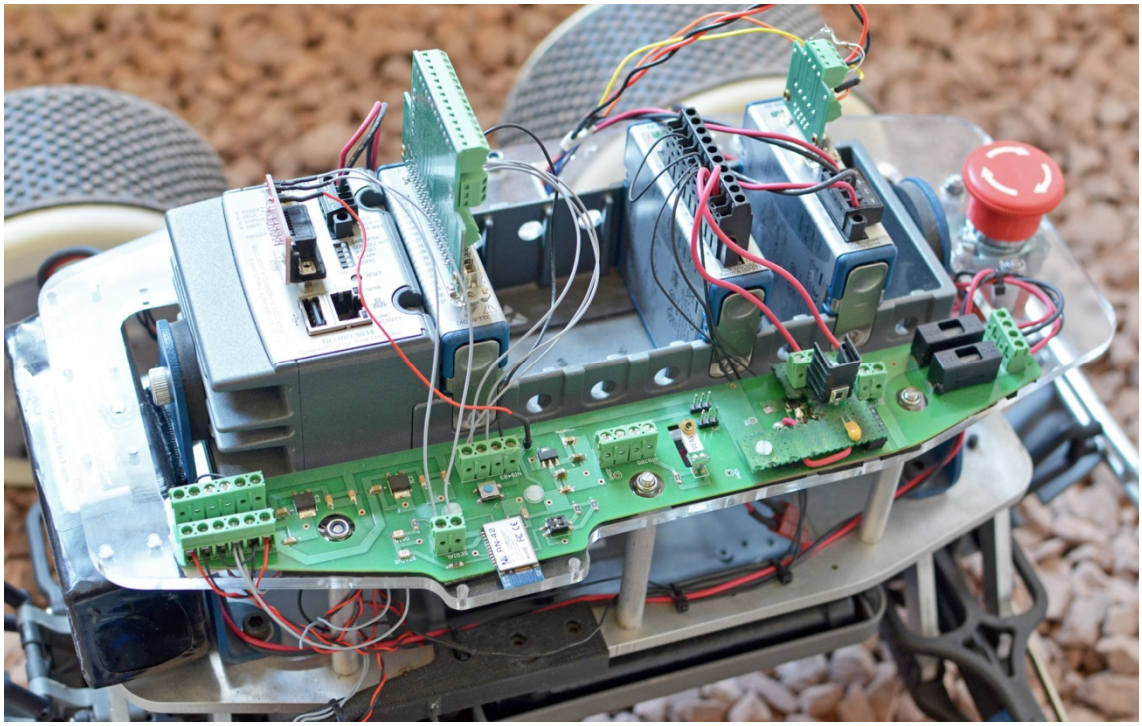

Figure 6.46 – Upper electronics layer. A lightweight layer was installed on top of the large aluminium plate to provide a platform to mount various other electronics components onto.

The final modification to the chassis was the addition of a lightweight upper layer seen in Figure 6.46 above, which attached to the aluminium plate and was used to mount the other electronic components that manage the system.

6.4.2 Platform Electronics

The platform contains a new suite of electronics for vehicle control and data management. The Main System Controller labelled (1) in Figure 6.47 is in the form of National Instruments Compact RIO (cRIO), a real-time embedded controller which boasts a powerful 400MHz processor, 128MB RAM and 2GB on-board storage. This highly capable system includes a reconfigurable chassis and hot swappable I/O modules and works with LabVIEW software for advanced graphical programming.

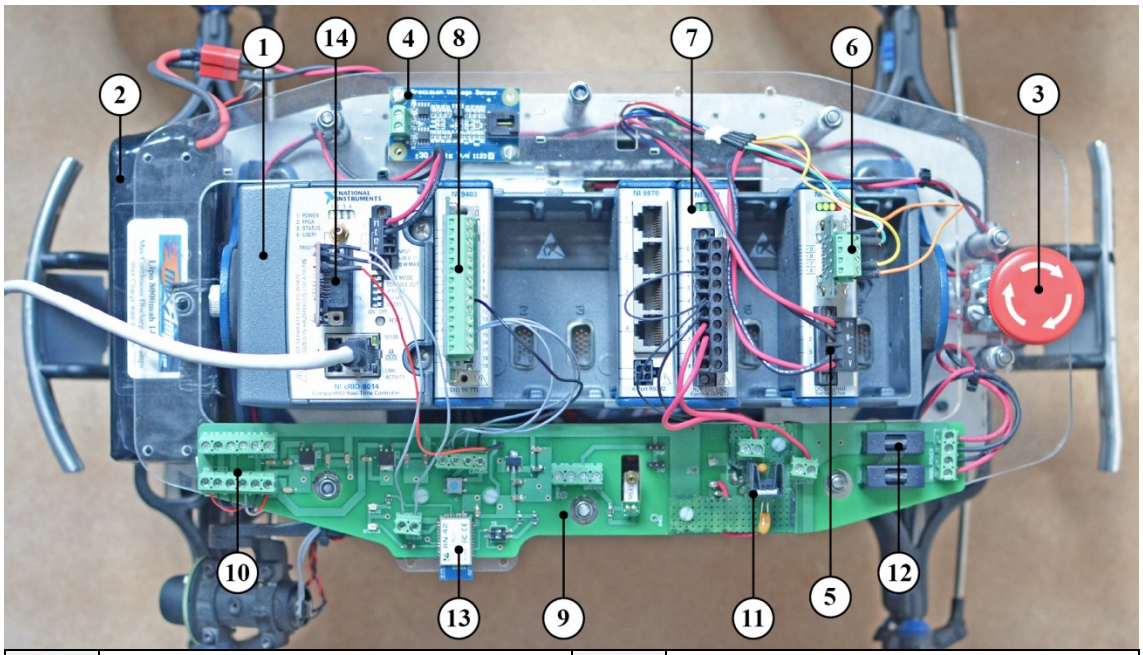

1	Main System Controller (cRIO)	8	Digital I/O Module (NI 9403)
2	Power Supply (14.8V LiPo)	9	Power/Data Board
3	Emergency Button (on/off)	10	Camera Control Circuit
4	Low Voltage Sensor	11	Voltage Regulators (3.3V/5V)
5	Motor Control Module (NI 9505)	12	Safety Fuses (6A)
6	Encoder Management (NI 9505)	13	Bluetooth Module (RN42)
7	Relay Module (NI 9481)	14	Serial Data Converter

Figure 6.47 – Outline of platform electronics. This image displays the main electronic components installed on the platform for vehicle control and data management.

Power is supplied to the system by an 8Ah, 14.8V LiPo (2) via the emergency button (3) and monitored using a low voltage sensor (4). The cRIO controls vehicle motion using a motor controller module with built-in current sensor (5) and encoder management (6). A relay module (7) is used to manage power distribution and a digital I/O module (8) is used to control other electronic components.

A bespoke PCB (9) was designed to control the on-board cameras (10) and manage power distribution using voltage regulators (11) with fuses for safety (12). The main function of this board was to pass real-time sensor data from the FSW to the cRIO via a Bluetooth module (13) and serial data converter (14).

6.4.3 On-board Cameras

Two 720p HD cameras were installed on the platform using custom mounts to record the experiment from different perspectives. One was mounted alongside the FSW looking at the terrain ahead (left image Figure 6.48) and the second was mounted under the chassis facing towards the bottom of the FSW where wheel-terrain interaction occurs (right image Figure 6.48). These cameras, controlled by the cRIO, also included bespoke ring lights to illuminate the view.

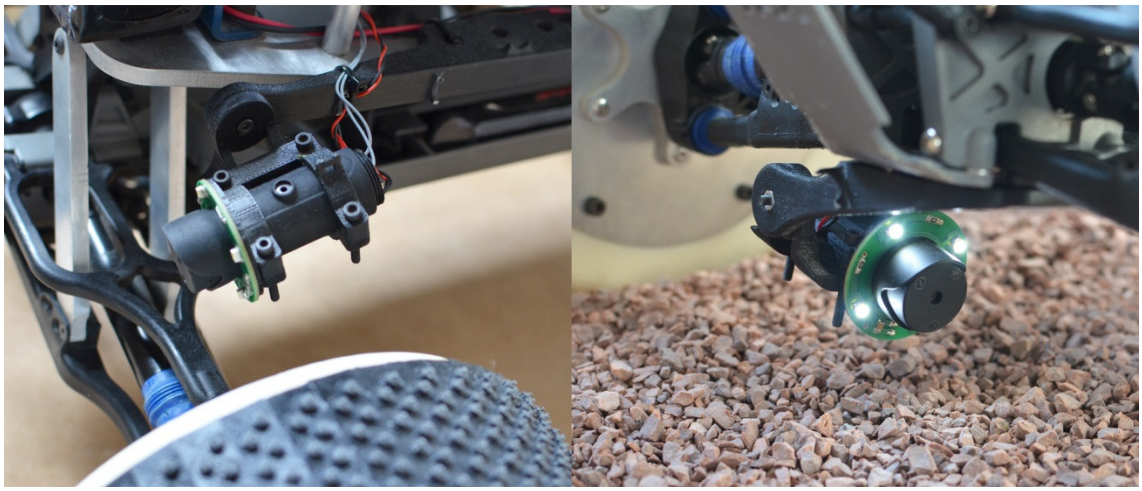

Figure 6.48 – On-board cameras. Two cameras with bespoke light rings were installed to record the experiment from different perspectives: looking ahead and at the point of wheel-terrain interaction.

6.4.4 Dummy Wheels

The platform needed three other wheels to complete the platform. These ‘dummy’ wheels needed to have similar properties to the FSW and were therefore designed using CAD tools and realised using the 3D printer (left image Figure 6.49). The tread needed to mimic that of the Sensor Units on the FSW, therefore a simple mould was created to cast a rubber tyre which was attached onto the dummy wheels (right image Figure 6.49).

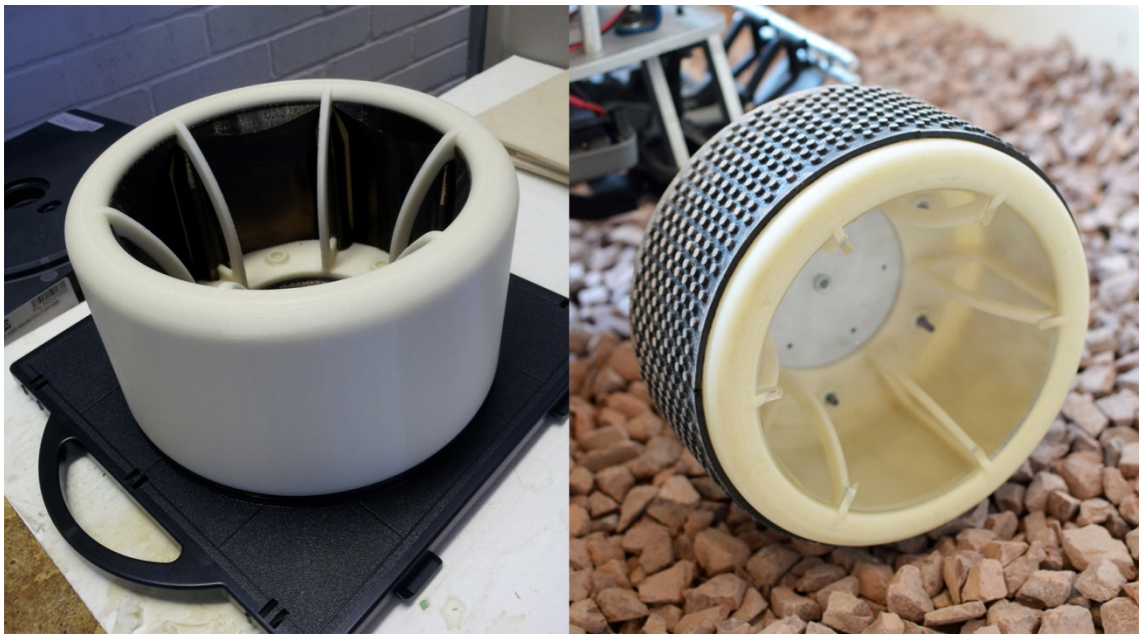

Figure 6.49 – Dummy wheels installed on the platform. Three dummy wheels were designed and manufactured using the 3D printer and included tread with similar properties to the FSW Sensor Units.

6.4.5 Final Assembled Platform

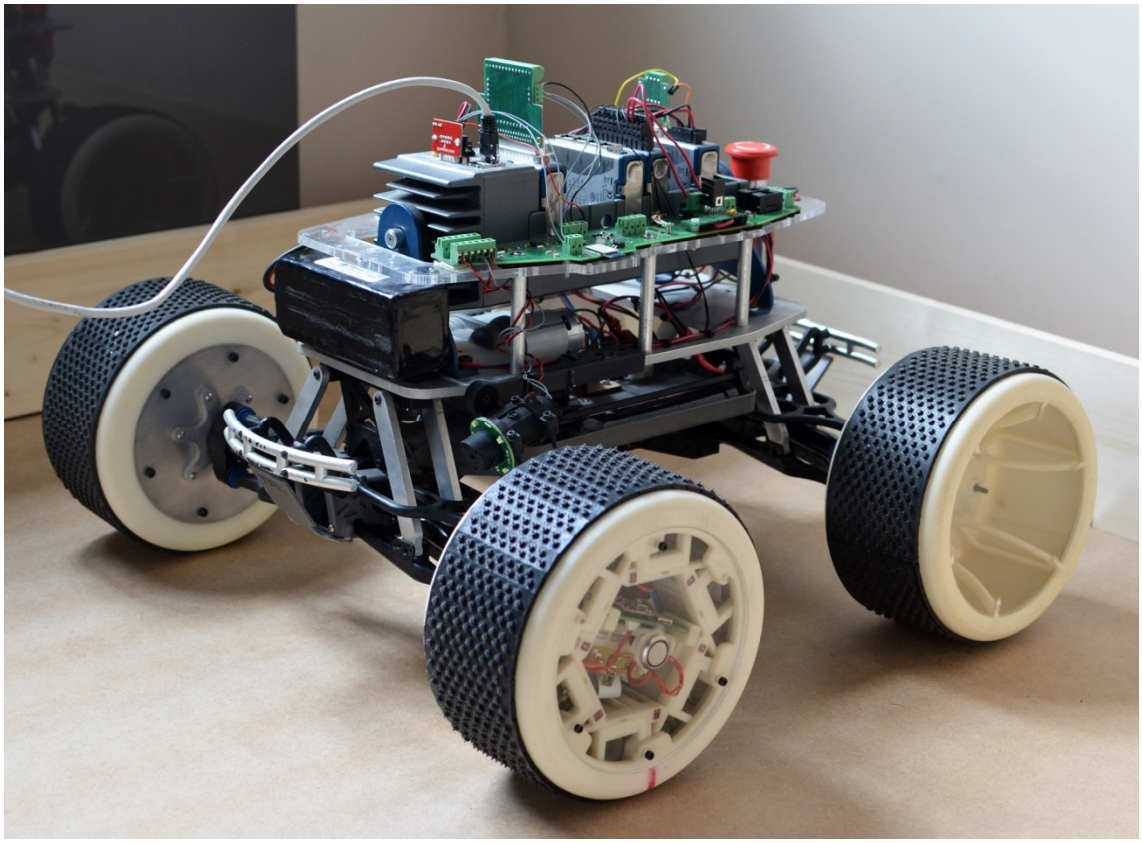

Figure 6.50 – Completed vehicle platform. With all the chassis modifications, installation of the electronics and dummy wheels; the FSW was attached to complete the build of the system's hardware.

6.5 Discussions

The outcome of the review into terramechanics led to the discovery of the key parameters involved during wheel-terrain interaction, presented graphically in the diagram shown in Figure 6.2. This highlighted a unique opportunity to classify terrain conditions in real-time using pressure distribution measurements across the wheel-terrain interface. To validate this concept a novel embedded system in the form of the Force Sensing Wheel was developed.

As outlined in this chapter the innovative FSW design includes a modular structure, containing bespoke embedded electronics and an array of custom sensors integrated across the entire wheel surface. The intelligent self-contained system is capable of actively measuring force distribution across the wheel-terrain interface and wirelessly sending real-time data to the Main System Controller, where it is stored and/or analysed. This novel method of exteroceptive sensing is unlike other passive methods (discussed in Chapter 2) as it actively measures terrain conditions taking wheel interaction into account, which offers a more accurate representation of the terrain's properties.

The FSW was fully calibrated so that accurate calculations can be made from measurements. The highly capable cRIO system was integrated into the platform to control vehicle motion and manage real-time data sent from the FSW. The completed platform was now ready for the main experiment to gather wheel-terrain interaction measurements in order to create a unique terrain classification technique.

CHAPTER 7
TERRAIN SENSING AND CLASSIFICATION

7.1 Experimental Design

The objective of the main experiment was to measure the normal (radial) force distribution[3] across the 3D contact area at the wheel-terrain interface during different terrain conditions, to determine potential relationships that could be exploited to create a unique classification technique.

7.1.1 Independent/Dependent Variables

This experiment aimed to use the effect that terrain has on the wheel-terrain interface to create a unique classification technique, making terrain the independent variable. Granular terrain was used for the tests with variations within this terrain class used as the independent variables. The dependent variables of the experiment were those of the interaction affected by terrain properties, which were contact angle θ, radial pressure distribution and the location of maximum pressure θ_m at the wheel-terrain interface.

7.1.2 Control Variables

Certain variables were controlled in order to ensure that the dependent variables were not affected by other conditions. An indoor terrain test-bed was devised to decrease the amount of uncontrollable, intervening variables (such as weather), allowing terrain variables such as slope/gradient and moisture content to be controlled. Vehicle parameters controlled included vertical load W, wheel radius r, wheel width b and wheel angular speed ω. Finally the vehicle's differentials and suspension were locked to stop them affecting wheel angular velocity and force exerted on the contact patch.

[3] With the emphasis being on normal stress, shear stresses were not considered within this study.

7.1.3 Sampling (Site Selection)

For the main experiment non-random/non-probability sampling was selected where variations of one terrain type represented a change in terrain conditions. The main tests were carried out across three variations of gravel from the (granular) terrain class 'Coarse Soil' as per ISO 14688-1 seen earlier in Table 2.1. Gravel was chosen due to its availability and because the variation in particle (grain) size would yield better results. The tests carried out included one of each gravel sub-fraction defined by particle size: fine (2-5mm), medium (10-20mm) and coarse (20-40mm); seen in Figure 7.1 below.

Figure 7.1 – Three grades of Gravel used for the experiment. Fine, medium and coarse gravel types were chosen as per ISO 14688-1 with the variation in grain size representing different terrain conditions.

7.1.4 Sample Size

As discussed, an indoor test-bed was devised to allow control of external conditions which increased adjustability and consistency in terrain conditions. This also gave more flexibility to sample size and easily allowed five runs per test without any vast changes in the test-bed environment. This sample size was selected as it provided sufficient data to give confidence in the results without overwhelming data processing.

The size of the test-bed was 2.5 x 1.5m and filled to a depth of 0.2m (Figure 7.2). This size was dictated by the space available however it was sufficient enough to provide data from at least two full wheel rotations, avoiding false values from test-bed borders.

Figure 7.2 – Final terrain test-bed. The test-bed was 2.5 x 1.5m with a depth of 0.2m giving sufficient results from at least two wheel rotations without false values from the borders and base.

7.1.5 Controlled Test

As discussed earlier the match-control method was utilised for this study. This involved carrying out an initial (control) test which was done across a flat surface with reasonable frictional because it would have the least effect on vehicle performance. The results gathered from this test were used as a (datum) reference of optimum interaction conditions to compare other test results to. As this controlled test was carried out on a surface of known properties then it was also used to validate the test-rig.

7.1.6 Main Experiment Procedure

The main experiment involved five test runs across the three gravel types. The test-bed was filled with one gravel type and levelled before placing the vehicle at the start ready to begin testing. Once five runs were completed the test-bed was fully emptied and filled with the next gravel type. This was repeated until all tests were completed.

Controlling the experiment was achieved using a LabVIEW control panel running on a host PC connected to the cRIO (Figure 7.3); this was used to start/stop the vehicle and the on-board cameras while regulating the vehicle's speed. The vehicle's linear velocity was fixed to 0.3m/s using FPGA based motor control to regulate the motor to 540rpm, which translated to a wheel angular velocity of 30rpm with the 18:1 gearbox. This was achieved by performing Proportional Integrated Derivative (PID) control and driving the motor using Pulse Width Modulation (PWM) accordingly.

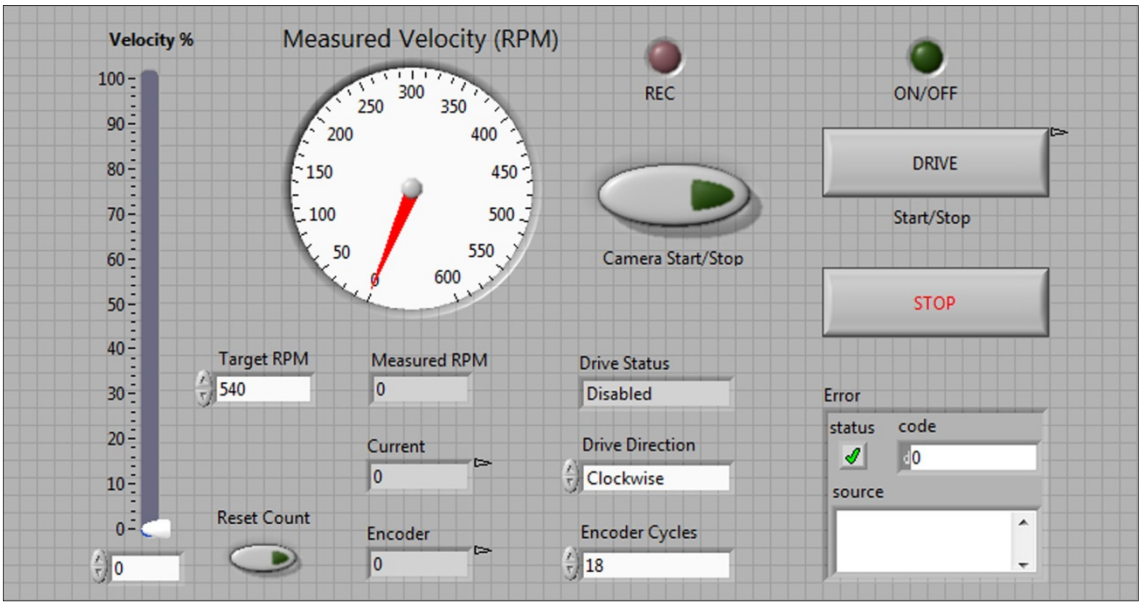

Figure 7.3 – LabVIEW experiment control panel. A control panel running on a host PC connected to the Main System Controller (cRIO) was used to control the vehicle during the experiment.

During the experiment certain values displayed on the control panel, such as current draw and encoder position, needed to be recorded for analysis. Consequently these values were set as global variables within the LabVIEW project in order to share them with the main data-logging program yet to be discussed. The Drive start/stop button (seen top right on the control panel) was also linked to the main program to inform the system when to start/stop recording data.

At the end of every group of tests across the same gravel type, video files were downloaded from the on-board cameras (Figure 7.4) in addition to a fixed camera used to record the experiments from an external view. Finally the gathered data was checked to make sure it was successfully logged and once confident with the results, the gravel was emptied and the next test was prepared.

Figure 7.4 – View from an on-board camera during the various tests. The tests were recorded from various perspectives to capture the experiment and help (offline) visual analysis.

7.1.7 Gathering/Storing Data

The Force Sensing Wheel reads all 768 sensors in real-time and organises the raw data values into a 2D x/y coordinate chart, where *x* represents a sensor's radial position and *y* represents the sensor's location across the wheel width. The coordinate chart also takes into account the array pattern including the blank spaces between sensors, making the size of the chart: x = 96 and y=16. Once the FSW has placed a set of sensor values into the chart then it is instantly sent as a complete 'data packet' via serial (Bluetooth) communications to the cRIO at 14.4KB/s (115200 baud). As the size of each data packet doesn't exceeding 4KB, then all 768 sensor values are obtained by the cRIO approximately every 300ms. In order to eliminate errors during the sending/receiving of packets and preventing data loss 'Handshaking' flow control methods are utilised. This involves the transmitter (FSW) only sending data when the receiver (cRIO) communicates that it is ready to receive data, once the buffer is clear from the previous data transmission. As each data packet is received by the cRIO it is 'unpacked' and logged by the main data-logging program.

The front panel of the main data-logging program included a 3D surface map displaying a live view of the contact interface during the tests (Figure 7.5). As previously mentioned data logging was automatically started and stopped with vehicle motion via the experiment control panel, indicated by a status light. Additionally drop down menus gave options to correctly label the logged data which was stored directly on the host PC.

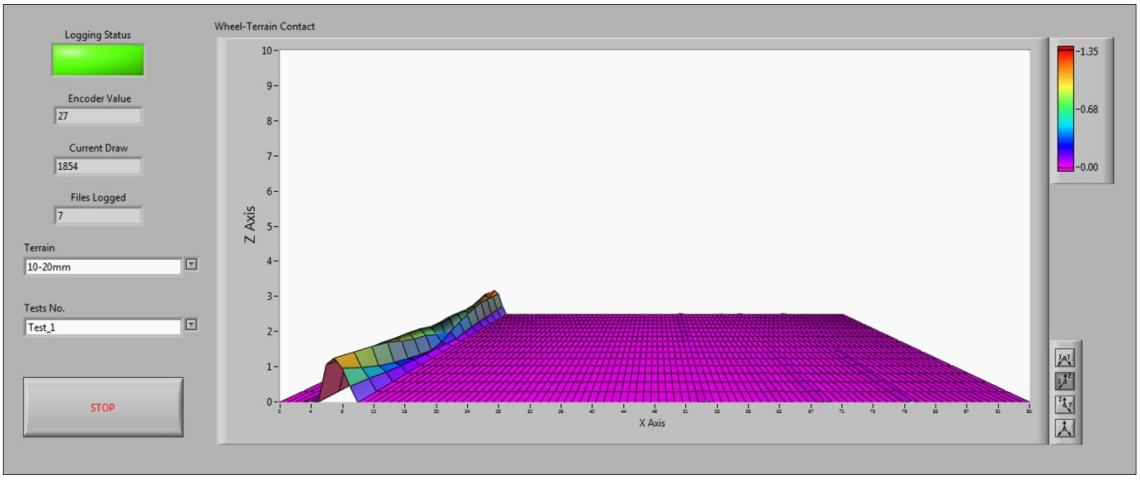

Figure 7.5 – Data-logging front panel. The main data-logging program included options to input test information and offered a live view of the experiment via a 3D surface map showing contact data.

7.1.8 Data Processing

The received data required processing therefore after it was unpacked, individual values were constructed back into the x/y coordinate format by placing them into a 2D array as seen in Figure 7.6 below. The x/y coordinate layout was designed to take into account the physical spaces between sensors in order to correctly align data values in the array pattern; however this caused intermittent data points when results were displayed. To produce smoother data curves, values form laterally adjacent sensors were averaged and inserted into blank cells.

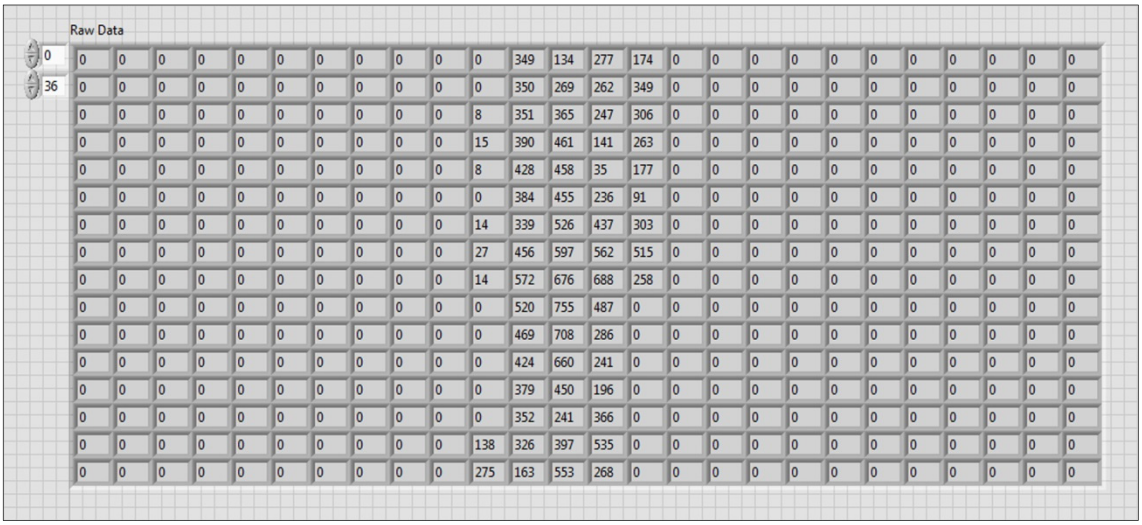

Figure 7.6 – Sensor data arranged in a 2D array. Once data packets were received from the FSW they were unpacked and arranged back into the x/y chart format using 2D arrays in LabVIEW.

The final process was to convert raw sensor data into meaningful force measurements for which the unique calibration numbers discussed in Chapter 6 were required. These unique values that were obtained during the calibration tests including both exponential relationships (<1N and >1N) alongside the threshold number known as the decider value. To convert raw data into actual force values, the exponential function seen in Equation (12) was utilised; where C and B are unique values of the exponential relationship, v is the voltage converted from raw data, e is Euler's irrational number (2.71828) and F is the calculated force:

$$F = C\left(e^{(Bv)}\right) \tag{12}$$

7.2 Terrain Sensing Results

Once the gathered data was processed the results of the experiment were arranged graphically for analysis. These graphs display the contact angles and (normal) force distribution during wheel-terrain interaction across the different terrain types. A larger range of results for all tests can be seen in Appendices F-I with a selection shown here.

The first set of graphs for each test approach wheel-terrain interaction from a 2D perspective as per terramechanic theories. However the novel FSW facilitated direct force measurements across the entire wheel-terrain contact interface which led to a unique set of results, presented using 3D surface maps.

7.2.1 Controlled Test (Datum)

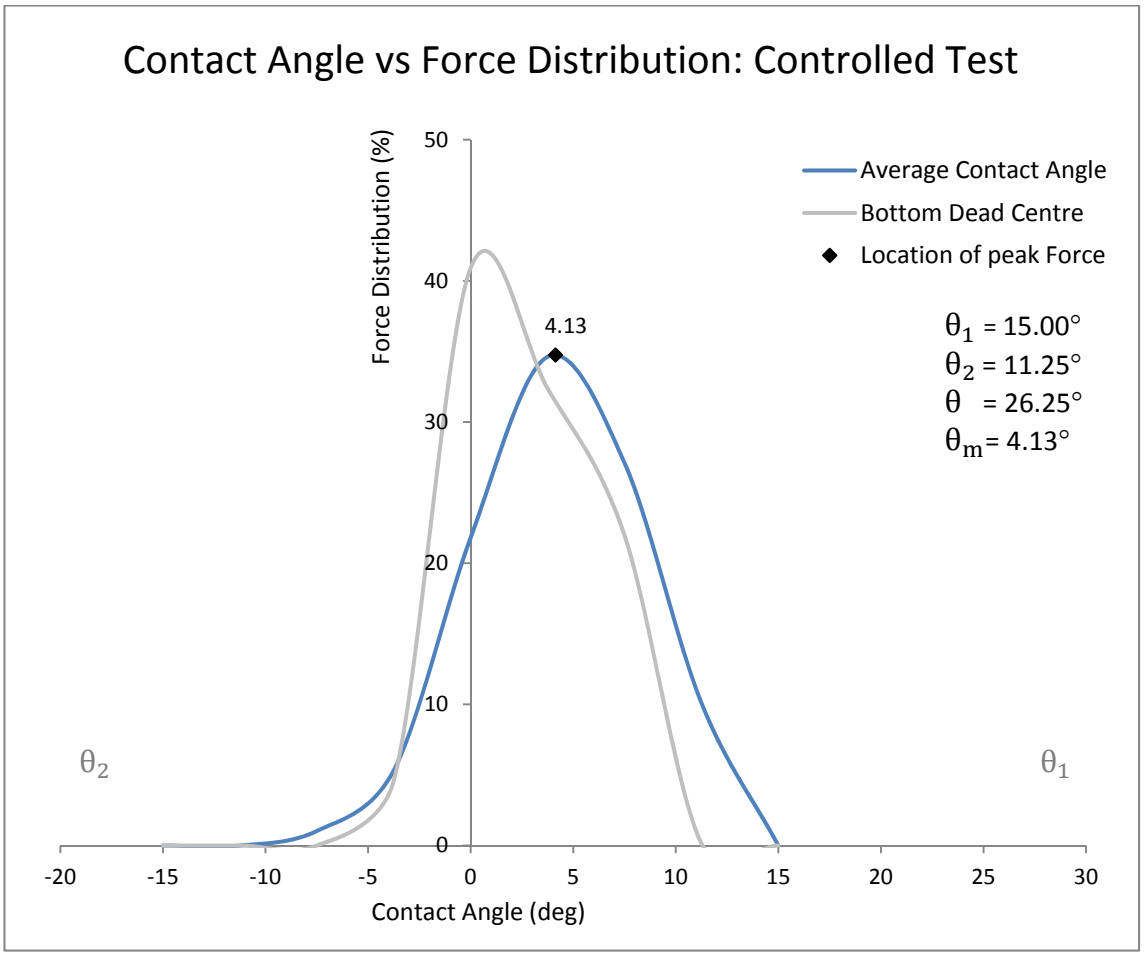

Figure 7.7 – Contact angle results from the controlled test. The results show the location of peak force during the controlled datum tests (blue) compared to bottom dead centre under the wheel (grey).

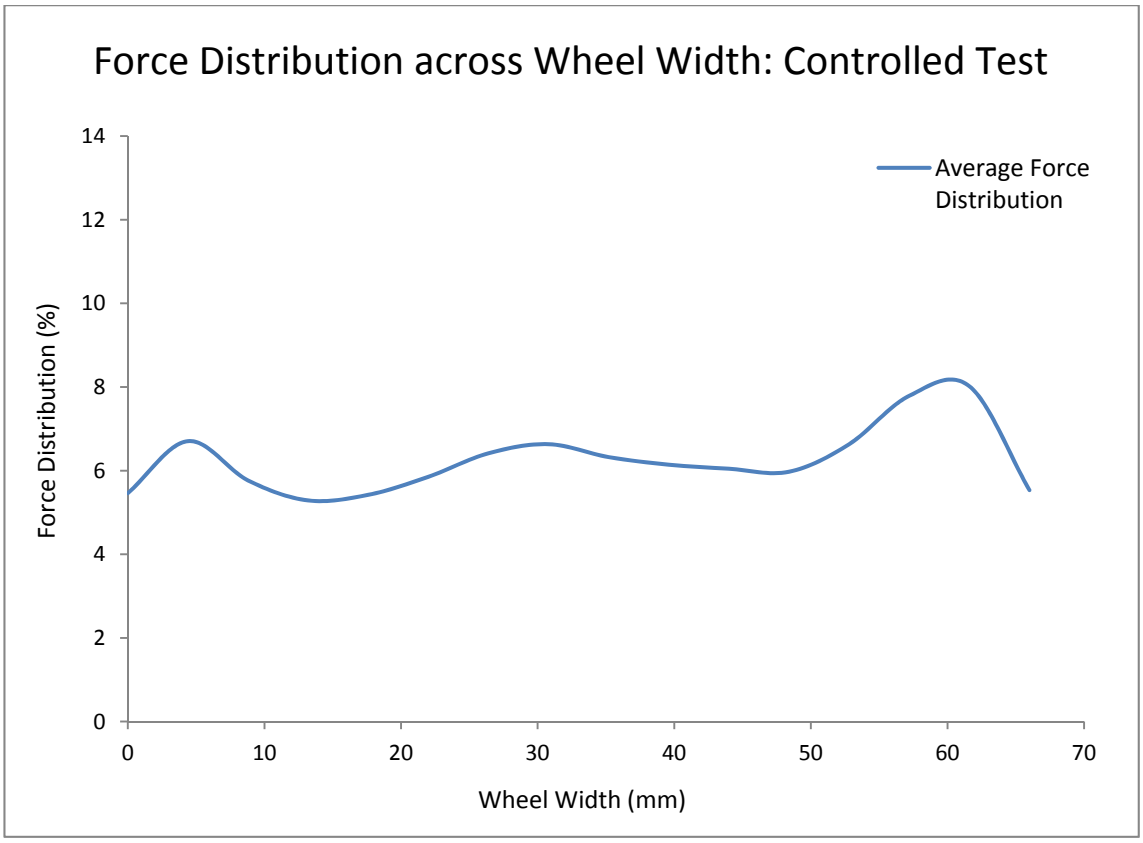

Figure 7.8 – Wheel width results from the controlled test. The blue curve seen in this graph displays the distribution of force across the wheel width during the controlled datum test.

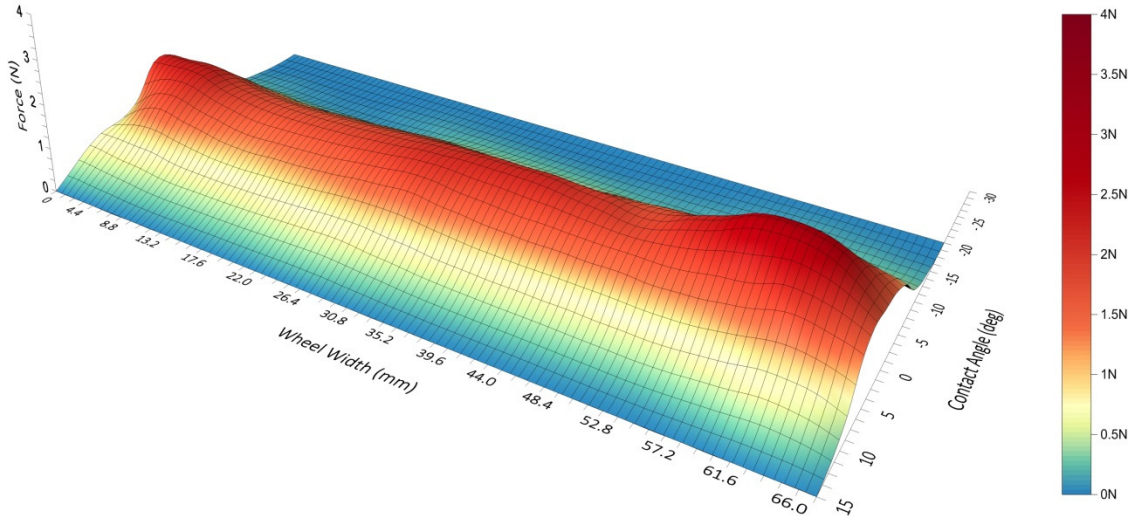

Figure 7.9 – Controlled test results displayed on a 3D surface map. This image displays direct force measurements across the entire wheel-terrain contact interface during the controlled test.

The first graph in Figure 7.7 displays the results from the controlled datum test, presented as a 2D longitudinal view of the wheel-terrain interaction. The grey curve displays the distribution of force while the vehicle was static, confirming the location of 'bottom dead centre' under the wheel. This result was used alongside encoder measurements to locate the wheel's vertical axis in order to determine the location of peak force during the test. The full set of data gathered from the controlled tests were averaged and presented as the blue curve in Figure 7.7 displaying the contact angles, percentage of force distribution and location of peak force. The second graph in Figure 7.8 shows the 2D lateral view of force distribution across the wheel width. Finally the average of force measurements across the entire contact interface during the test is shown as a 3D surface map in Figure 7.9. These controlled test results confirm the uniform force distribution expected from a flat surface. More results from the controlled (datum) test can be seen in Appendix F.

7.2.2 2-5mm Gravel Test

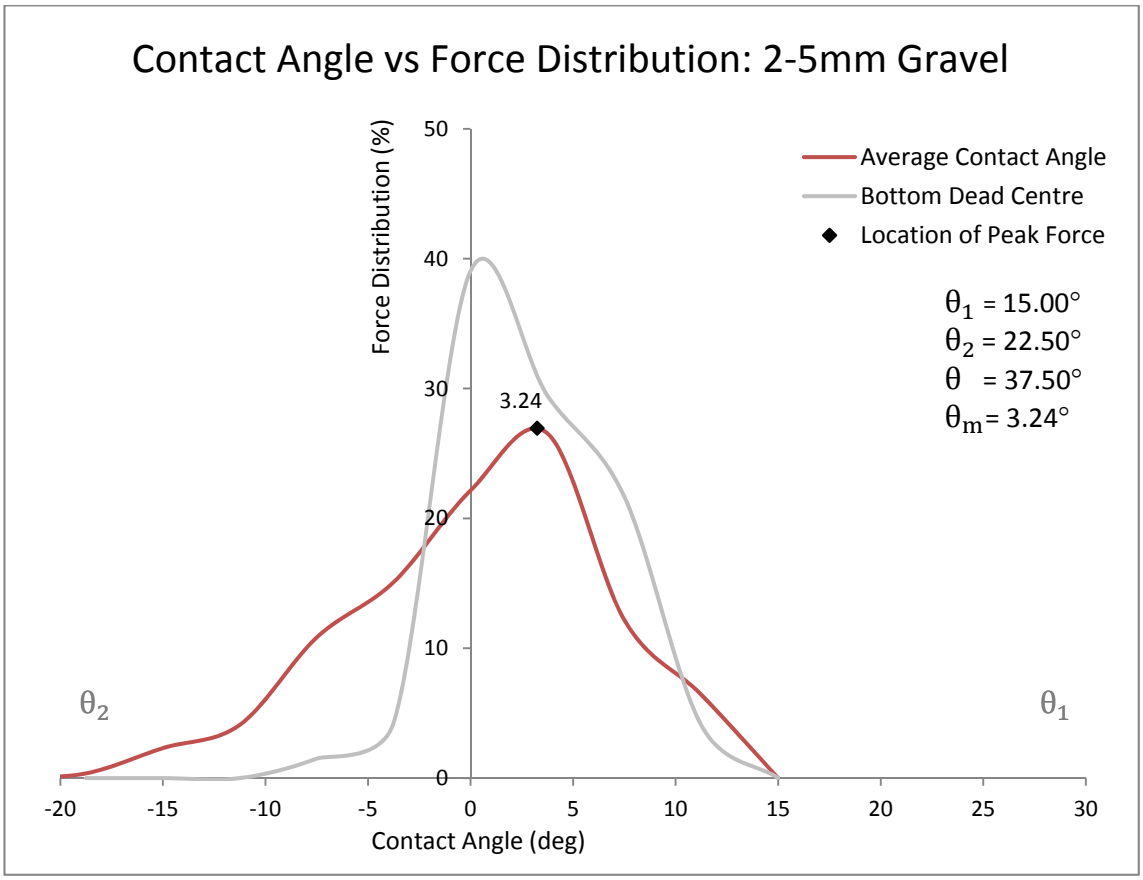

Figure 7.10 – Contact angle results from 2-5mm gravel test. The results show the location of peak force during the 2-5mm gravel tests (red) compared to bottom dead centre under the wheel (grey).

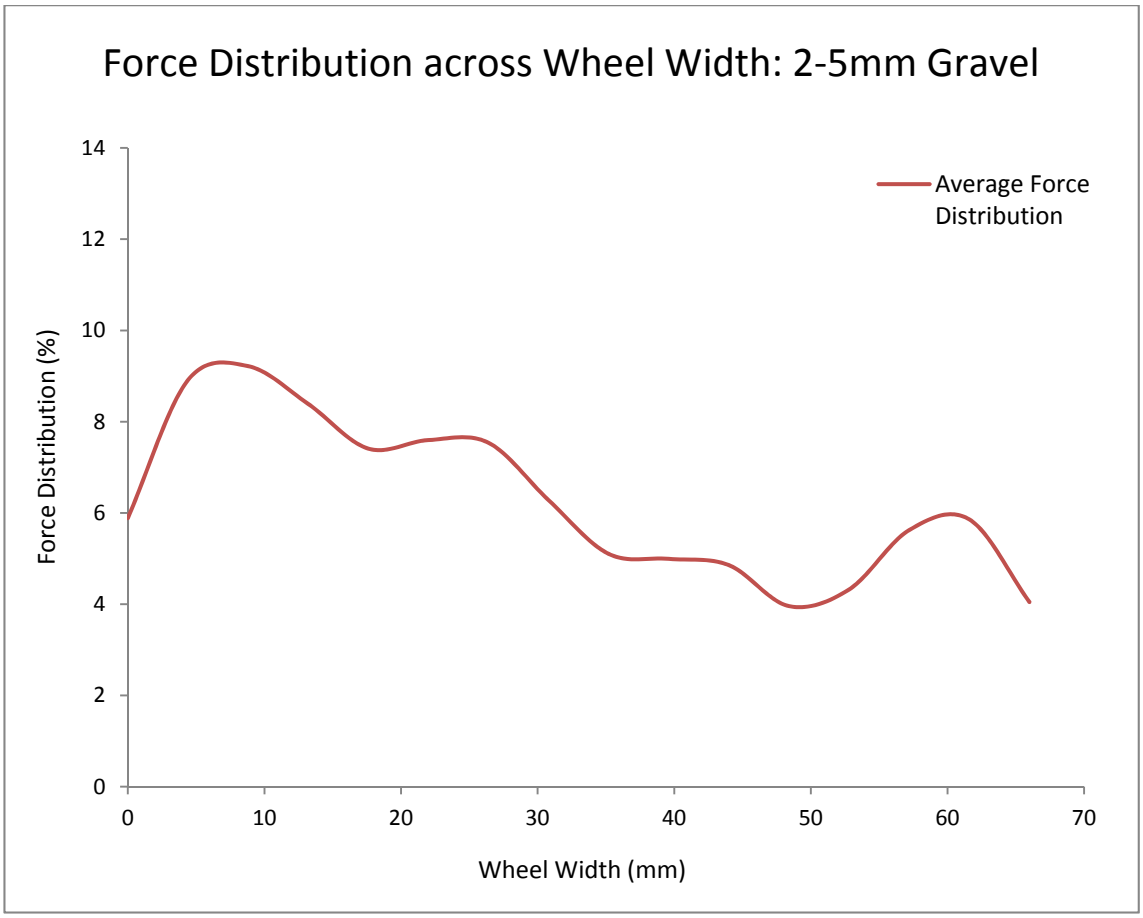

Figure 7.11 – Wheel width results from the 2-5mm gravel test. The red curve seen in this graph displays the distribution of force across the wheel width during the 2-5mm gravel test.

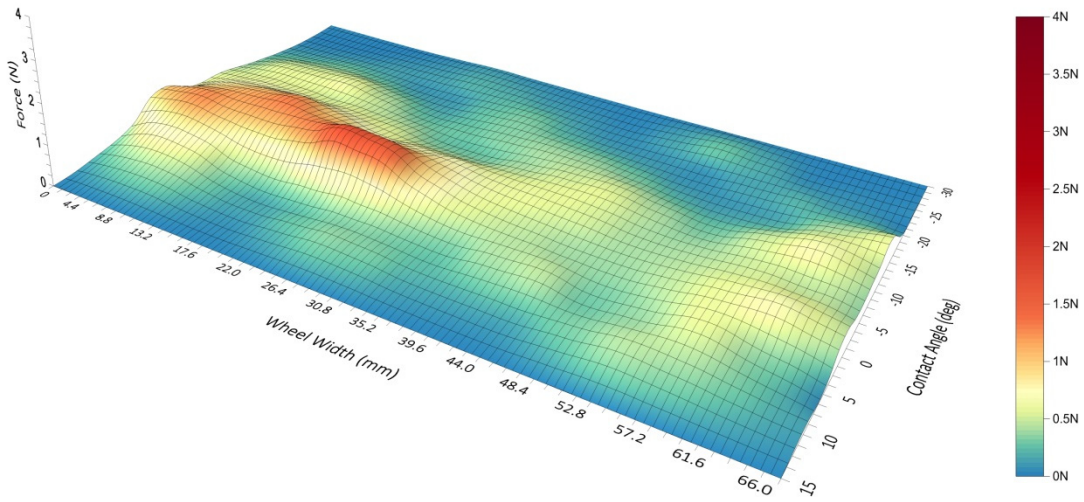

Figure 7.12 – 2-5mm gravel test results displayed on a 3D surface map. This image displays direct force measurements across the entire wheel-terrain contact interface during the 2-5mm gravel test.

The first set of terrain tests were carried out across the 2-5mm gravel, the results of which are presented in Figures 7.10 - 7.12. The first graph (Figure 7.10) presents the 2D longitudinal view where the bottom dead centre result is again shown as the grey curve and the averaged result from the main test as the red curve. The contact angles, force distribution and location of peak force are again presented which immediately display considerable differences to those of the datum test. The second graph displays the same results across the wheel width (Figure 7.11) which shows that the distribution of force across the wheel's width was uneven, demonstrating that pressure is not equally distributed laterally during interaction with uneven terrain. This can be seen clearer in the 3D surface map in Figure 7.12 where force is widely distributed across a larger contact interface, which was due to sinkage characteristics of granular terrain during wheel-terrain interaction. More results from the 2-5mm test can be seen in Appendix G.

7.2.3 10-20mm Gravel Test

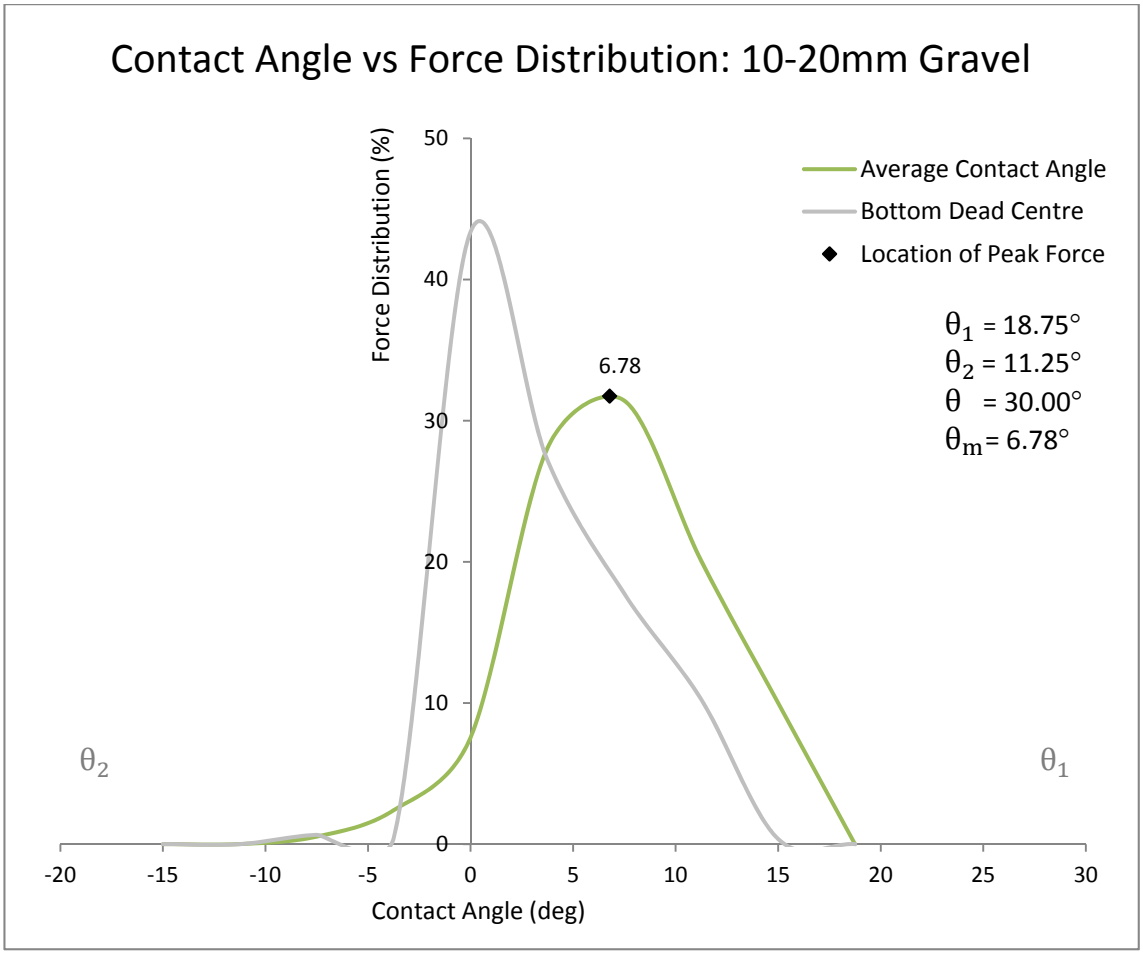

Figure 7.13 – Contact angle results from the 10-20mm gravel test. The results show the location of peak force during 10-20mm gravel tests (green) and bottom dead centre under the wheel (grey).

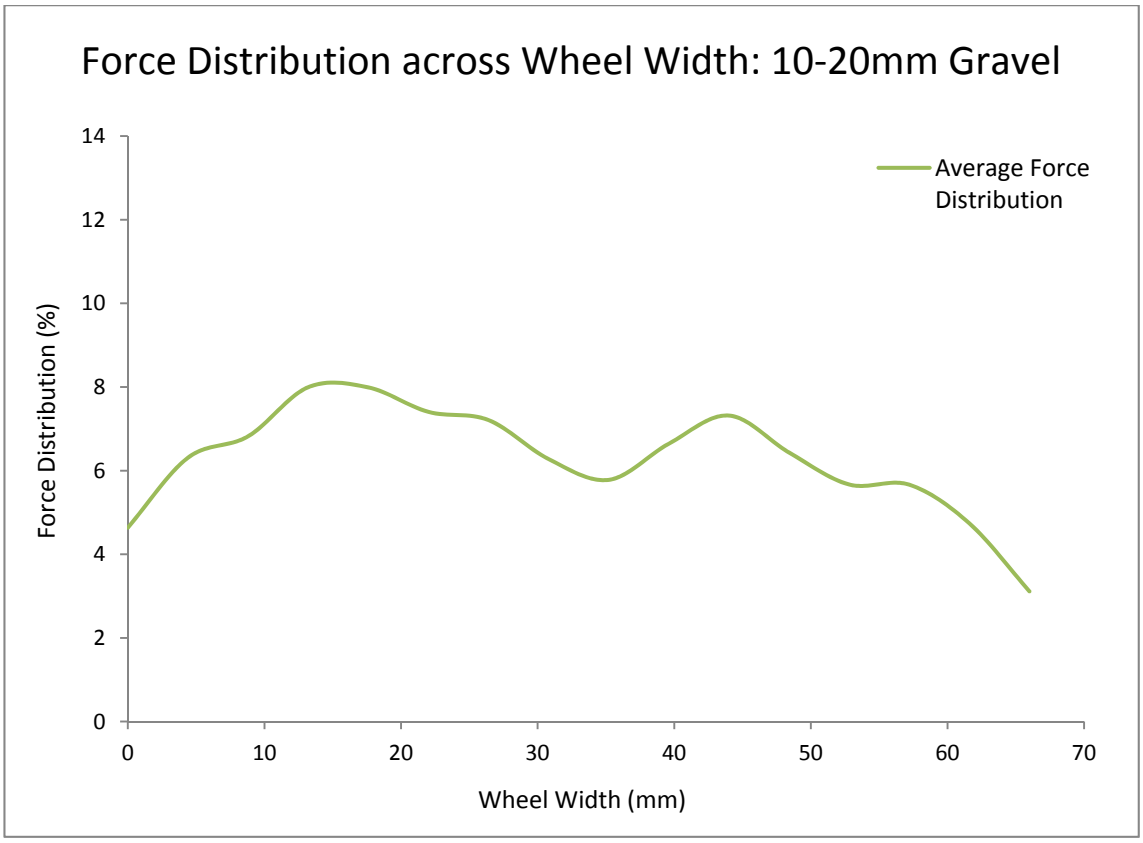

Figure 7.14 – Wheel width results from the 10-20mm gravel test. The green curve seen in this graph displays the distribution of force across the wheel width during the 10-20mm gravel test.

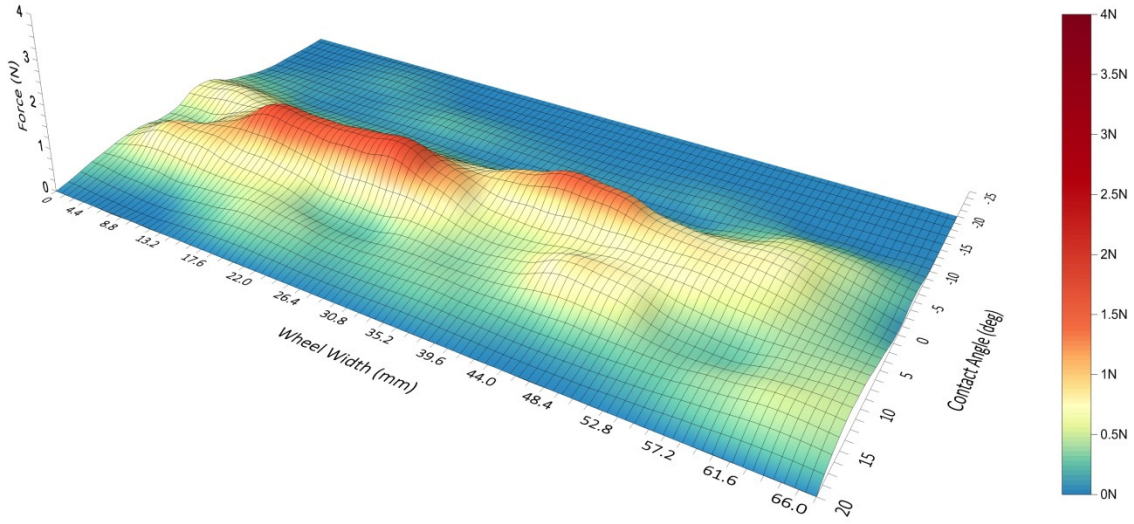

Figure 7.15 – 10-20mm gravel test results displayed on a 3D surface map. This image displays direct force measurements across the entire wheel-terrain contact interface during the 10-20mm gravel test.

The second tests were carried out across the medium grade 10-20mm gravel with the results graphically presented in Figures 7.13 - 7.15. The first graph seen in Figure 7.13 displays the 2D perspective of wheel-terrain interaction with the grey curve again determining the location of the wheel's vertical axis using the bottom dead centre result. The green curve shows the averaged result from the main tests which again show the distribution of force and contact angles. These results immediately show differences to previous tests, however they yield a uniform curve similar to the datum tests which could be mistaken as a uniform surface if taken as a single result. The second graph in Figure 7.14 differentiates the results from the datum test as it shows larger variance in distributed force across the wheel width as expected from an uneven surface. The 3D surface map (Figure7.15) better highlights this variance with more peak values than the 2-5mm gravel due to the larger size of the gravel particles. More results from the 10-20mm gravel test can be seen in Appendix H.

7.2.4 20-40mm Gravel Test

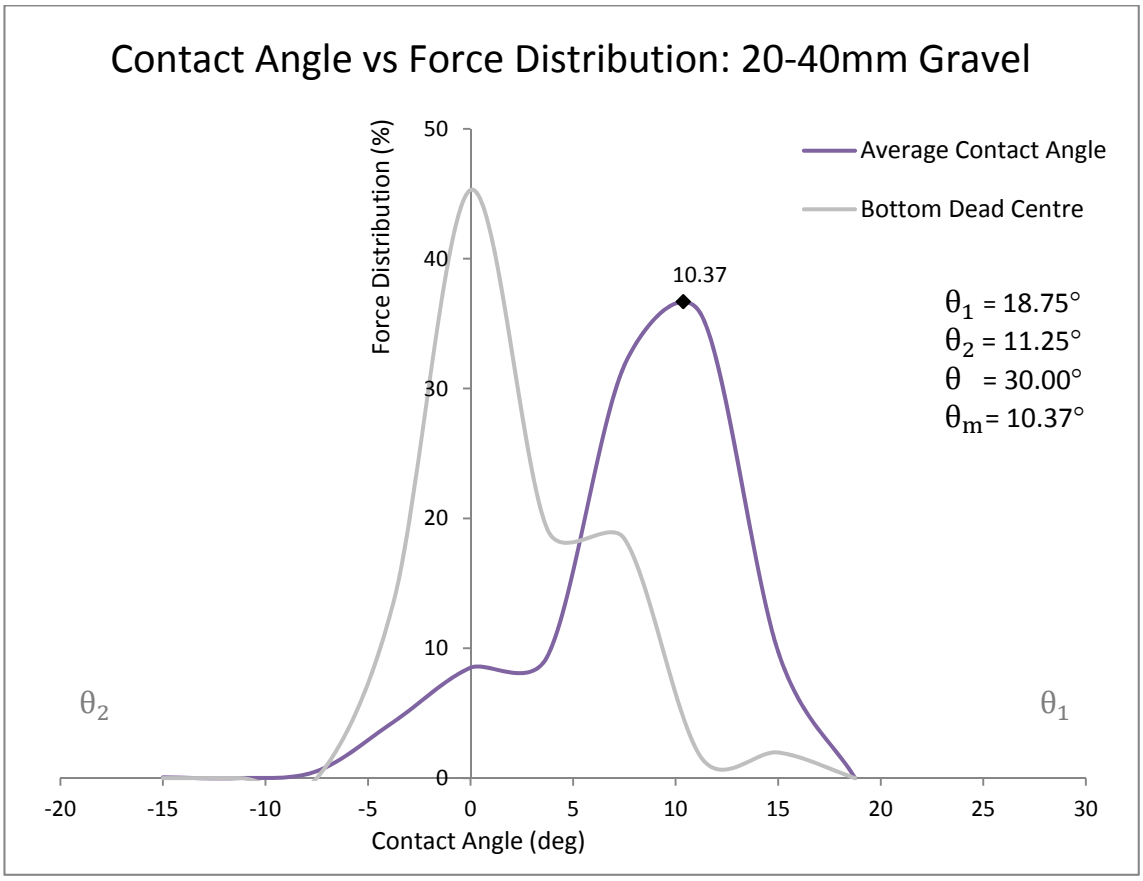

Figure 7.16 – Contact angle results from 20-40mm gravel test. The results show the location of peak force during 20-40mm gravel tests (purple) and bottom dead centre under the wheel (grey).

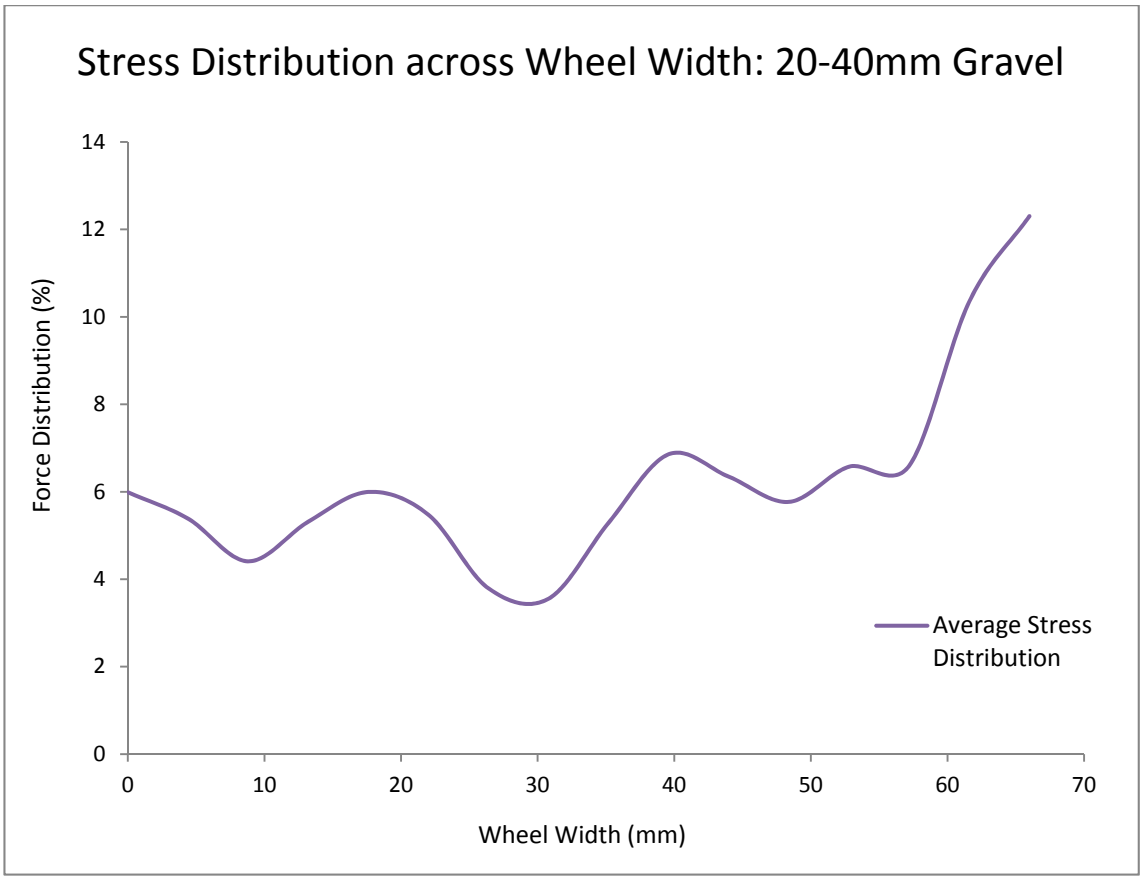

Figure 7.17 – Wheel width results from the 20-40mm gravel test. The purple curve seen in this graph displays the distribution of force across the wheel width during the 20-40mm gravel test.

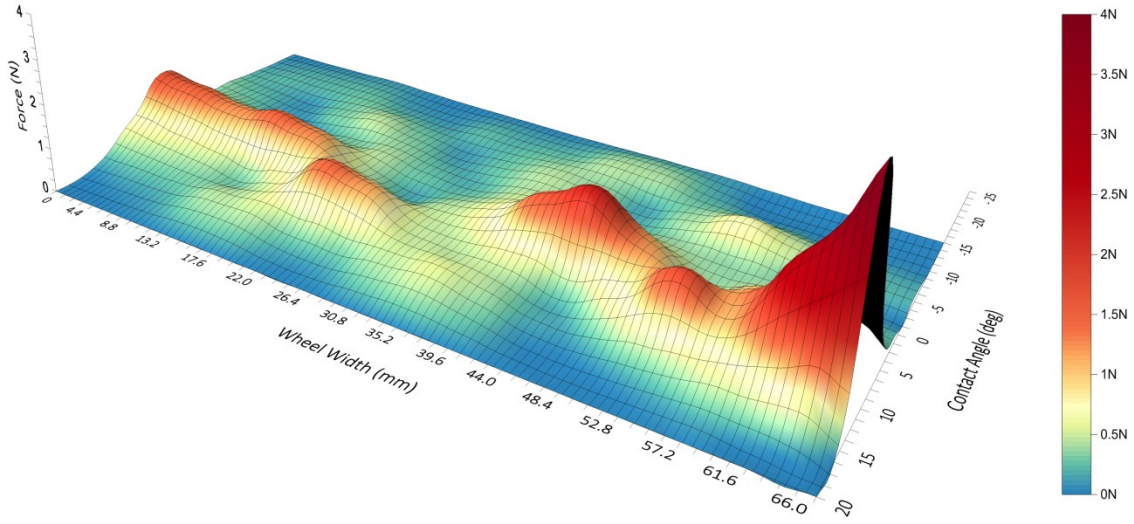

Figure 7.18 – 20-40mm gravel test results displayed on a 3D surface map. This image displays direct force measurements across the entire wheel-terrain contact interface during the 20-40mm gravel test.

The final tests were performed across the 20-40mm coarse gravel with the results presented across three graphs as before. The first graph (Figure 7.16) displays the longitudinal 2D view with the grey curve again used to locate the wheel's vertical axis alongside the averaged results displayed as a purple curve. These results show a higher peak force with narrow distribution as expected from the large gravel size. The results seen in Figure 7.17 coincide with this displaying the largest variance of force distribution across the wheel width. The 3D surface map displayed in Figure 7.18 better demonstrates this with an extensive number of peak force points as a consequence of interacting with a rough terrain type. More results from the 20-40mm gravel test can be seen in Appendix I.

7.3 Data Analysis

All tests results were thoroughly analysed in order to discover potential relationships that could be exploited to create a unique classification technique. The key parameters of the wheel-terrain contact interface are the contact angle θ and location of maximum pressure θ_m as previously presented in Figure 6.2. Additionally the FSW's novel sensing capabilities facilitated the measurement of these parameters across the entire contact interface, offering a unique perspective of the wheel-terrain interaction. This method provided force distribution measurements across the entire contact patch presented as 3D surface maps, which were scrutinised to identify significant features.

7.3.1 Contact Angle

The contact angles of the wheel-terrain interface across all the tests were combined for analysis as seen in Figure 7.19. Firstly, region θ_2 was expected to be negligible as noted by terramechanic studies assuming $\theta_2 = 0$ (Iagnemma, Dubowsky 2004, p25); however as seen across all results θ_2 is significantly larger and has an effect on the total contact angle (θ) as seen in Table 7.1 and therefore cannot be completely discounted . The total contact angle results of the gravel tests were all larger than the datum test due to deformation characteristics expected with granular terrain. The contact angle generally increases with smaller grained terrain types as seen with the 2-5mm gravel having the largest contact angle compared to larger gravel sizes.

Table 7.1 – Table displaying key values from the experiment. The most significant values obtained from the experiment are displayed here, showing relationships between certain parameters and gravel size.

Terrain	θ_1 (degrees)	θ_2 (degrees)	θ (degrees)	θ_m (degrees)	F_p (N)	Maximum Force Distribution (%)
Datum Test	15.00	11.25	26.25	4.13	1.65	34.75
2-5mm Gravel	15.00	22.50	37.50	3.24	0.74	26.95
10-20mm Gravel	18.75	11.25	30.00	6.78	0.77	31.75
20-40mm Gravel	18.75	11.25	30.00	10.37	1.06	36.70

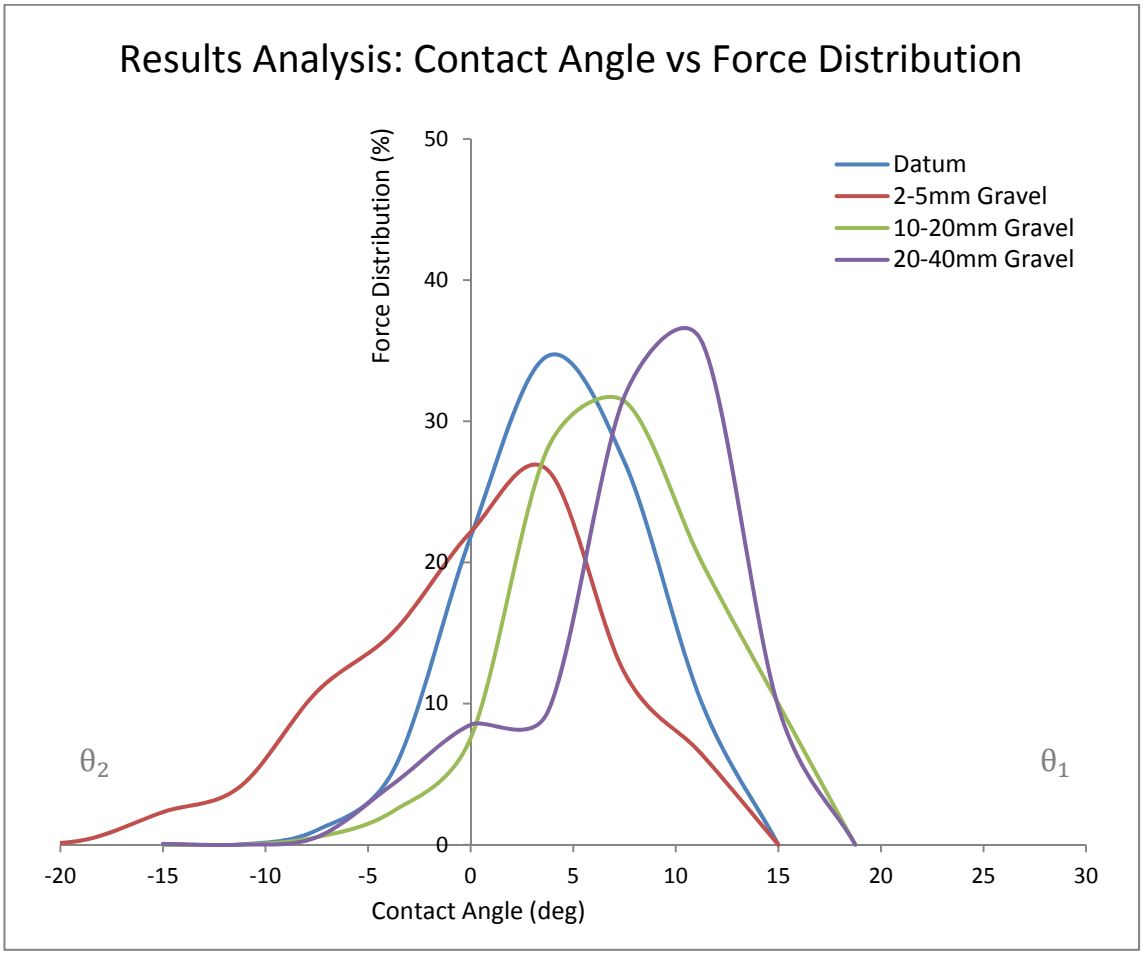

Figure 7.19 – Comparing contact angle results across all tests. The results show the difference in contact angle which changes with gravel size due to deformation characteristics of granular terrain.

7.3.2 Contact Surface Area

The contact surface area (A) at the wheel-terrain interface could be accurately calculated as a result of the entire contact patch being measured throughout the experiment. 2D contour maps were created from the test results in order to visualise the contact patch during each test, seen in Figure 7.20. These contour maps show clear variations in contact surface area and the distribution of force on the contact patch across the different surfaces. The datum result exhibits a regular shaped contact patch with an equal distribution of force; in comparison the gravel test results vary in shape and force distribution due to the deformation characteristics of granular terrain. As the gravel size increases the shape of the contact patch becomes less regular and the overall contact surface decreases, leading to more irregular peaks.

7.3.3 Location of Maximum Pressure

The location of maximum pressure (θ_m) is a significant parameter within the wheel-terrain interaction model as per terramechanic studies, which suggest that θ_m exists within θ_1. This is supported by the results of this experiment, as seen in Figure 7.21, which graphically presents the peak force (F_p) measured during all tests. These studies also state that θ_m is related to properties of the terrain, which is again supported by the test results where θ_m varies across different terrain types. The results show that θ_m shifts forward as the gravel size increases, however the distribution of force may not be equal across the width of the contact interface as previously highlighted.

7.3.4 Lateral Pressure Variation

The 3D surface map from the datum results displayed in Figure 7.22 shows an equal distribution of pressure across the width expected from a flat, even surface; however Figure 7.23 shows that force becomes more unevenly distributed with increasing gravel size, resulting in lateral pressure variations (denoted L_v). These variations cause a number of peaks across the contact patch signifying that θ_m also varies laterally during interaction with rougher terrain. This highlights that 2D model parameters do not accurately represent interaction properties across the wheel width, whereas novel 3D measurements present unique quantitative properties which identify terrain features.

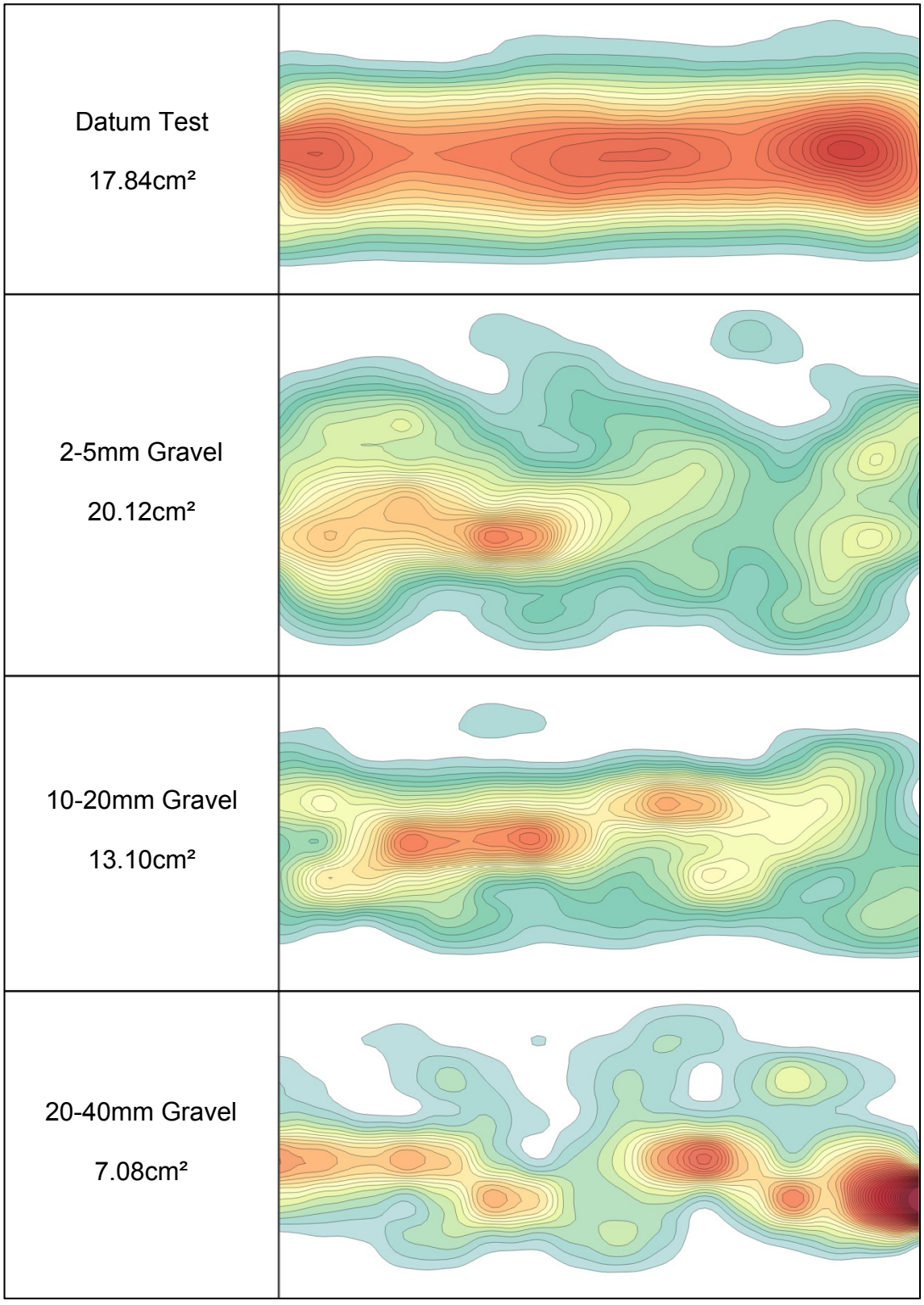

Figure 7.20 – 2D contour maps comparing contact surface area. The 2D contour maps exhibit distinct differences across terrain types due to deformation and surface roughness, affecting pressure distribution.

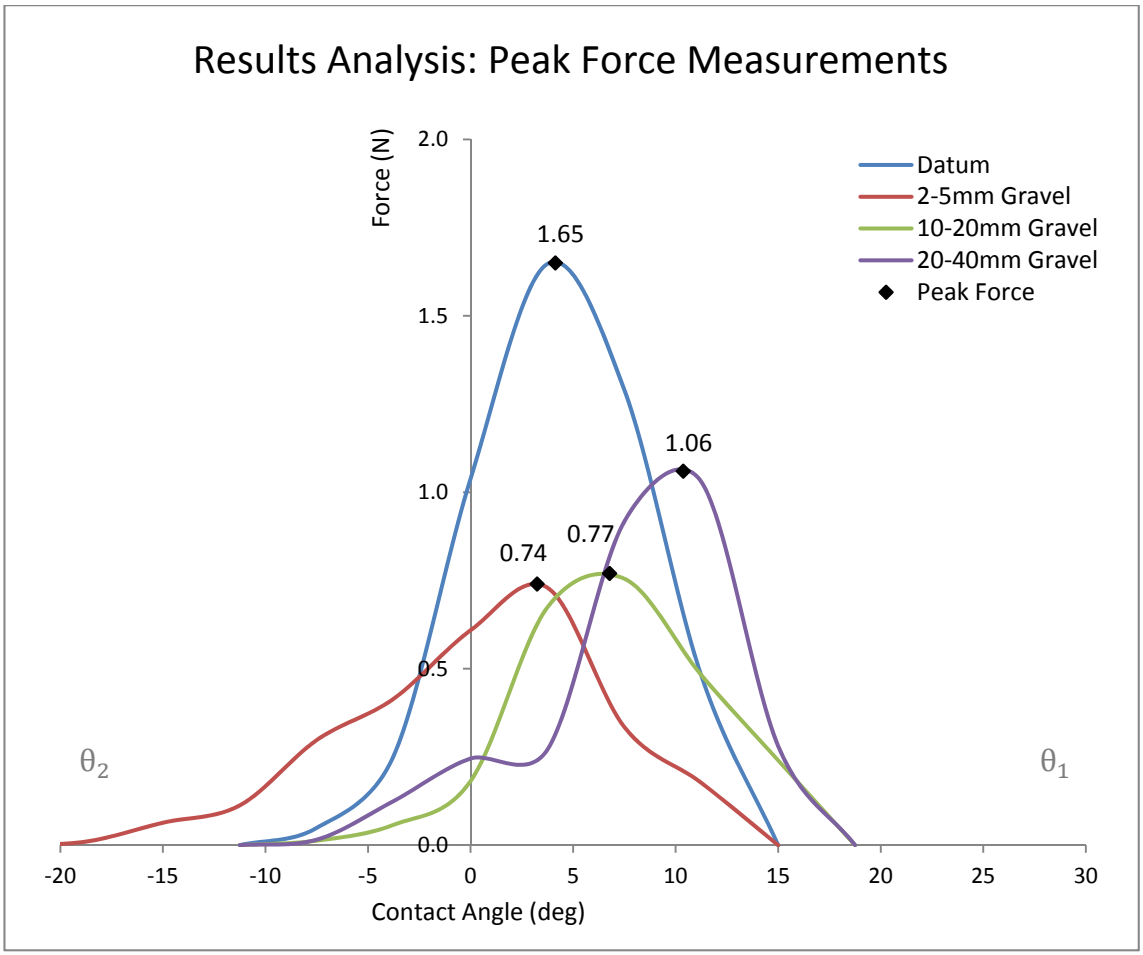

Figure 7.21 – Comparing peak force measurements across all tests. The results show the shift of peak force, highlighting a relationship between gravel size and location of maximum pressure.

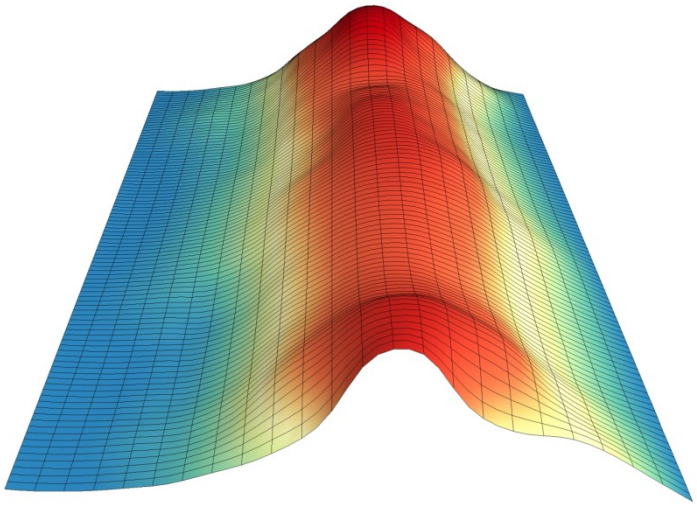

Figure 7.22 – 3D surface map showing pressure distribution during the datum test. This image displays the uniform distribution of pressure across the wheel's width.

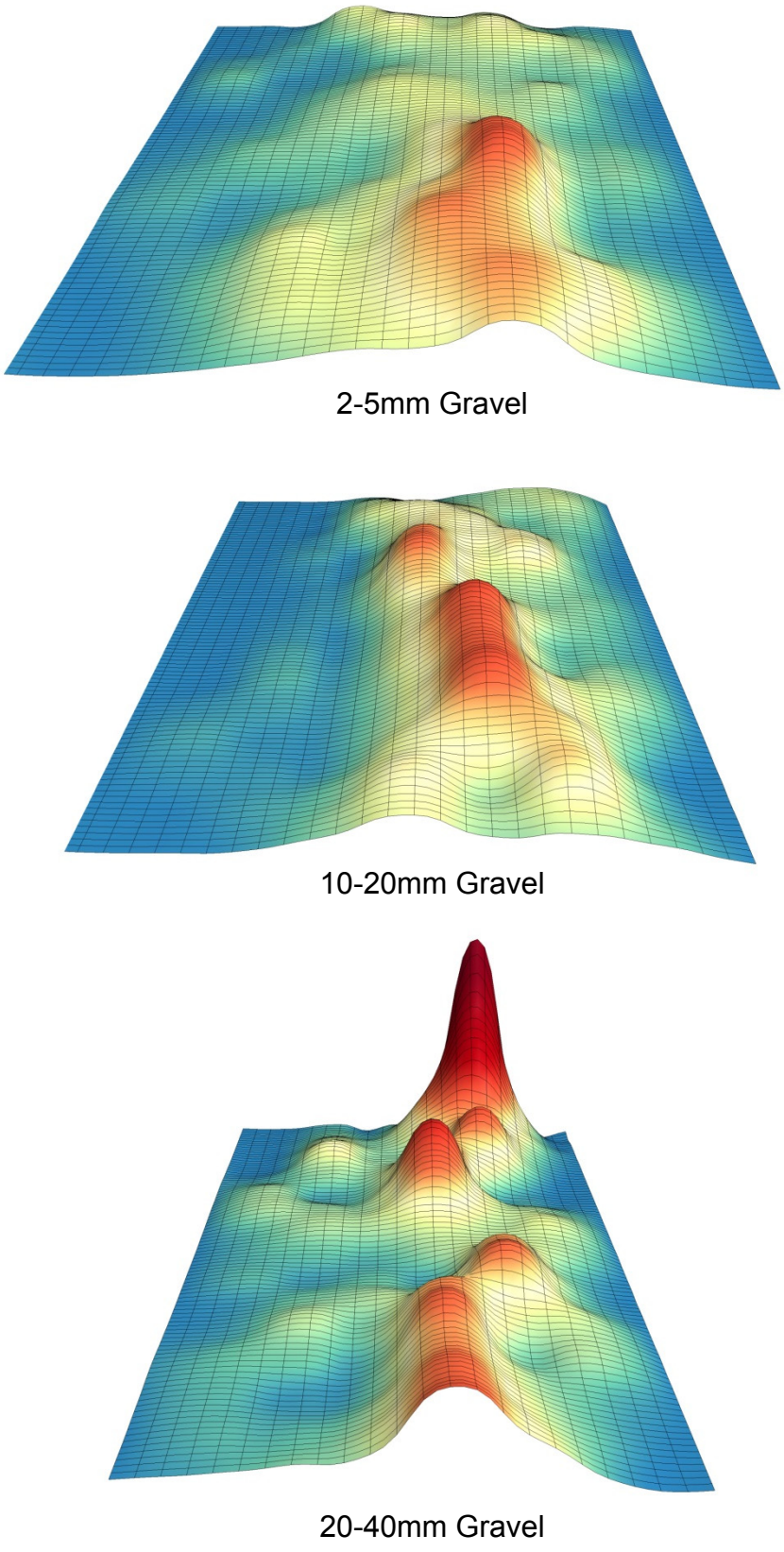

Figure 7.23 – 3D surface maps showing pressure distribution during gravel tests. These images display the lateral pressure variation patterns during interaction with the various terrain types.

7.4 Classification

As previously discussed θ and θ_m were considered the most significant parameters relating to wheel-terrain interaction. The experiment results indicated that these parameters do relate to terrain properties; however they approach wheel-terrain interaction from a 2D perspective, which lacks accuracy when (solely) used to classify terrain. The outcome of the experiment presented a novel 3D view of the wheel-terrain interface leading to the discovery of distinctive relationships between the contact surface area, lateral pressure variation and terrain properties; consequently these parameters were used to create a unique terrain classification system.

7.4.1 Fuzzy Logic

With the imprecise nature of terrain parameters, fuzzy logic was utilised to create the classification system. As contact surface area (A) and lateral pressure variation (L_v) were observed as the key interaction parameters relating to features of the terrain, they were used to classify terrain using the 'truth table' seen in Figure 7.24 below:

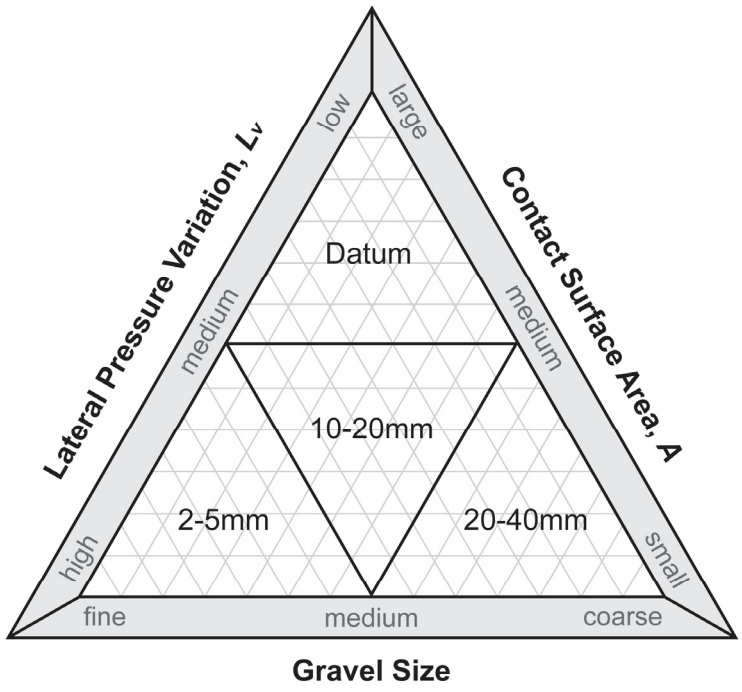

Figure 7.24 – Terrain classification truth table. The variables within this diagram were used to create the rule sets used by the fuzzy controller to classify terrain.

The two main parameters A and L_v are used as the main *linguistic* input variables for the fuzzy logic system with the linguistic terms being small/medium/large for A and low/medium/high for L_v (seen in Figure 7.24). These variables determine the terrain type which is classified by gravel size from fine through to coarse. Contact surface area is calculated using Equation (13) where the area of each sensor (0.27cm²) is multiplied by the number of cells where force values F are greater than zero:

$$A = 0.27(F > 0) \tag{13}$$

Lateral pressure variation is the total standard deviation of lateral force measurements, calculated using Equation (14) where x is the (radial) sensor row, y is each lateral sensor value and $\bar{y}$ is the mean of lateral sensor values:

$$L_v = \sum x \left(\sqrt{\frac{\sum (y - \bar{y})^2}{16}} \right) \tag{14}$$

The range of A and L_v values for each terrain type were obtained from the experiment results (seen in Appendices F-I) and used to create membership function plots. These membership functions (seen in Figures 7.25 and 7.26) are used by the fuzzy logic system to determine the degree of membership for given contact interface measurements. Terrain is then classified using the rule set listed below, derived from the truth table presented in Figure 7.24:

If A is LARGE and L_v is LOW then terrain = Datum
If A is LARGE and $L_v$is HIGH then terrain = 2-5mm Gravel
If A is MEDIUM and L_v is LOW then terrain = 2-5mm Gravel
If A is LARGE and L_v is MEDIUM then terrain = 2-5mm Gravel
If A is MEDIUM and L_v is HIGH then terrain = 10-20mm Gravel
If A is SMALL and L_v is LOW then terrain = 10-20mm Gravel
If A is MEDIUM and L_v is MEDIUM then terrain = 10-20mm Gravel
If A is SMALL and L_v is HIGH then terrain = 20-40mm Gravel
If A is SMALL and L_v is MEDIUM then terrain = 20-40mm Gravel

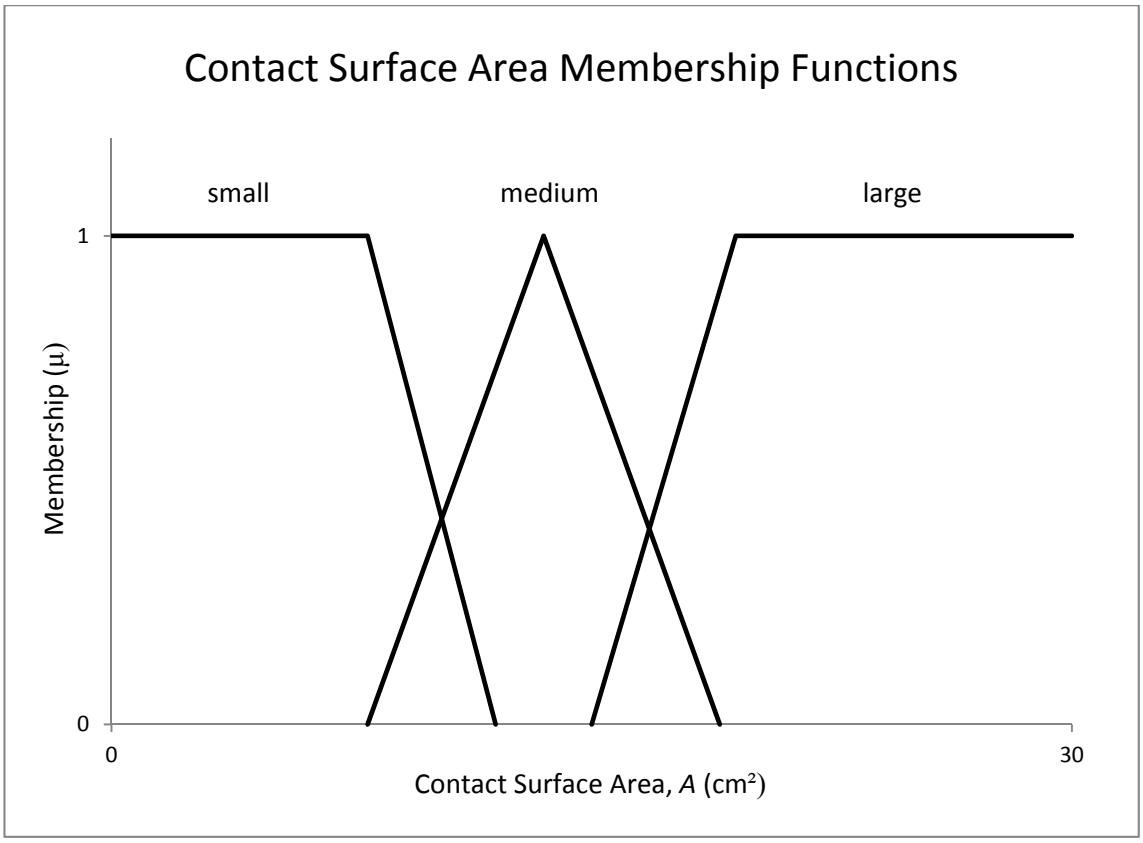

Figure 7.25 – Contact area membership functions; used to determine the degree of membership.

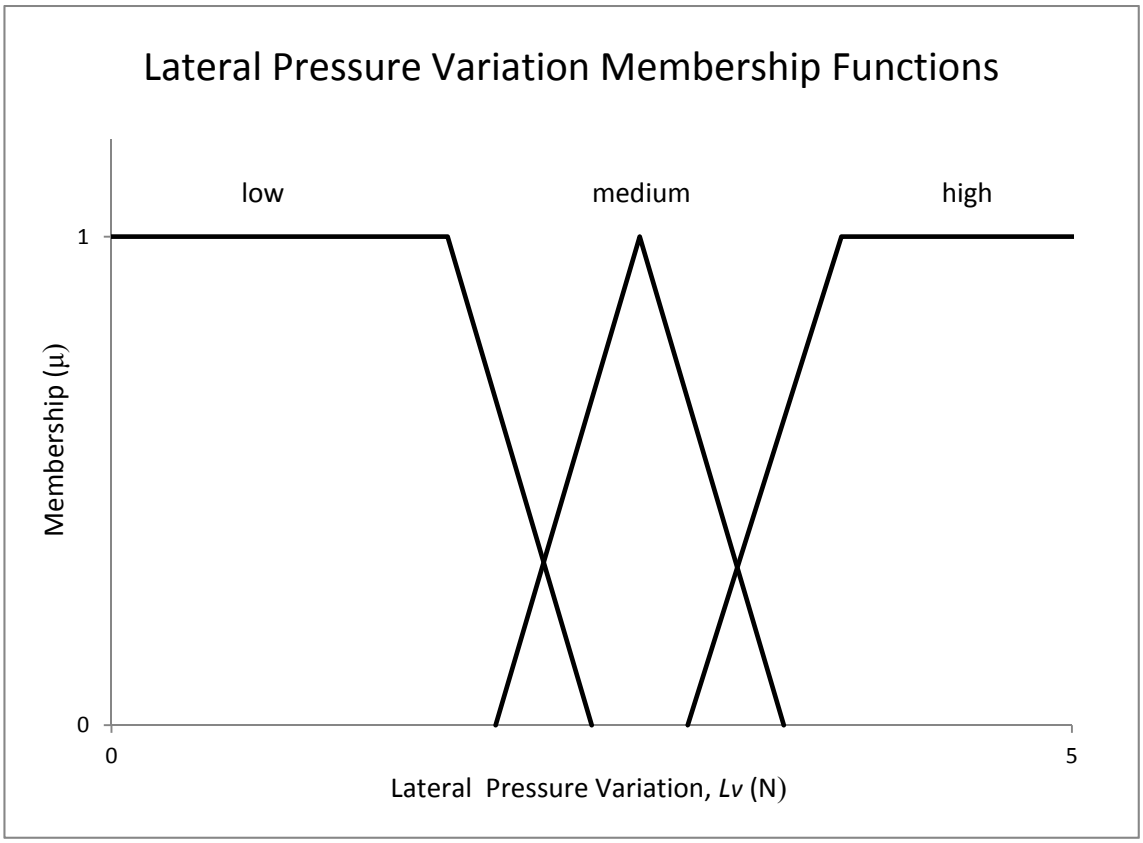

Figure 7.26 – Lateral variation membership functions; used to determine the degree of membership.

LabVIEW tools were used to develop the fuzzy logic system for implementation. The variables, rule set and membership functions were entered into the controller and its precision was tested using data extracted from other test results. The controller initially had a moderate success rate of around 70%, however this was found to be because of irregularities within individual data sets rather than controller imprecisions. To yield better results three data sets were averaged before A and L_v values were calculated and entered into the fuzzy controller, which increased success rate to >90%. Once fully developed, the robust fuzzy logic controller was combined with data gathering and processing elements of the main program to classify terrain in real-time.

7.4.2 Real-time Classification

The various novel developments from the study were combined to create a complete real-time terrain classification system, an outline of which can be seen in Figure 7.27 below. The contact interface is measured by the FSW and sends raw data to the main controller where it is processed and analysed on-board; the unique parameters are then calculated and entered into the fuzzy controller which classifies the terrain.

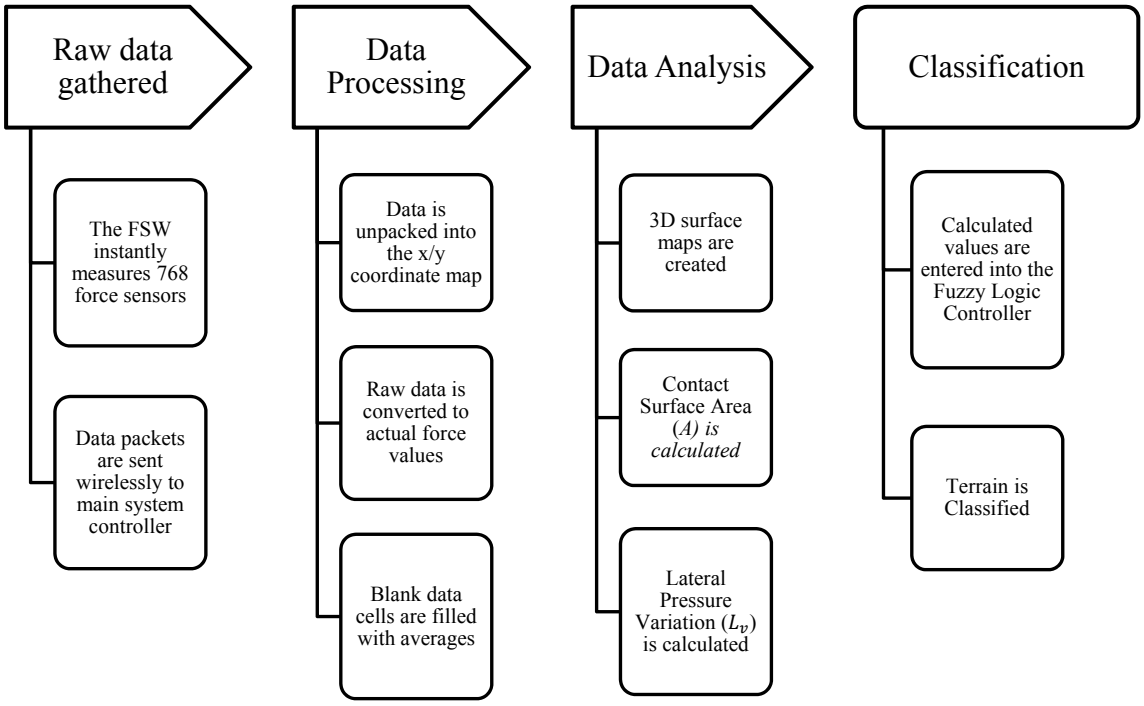

Figure 7.27 – Outline of the real-time terrain classification system. The various processes developed for this study were combined to create a complete real-time terrain classification system.

Gathering data, communicating it wirelessly and unpacking raw data were already operating in real-time; therefore the other stages seen in Figure 7.27 required further development to incorporate them into the real-time system. The first process was to convert raw data into meaningful values on-line using the unique calibration values previously obtained. A series of 'read measurement file' functions in LabVIEW (Figure 7.28) were introduced into the initialisation phase of the main program to retrieve all the calibration values to store them in local variables ready to be used by the calibration algorithm (Figure 7.29).

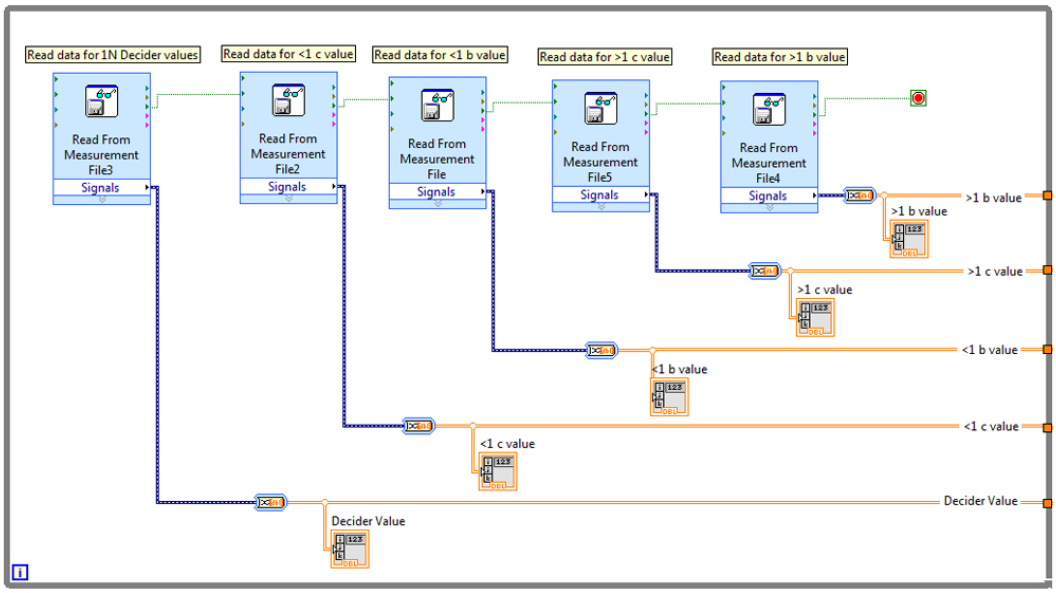

Figure 7.28 – Read measurement file LabVIEW functions. These functions were used during the initialisation of the main program to place the unique relationship values into local variables.

The state diagram presented in Figure 7.29 displays the basic function of the calibration algorithm. Actual force values were calculated from raw data using the unique *B* and *C* values, with each sensor's decider value being used to determine which set of unique relationship values were used in the formula. This calibration process was completed as data was gathered and unpacked to calculate actual force values in real-time.

Following raw data conversion, the blank cells within the x/y map required data input as before. The method of filling the blank cells with averaged values from laterally adjacent cells was incorporated into the real-time system. Figure 7.30 displays the segment within the LabVIEW program that completed this process, where two program structures were used to account for the alternating sensor array pattern.

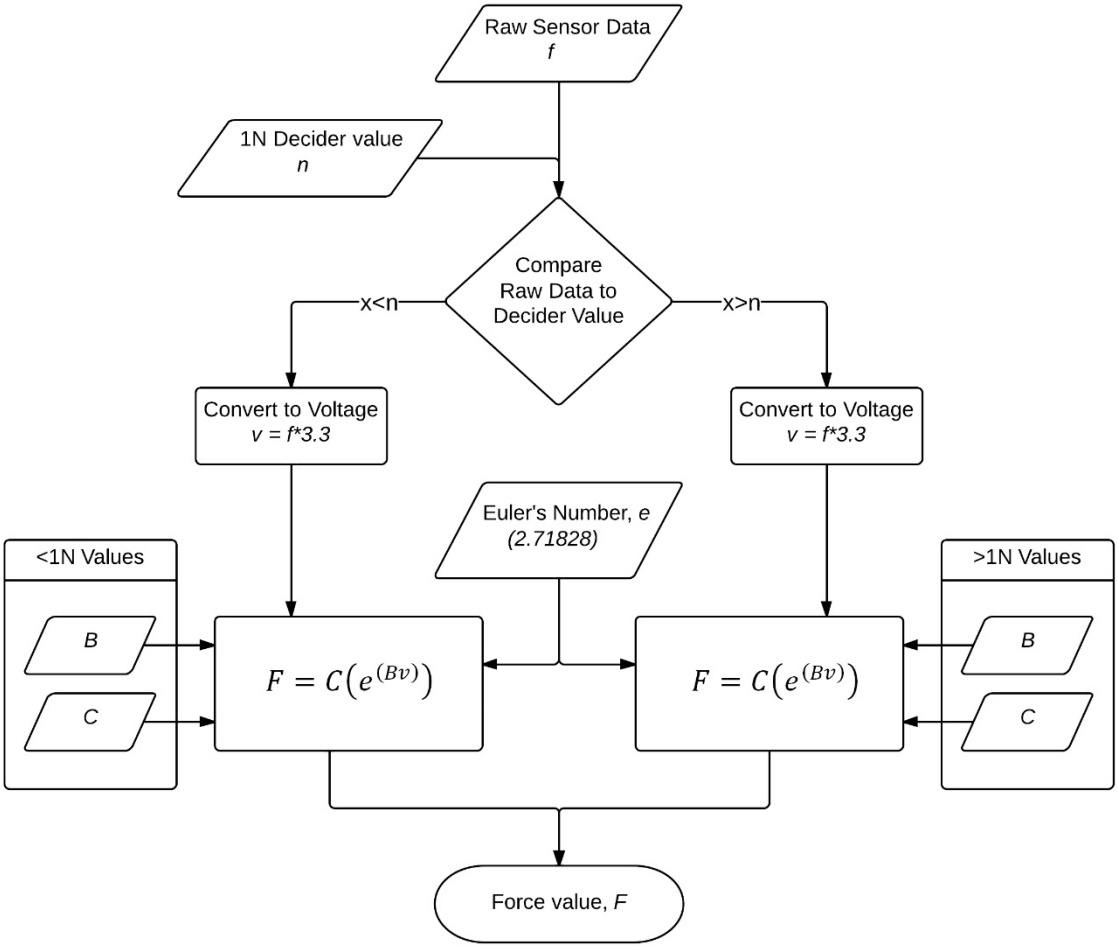

Figure 7.29 – State diagram of the calibration algorithm. The calibration algorithm used each sensor's decider value to determine which unique values to use to calculate actual force values in real-time.

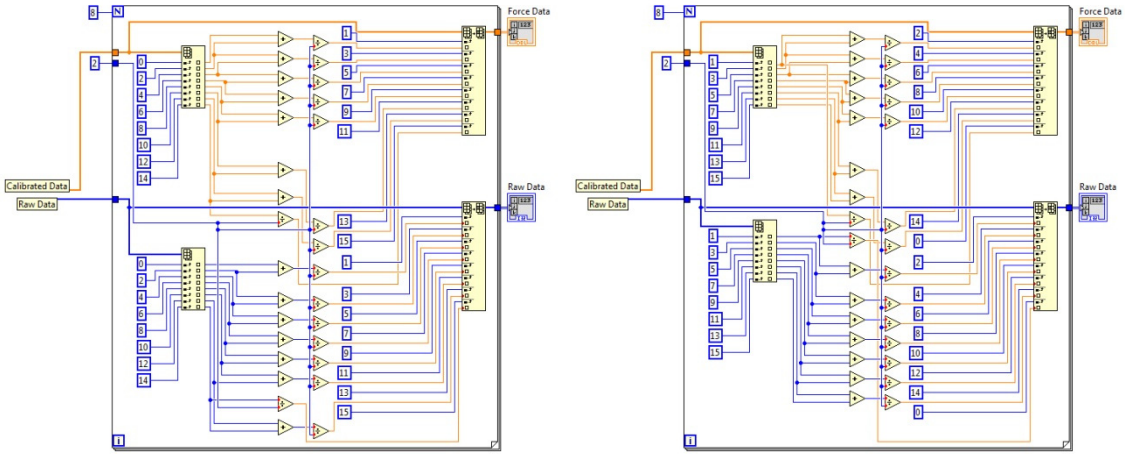

Figure 7.30 – Averaging program structures in LabVIEW. Values from (laterally) adjacent sensors were averaged and inserted into blank spaces in the x/y chart to produce better results.

The gathered data was now fully processed and needed to be analysed on-board. Firstly A and L_v values were calculated using Equations (13 &14) which were then entered into the fuzzy logic controller. The fuzzy controller developed using LabVIEW tools as seen in Figure 7.31, took these calculated values and classified the terrain using the previously entered membership functions and rule set. This completed the real-time classification algorithm which is diagrammatically displayed in Figure 7.32.

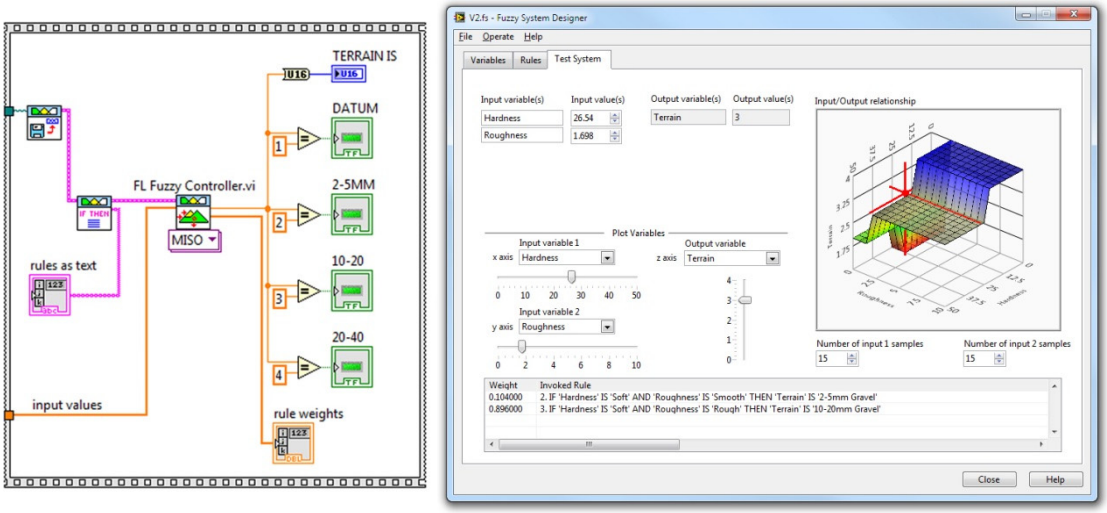

Figure 7.31 – Fuzzy logic controller developed in LabVIEW. The fuzzy controller classified terrain in real-time from calculated values, using the membership functions and rule set previously entered.

7.4.3 System Validation

The completed algorithm, developed in LabVIEW, was now capable of on-board data processing, analysis and classification and communicated the results to a front panel based on the host PC (Figure 7.33). This panel not only displayed the classification results but also presented a live view of the contact interface using a 3D surface map to display the pressure distribution across the contact patch, a 2D heat map showing the calculated contact surface area and a 2D chart presenting the lateral pressure variation.

Finally, the classification system was tested to verify its ability to classify terrain conditions (within this study) in real-time. Table 7.2 displays the results from these tests, which all returned 100% success rate; validating the real-time terrain classification system. The full set of results from these tests are presented in Appendix J.

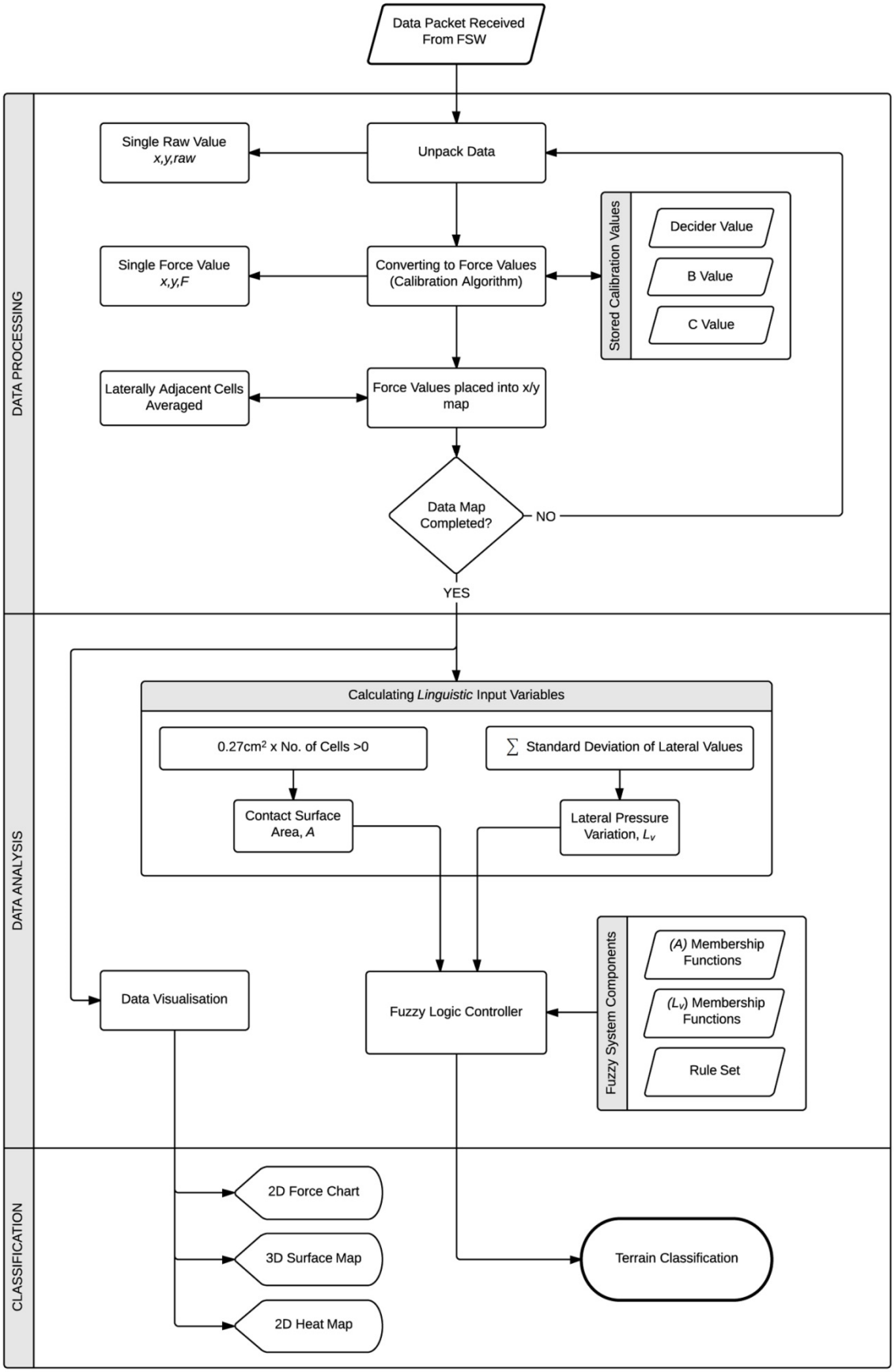

Figure 7.32 – Diagram of the complete real-time classification algorithm. This state diagram presents all the processes that took place to classify terrain in real-time from raw data gathered by the FSW.

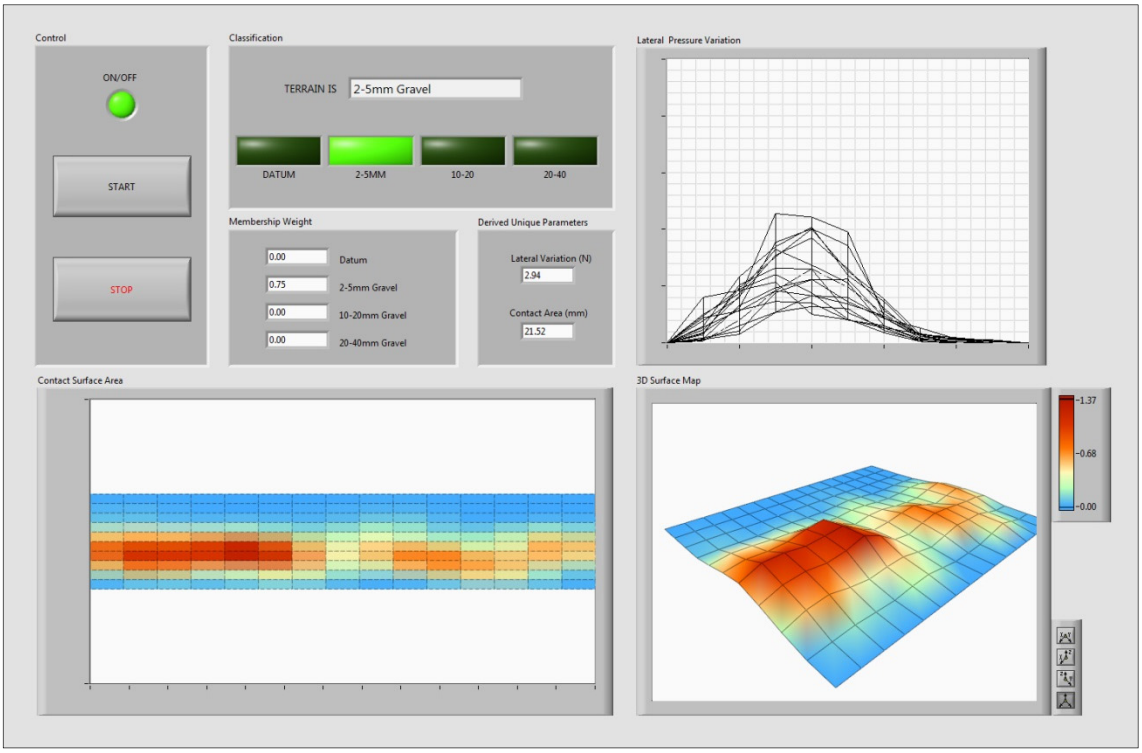

Figure 7.33 – Real-time classification and visualisation panel. The host PC front panel presented a live view of the contact interface using 2D and 3D maps in addition to the real-time classification results.

Table 7.2 – Table displaying results of classification validation tests. The complete real-time system was tested to verify its capabilities, the results of which are displayed in this table (full set in Appendix J).

Test No.	Terrain	A (cm^2)	L_v (N)	Membership (μ)	Classification
01	Datum	17.97	1.72	0.66	Datum
02	2-5mm Gravel	21.52	2.94	0.75	2-5mm Gravel
03	10-20mm Gravel	13.13	3.02	0.67	10-20mm Gravel
04	20-40mm Gravel	8.85	5.13	0.79	20-40mm Gravel

7.5 Discussions

The experiment was designed to use the Force Sensing Wheel (FSW) to measure (normal) force distribution at the contact interface while traversing across various terrain conditions, represented by different gravel sizes. The novel FSW measurements gathered during the experiment were analysed offline to discover potential relationships that could be exploited to create a unique terrain classification technique.

The results from the experiment were initially presented using the key parameters derived from terramechanic studies: contact angle θ and location of maximum pressure θ_m; however this approach presents wheel-terrain interaction from a 2D perspective. As the FSW obtained force measurements across the entire wheel-terrain interface then results could be presented using 3D surface maps. These novel results highlighted that θ and θ_m are not accurate enough to classify terrain conditions as they vary across the wheel width. Contact surface area A and lateral pressure variation L_v (the 3D parameters relative to θ and θ_m) were therefore chosen to identify unique features of the wheel-terrain contact interface.

Additionally A and L_v are more suited for this study as they are far more measureable for a real-time system compared to θ and θ_m which require constant knowledge of wheel angular position. The results of the controlled test displayed ideal interaction conditions with regular contact patch patterns and uniform lateral pressure distribution, offering a datum to compare the granular terrain to. The main terrain tests exhibited varied results that related to gravel size; highlighting relationships between features of the contact interface and gravel size, which presented an opportunity to create a unique terrain classification system.

The outcome of the results analysis led to the development of a classification system using A and L_v measurements as unique input variables within a fuzzy logic system. A fuzzy system was selected for this study as input and output values can be less precise, which is ideal when classifying such a variable element as natural terrain. The final system was developed to operate in real-time by using the FSW to gather data and process, analyse and calculate values on-board. The calculated parameters were then entered into the fuzzy controller where a rule set and membership functions were used to classify the terrain.

The system's ability to classify terrain in real-time was validated through final tests. The successful outcome of these tests confirmed that this novel method is able to offer accurate, real-time information about the terrain while the vehicle is traversing it.

CHAPTER 8
CONCLUSIONS AND FUTHER WORK

8.1 Conclusions

This study aimed to increase the terrain perception of autonomous UGVs. The study was motivated by circumstances where terrain has caused a vehicle to become stuck due to a lack of information regarding (direct) terrain conditions. One such example can be seen with the space rover Spirit when it became stuck in unforgiving Martian terrain, ending its mission.

This thesis establishes a novel tool for measuring direct terrain features at the contact interface and a unique classification technique to identify terrain in real-time. The study was driven by the research questions, which through answering led to the unique contributions.

8.1.1 Answering the Research Questions

- What sensory modes have been utilised to identify terrain?

Through an initial literature review it was discovered that current autonomous vehicles use look-ahead vision systems and passive laser scanners to map their local environments (Chapter 2). This has been proved effective for safely navigating across structured paths; however this method lacks detail when considering unstructured terrain, as these systems make predictions using estimations of terrain's appearance alone. From the review into terrain it was established that the various internal elements of natural terrain will cause it to behave differently when interacted with, which could change its ability to support a load. This information is crucial for autonomous vehicles that operate in unstructured environments because if they unknowingly venture into unforgiving terrain they will become stuck, ending their mission.

A potential solution was proposed through the hypothesis suggesting that *data gathered from performance measurements of the vehicle's reaction to the terrain (the interaction) can be used as a unique method of classifying terrain in real-time.* To verify this, an early experiment was completed to identify terrain properties using internal measurements of vehicle parameters (proprioceptive sensing) in reaction to terrain conditions (Chapter 3). Even though this method had some degree of success by measuring environmental properties through vehicle-terrain interaction, it lacked accuracy and reliability when regarding direct elements of the terrain.

- What are the significant parameters during wheel-terrain interaction?

To search for a more direct method, an additional review was carried out looking at the fundamentals of terrain mechanics and complex quantitative parameters of the interaction between the wheel and terrain, better known as terramechanics (Chapter 5). This review led to the discovery of interaction parameters which are significant to the study as they consist of elements that are far more measurable.

Analytical models (Figure 5.6 and 5.8) and balance Equations (5-7) are used to calculate interaction parameters to predict vehicle performance; however previous knowledge of terrain parameters are required and therefore these could not exclusively be utilised to classify terrain. These models did however highlight the significant parameters of the interaction to be contact angle (θ) and the location of maximum pressure (θ_m) at the wheel-terrain interface, outlined in Figure 6.2. These were subsequently highlighted as the key parameters that could potentially be exploited to classify terrain.

- How could new sensor technologies/methods be used to better identify terrain?

A novel sensing method was required to determine the contact angle θ and location of maximum pressure θ_m during wheel-terrain interaction. The Force Sensing Wheel (FSW) was therefore developed, which contains embedded electronics and a large array of force sensors across its entire surface, giving it the ability to continuously measure the distribution of pressure across the contact interface (Chapter 6).

The wheel, built using modern rapid prototyping/manufacturing tools, includes an innovative modular wheel design which fully incorporates all the embedded electronics required to simultaneously manage 768 force sensors and send raw data in real-time to the Main system Controller. An extensive sensor calibration process meant that accurate force calculations could be made from raw measurements.

The completed FSW was mounted onto the vehicle platform which included the Main System Controller. The complete system was then used for the main empirical study where the vehicle was driven across different granular (gravel) terrain types while force data from the contact interface was collected.

- What parameters can be utilised to classify terrain in real-time?

The raw data collected from the experiment was processed and the final results were presented graphically. These results were thoroughly analysed to identify θ and θ_m for each test (Chapter 7), which supported terramechanic models that suggest these parameters are related to certain terrain properties. These parameters however, approach wheel-terrain interaction from a 2D perspective, assuming that pressure is evenly distributed across the wheel's width. The novel data collection instrument (FSW) offered a unique perspective of the contact interface which was presented using 3D surface maps. The 3D results showed that pressure distribution was laterally uniform only when traversing the flat (datum) surface and became more varied with increasing gravel size. Additionally the size and shape of the contact patch changed both laterally and longitudinally during the tests. This highlighted that θ and θ_m do not accurately represent interaction conditions and therefore cannot solely be used to classify terrain.

Further analysis showed that distinct relationships exist between the contact surface area A (relative to θ), lateral pressure variation L_v (relative to θ_m) and terrain properties. These 3D parameters were deemed to more accurately represent terrain conditions and can be calculated in real-time without requiring knowledge of other parameters. Consequently these parameters were used as unique input variables within a fuzzy logic system to classify terrain in real-time.

8.1.2 Real-time Classification System

Finally, a unique real-time terrain classification algorithm was developed from the results of the empirical study (Figure 7.32). This system successfully collected contact interface measurements and carried out on-board data processing and analysis before entering A and L_v calculations into the fuzzy controller to classify terrain in real-time.

The unique classification system presented in this study could complement current passive sensors which are used to look ahead to determine what is going to happen in order to make early navigation decisions; whereas the novel terrain measurement and classification system could provide information on what is happening now at the wheel-terrain interface. When used alongside current sensing methods, the unique classification system could help to validate terrain estimations and traversability predictions made from vision and look-ahead sensor measurements, enabling more accurate future predictions. Additionally the system could continuously monitor the contact interface during operation, giving an immediate alert if the situation changes and warning of any potential pitfalls before it's too late.

8.2 Contributions to Knowledge

This study proposes a new method of sensing and classifying terrain in real-time. The principle contributions to knowledge are:

- A novel sensing method capable of directly measuring pressure distribution across the contact interface during wheel-terrain interaction.

The innovative Force Sensing Wheel is capable of continuously measuring pressure distribution using 768 force sensors embedded across its entire surface. This self-contained unit measures the wheel-terrain contact interface in real-time and wirelessly sends data via Bluetooth to the Main system Controller to be analysed. This novel sensing method also offers a unique 3D perspective of the contact interface.

- An on-line terrain classification algorithm that uses unique parameters of the wheel-terrain contact interface to accurately identify terrain features in real-time.

This study presents the two unique parameters of the wheel-terrain contact interface to be: Contact Surface Area denoted A and Lateral Pressure Variation denoted L_v. These parameters are used to classify terrain from FSW measurements by using them as the main linguistic input variables within a fuzzy logic system. The final algorithm offers a complete system capable of collecting data and processing it to classify terrain in real-time.

- A number of contributions made towards international research papers (listed in the Publications Section).

8.3 Further Work

There are a number of directions that could be addressed for further work. The three grades of gravel terrain selected for the study offered a limited sample of terrain properties; therefore the first direction would be to test the system across a wider range of terrain types to increase its capabilities.

In order to measure a larger range of terrain types, the force sensors embedded on the FSW would need further developments. Their resolution and sensitivity would need to be increased to be able to measure unique features during interaction with finer terrain such as sand, which might be beyond the capabilities of the FSW in its current configuration. This was initially explored in Chapter 6 (Section 6.2.5) where various compounds that exhibited relationships between voltage and force were created; however a more consistently reliable solution would need to be developed.

Another direction for the study would be to investigate how (negative and positive) wheel slip would affect the terrain classification technique. A final recommendation would be to integrate the novel terrain classification technique with existing look-ahead systems as discussed, in order to verify that the combination of these sensing methods would lead to better traversal decisions, creating a more Terrain Capable system.

REFERENCES

ALIAGA, M. and GUNDERSON, B. (1999). *Interactive Statistics.* Pearson, Prentice Hall.

AMOS, J. (2013). Mars Lake 'much like early Earth'. *BBC News* [online]. Available from: http://www.bbc.co.uk/news/science-environment-25191316 [Accessed 10 May 2014].

ASIMOV, I. (1950). *IRobot*. Gnome Press, New York.

BAKER, D. (2013). *NASA Mars Rovers 1997-2013 (Sojourner, Spirit, Opportunity and Curiosity).* Haynes Publishing, Yeovil.

BEKKER, M.G. (1969). *Introduction to Terrain-Vehicle Systems.* University of Michigan Press, Michigan.

BEKKER, M.G. (1960). *Off-The-Road Locomotion.* University of Michigan Press, Michigan.

BEKKER, M.G. (1956). *Theory of Land Locomotion: The Mechanics of Vehicle Mobility.* University of Michigan Press, Michigan.

BME OMIKK. (2000). Ferenc Pavlics. *Budapest University of Technology and Economics* [online]. Available from: http://www.omikk.bme.hu/archivum/angol/htm/pavlics_f.htm [Accessed 20 June 2014].

BROOKS, C. and IAGNEMMA, K. (2007). Self-supervised classification for planetary rover terrain sensing. *Proceedings of the IEEE International Conference on Aerospace,* Big Sky, Montana, USA, 3-10 March, pp. 1-9.

CAMBONE, S., KRIEG, K., PACE, P. and WELLS, L. (2005). *Unmanned Aircraft Systems Roadmap 2005-2030.* United States Department of Defence.

CAPEK, K., PLAYFAIR, N., SELVER, P. and LANDES, W. (1920). Rossum's universal Robots (R.U.R.). *Prague, CZ* .

COLEMAN, D. and CROSSLEY JR, D. (2004). *Fundamentals of soil ecology.* Academic press.

CRESWELL, J. (2003). *Research Design: Qualitative, Quantitative, and Mixed Methods Approaches.* SAGE Publications, London/New Delhi.

DARPA. (2013). The DARPA Grand Challenge: Ten Years Later. Available from: http://www.darpa.mil/NewsEvents/Releases/2014/03/13.aspx [Accessed 10 May2014].

GENNERY, D. (1999). Traversability analysis and path planning for a planetary rover. *Autonomous Robots,* 6(2), pp. 131-146.

GILMORE, H., RAMSEY, R. and RAHY, T. (1962). *Feasibility Study of Terrain Sensors and Terrain Sensing (DA04-495-ORD3569).* Emerson Electric, Santa Barbara, California, USA.

HOOPER, J. (2004). From DARPA grand Challenge 2004: DARPA's Debacle in the Desert. *Popular Science* [online]. Available from: http://www.popsci.com/scitech/ article/2004-06/darpa-grand-challenge-2004darpas-debacle-desert [Accessed 11 May 2014].

IAGNEMMA, K. and DUBOWSKY, S. (2004). *Mobile Robots in Rough Terrain: Estimation, Motion Planning, and Control with Application to Planetary Rovers.* Springer Publishing Company, Heidelberg, Germany.

IAGNEMMA, K., SHIBLY, H. and DUBOWSKY, S. (2002). On-line terrain parameter estimation for planetary rovers. *Proceedings of the IEEE International Conference on Robotics and Automation*, Washington DC, USA, 11-15 May, pp. 3142-3147.

ICASUALTIES. (2009). Iraq Coalition Casualty Count: IED Fatalities. Available from: http://www.icasualties.org/oif/IED.aspx [Accessed 9 May 2014].

ISO. (2002). *14688-1:2002 Geotechnical investigation and testing - Identification and classification of soil - Part 1: Identification and description*. International Organization for Standardization.

IROBOT. (2014). iRobot 510 Packbot. Available from: http://www.irobot.com/us/learn/defense/packbot.aspx [Accessed 9 May 2014].

KACZMAREK, R. (1984). Central Tire Inflation Systems (CTIS) - A Means to Enhance Vehicle Mobility. *Proceedings of the 8th International Conference on the Performance of Off-road Machines,* 3, pp. 1255-1271.

KUMAR, R. (2005). *Research Methodology: A Step-by-Step Guide for Beginners.* SAGE Publications, London/New Delhi.

LACROIX, S., CHATILA, R., FLEURY, S., HERRB, M. and SIMEON, T. (1994). Autonomous navigation in outdoor environment: Adaptive approach and experiment. *Proceedings of the IEEE International Conference on Robotics and Automation*, San Diego, California, USA, 8-13 May, pp. 426-432.

LEPPANEN, I., VIREKOSKI, P. and HALME, A. (2008). Sensing terrain parameters and the characteristics of vehicle-terrain interaction using the multimode locomotion system of a robot. *IEEE International Conference on Intelligent Robots and Systems,* Nice, France, 22-26 September, pp. 500-505.

MATSON, E. (2010). *iRobot Maritime Research.* iRobot.

MEIRION-GRIFFITH, G., NIE, C. and SPENKO, M. (2014). Development and experimental validation of an improved pressure-sinkage model for small-wheeled vehicles on dilative, deformable terrain. *Journal of Terramechanics,* 51, pp. 19-29.

MEIRION-GRIFFITH, G. and SPENKO, M. (2010). A New Pressure-Sinkage Model for Small, Rigid Wheels on Deformable Terrains. *Proceedings of the Joint 9th Asia-Pacific ISTVS Conference and Annual Meeting of Japanese Society for Terramechanics*, Sapporo, Japan, 27-30 September.

MILLER, B. and ATKINSON, R. (2013). Are Robots Taking Our Jobs, or Making Them? *Information Technology & Innovation Foundation,* 2, pp. 1-36.

MINISTRY OF DEFENCE. (2000). *Guide to the Common Technical Requirements for Military Logistic Vehicles and Towed Equipment (Issue 3).* Defence Standard: 23-06. U.K. Ministry of Defence.

MOORE, G. (1965). Cramming more components onto integrated circuits. *Electronic, 38(8),* 114.

MURO, T. and O'BRIEN, J. (2004). *Terramechanics: Land Locomotion Mechanics.* Swets & Zeitinger, Lisse, The Netherlands.

NAGATANI, K., IKEDA, A., SATO, K. and YOSHIDA, K. (2009). Accurate estimation of drawbar pull of wheeled mobile robots traversing sandy terrain using built-in force sensor array wheel. *IEEE/RSJ International Conference on Intelligent Robots and Systems,* St Louis, Missouri, USA, 11-15 October, pp. 2373-2378.

NASA/JPL. (2013). Curiosity's First Sample Drilling. Available from: http://photojournal.jpl.nasa.gov/catalog/PIA16726 [Accessed 10 May 2014].

NASA/JPL. (2012). Three Generations of Rovers with Crouching Engineers. Available from: http://photojournal.jpl.nasa.gov/catalog/PIA15280 [Accessed 10 May 2014].

NASA/JPL. (2009). Little Movement in Spirit's Sol 2009 Drive. Available from: http://photojournal.jpl.nasa.gov/catalog/PIA12477 [Accessed 11 May 2014].

NASA/JPL. (2009). Rover's Wheel Churns Up Bright Martian Soil. Available from: http://photojournal.jpl.nasa.gov/catalog/PIA11756 [Accessed 09 May 2014].

NASA/JPL. (1999). Newly Deployed Sojourner Rover. Available from: http://photojournal.jpl.nasa.gov/catalog/PIA01551 [Accessed 09 May 2014].

ODEDRA, S. (2011). Using Unmanned Ground Vehicle Performance Measurements as a Unique Method of Terrain Classification. *IEEE/RSJ International Conference on Intelligent Robots and Systems,* San Francisco, California, USA, 25-30 September, pp. 286-291.

ODEDRA, S., PRIOR, S. and KARAMANOGLU, M. (2007). Improving the Mobility Performance of Autonomous Unmanned Ground Vehicles by Adding the Ability to 'Sense/Feel 'Their Local Environment. *Proceedings of the 12th HCI International Conference,* Beijing, China, 22-27 July, pp. 514-522.

ODEDRA, S., PRIOR, S., KARAMANOGLU, M. and SHEN, S. (2009). Increasing the Trafficability of Unmanned Ground Vehicles Through Intelligent Morphing. *ASME/ IFToMM International Conference on Reconfigurable Mechanisms and Robots,* London, U.K, 22-24 June, pp. 674-681.

ORENSTEIN, D. (2005) Stanford team's win in robot car race nets $2 million prize. *Stanford University* [online]. Available from: http://news.stanford.edu/ news/2005/october12/stanleyfinish-100905.html [Accessed 30 June 2014].

ROSE, M. (2002). Technology Development for Army Unmanned Ground Vehicles. *Committee on Army Unmanned Ground Vehicle Technology, Board on Army Science & Technology, National Research Council*. National Academies Press, Washington DC.

SADHUKHAN, D. (2004). *Autonomous Ground Vehicle Terrain Classification Using Internal Sensors.* MSc Thesis, Department of Mechanical Engineering, Florida State University.

SCHMITT, E. (2004). Despite New GI Tactics, Bombs Are Still Biggest Peril. *New York Times* [online]. Available from: http://www.nytimes.com/2004/03/05/world/ despite-new-gi-tactics-bombs-are-still-biggest-peril.html [Accessed 5 May 2014].

SENATORE, C. and IAGNEMMA, K. (2014). Analysis of stress distributions under lightweight wheeled vehicles. *Journal of Terramechanics,* 51, pp. 1-17.

SERAJI, H. and HOWARD, A. (2002). Behavior-based robot navigation on challenging terrain: A fuzzy logic approach. *IEEE Transactions on Robotics and Automation,* 18(3), pp. 308-321.

SHIBLY, H., IAGNEMMA, K. and DUBOWSKY, S. (2005). An equivalent soil mechanics formulation for rigid wheels in deformable terrain, with application to planetary exploration rovers. *Journal of Terramechanics,* 42(1), pp. 1-13.

SHIRKHODAIE, A. (2007). Mobile robots traversability awareness based on terrain visual sensory data fusion. *Proceedings of the SPIE Defense & Security Symposium on Unmanned Systems Technology IX*, (6561), Orlando, USA, 9-13 April.

SINGER, P.W. (2009). *Wired for war: The robotics revolution and conflict in the twenty-first century.* Penguin, New York.

SMITH, J.A. and ONSTOTT, T.C., 2011. "Follow the Water": Steve Squyres and the Mars Exploration Rovers. *Journal of the Franklin Institute,* 348(3), pp. 446-452.

SQUYRES, S. (2005). *Roving Mars: Spirit, Opportunity, and the exploration of the red planet* (1st edition). Hyperion, New York.

STOKER, C. (1998). The search for life on Mars: The role of rovers. *Journal of Geophysical Research: Planets (1991–2012),* 103(12), pp. 28557-28575.

THE WASHINGTON POST. (2014). Faces of the Fallen - IED's. Available from: http://apps.washingtonpost.com/national/fallen/causes-of-death/ied/ [Accessed 9 May 2014].

THRUN, S., MONTEMERLO, M., DAHLKAMP, H., STAVENS, D., ARON, A., DIEBEL, J., FONG, P., GALE, J., HALPENNY, M. and HOFFMANN, G. (2006). Stanley: The robot that won the DARPA Grand Challenge. *Journal of field Robotics,* 23(9), pp. 661-692.

TRAXXAS. (2014). E-Maxx: The Ultimate Electric 4X4 Maxx Monster. Available from: http://traxxas.com/products/models/electric/3903emaxx [Accessed 21 June 2014].

VOLPE, R., ESTLIN, T., LAUBACH, S., OLSON, C. and BALARAM, J. (2000). Enhanced mars rover navigation techniques. *Proceedings of the IEEE International Conference on Robotics and Automation,* San Francisco, California, USA, 24-28 April, pp. 926-931.

WATERWAYS EXPERIMENT STATION. (1948). *Trafficability of Soils - Developments of Testing Instruments.* U.S. Army Corps of Engineers, Vicksburg, MS.

WEBSTER, G. (2011). NASA's Spirit Rover Completes Mission on Mars. *NASA* [online]. Available from: http://www.nasa.gov/mission_pages/mer/news/mer20110525.html [Accessed 9 May 2014].

WILCOX, B. and NGUYEN, T. (1998). Sojourner on mars and lessons learned for future planetary rovers. *SAE Technical Paper 981695,* pp. 5-7.

WINNEFELD, J. and KENDALL, F. (2013). *Unmanned Systems Integrated Roadmap FY2013-2038.* U.S. Department of Defense, USA.

WONG, J. (2010). *Terramechanics and Off-road Vehicle Engineering* (2nd edition). Elsevier, Oxford.

WONG, J. (2001). *Theory of Ground Vehicles* (3rd edition). John Wiley & Sons, Canada.

WONG, J. and REECE, A. (1967). Prediction of rigid wheel performance based on the analysis of soil-wheel stresses part I. Performance of driven rigid wheels. *Journal of Terramechanics,* 4(1), pp. 81-98.

PUBLICATIONS

ODEDRA, S. (2011). Using Unmanned Ground Vehicle Performance Measurements as a Unique Method of Terrain Classification. *IEEE/RSJ International Conference on Intelligent Robots and Systems,* San Francisco, California, USA, 25-30 September, pp. 286-291.

ODEDRA, S., PRIOR, S. and KARAMANOGLU, M. (2009). Investigating the Mobility of Unmanned Ground Vehicles. *Proceedings of the International Conference on Manufacturing Engineering Systems*, Yunlin, Taiwan, 17-19 December, pp. 380-385.

ODEDRA, S., PRIOR, S., KARAMANOGLU, M., ERBIL, M. and SHEN, S. (2009). Using Acoustic Sensor Technologies to Create a More Terrain Capable Unmanned Ground Vehicle. *Proceedings of the 13th HCI International Conference,* San Diego, California, USA, 19-24 July pp. 574-579.

ODEDRA, S., PRIOR, S., KARAMANOGLU, M. and SHEN, S. (2009). Increasing the Trafficability of Unmanned Ground Vehicles Through Intelligent Morphing. *ASME/ IFToMM International Conference on Reconfigurable Mechanisms and Robots,* London, U.K, 22-24 June, pp. 674-681.

ODEDRA, S., PRIOR, S. and KARAMANOGLU, M. (2007). Improving the Mobility Performance of Autonomous Unmanned Ground Vehicles by Adding the Ability to 'Sense/Feel 'Their Local Environment. *Proceedings of the 12th HCI International Conference,* Beijing, China, 22-27 July, pp. 514-522.

ODEDRA, S., PRIOR, S. and KARAMANOGLU, M. (2007). Towards Solving the Mobility Issues of Unmanned Ground Vehicles. *Proceedings of the SPIE Defense & Security Symposium on Unmanned Systems Technology IX*, (6561), Orlando, Florida, USA. 9-13 April.

APPENDICES

A. List of Soil Properties

B. List of Sensors Used on Proprioceptive Sensing Platform

C. Platform Developments for Initial Experiment

D. Proprioceptive Sensing Experiment Results

E. FSW Calibration Test Results

F. Controlled (Datum) Test Results

G. 2-5mm Gravel Results

H. 10-20mm Gravel Results

I. 20-40mm Gravel Results

J. Classification Validation Results

APPENDIX A

List of Soil Properties

Properties and tests relevant to 'soil testing'	
Soil	Dry Density/ Moisture Content Relationship (U)
	Moisture Condition Value (MCV) Test (U)
	One-dimensional Consolidation Properties (U)
	Quick Undrained Shear Strength Triaxial Test (U)
	Friction angle
	Cohesion
	permeability
	compaction
	susceptibility to frost
	unit weight
	Coefficient of Compressibility
	California bearing ratio (**CBR**)
	Particle size
	Soil Ph
	Hazen-Williams coefficients
Soil properties	Hydraulic conductivity
	Water content
	Void ratio
	Bulk density
	Thixotropy
	Reynolds' dilatancy
	Angle of repose
	Cohesion
	Porosity
	Permeability
	Specific storage
	Unit weight - the weight per unit volume of a material
	Porosity - void ratio
	Permeability
	Consolidation
	Shear strength
	Atterberg limits
	liquid limit
	plastic limit
	shrinkage limit
Lab Test	Atterberg limits
	California bearing ratio
	hydraulic conductivity
	consolidation
	particle-size analysis
	soil compaction
	triaxial shear
	Sieve analysis
	Direct shear test
	Hydrometer
	Proctor compaction test
	R-value
	unconfined compression
	water content tests

Geotechnical Investigation	Cone penetration test
	Standard penetration test
	Exploration geophysics
	Monitoring well
	Borehole
Our initial list	density
	shear strength
	compressibility
	hardness
	permeability
	porosity
	plasticity
	stiffness
	deformation
	compact factor
	loading
	drainage
	particle size
	particle shape
	water content
	dielectric permittivity
	conductivity
	volume of
	air
	water
	solid
	consistency of particles
	volume weight
	voids
	depth
other	surface texture
	Environmental factors
	negative/positive obstacles
soil mechanics	Effective stress
	Pore water pressure
	Shear strength
	Overburden pressure
	Consolidation
	Soil compaction
	Soil classification
	Shear wave
	Lateral earth pressure

APPENDIX B

List of Sensors Used on Proprioceptive Sensing Platform

Vehicle-Terrain Interaction Test Platform Sensor List

Sensing Stage	Property to measure	How	Sensor Type	Used To Measure	Range	Units	Accuracy
Environmental Properties	Slope	Vehicle tilt angle/rate (around the X-axis).	Tilt sensor	X-axis rotation angle	±60	degrees	<0.1 degrees
	Gradient	Vehicle tilt angle/rate (around the Y-axis).	Tilt sensor	Y-axis rotation angle	±60	degrees	<0.1 degrees
	Topology	Surface roughness measured by suspension travel and frequency (rate of vibration).	Linear potentiometer	Suspension stroke	0-60	mm	0.06 mm
Terrain Properties	Slippage	Compare the difference between linear velocity (on the X-axis) and angular velocity at the wheels/gearbox.	Encoder	Angular velocity	0-937*	rpm	360 pulses per rev
			Accelerometer	X-axis linear velocity	±3	*g*(gravity force)	330 mV/*g*
		Also, linear velocity in a perpendicular direction (Y-axis) to that of travel implies slip.	Accelerometer	Y -axis linear velocity	±3	*g*(gravity force)	330 mV/*g*
	Sinkage	Rolling Resistance (Viscosity of terrain during sinkage): If current draw increases then rolling resistance has increased (taking slope/gradient into consideration).	Current Sensor	Current	±30	Amps	0.1A
		Also comparison of the difference in suspesion position and ground clearance.	Ultrasonic Sensor	Distance	0.03-6	m	0.01m

*notes:	Motor speed @14.4v = 17500rpm Gear ratio = 18.67:1 therefore output speed = 937rpm

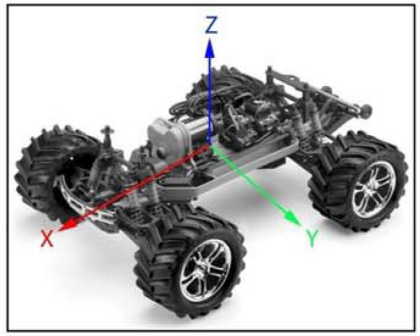

APPENDIX C

Platform Developments for Initial Experiment

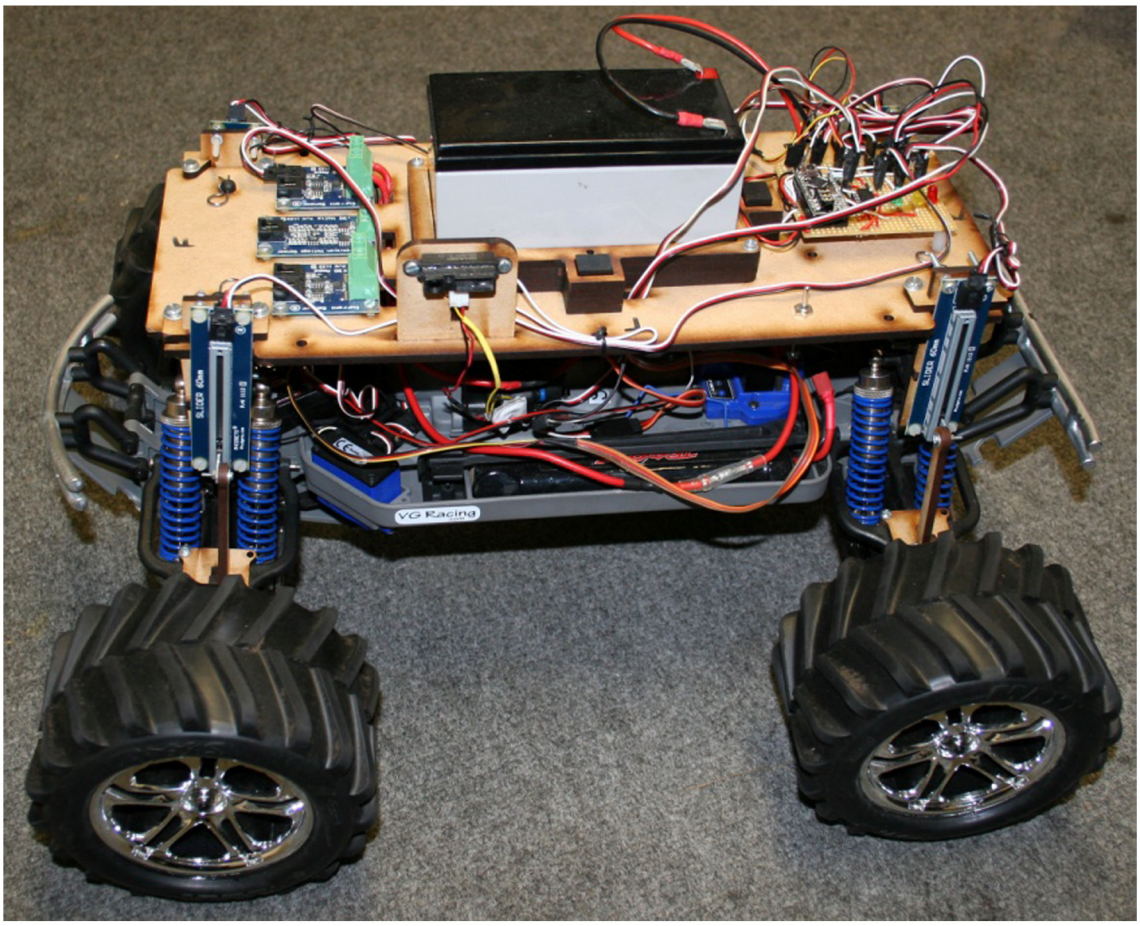

Final Vehicle Platform with Sensors

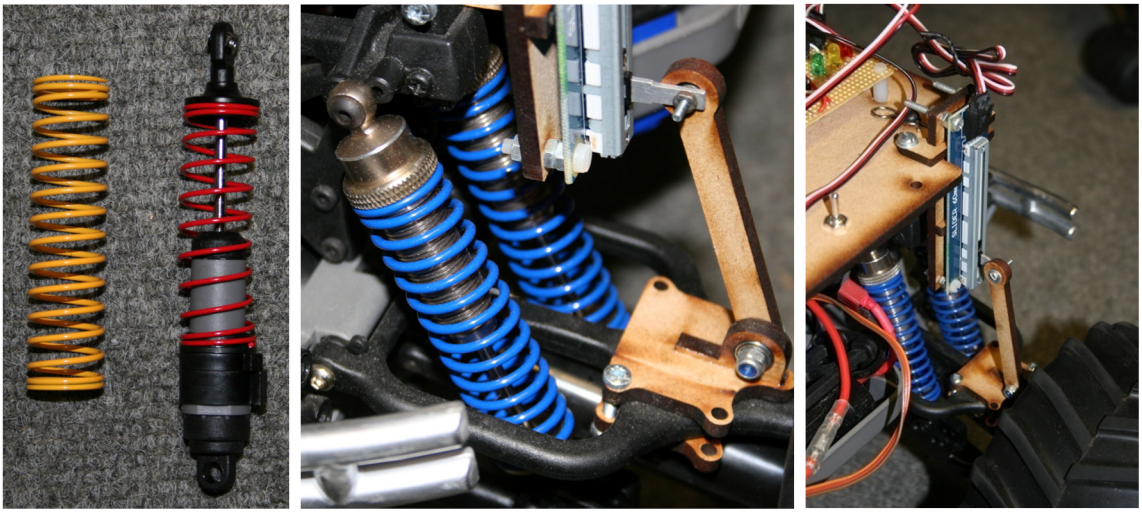

Suspension Modifications & Linear Potentiometer

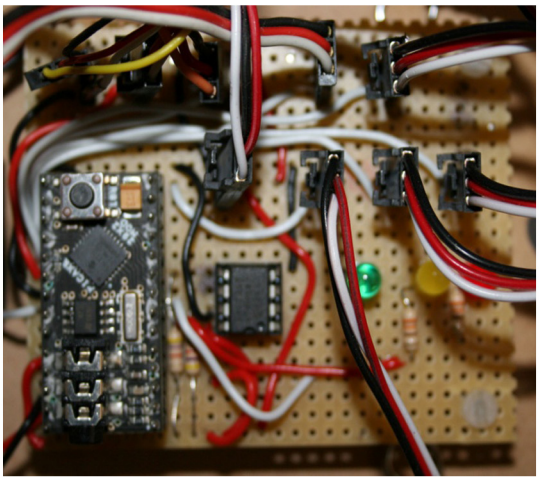

Electronic Board Including PICAXE and EPROM Chip

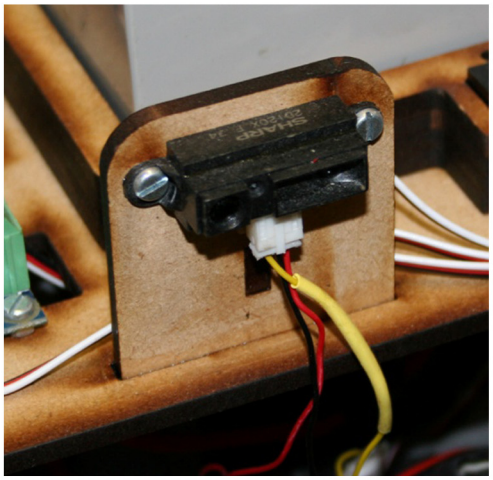

IR Sensor for Start and Stop Signals

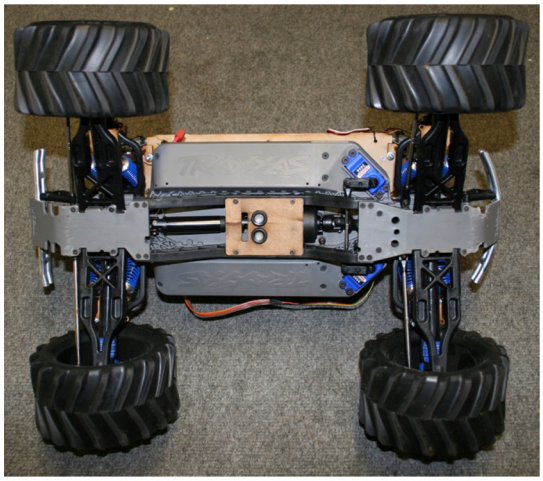

Integrated Ultrasonic Sensor to Measure Ground Height

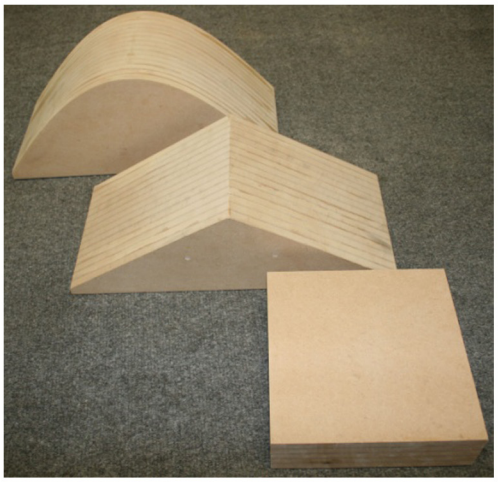

Obstacle for Calibration Runway

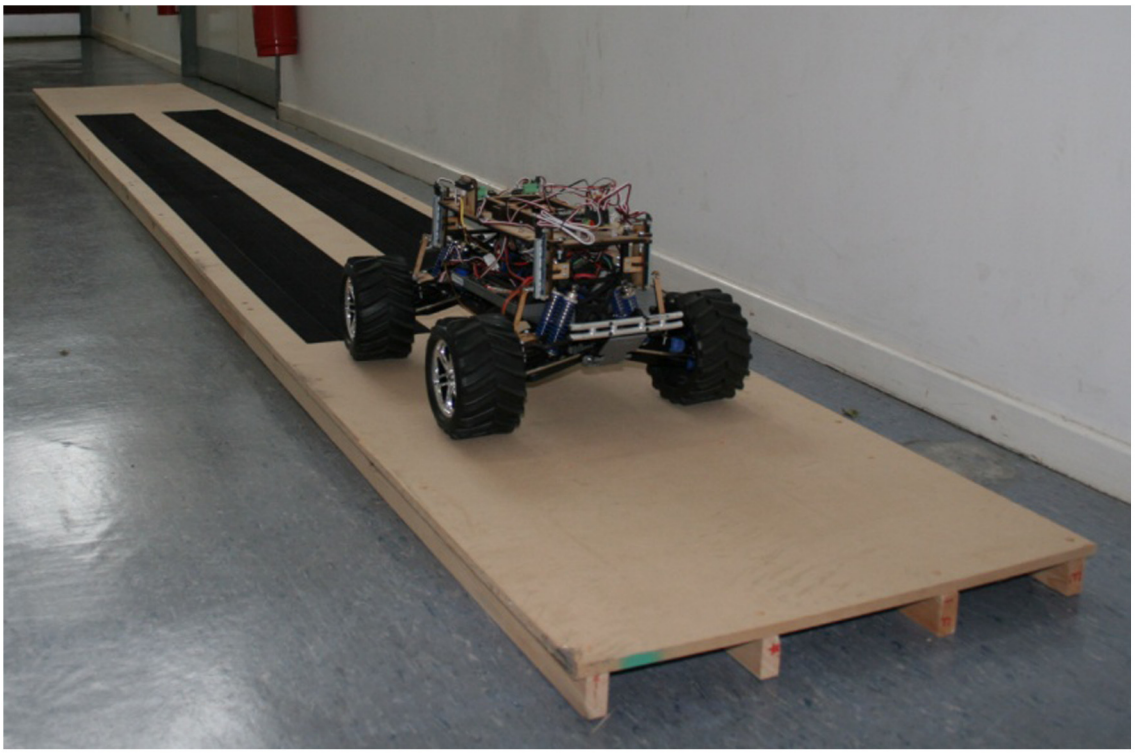

Platform on Calibration Runway

APPENDIX D

Proprioceptive Sensing Experiment Results

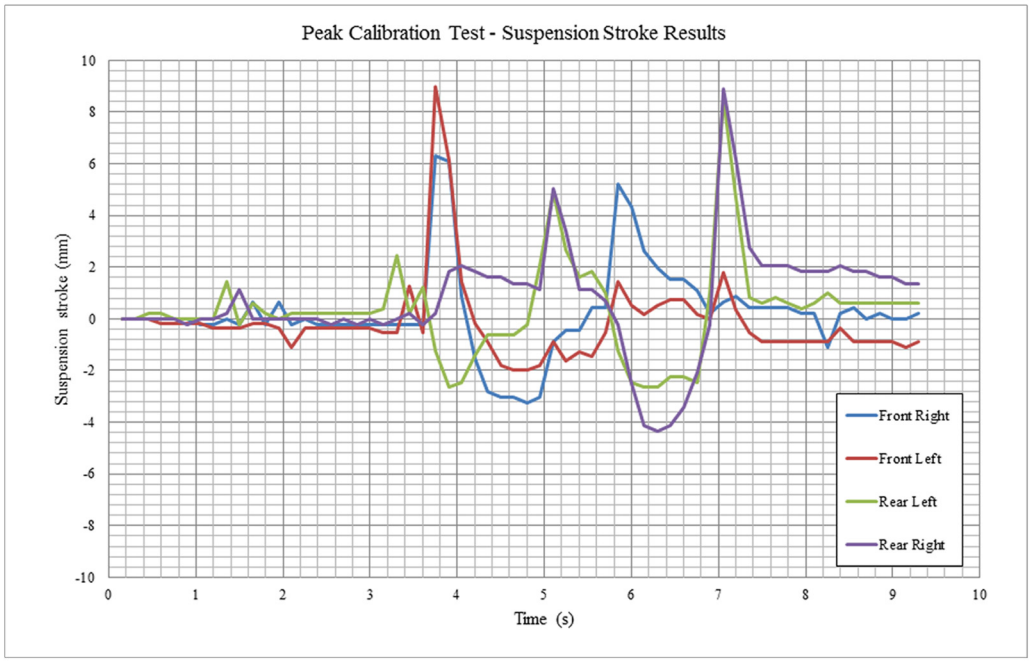

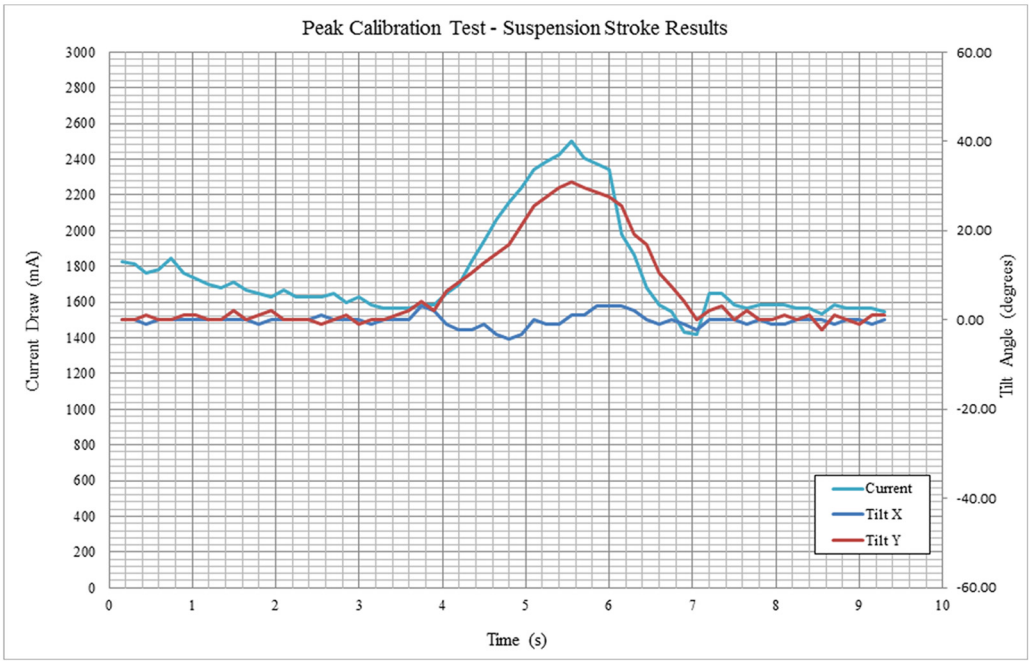

Sensor Calibration Values

Suspension

Corner	Input pin	Variable	Bottom	Mid	Top	min	max (mm)	range (bytes)	mm/ byte	start position (mm)
FR	0	B0	249	237	47	0	44	202	0.22	41.39
FL	1	B1	249	242	49	0	36	200	0.18	34.74
RL	2	B2	252	243	51	0	41	201	0.20	39.16
RR	3	B3	249	232	65	0	42	184	0.23	38.12

Tilt Y

		Degrees	Byte	deg/byte
Uphill	+	30	134	0.88
		15	120	0.75
		7	109	0.78
Mid	0	0	100	0.00
Downhill	-	7	91	0.78
		15	81	0.79
		30	66	0.88
		ave deg/byte		0.81

Tilt X

		Degrees	Byte	deg/byte
Left	+	30	124	4.29
		24	122	4.80
		10	119	5.00
Mid	0	0	117	0.00
Right	-	10	115	5.00
		24	111	4.00
		30	109	3.75
		ave deg/byte		4.47

Current

Test No.	mA	byte (ave)	mA/ byte
# 1	1400	58	-
2	4400	240	-
Diff	3000	182	16.48

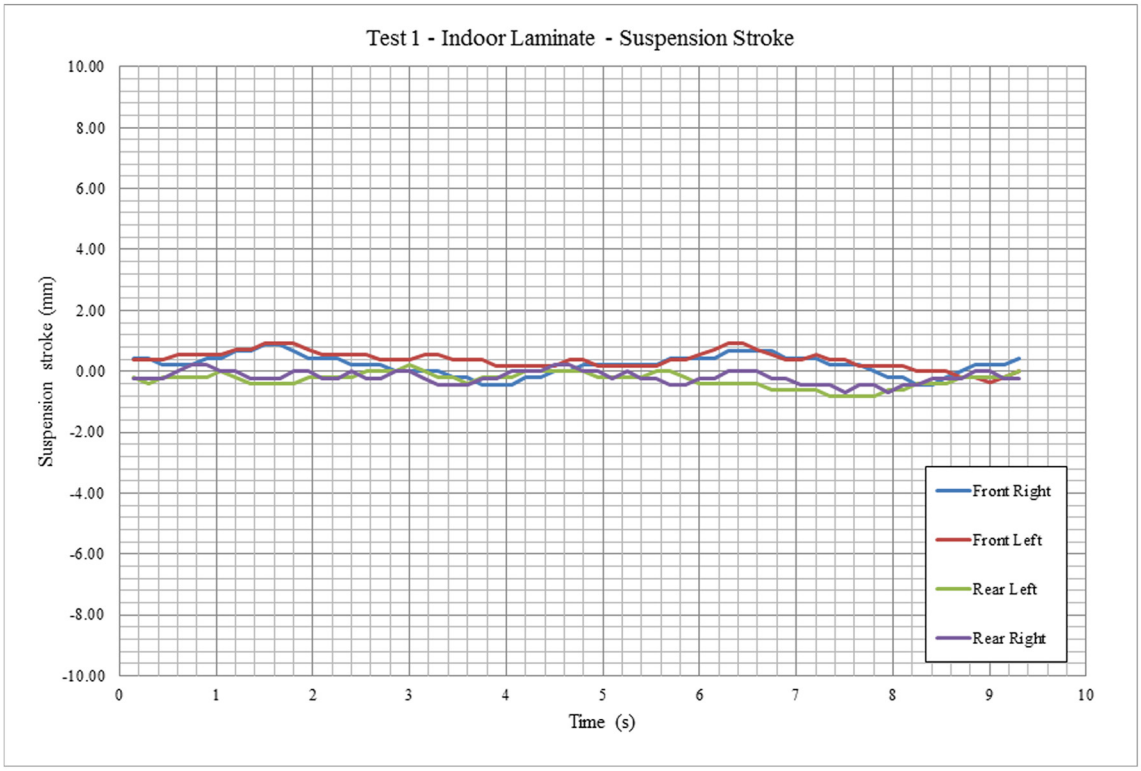
Test 1 - Indoor Laminate - Suspension Stroke
Suspension stroke (mm)
10.00
8.00
6.00
4.00
2.00
0.00
-2.00
-4.00
-6.00
-8.00
-10.00
0
1
2
3
4
5
6
7
8
9
10
Time (s)
Front Right
Front Left
Rear Left
Rear Right

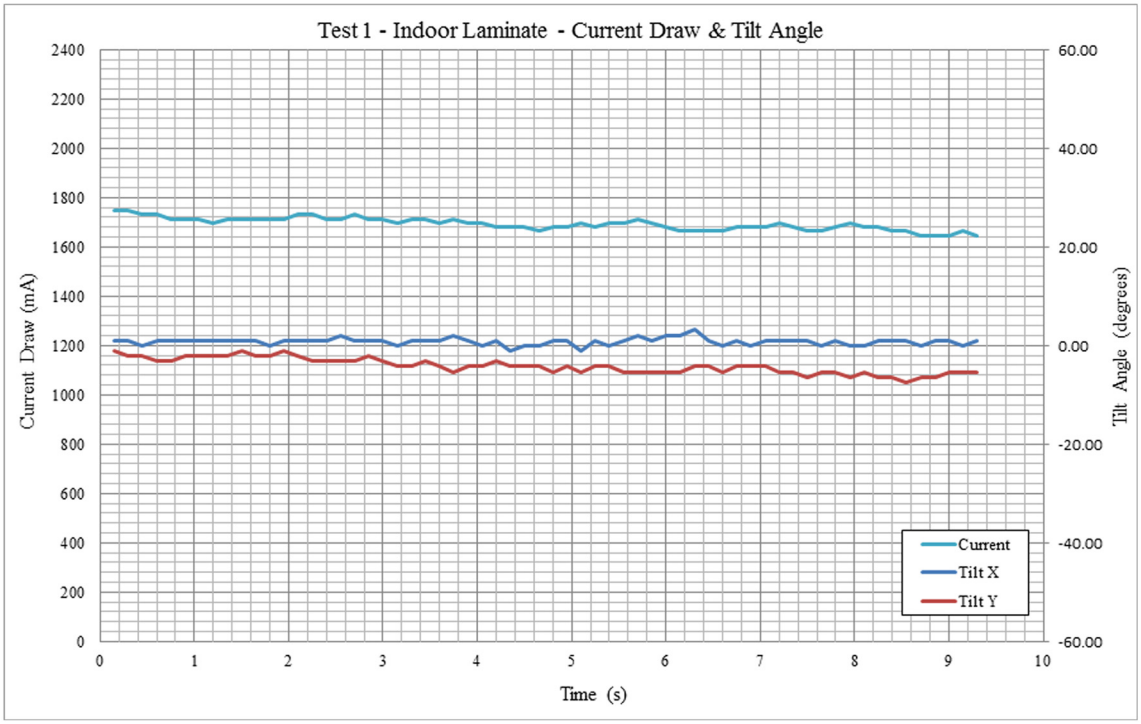
Test 1 - Indoor Laminate - Current Draw & Tilt Angle
Current Draw (mA)
2400
2200
2000
1800
1600
1400
1200
1000
800
600
400
200
0
Tilt Angle (degrees)
60.00
40.00
20.00
0.00
-20.00
-40.00
-60.00
0
1
2
3
4
5
6
7
8
9
10
Time (s)
Current
Tilt X
Tilt Y

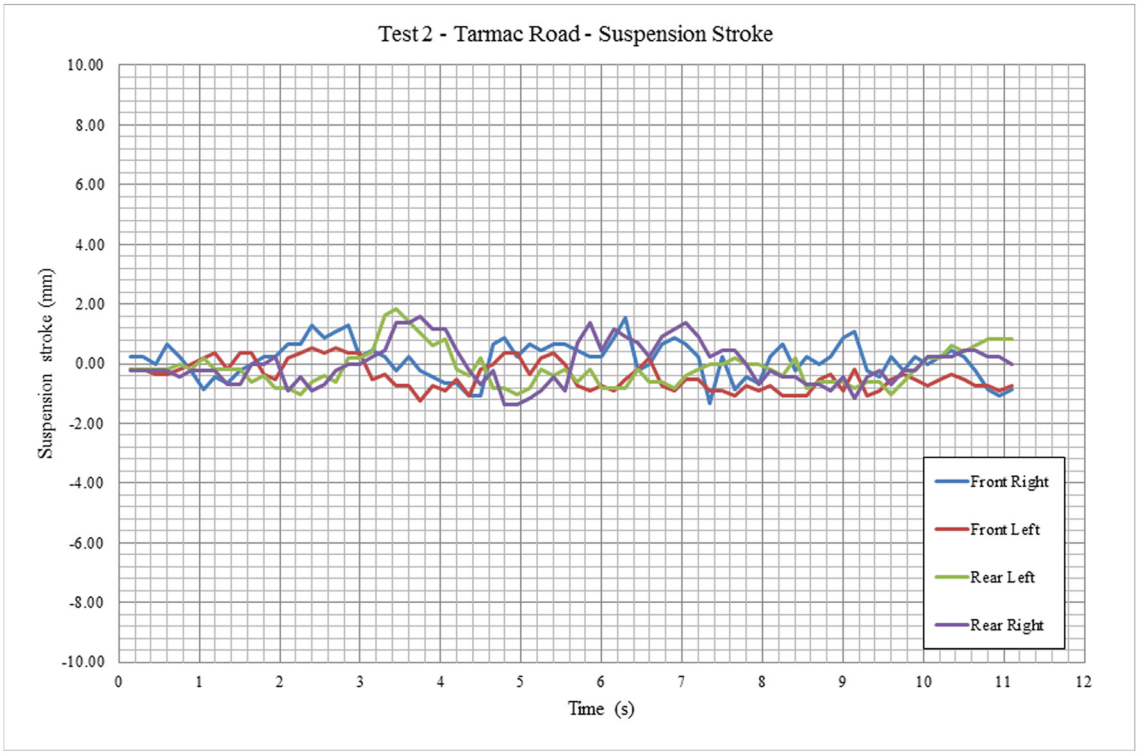
Test 2 - Tarmac Road - Suspension Stroke
Suspension stroke (mm)
10.00
8.00
6.00
4.00
2.00
0.00
-2.00
-4.00
-6.00
-8.00
-10.00
0
1
2
3
4
5
6
7
8
9
10
11
12
Time (s)
Front Right
Front Left
Rear Left
Rear Right

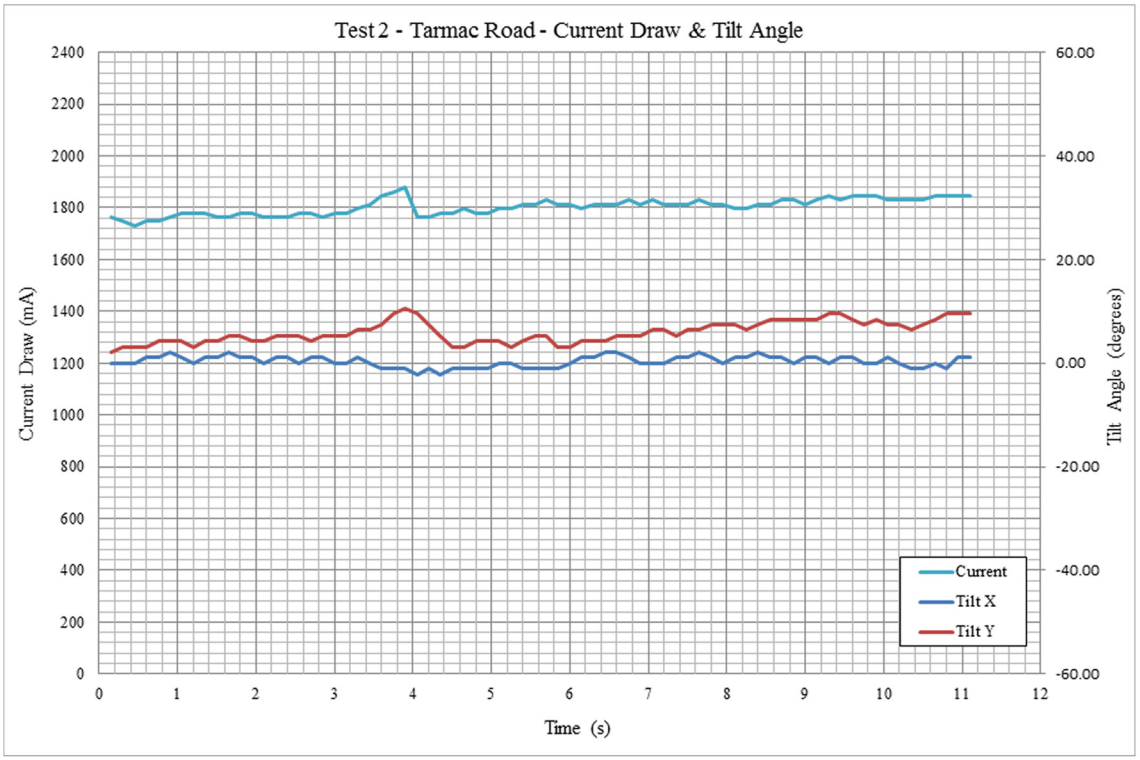
Test 2 - Tarmac Road - Current Draw & Tilt Angle
Current Draw (mA)
2400
2200
2000
1800
1600
1400
1200
1000
800
600
400
200
0
Tilt Angle (degrees)
60.00
40.00
20.00
0.00
-20.00
-40.00
-60.00
0
1
2
3
4
5
6
7
8
9
10
11
12
Time (s)
Current
Tilt X
Tilt Y

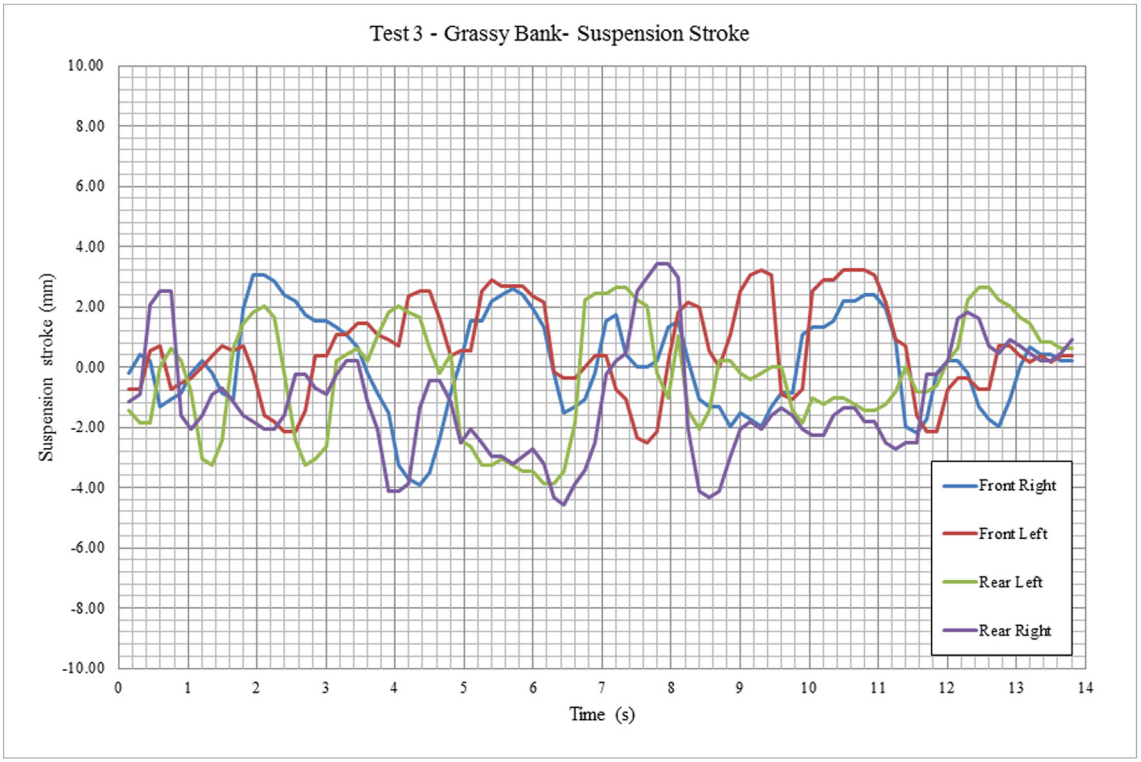
Test 3 - Grassy Bank- Suspension Stroke
Suspension stroke (mm)
10.00
8.00
6.00
4.00
2.00
0.00
-2.00
-4.00
-6.00
-8.00
-10.00
0
1
2
3
4
5
6
7
8
9
10
11
12
13
14
Time (s)
Front Right
Front Left
Rear Left
Rear Right

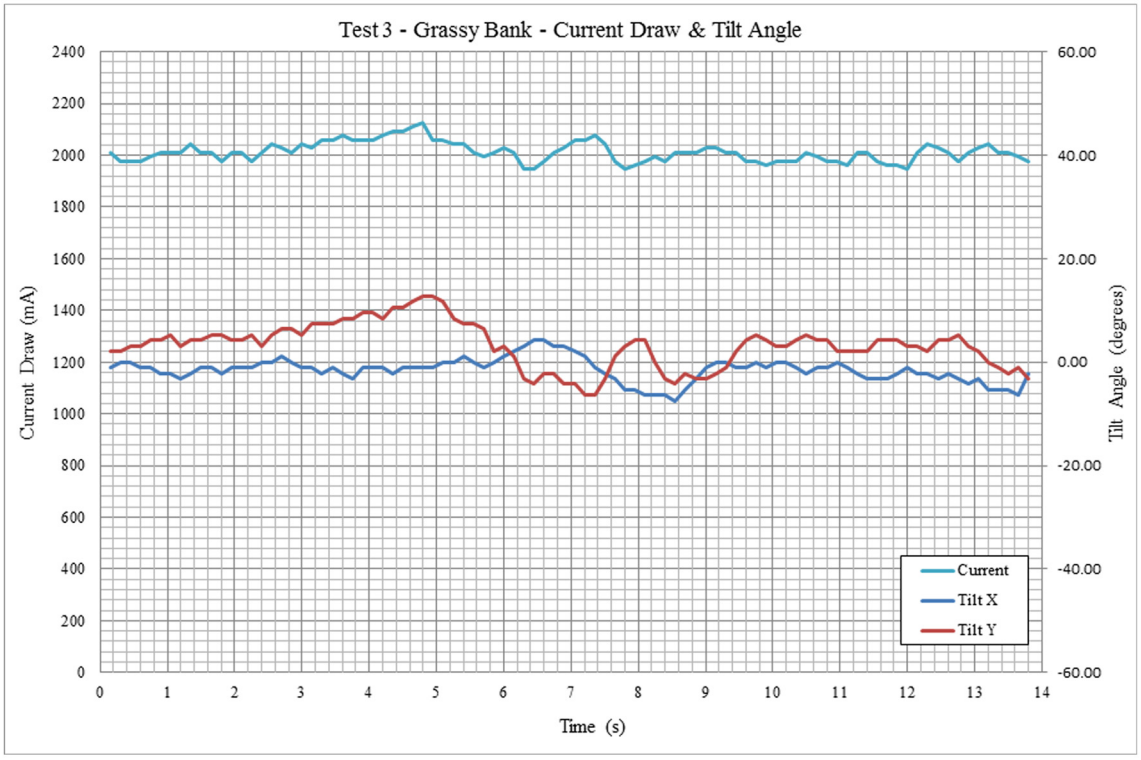
Test 3 - Grassy Bank - Current Draw & Tilt Angle
Current Draw (mA)
2400
2200
2000
1800
1600
1400
1200
1000
800
600
400
200
0
Tilt Angle (degrees)
60.00
40.00
20.00
0.00
-20.00
-40.00
-60.00
0
1
2
3
4
5
6
7
8
9
10
11
12
13
14
Time (s)
Current
Tilt X
Tilt Y

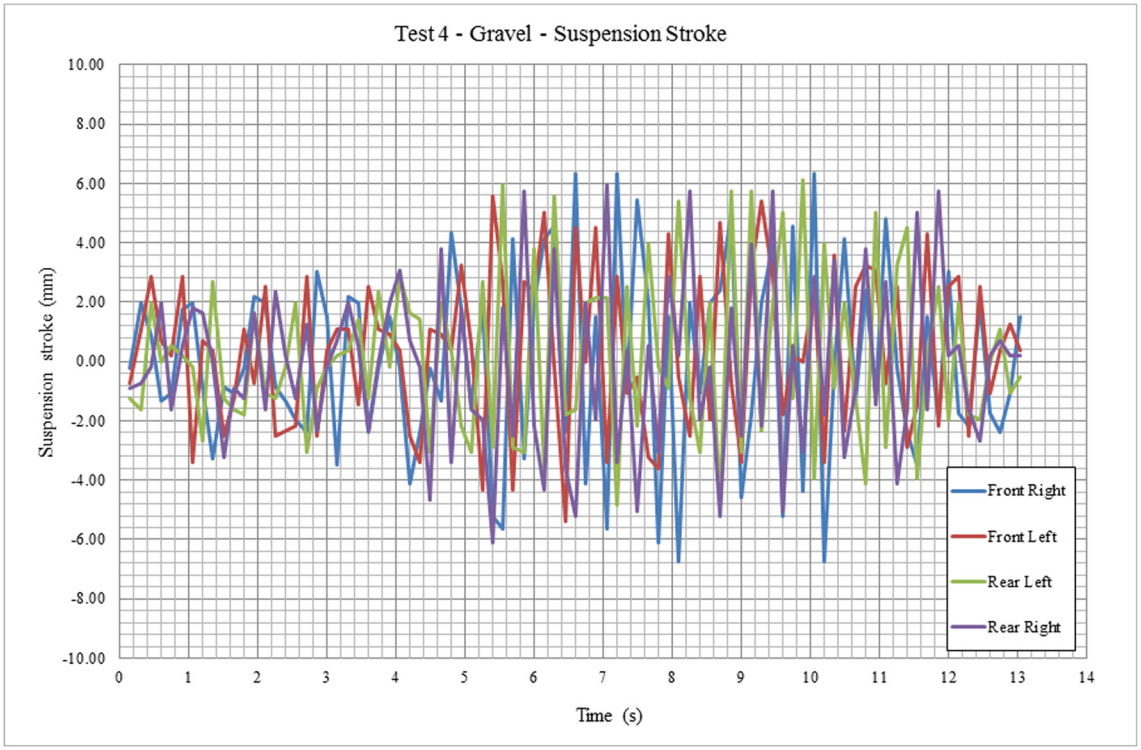
Test 4 - Gravel - Suspension Stroke
Suspension stroke (mm)
10.00
8.00
6.00
4.00
2.00
0.00
-2.00
-4.00
-6.00
-8.00
-10.00
0
1
2
3
4
5
6
7
8
9
10
11
12
13
14
Time (s)
Front Right
Front Left
Rear Left
Rear Right

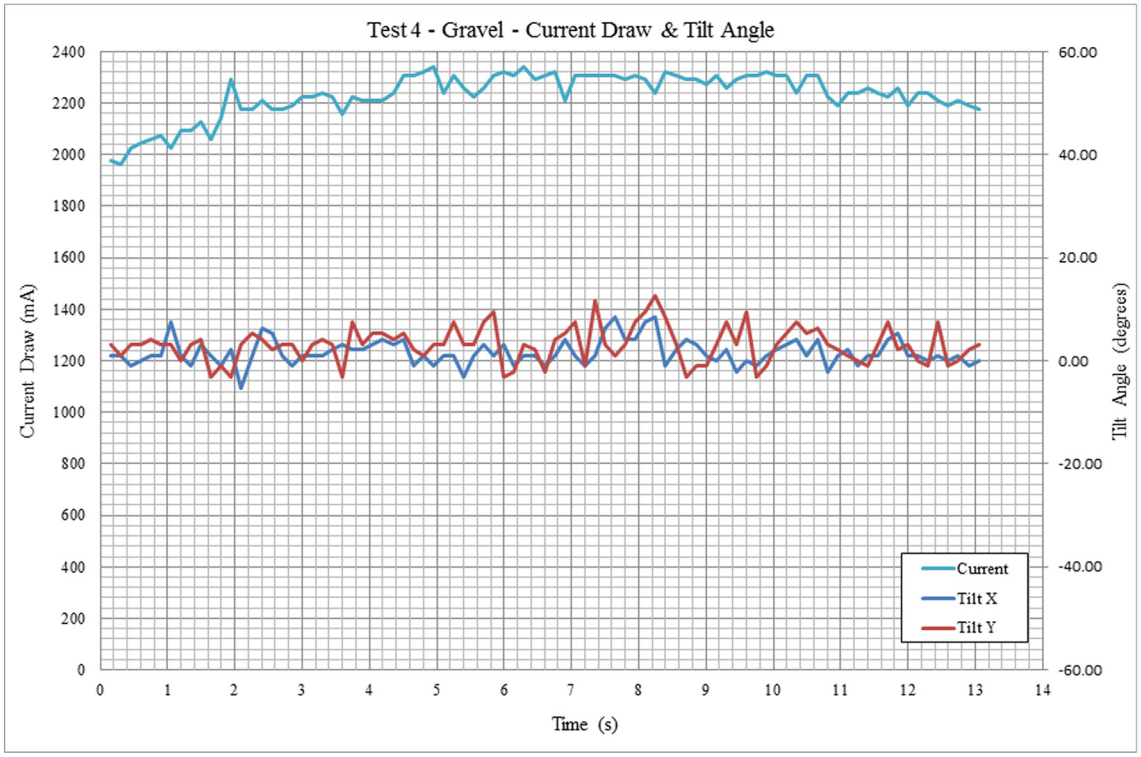
Test 4 - Gravel - Current Draw & Tilt Angle
Current Draw (mA)
2400
2200
2000
1800
1600
1400
1200
1000
800
600
400
200
0
Tilt Angle (degrees)
60.00
40.00
20.00
0.00
-20.00
-40.00
-60.00
0
1
2
3
4
5
6
7
8
9
10
11
12
13
14
Time (s)
Current
Tilt X
Tilt Y

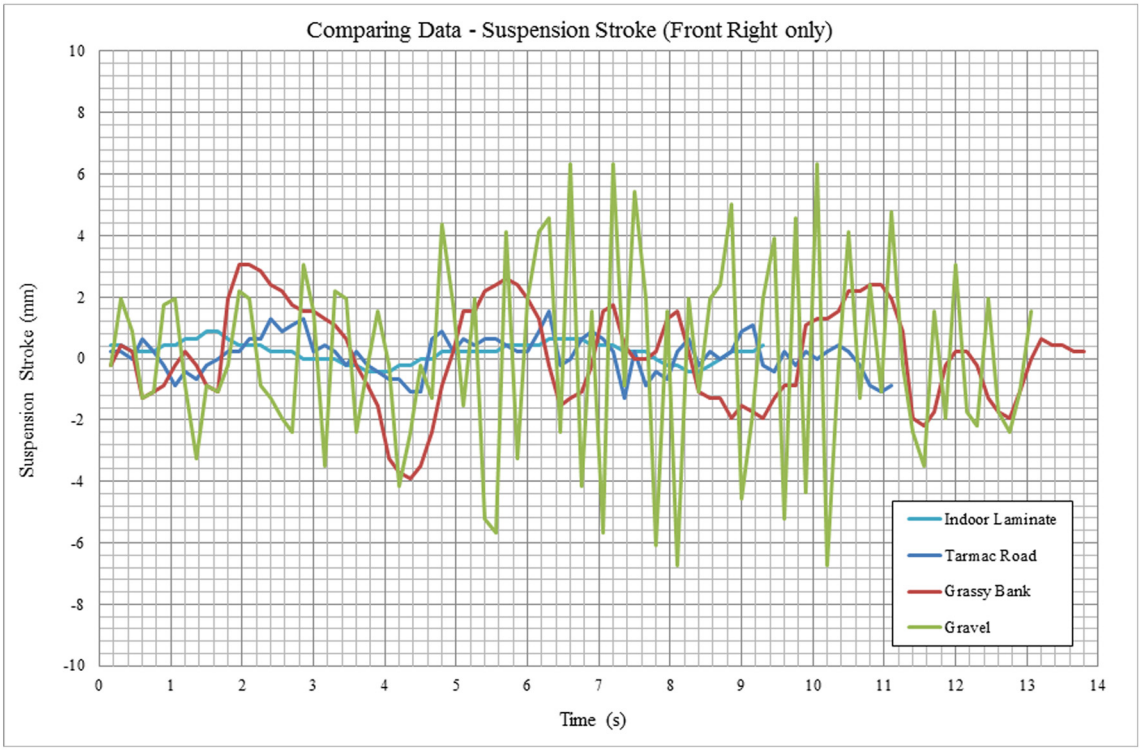
Comparing Data - Suspension Stroke (Front Right only)
Suspension Stroke (mm)
Time (s)
Indoor Laminate
Tarmac Road
Grassy Bank
Gravel

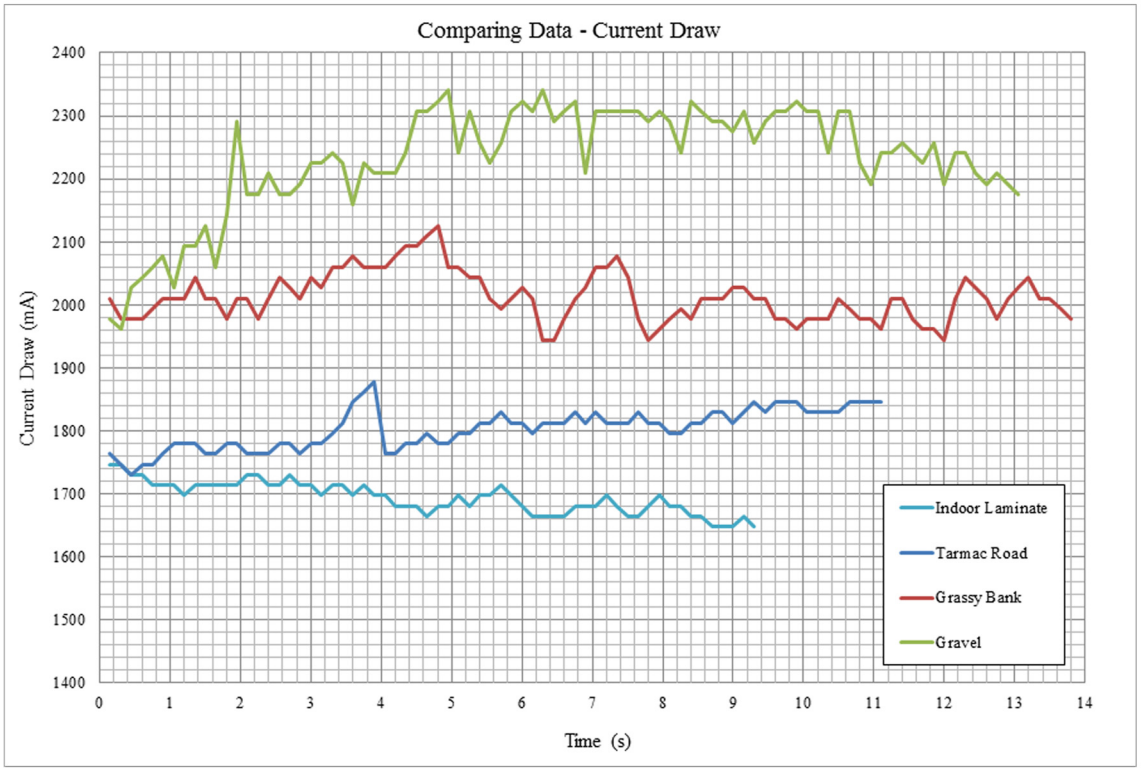
Comparing Data - Current Draw
Current Draw (mA)
Time (s)
Indoor Laminate
Tarmac Road
Grassy Bank
Gravel

APPENDIX E

FSW Calibration Test Results

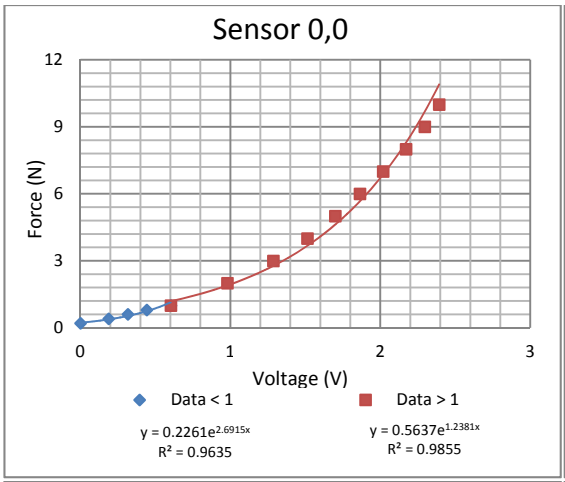
Sensor 0,0
Force (N)
Voltage (V)
Data < 1
Data > 1
y = 0.2261e^2.6915x
R² = 0.9635
y = 0.5637e^1.2381x
R² = 0.9855

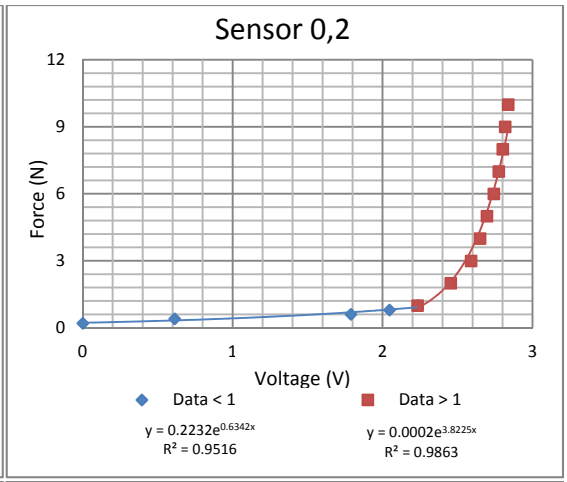
Sensor 0,2
Force (N)
Voltage (V)
Data < 1
Data > 1
y = 0.2232e^0.6342x
R² = 0.9516
y = 0.0002e^3.8225x
R² = 0.9863

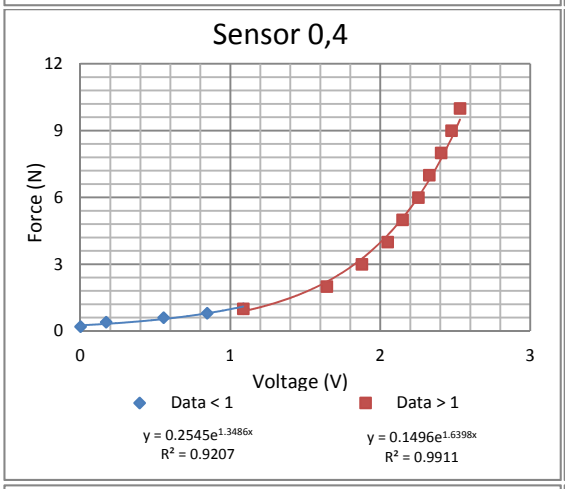
Sensor 0,4
Force (N)
Voltage (V)
Data < 1
Data > 1
y = 0.2545e^1.3486x
R² = 0.9207
y = 0.1496e^1.6398x
R² = 0.9911

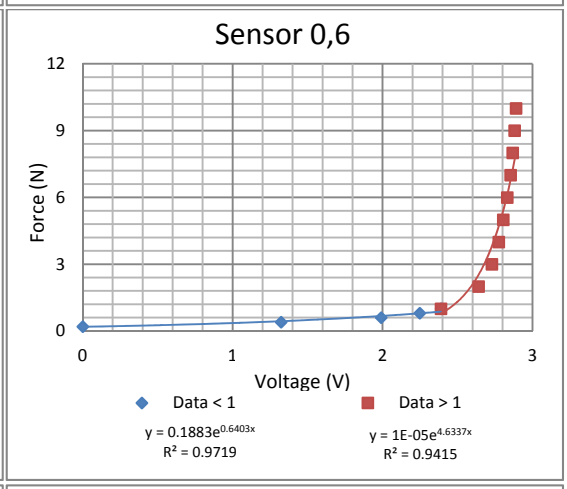
Sensor 0,6
Force (N)
Voltage (V)
Data < 1
Data > 1
y = 0.1883e^0.6403x
R² = 0.9719
y = 1E-05e^4.6337x
R² = 0.9415

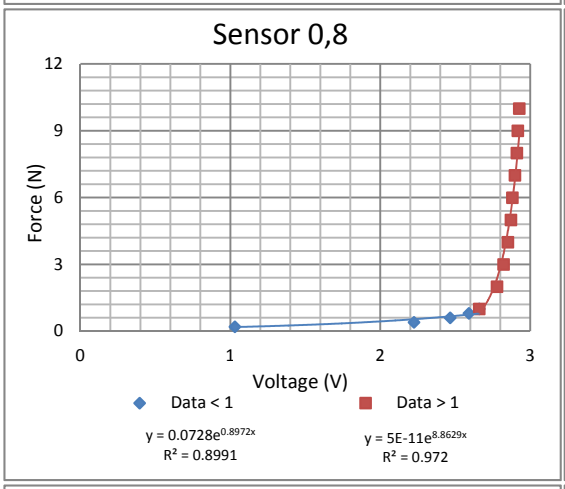
Sensor 0,8
Force (N)
Voltage (V)
Data < 1
Data > 1
y = 0.0728e^0.8972x
R² = 0.8991
y = 5E-11e^8.8629x
R² = 0.972

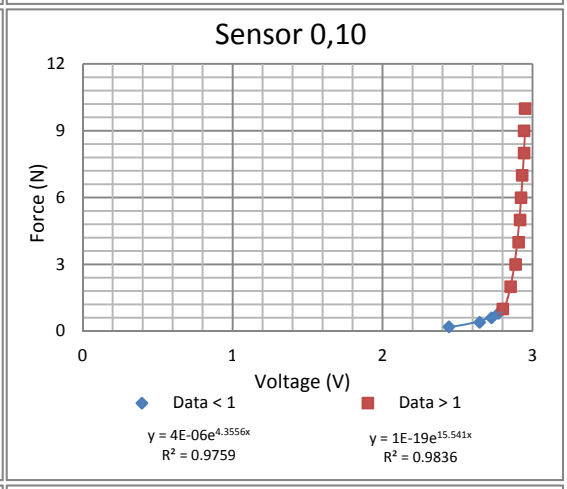
Sensor 0,10
Force (N)
Voltage (V)
Data < 1
Data > 1
y = 4E-06e^4.3556x
R² = 0.9759
y = 1E-19e^15.541x
R² = 0.9836

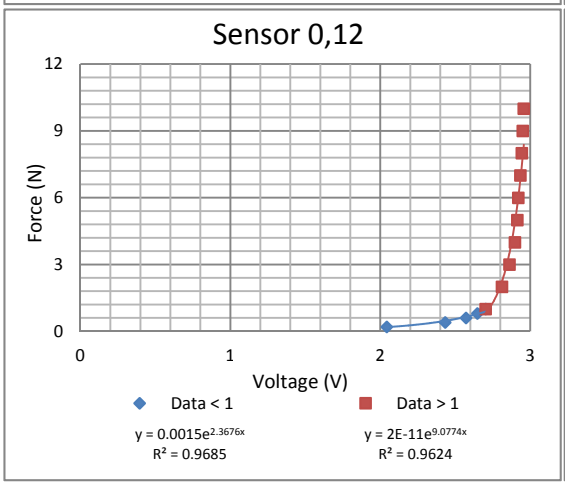
Sensor 0,12
Force (N)
Voltage (V)
Data < 1
Data > 1
y = 0.0015e^2.3676x
R² = 0.9685
y = 2E-11e^9.0774x
R² = 0.9624

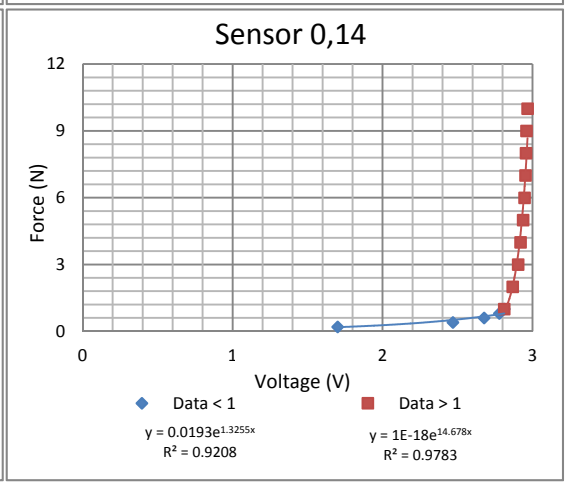
Sensor 0,14
Force (N)
Voltage (V)
Data < 1
Data > 1
y = 0.0193e^1.3255x
R² = 0.9208
y = 1E-18e^14.678x
R² = 0.9783

Appendix E

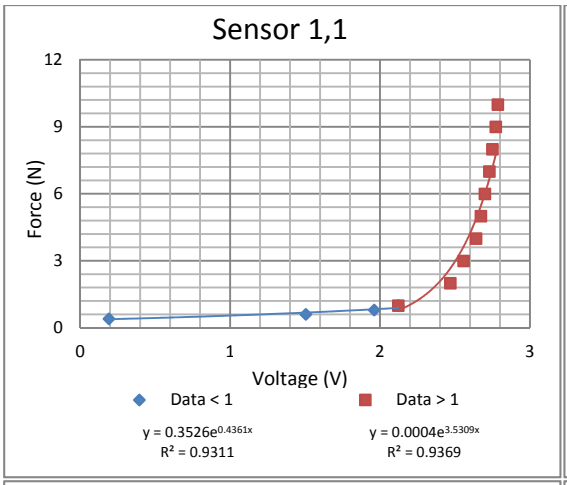
Sensor 1,1
Force (N)
Voltage (V)
Data < 1
Data > 1
y = 0.3526e^0.4361x
R² = 0.9311
y = 0.0004e^3.5309x
R² = 0.9369

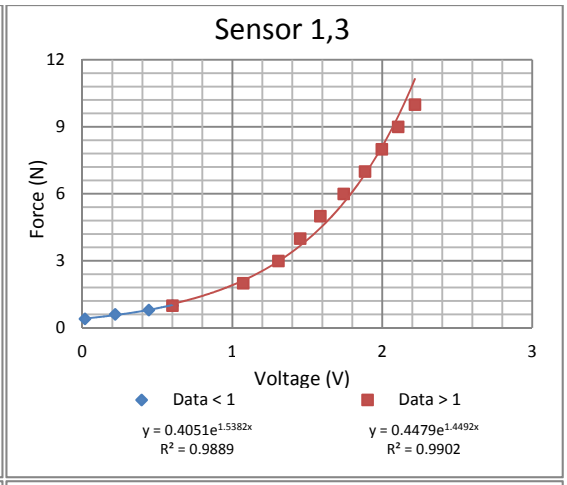
Sensor 1,3
Force (N)
Voltage (V)
Data < 1
Data > 1
y = 0.4051e^1.5382x
R² = 0.9889
y = 0.4479e^1.4492x
R² = 0.9902

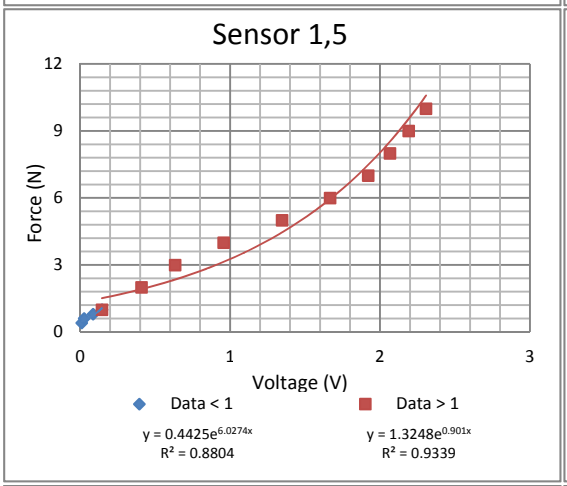
Sensor 1,5
Force (N)
Voltage (V)
Data < 1
Data > 1
y = 0.4425e^6.0274x
R² = 0.8804
y = 1.3248e^0.901x
R² = 0.9339

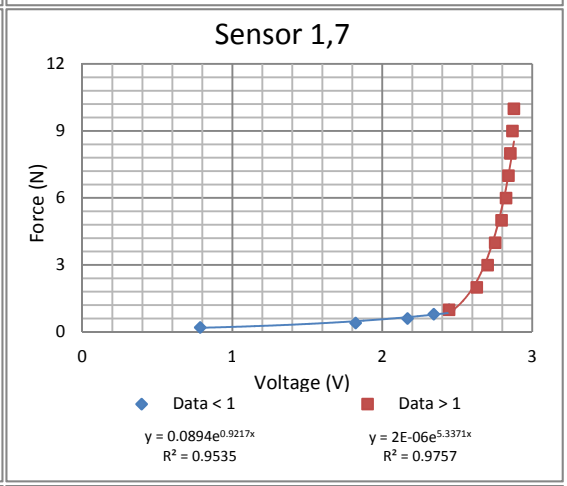
Sensor 1,7
Force (N)
Voltage (V)
Data < 1
Data > 1
y = 0.0894e^0.9217x
R² = 0.9535
y = 2E-06e^5.3371x
R² = 0.9757

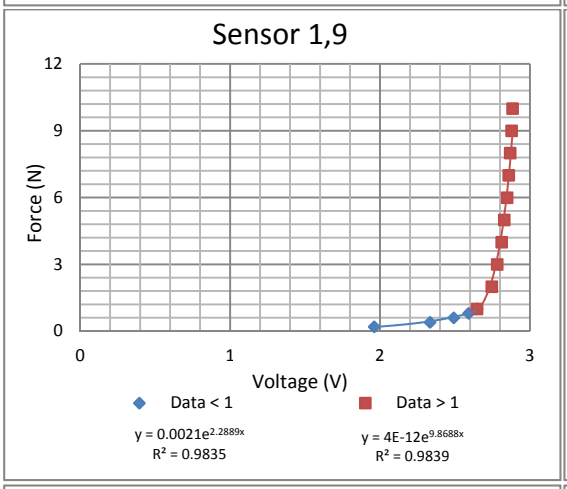
Sensor 1,9
Force (N)
Voltage (V)
Data < 1
Data > 1
y = 0.0021e^2.2889x
R² = 0.9835
y = 4E-12e^9.8688x
R² = 0.9839

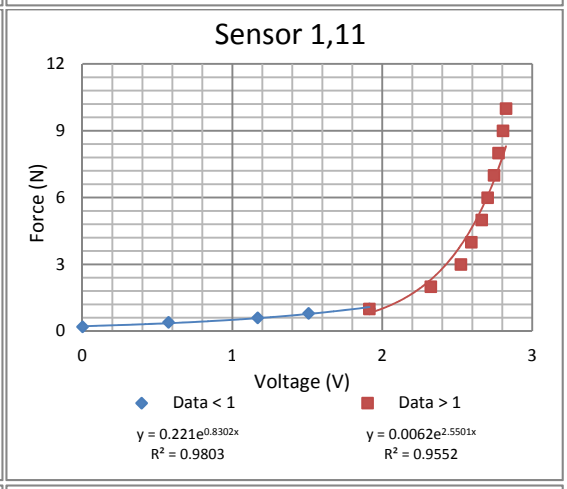
Sensor 1,11
Force (N)
Voltage (V)
Data < 1
Data > 1
y = 0.221e^0.8302x
R² = 0.9803
y = 0.0062e^2.5501x
R² = 0.9552

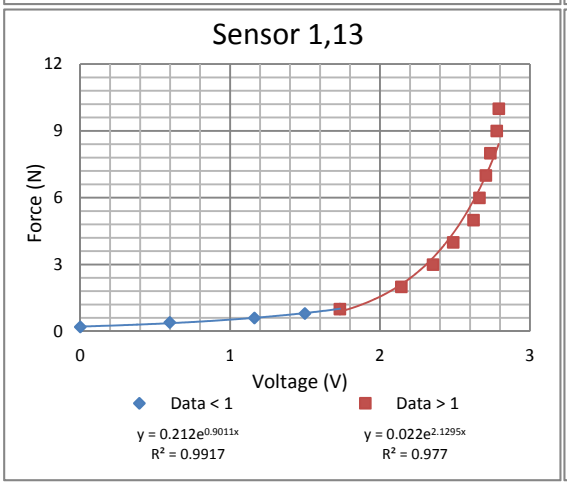
Sensor 1,13
Force (N)
Voltage (V)
Data < 1
Data > 1
y = 0.212e^0.9011x
R² = 0.9917
y = 0.022e^2.1295x
R² = 0.977

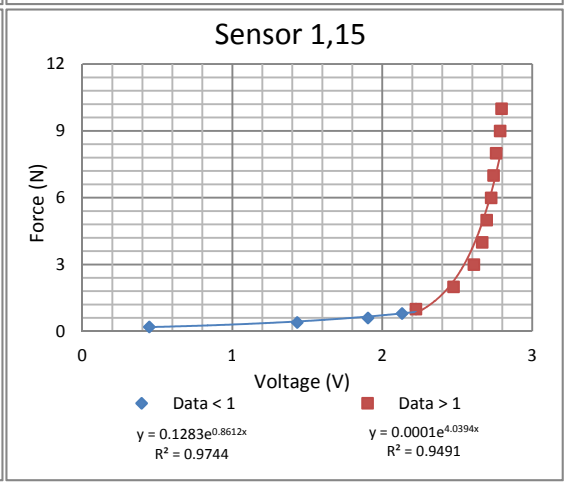
Sensor 1,15
Force (N)
Voltage (V)
Data < 1
Data > 1
y = 0.1283e^0.8612x
R² = 0.9744
y = 0.0001e^4.0394x
R² = 0.9491

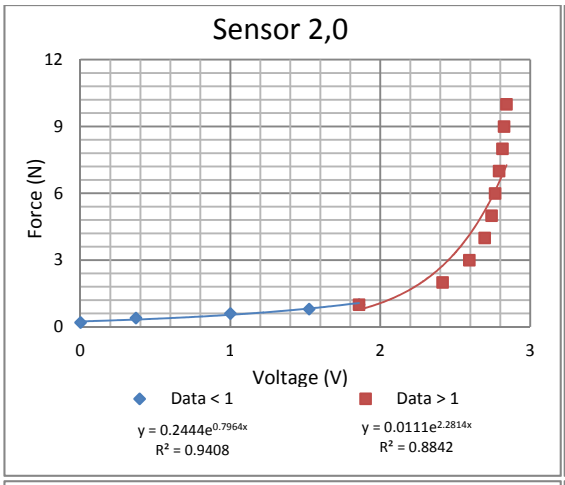
Sensor 2,0
Force (N)
Voltage (V)
Data < 1
Data > 1
y = 0.2444e^0.7964x
R² = 0.9408
y = 0.0111e^2.2814x
R² = 0.8842

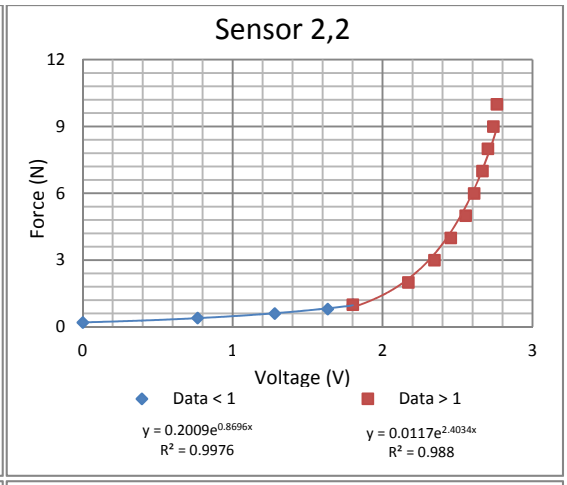
Sensor 2,2
Force (N)
Voltage (V)
Data < 1
Data > 1
y = 0.2009e^0.8696x
R² = 0.9976
y = 0.0117e^2.4034x
R² = 0.988

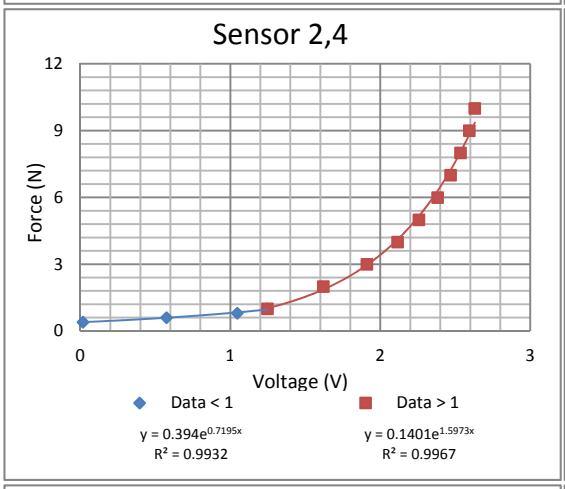
Sensor 2,4
Force (N)
Voltage (V)
Data < 1
Data > 1
y = 0.394e^0.7195x
R² = 0.9932
y = 0.1401e^1.5973x
R² = 0.9967

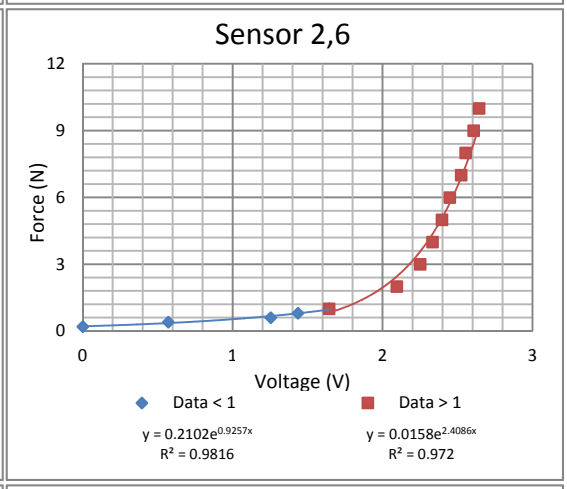
Sensor 2,6
Force (N)
Voltage (V)
Data < 1
Data > 1
y = 0.2102e^0.9257x
R² = 0.9816
y = 0.0158e^2.4086x
R² = 0.972

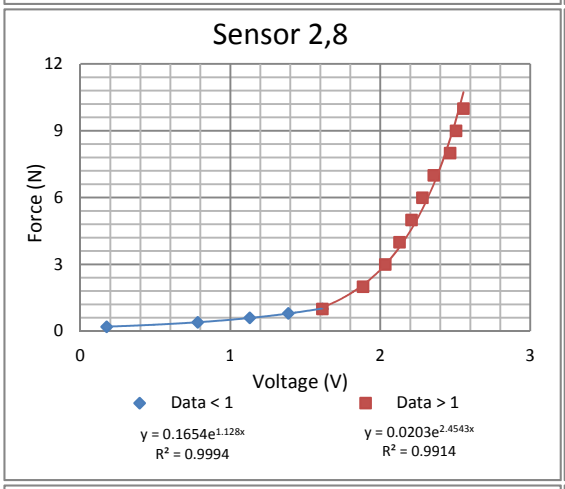
Sensor 2,8
Force (N)
Voltage (V)
Data < 1
Data > 1
y = 0.1654e^1.128x
R² = 0.9994
y = 0.0203e^2.4543x
R² = 0.9914

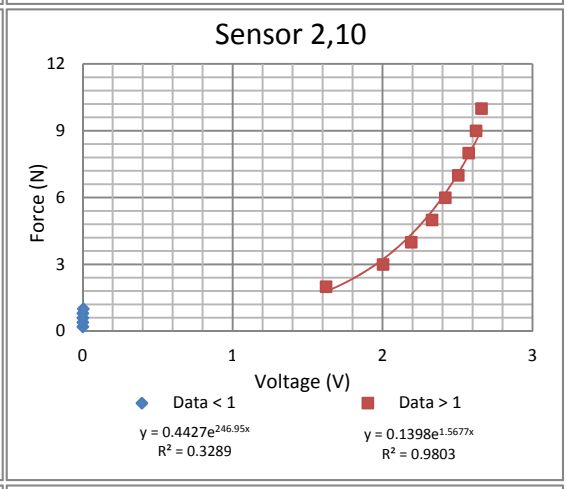
Sensor 2,10
Force (N)
Voltage (V)
Data < 1
Data > 1
y = 0.4427e^246.95x
R² = 0.3289
y = 0.1398e^1.5677x
R² = 0.9803

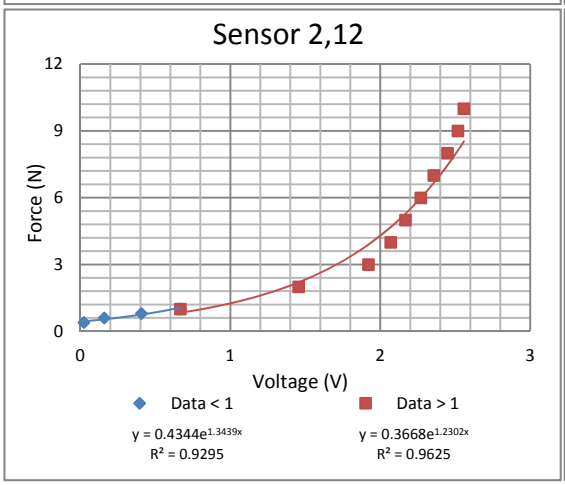
Sensor 2,12
Force (N)
Voltage (V)
Data < 1
Data > 1
y = 0.4344e^1.3439x
R² = 0.9295
y = 0.3668e^1.2302x
R² = 0.9625

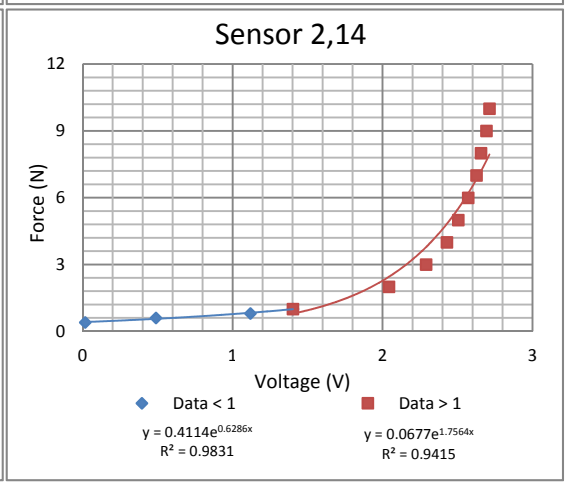
Sensor 2,14
Force (N)
Voltage (V)
Data < 1
Data > 1
y = 0.4114e^0.6286x
R² = 0.9831
y = 0.0677e^1.7564x
R² = 0.9415

Appendix E

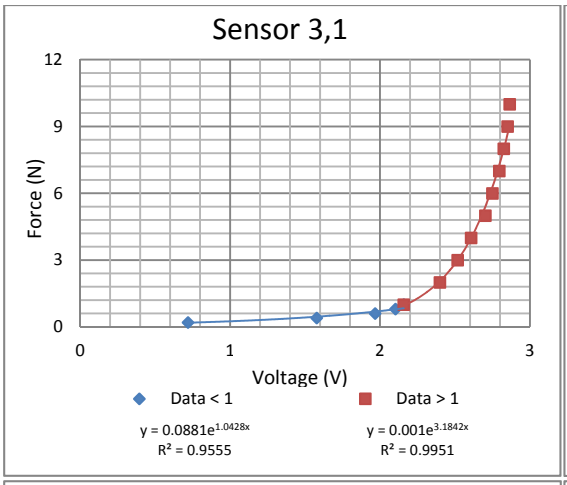
Sensor 3,1
Force (N)
Voltage (V)
Data < 1
Data > 1
y = 0.0881e^1.0428x
R² = 0.9555
y = 0.001e^3.1842x
R² = 0.9951

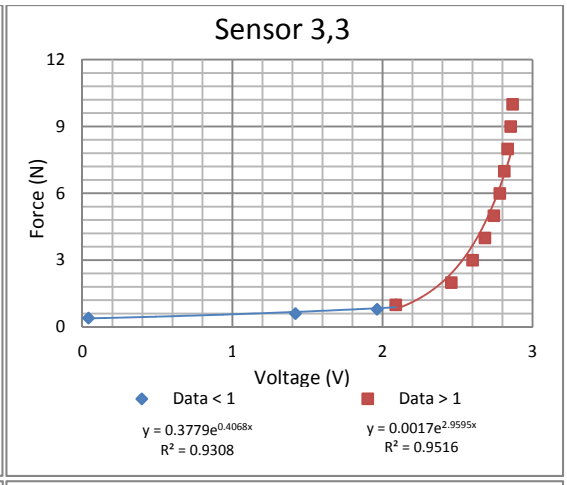
Sensor 3,3
Force (N)
Voltage (V)
Data < 1
Data > 1
y = 0.3779e^0.4068x
R² = 0.9308
y = 0.0017e^2.9595x
R² = 0.9516

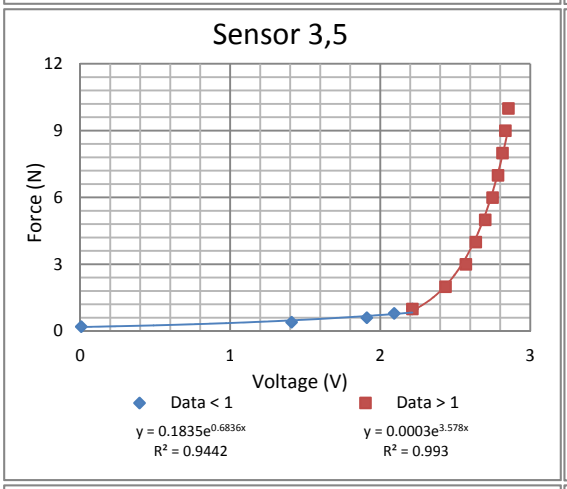
Sensor 3,5
Force (N)
Voltage (V)
Data < 1
Data > 1
y = 0.1835e^0.6836x
R² = 0.9442
y = 0.0003e^3.578x
R² = 0.993

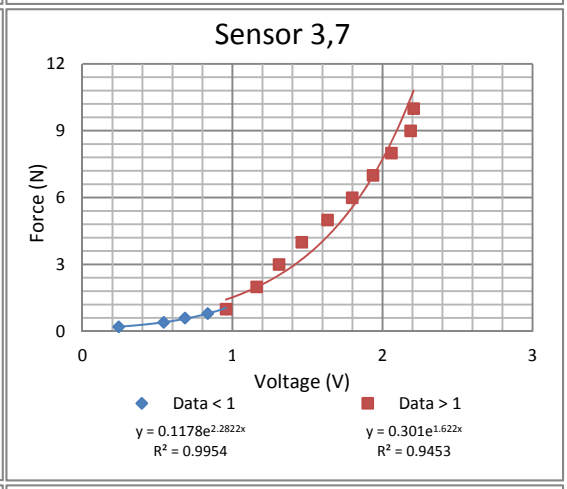
Sensor 3,7
Force (N)
Voltage (V)
Data < 1
Data > 1
y = 0.1178e^2.2822x
R² = 0.9954
y = 0.301e^1.622x
R² = 0.9453

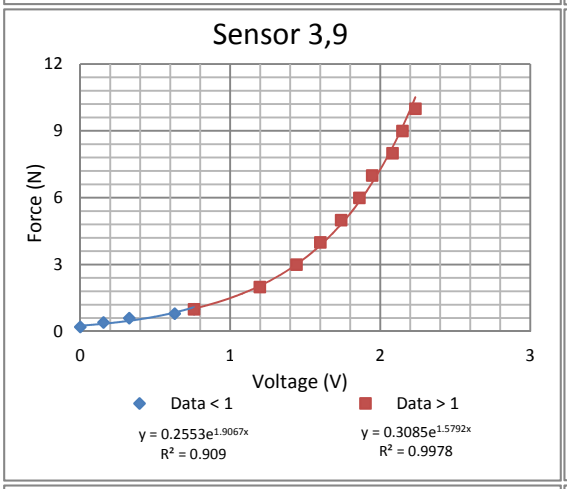
Sensor 3,9
Force (N)
Voltage (V)
Data < 1
Data > 1
y = 0.2553e^1.9067x
R² = 0.909
y = 0.3085e^1.5792x
R² = 0.9978

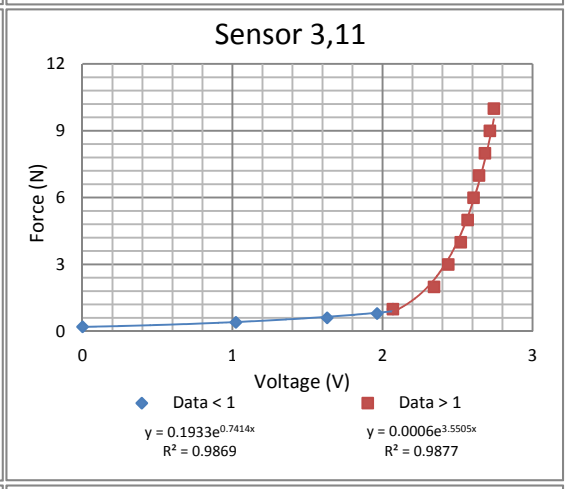
Sensor 3,11
Force (N)
Voltage (V)
Data < 1
Data > 1
y = 0.1933e^0.7414x
R² = 0.9869
y = 0.0006e^3.5505x
R² = 0.9877

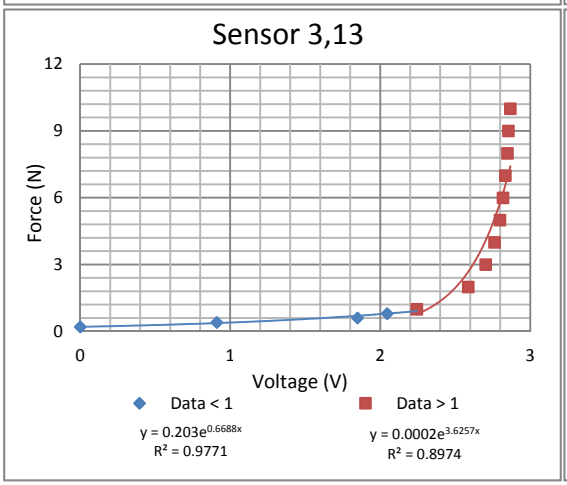
Sensor 3,13
Force (N)
Voltage (V)
Data < 1
Data > 1
y = 0.203e^0.6688x
R² = 0.9771
y = 0.0002e^3.6257x
R² = 0.8974

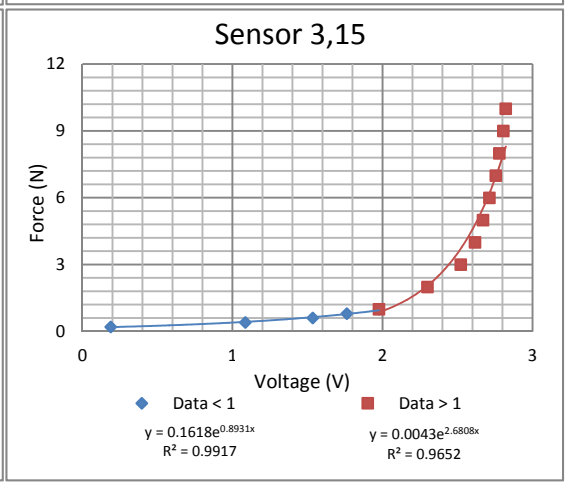
Sensor 3,15
Force (N)
Voltage (V)
Data < 1
Data > 1
y = 0.1618e^0.8931x
R² = 0.9917
y = 0.0043e^2.6808x
R² = 0.9652

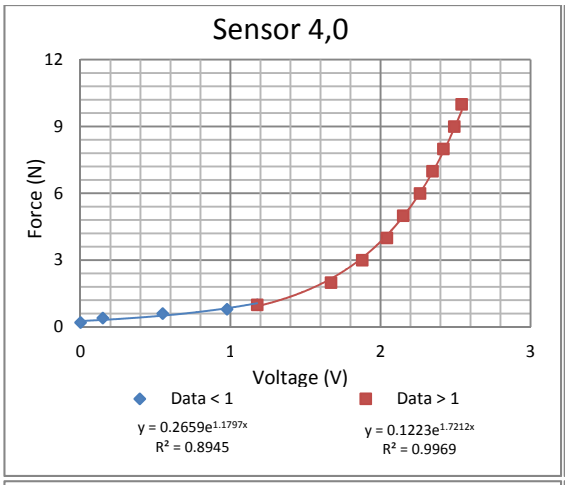
Sensor 4,0
Force (N)
Voltage (V)
Data < 1
Data > 1
y = 0.2659e^1.1797x
R² = 0.8945
y = 0.1223e^1.7212x
R² = 0.9969

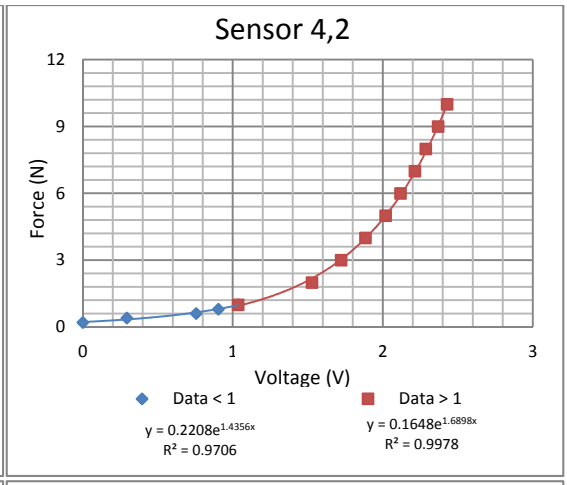
Sensor 4,2
Force (N)
Voltage (V)
Data < 1
Data > 1
y = 0.2208e^1.4356x
R² = 0.9706
y = 0.1648e^1.6898x
R² = 0.9978

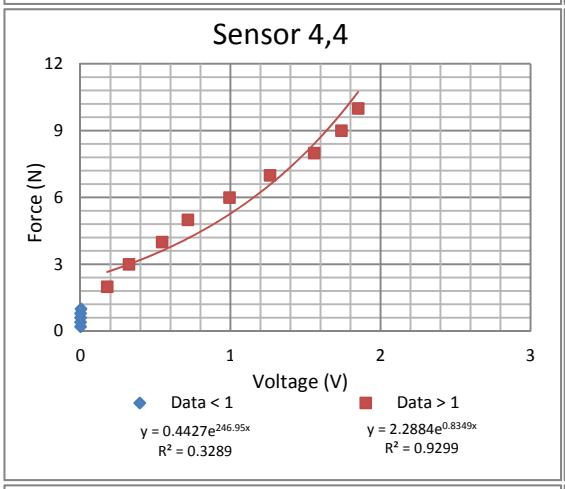
Sensor 4,4
Force (N)
Voltage (V)
Data < 1
Data > 1
y = 0.4427e^246.95x
R² = 0.3289
y = 2.2884e^0.8349x
R² = 0.9299

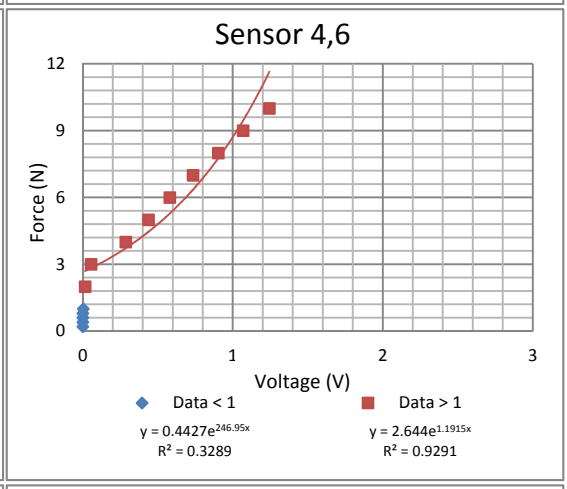
Sensor 4,6
Force (N)
Voltage (V)
Data < 1
Data > 1
y = 0.4427e^246.95x
R² = 0.3289
y = 2.644e^1.1915x
R² = 0.9291

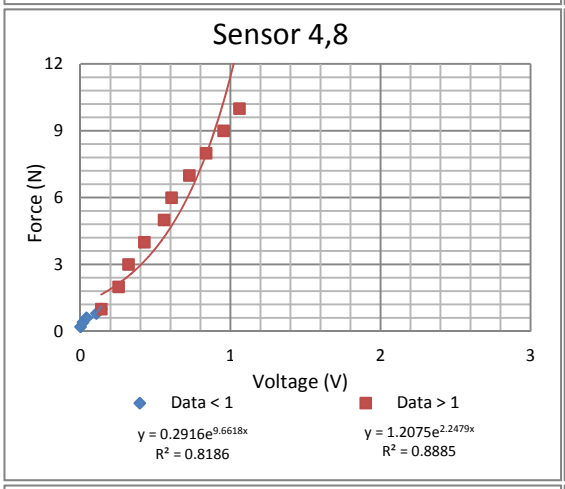
Sensor 4,8
Force (N)
Voltage (V)
Data < 1
Data > 1
y = 0.2916e^9.6618x
R² = 0.8186
y = 1.2075e^2.2479x
R² = 0.8885

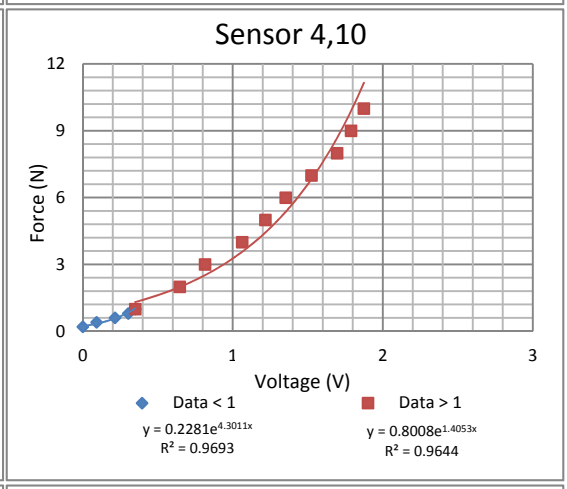
Sensor 4,10
Force (N)
Voltage (V)
Data < 1
Data > 1
y = 0.2281e^4.3011x
R² = 0.9693
y = 0.8008e^1.4053x
R² = 0.9644

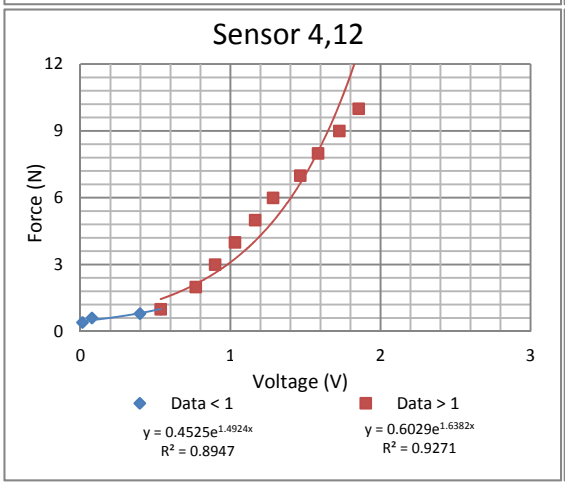
Sensor 4,12
Force (N)
Voltage (V)
Data < 1
Data > 1
y = 0.4525e^1.4924x
R² = 0.8947
y = 0.6029e^1.6382x
R² = 0.9271

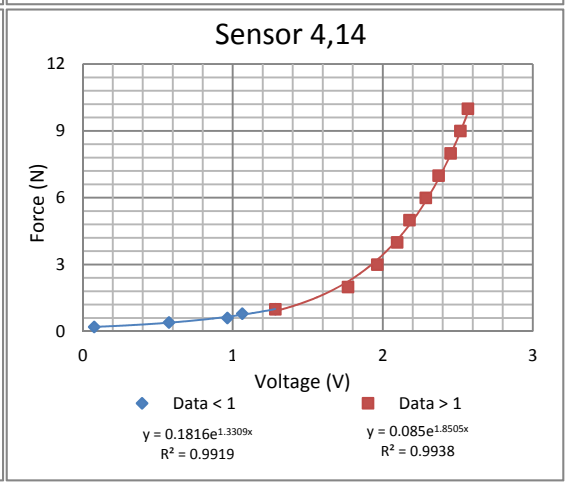
Sensor 4,14
Force (N)
Voltage (V)
Data < 1
Data > 1
y = 0.1816e^1.3309x
R² = 0.9919
y = 0.085e^1.8505x
R² = 0.9938

Appendix E

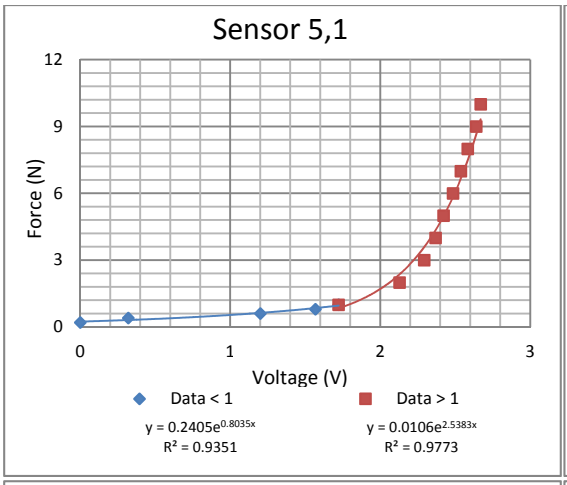
Sensor 5,1
Force (N)
Voltage (V)
Data < 1
Data > 1
y = 0.2405e^0.8035x
R² = 0.9351
y = 0.0106e^2.5383x
R² = 0.9773

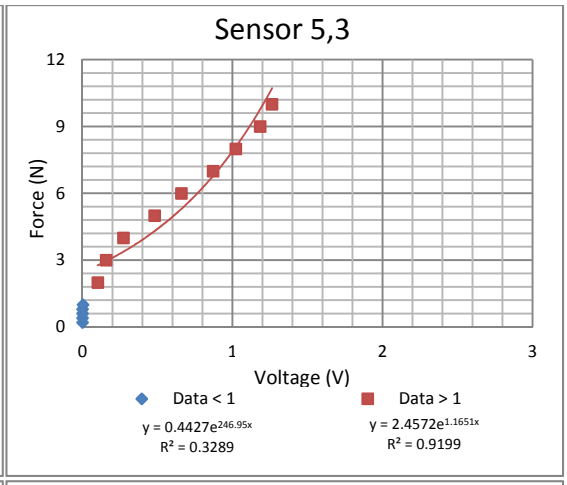
Sensor 5,3
Force (N)
Voltage (V)
Data < 1
Data > 1
y = 0.4427e^246.95x
R² = 0.3289
y = 2.4572e^1.1651x
R² = 0.9199

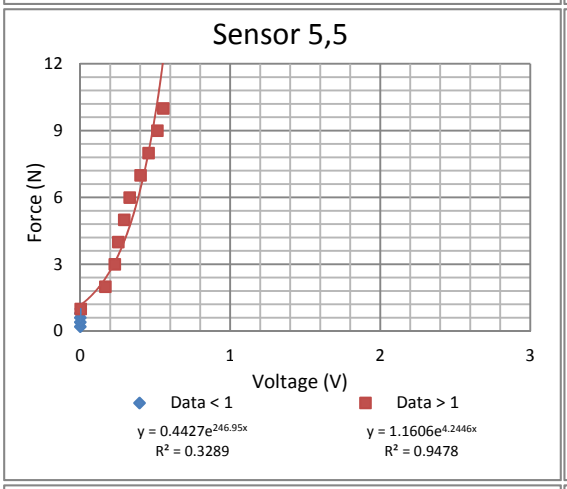
Sensor 5,5
Force (N)
Voltage (V)
Data < 1
Data > 1
y = 0.4427e^246.95x
R² = 0.3289
y = 1.1606e^4.2446x
R² = 0.9478

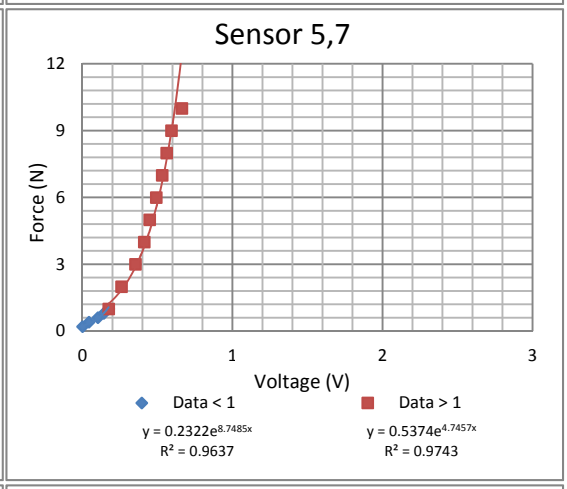
Sensor 5,7
Force (N)
Voltage (V)
Data < 1
Data > 1
y = 0.2322e^8.7485x
R² = 0.9637
y = 0.5374e^4.7457x
R² = 0.9743

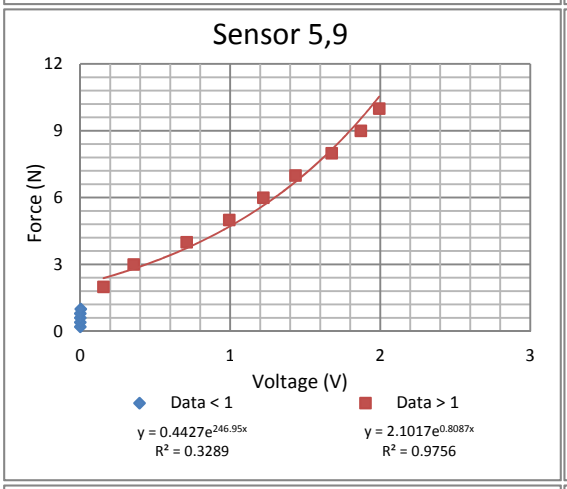
Sensor 5,9
Force (N)
Voltage (V)
Data < 1
Data > 1
y = 0.4427e^246.95x
R² = 0.3289
y = 2.1017e^0.8087x
R² = 0.9756

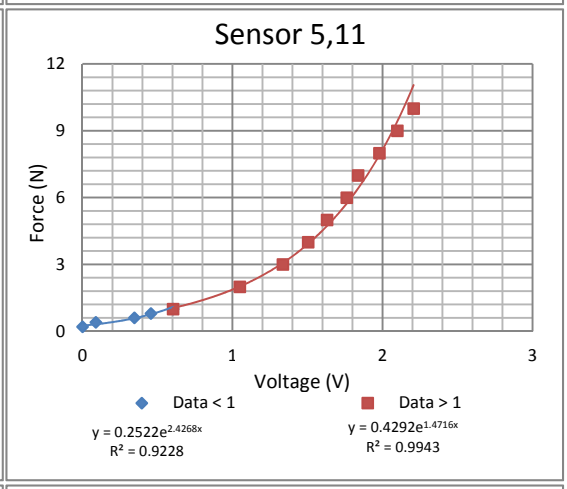
Sensor 5,11
Force (N)
Voltage (V)
Data < 1
Data > 1
y = 0.2522e^2.4268x
R² = 0.9228
y = 0.4292e^1.4716x
R² = 0.9943

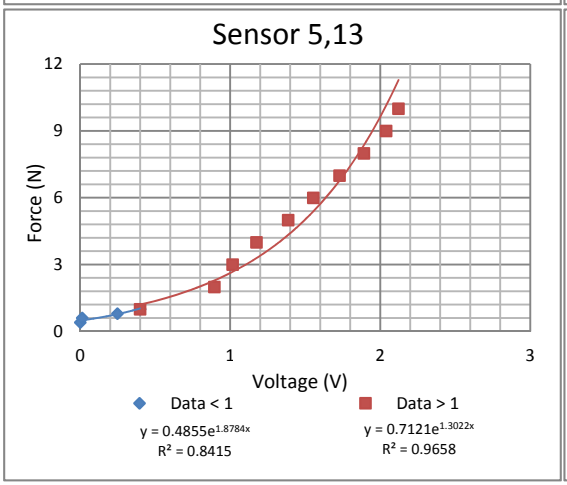
Sensor 5,13
Force (N)
Voltage (V)
Data < 1
Data > 1
y = 0.4855e^1.8784x
R² = 0.8415
y = 0.7121e^1.3022x
R² = 0.9658

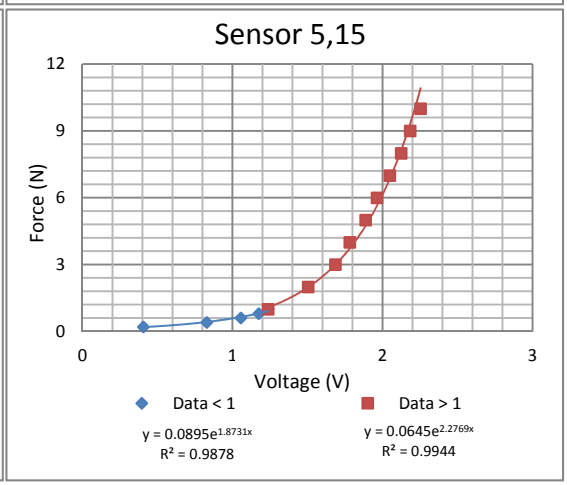
Sensor 5,15
Force (N)
Voltage (V)
Data < 1
Data > 1
y = 0.0895e^1.8731x
R² = 0.9878
y = 0.0645e^2.2769x
R² = 0.9944

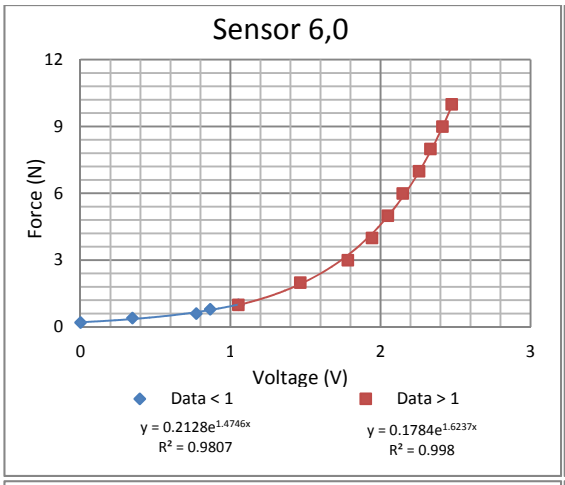
Sensor 6,0
Force (N)
Voltage (V)
Data < 1
Data > 1
y = 0.2128e^1.4746x
R² = 0.9807
y = 0.1784e^1.6237x
R² = 0.998

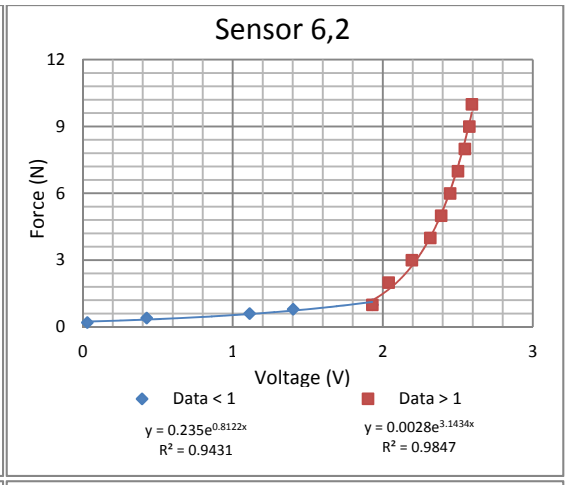
Sensor 6,2
Force (N)
Voltage (V)
Data < 1
Data > 1
y = 0.235e^0.8122x
R² = 0.9431
y = 0.0028e^3.1434x
R² = 0.9847

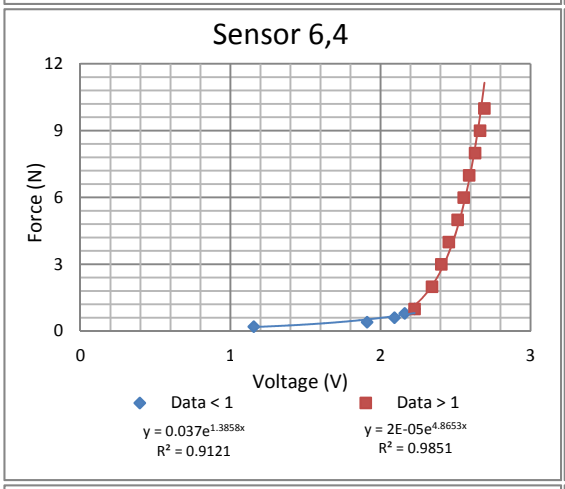
Sensor 6,4
Force (N)
Voltage (V)
Data < 1
Data > 1
y = 0.037e^1.3858x
R² = 0.9121
y = 2E-05e^4.8653x
R² = 0.9851

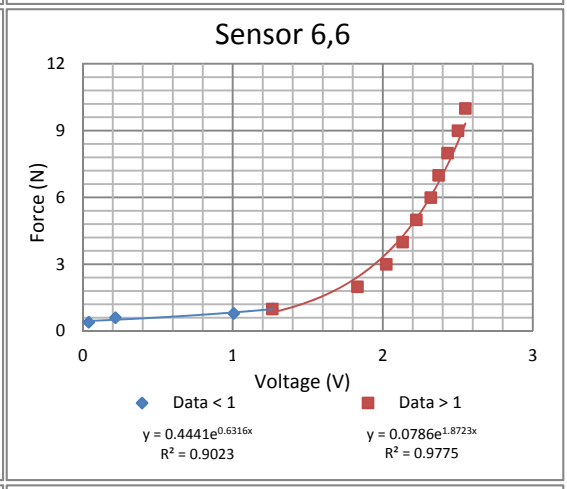
Sensor 6,6
Force (N)
Voltage (V)
Data < 1
Data > 1
y = 0.4441e^0.6316x
R² = 0.9023
y = 0.0786e^1.8723x
R² = 0.9775

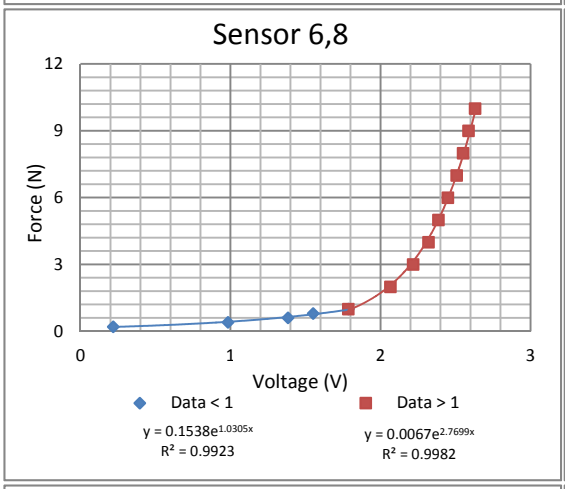
Sensor 6,8
Force (N)
Voltage (V)
Data < 1
Data > 1
y = 0.1538e^1.0305x
R² = 0.9923
y = 0.0067e^2.7699x
R² = 0.9982

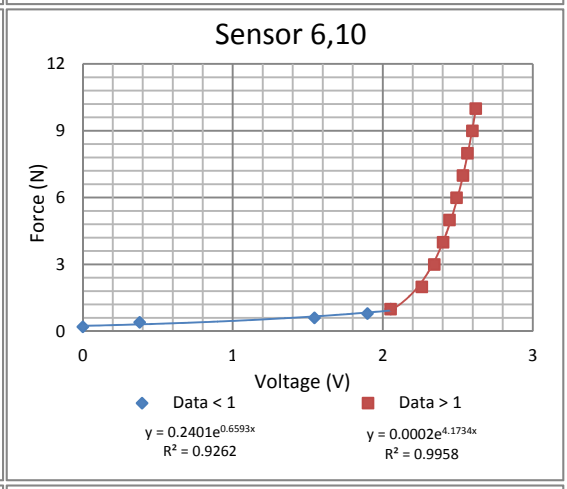
Sensor 6,10
Force (N)
Voltage (V)
Data < 1
Data > 1
y = 0.2401e^0.6593x
R² = 0.9262
y = 0.0002e^4.1734x
R² = 0.9958

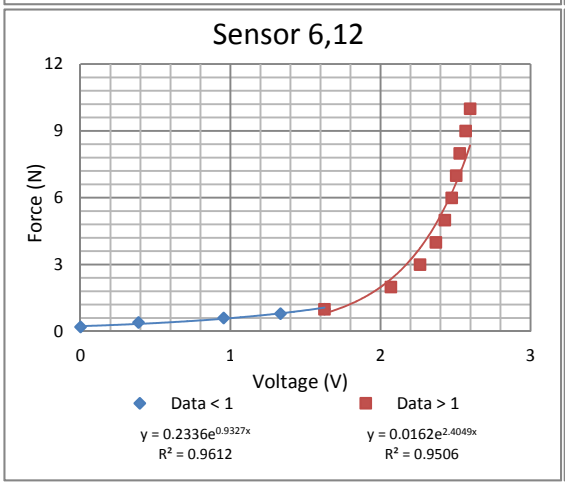
Sensor 6,12
Force (N)
Voltage (V)
Data < 1
Data > 1
y = 0.2336e^0.9327x
R² = 0.9612
y = 0.0162e^2.4049x
R² = 0.9506

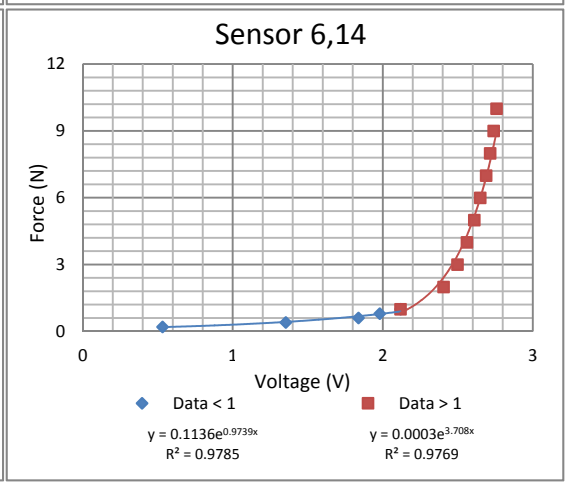
Sensor 6,14
Force (N)
Voltage (V)
Data < 1
Data > 1
y = 0.1136e^0.9739x
R² = 0.9785
y = 0.0003e^3.708x
R² = 0.9769

Appendix E

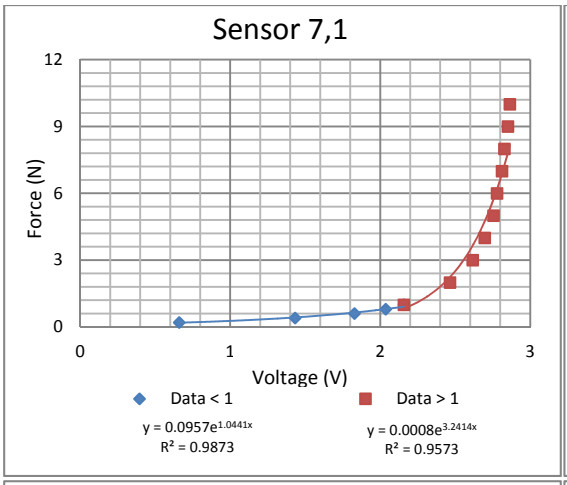
Sensor 7,1
Force (N)
Voltage (V)
Data < 1
Data > 1
y = 0.0957e^1.0441x
R² = 0.9873
y = 0.0008e^3.2414x
R² = 0.9573

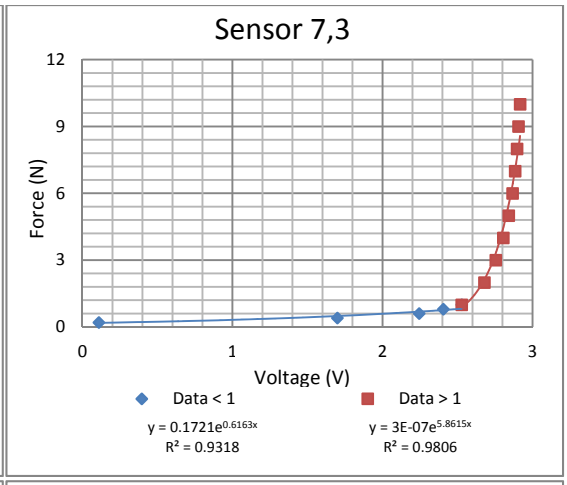
Sensor 7,3
Force (N)
Voltage (V)
Data < 1
Data > 1
y = 0.1721e^0.6163x
R² = 0.9318
y = 3E-07e^5.8615x
R² = 0.9806

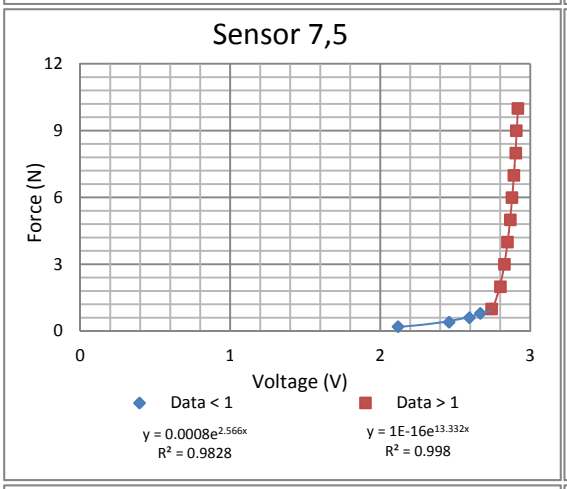
Sensor 7,5
Force (N)
Voltage (V)
Data < 1
Data > 1
y = 0.0008e^2.566x
R² = 0.9828
y = 1E-16e^13.332x
R² = 0.998

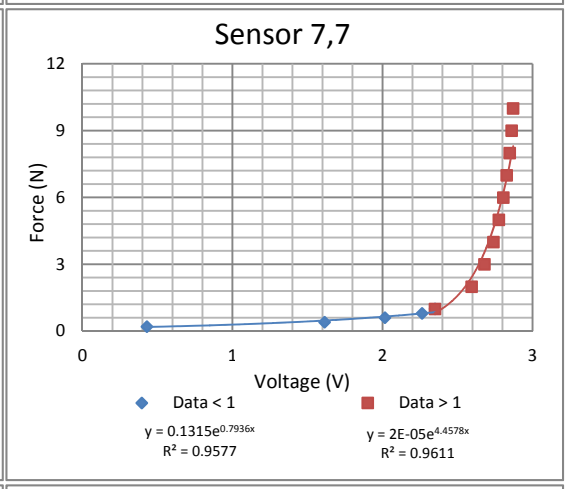
Sensor 7,7
Force (N)
Voltage (V)
Data < 1
Data > 1
y = 0.1315e^0.7936x
R² = 0.9577
y = 2E-05e^4.4578x
R² = 0.9611

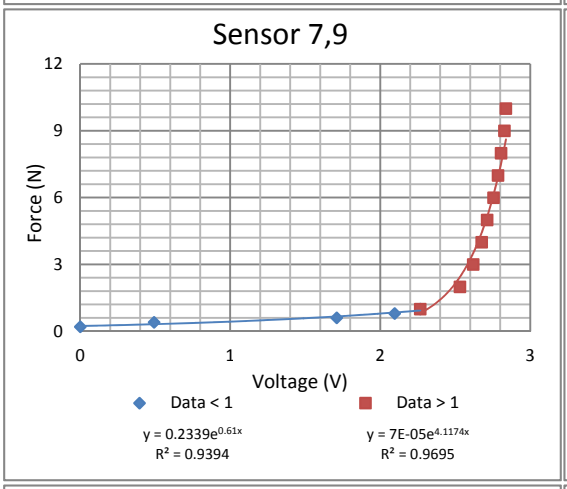
Sensor 7,9
Force (N)
Voltage (V)
Data < 1
Data > 1
y = 0.2339e^0.61x
R² = 0.9394
y = 7E-05e^4.1174x
R² = 0.9695

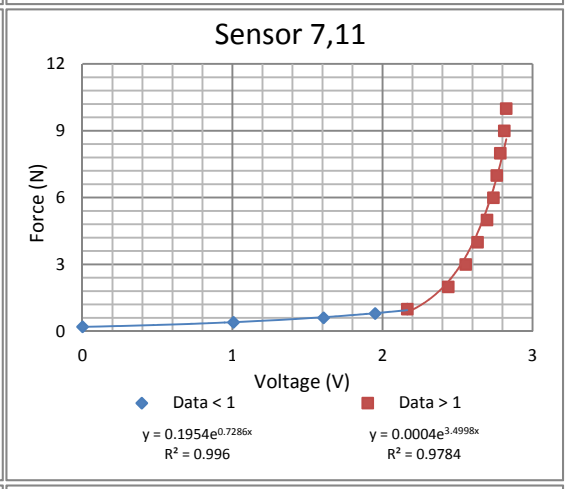
Sensor 7,11
Force (N)
Voltage (V)
Data < 1
Data > 1
y = 0.1954e^0.7286x
R² = 0.996
y = 0.0004e^3.4998x
R² = 0.9784

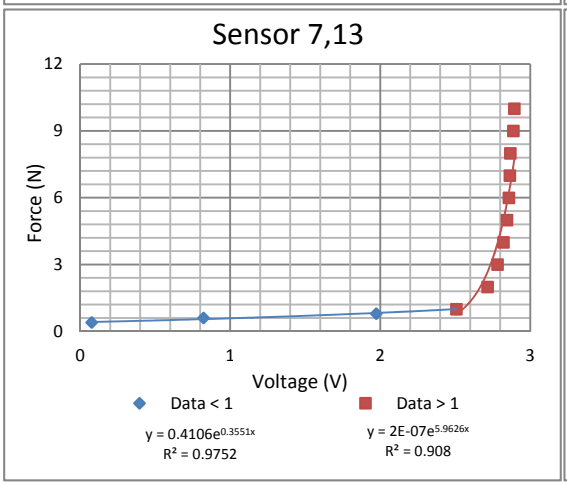
Sensor 7,13
Force (N)
Voltage (V)
Data < 1
Data > 1
y = 0.4106e^0.3551x
R² = 0.9752
y = 2E-07e^5.9626x
R² = 0.908

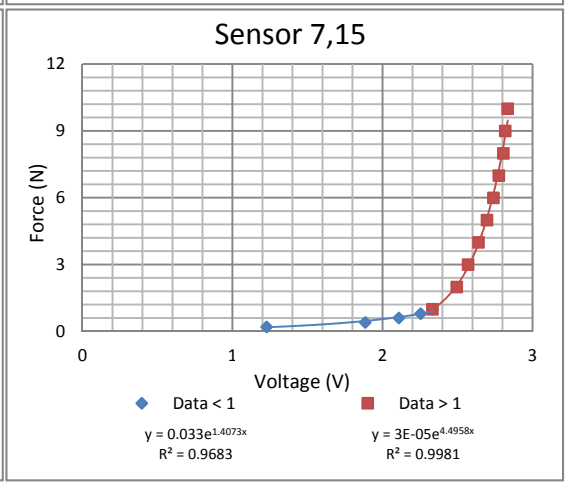
Sensor 7,15
Force (N)
Voltage (V)
Data < 1
Data > 1
y = 0.033e^1.4073x
R² = 0.9683
y = 3E-05e^4.4958x
R² = 0.9981

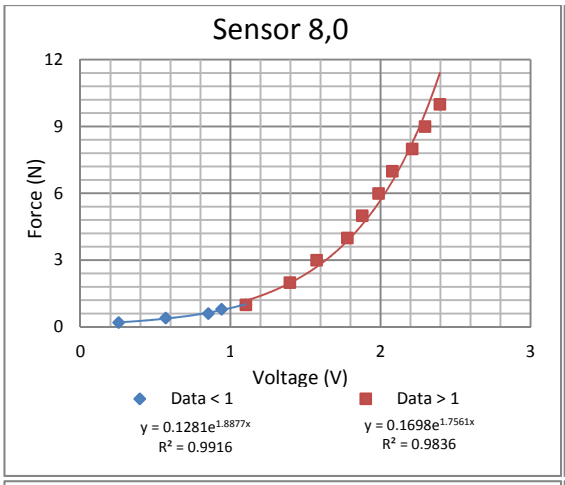
Sensor 8,0
Force (N)
Voltage (V)
Data < 1
Data > 1
y = 0.1281e^1.8877x
R² = 0.9916
y = 0.1698e^1.7561x
R² = 0.9836

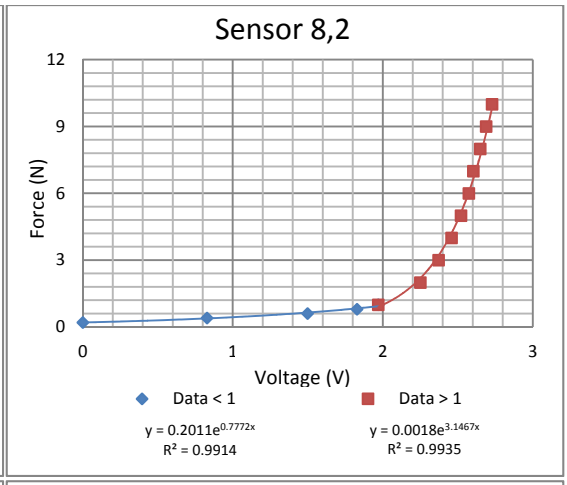
Sensor 8,2
Force (N)
Voltage (V)
Data < 1
Data > 1
y = 0.2011e^0.7772x
R² = 0.9914
y = 0.0018e^3.1467x
R² = 0.9935

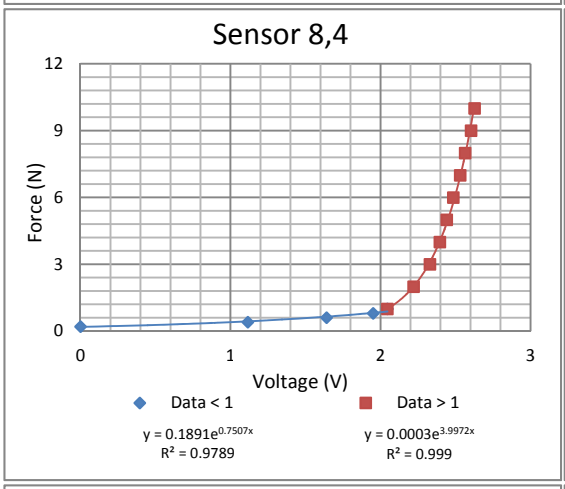
Sensor 8,4
Force (N)
Voltage (V)
Data < 1
Data > 1
y = 0.1891e^0.7507x
R² = 0.9789
y = 0.0003e^3.9972x
R² = 0.999

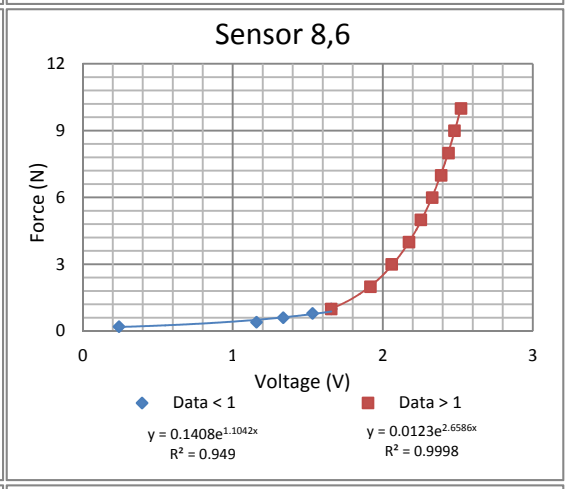
Sensor 8,6
Force (N)
Voltage (V)
Data < 1
Data > 1
y = 0.1408e^1.1042x
R² = 0.949
y = 0.0123e^2.6586x
R² = 0.9998

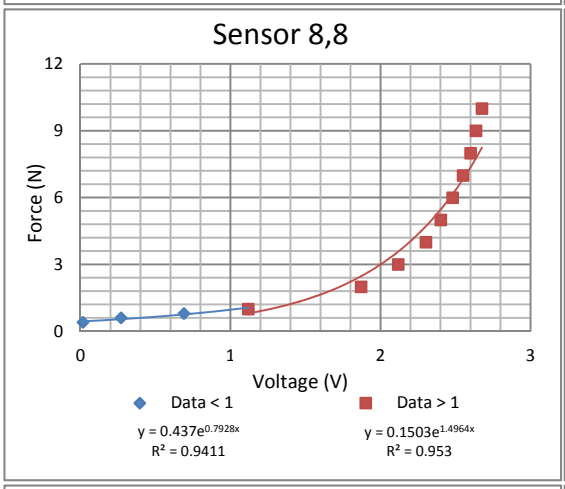
Sensor 8,8
Force (N)
Voltage (V)
Data < 1
Data > 1
y = 0.437e^0.7928x
R² = 0.9411
y = 0.1503e^1.4964x
R² = 0.953

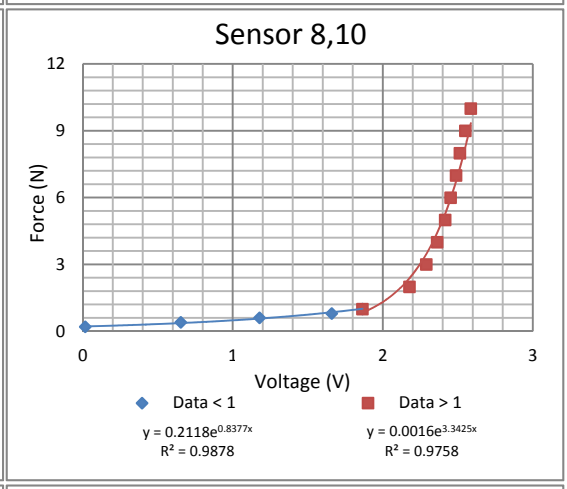
Sensor 8,10
Force (N)
Voltage (V)
Data < 1
Data > 1
y = 0.2118e^0.8377x
R² = 0.9878
y = 0.0016e^3.3425x
R² = 0.9758

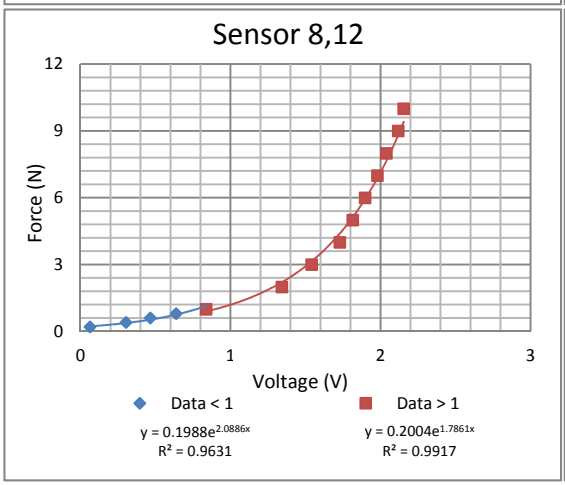
Sensor 8,12
Force (N)
Voltage (V)
Data < 1
Data > 1
y = 0.1988e^2.0886x
R² = 0.9631
y = 0.2004e^1.7861x
R² = 0.9917

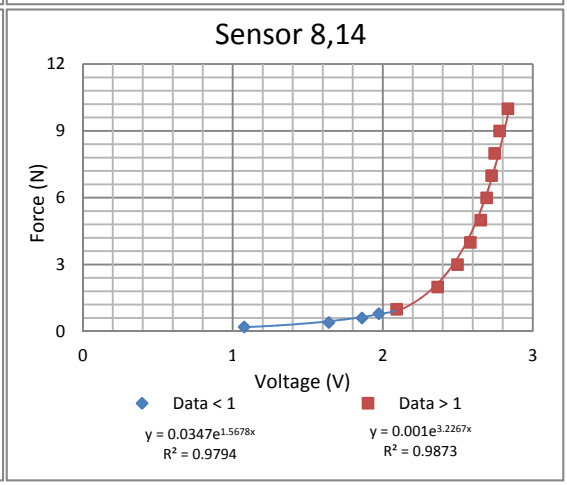
Sensor 8,14
Force (N)
Voltage (V)
Data < 1
Data > 1
y = 0.0347e^1.5678x
R² = 0.9794
y = 0.001e^3.2267x
R² = 0.9873

APPENDIX F

Controlled (Datum) Test Results

Datum Test		Lateral Wheel Width (mm)																Force (N)	Distribution (%)
No	1	0.0	4.4	8.8	13.2	17.6	22.0	26.4	30.8	35.2	39.6	44.0	48.4	52.8	57.2	61.6	66.0		
Longitudal Contact Angle (deg)	15.00	0.00	0.00	0.00	0.00	0.00	0.00	0.00	0.00	0.00	0.00	0.00	0.00	0.00	0.00	0.00	0.00	0.00	0.00
	11.25	0.89	0.79	0.70	1.16	1.61	1.69	1.76	1.69	1.62	1.56	1.51	1.20	0.90	2.03	3.16	1.58	23.84	23.17
	7.50	1.52	3.04	2.68	2.31	3.18	4.04	3.92	3.79	2.76	1.72	2.20	2.69	3.11	3.53	3.26	3.00	46.74	45.42
	3.75	1.61	1.26	0.90	1.30	1.69	1.65	1.61	1.83	2.06	1.96	1.87	1.79	1.71	1.96	2.22	1.11	26.51	25.76
	0.00	0.19	0.38	0.39	0.40	0.46	0.53	0.26	0.00	0.00	0.00	0.30	0.60	0.59	0.57	0.58	0.59	5.82	5.66
	-3.75	0.00	0.00	0.00	0.00	0.00	0.00	0.00	0.00	0.00	0.00	0.00	0.00	0.00	0.00	0.00	0.00	0.00	0.00
	-7.50	0.00	0.00	0.00	0.00	0.00	0.00	0.00	0.00	0.00	0.00	0.00	0.00	0.00	0.00	0.00	0.00	0.00	0.00
	-11.25	0.00	0.00	0.00	0.00	0.00	0.00	0.00	0.00	0.00	0.00	0.00	0.00	0.00	0.00	0.00	0.00	0.00	0.00
Force (N)		4.21	5.47	4.67	5.16	6.93	7.90	7.55	7.31	6.43	5.25	5.88	6.28	6.29	8.09	9.22	6.27	A (cm^2)	16.69
Distribution (%)		4.09	5.32	4.53	5.01	6.74	7.68	7.34	7.11	6.25	5.10	5.71	6.10	6.12	7.86	8.96	6.10	L_v (N)	1.84

Datum Test

Test Number: 01

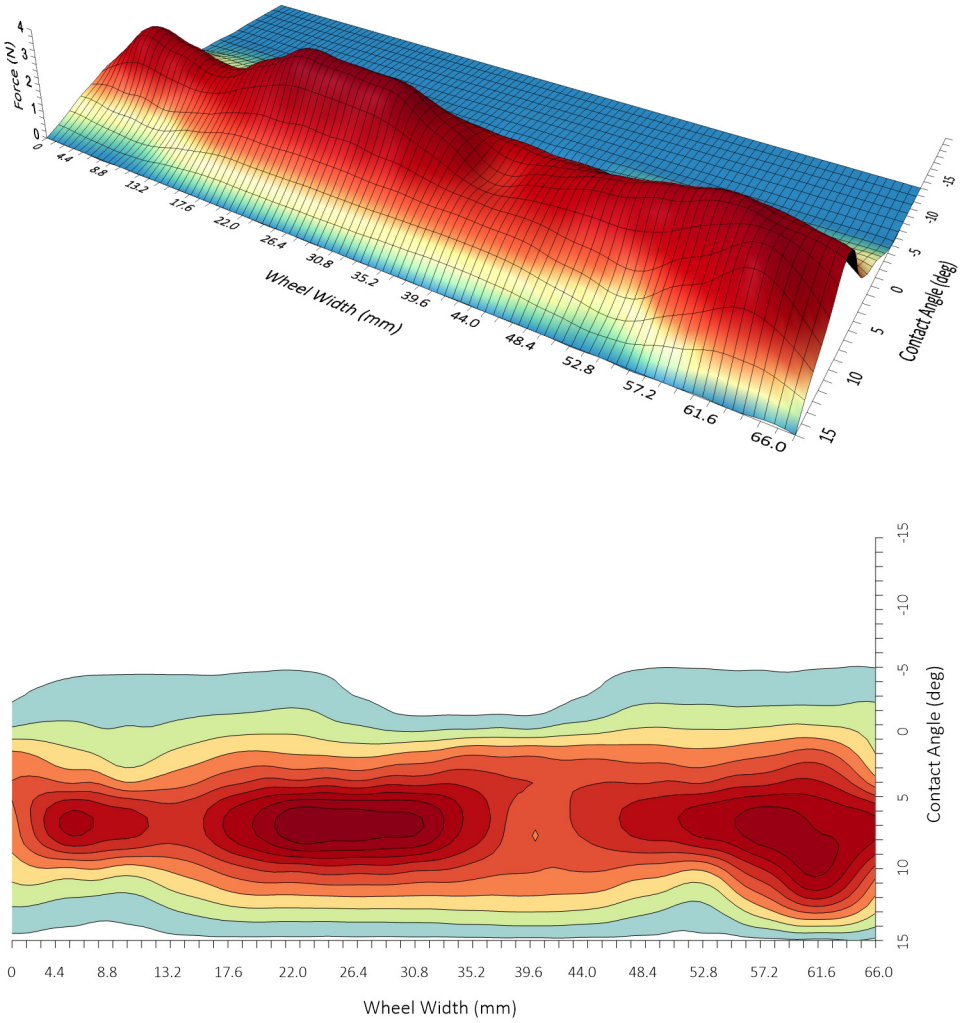

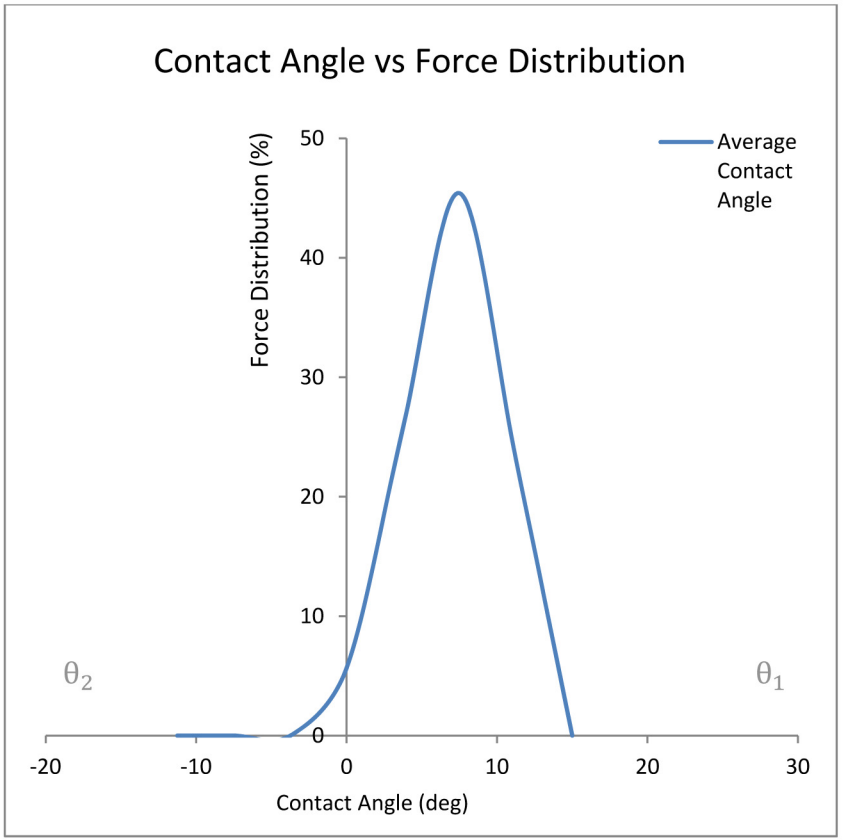

Datum Test		Lateral Wheel Width (mm)																Force (N)	Distribution (%)
No	2	0.0	4.4	8.8	13.2	17.6	22.0	26.4	30.8	35.2	39.6	44.0	48.4	52.8	57.2	61.6	66.0		
Longitudal Contact Angle (deg)	15.00	0.00	0.00	0.00	0.00	0.00	0.00	0.00	0.00	0.00	0.00	0.00	0.00	0.00	0.00	0.00	0.00	0.00	0.00
	11.25	1.76	1.30	0.84	0.42	0.00	0.70	1.39	0.95	0.50	0.65	0.80	0.40	0.00	0.15	0.29	0.15	10.28	8.93
	7.50	1.46	2.91	1.93	0.95	0.96	0.96	2.30	3.63	3.13	2.63	2.41	2.20	1.94	1.68	2.46	3.24	34.76	30.21
	3.75	1.90	2.46	3.03	3.03	3.03	3.01	2.99	3.04	3.08	3.32	3.57	3.15	2.73	3.21	3.68	1.84	47.07	40.90
	0.00	0.79	1.58	1.25	0.91	1.41	1.91	1.65	1.39	1.11	0.82	0.99	1.15	1.57	1.99	1.98	1.96	22.45	19.51
	-3.75	0.00	0.00	0.00	0.00	0.00	0.00	0.00	0.09	0.18	0.09	0.00	0.00	0.00	0.00	0.00	0.00	0.36	0.32
	-7.50	0.00	0.00	0.00	0.00	0.04	0.08	0.04	0.00	0.00	0.00	0.00	0.00	0.00	0.00	0.00	0.00	0.15	0.13
	-11.25	0.00	0.00	0.00	0.00	0.00	0.00	0.00	0.00	0.00	0.00	0.00	0.00	0.00	0.00	0.00	0.00	0.00	0.00
Force (N)		5.90	8.25	7.04	5.31	5.44	6.65	8.37	9.10	8.00	7.51	7.77	6.90	6.24	7.03	8.41	7.18	A (cm^2)	18.60
Distribution (%)		5.13	7.17	6.11	4.61	4.72	5.78	7.27	7.91	6.95	6.53	6.75	6.00	5.43	6.11	7.30	6.24	L_v (N)	2.27

Datum Test

Test Number: 02

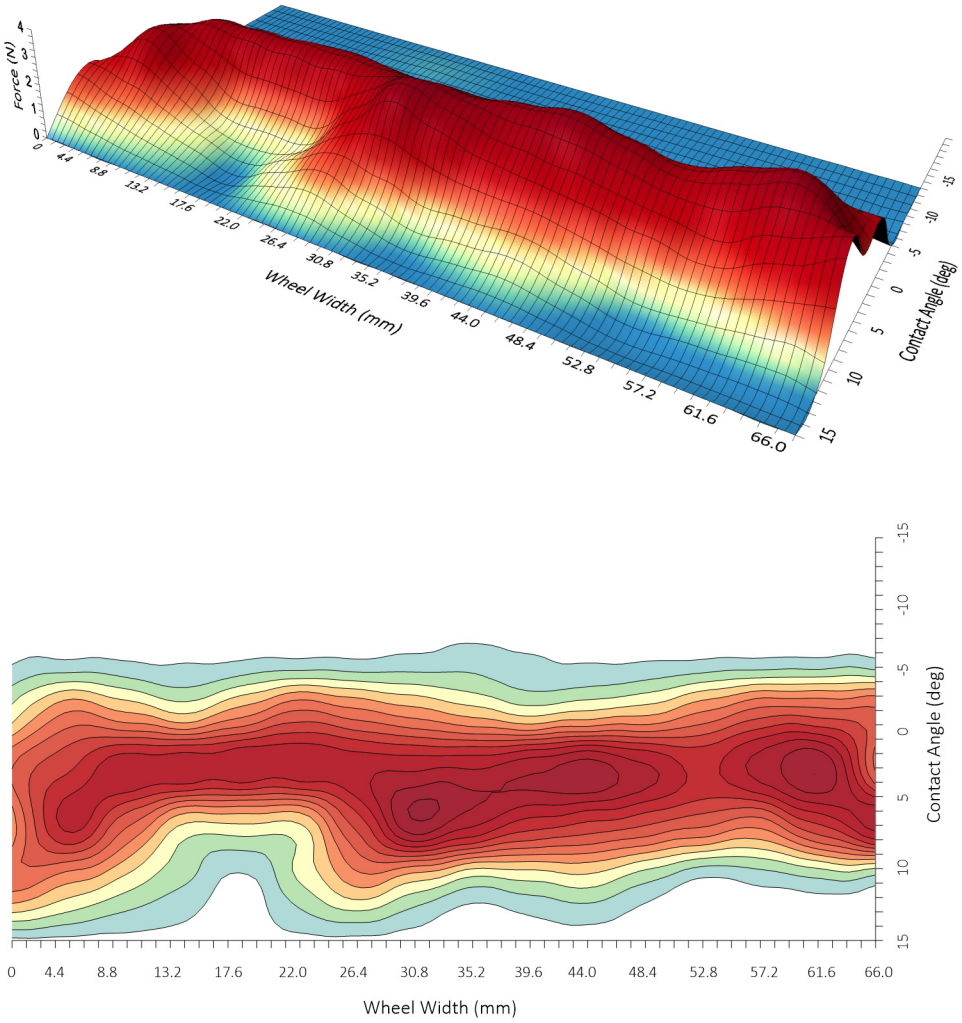

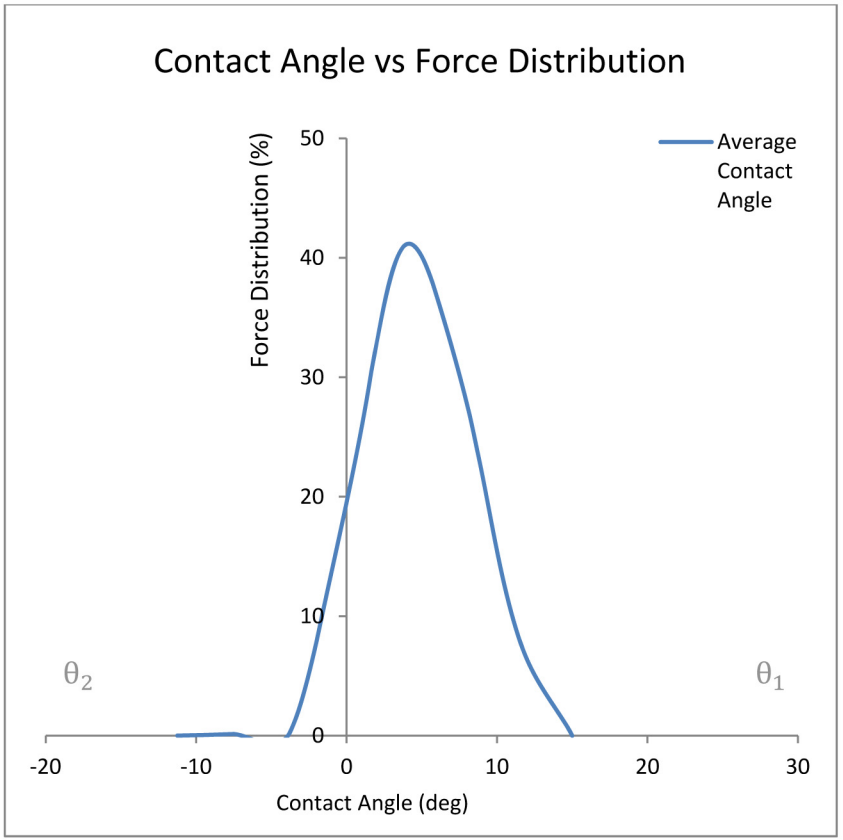

Datum Test		Lateral Wheel Width (mm)																Force (N)	Distribution (%)
No	3	0.0	4.4	8.8	13.2	17.6	22.0	26.4	30.8	35.2	39.6	44.0	48.4	52.8	57.2	61.6	66.0		
Longitudal Contact Angle (deg)	15.00	0.00	0.00	0.00	0.00	0.00	0.00	0.00	0.00	0.00	0.00	0.00	0.00	0.00	0.00	0.00	0.00	0.00	0.00
	11.25	0.48	0.62	0.76	0.74	0.73	1.08	1.44	1.06	0.68	0.65	0.62	0.75	0.87	0.57	0.27	0.14	11.44	18.75
	7.50	0.00	0.00	0.94	1.89	1.56	1.24	0.96	0.68	0.83	0.98	0.82	0.65	0.74	0.84	0.77	0.70	13.60	22.28
	3.75	3.14	2.54	1.95	1.51	1.08	1.35	1.62	0.81	0.00	0.38	0.77	0.85	0.93	0.77	0.62	0.31	18.63	30.53
	0.00	0.97	1.95	1.56	1.16	1.09	1.01	0.72	0.43	0.71	1.00	1.50	1.99	1.34	0.68	0.64	0.60	17.35	28.44
	-3.75	0.00	0.00	0.00	0.00	0.00	0.00	0.00	0.00	0.00	0.00	0.00	0.00	0.00	0.00	0.00	0.00	0.00	0.00
	-7.50	0.00	0.00	0.00	0.00	0.00	0.00	0.00	0.00	0.00	0.00	0.00	0.00	0.00	0.00	0.00	0.00	0.00	0.00
	-11.25	0.00	0.00	0.00	0.00	0.00	0.00	0.00	0.00	0.00	0.00	0.00	0.00	0.00	0.00	0.00	0.00	0.00	0.00
Force (N)		4.59	5.11	5.21	5.30	4.45	4.68	4.74	2.97	2.22	3.02	3.70	4.23	3.88	2.87	2.30	1.74	A (cm^2)	17.51
Distribution (%)		7.52	8.37	8.53	8.69	7.30	7.68	7.77	4.87	3.64	4.94	6.07	6.94	6.35	4.70	3.77	2.86	L_v (N)	2.02

Datum Test

Test Number: 03

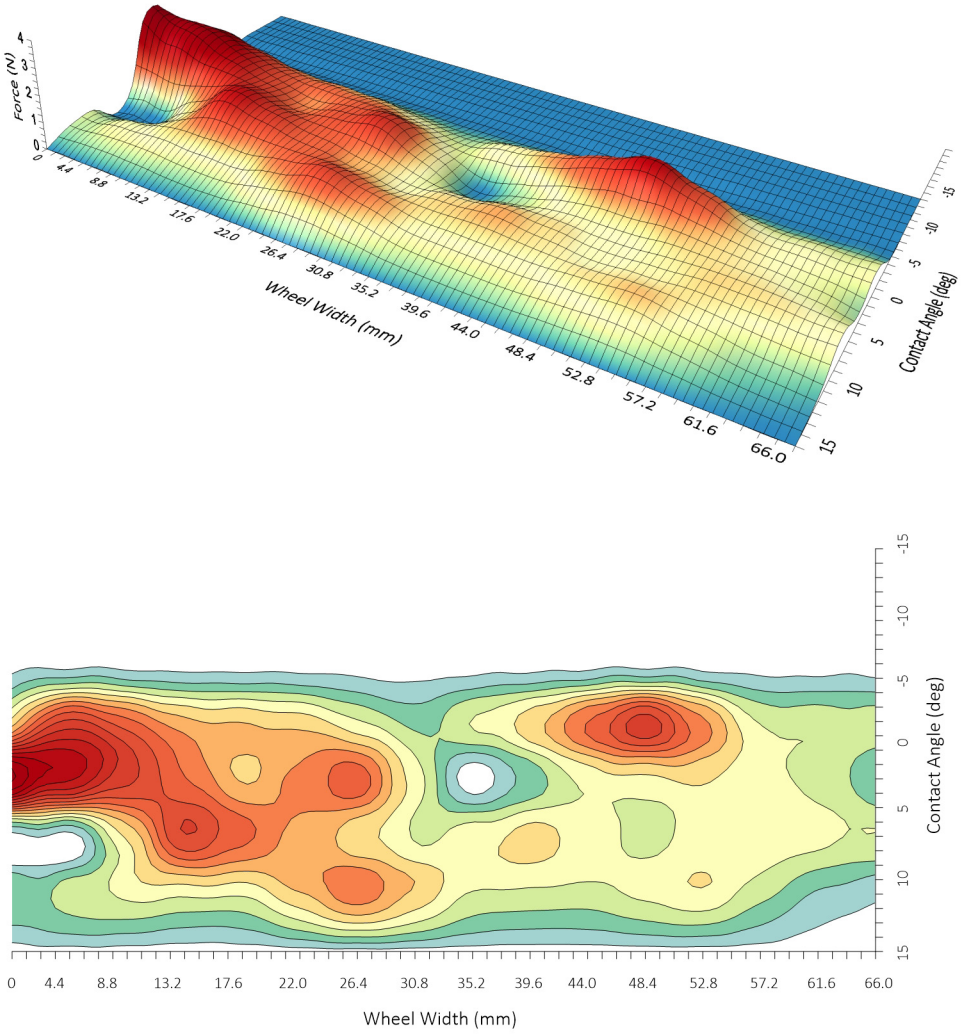

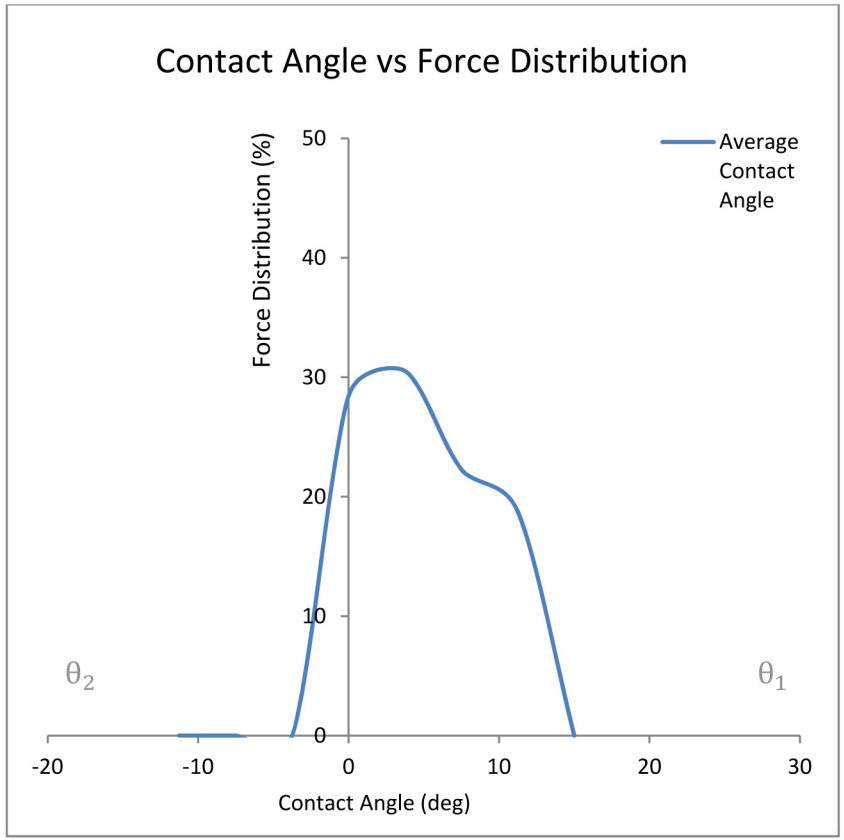

Appendix F

Datum Test		Lateral Wheel Width (mm)																Force (N)	Distribution (%)
No	4	0.0	4.4	8.8	13.2	17.6	22.0	26.4	30.8	35.2	39.6	44.0	48.4	52.8	57.2	61.6	66.0		
Longitudal Contact Angle (deg)	15.00	0.00	0.00	0.00	0.00	0.00	0.00	0.00	0.00	0.00	0.00	0.00	0.00	0.00	0.00	0.00	0.00	0.00	0.00
	11.25	0.68	0.56	0.45	0.51	0.58	0.63	0.69	0.67	0.65	0.45	0.25	0.25	0.25	0.16	0.08	0.04	6.88	7.26
	7.50	2.23	4.47	2.81	1.16	1.35	1.54	1.33	1.11	1.31	1.51	1.20	0.88	0.80	0.72	0.63	0.54	23.57	24.86
	3.75	4.44	3.93	3.42	2.95	2.48	2.64	2.81	2.54	2.28	1.97	1.65	1.62	1.59	1.57	1.55	0.77	38.19	40.27
	0.00	1.03	2.06	2.04	2.02	1.92	1.82	2.14	2.46	2.28	2.09	1.45	0.80	0.71	0.62	0.76	0.90	25.08	26.44
	-3.75	0.47	0.24	0.00	0.00	0.00	0.00	0.00	0.10	0.20	0.10	0.00	0.00	0.00	0.00	0.00	0.00	1.11	1.17
	-7.50	0.00	0.00	0.00	0.00	0.00	0.00	0.00	0.00	0.00	0.00	0.00	0.00	0.00	0.00	0.00	0.00	0.00	0.00
	-11.25	0.00	0.00	0.00	0.00	0.00	0.00	0.00	0.00	0.00	0.00	0.00	0.00	0.00	0.00	0.00	0.00	0.00	0.00
Force (N)		8.86	11.25	8.71	6.63	6.32	6.63	6.96	6.88	6.72	6.12	4.54	3.54	3.34	3.07	3.01	2.25	A (cm^2)	18.88
Distribution (%)		9.34	11.86	9.19	6.99	6.66	6.99	7.34	7.26	7.08	6.45	4.79	3.74	3.52	3.23	3.18	2.38	L_v (N)	2.88

Datum Test

Test Number: 04

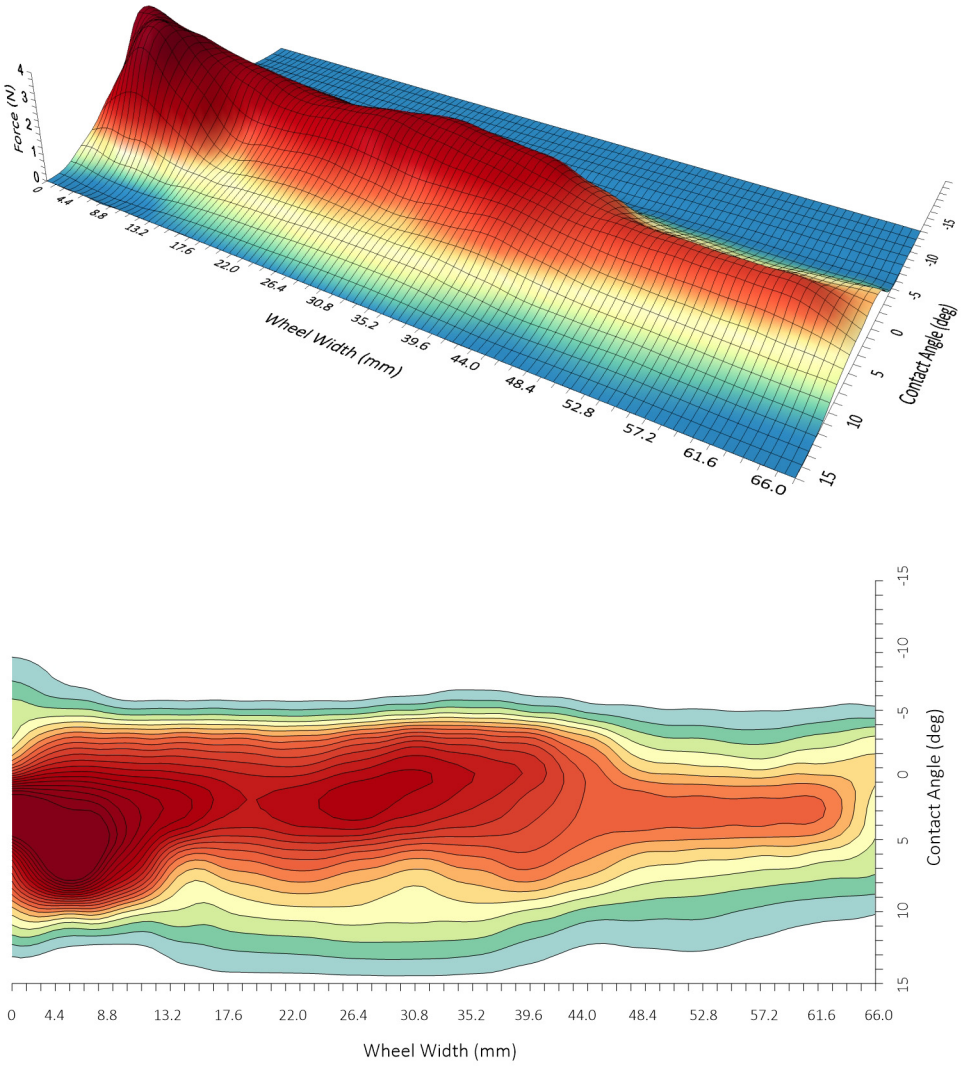

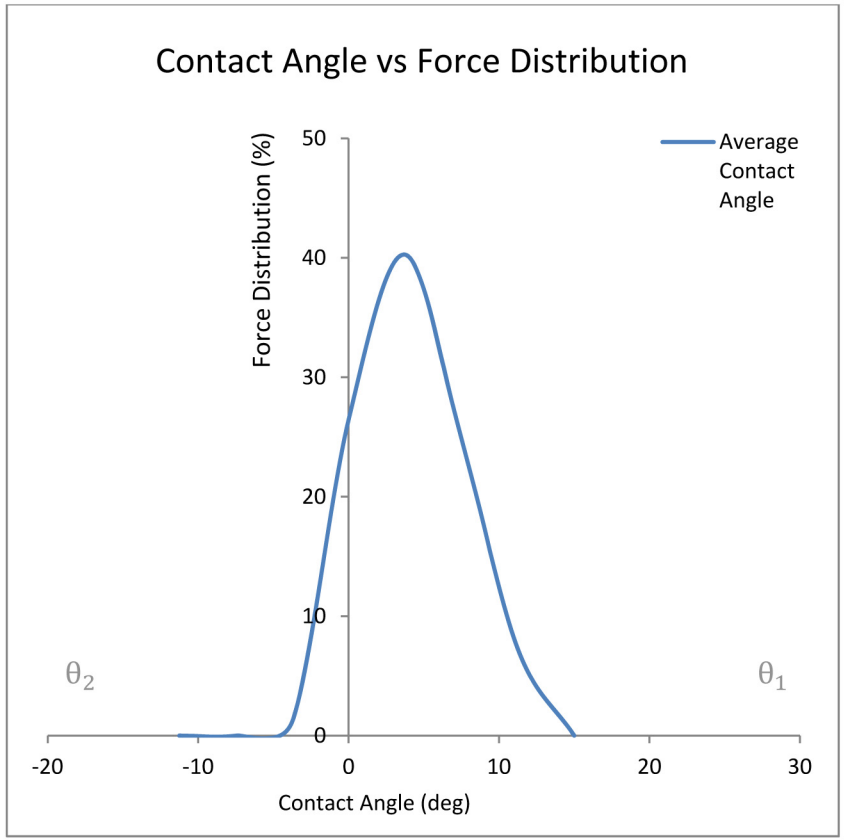

Datum Test		Lateral Wheel Width (mm)																Force (N)	Distribution (%)
No	5	0.0	4.4	8.8	13.2	17.6	22.0	26.4	30.8	35.2	39.6	44.0	48.4	52.8	57.2	61.6	66.0		
Longitudal Contact Angle (deg)	15.00	0.00	0.00	0.00	0.00	0.00	0.00	0.00	0.00	0.00	0.00	0.00	0.00	0.00	0.00	0.00	0.00	0.00	0.00
	11.25	1.37	1.14	0.91	0.94	0.96	0.99	1.02	0.86	0.71	0.69	0.66	0.75	0.84	0.80	0.75	0.38	13.77	26.88
	7.50	0.71	1.42	1.20	0.99	1.28	1.57	1.83	2.09	1.49	0.89	1.17	1.44	1.20	0.96	0.84	0.73	19.79	38.64
	3.75	1.03	0.98	0.93	0.78	0.63	0.73	0.84	0.77	0.71	0.35	0.00	0.32	0.64	0.60	0.55	0.28	10.14	19.81
	0.00	0.36	0.71	0.67	0.64	0.59	0.55	0.53	0.52	0.48	0.44	0.39	0.33	0.27	0.21	0.35	0.48	7.51	14.67
	-3.75	0.00	0.00	0.00	0.00	0.00	0.00	0.00	0.00	0.00	0.00	0.00	0.00	0.00	0.00	0.00	0.00	0.00	0.00
	-7.50	0.00	0.00	0.00	0.00	0.00	0.00	0.00	0.00	0.00	0.00	0.00	0.00	0.00	0.00	0.00	0.00	0.00	0.00
	-11.25	0.00	0.00	0.00	0.00	0.00	0.00	0.00	0.00	0.00	0.00	0.00	0.00	0.00	0.00	0.00	0.00	0.00	0.00
Force (N)		3.47	4.25	3.72	3.34	3.46	3.84	4.22	4.24	3.39	2.37	2.22	2.84	2.95	2.56	2.49	1.86	A (cm^2)	17.51
Distribution (%)		6.77	8.30	7.26	6.52	6.76	7.50	8.23	8.29	6.61	4.63	4.33	5.55	5.77	5.00	4.86	3.63	L_v (N)	1.01

Datum Test

Test Number: 05

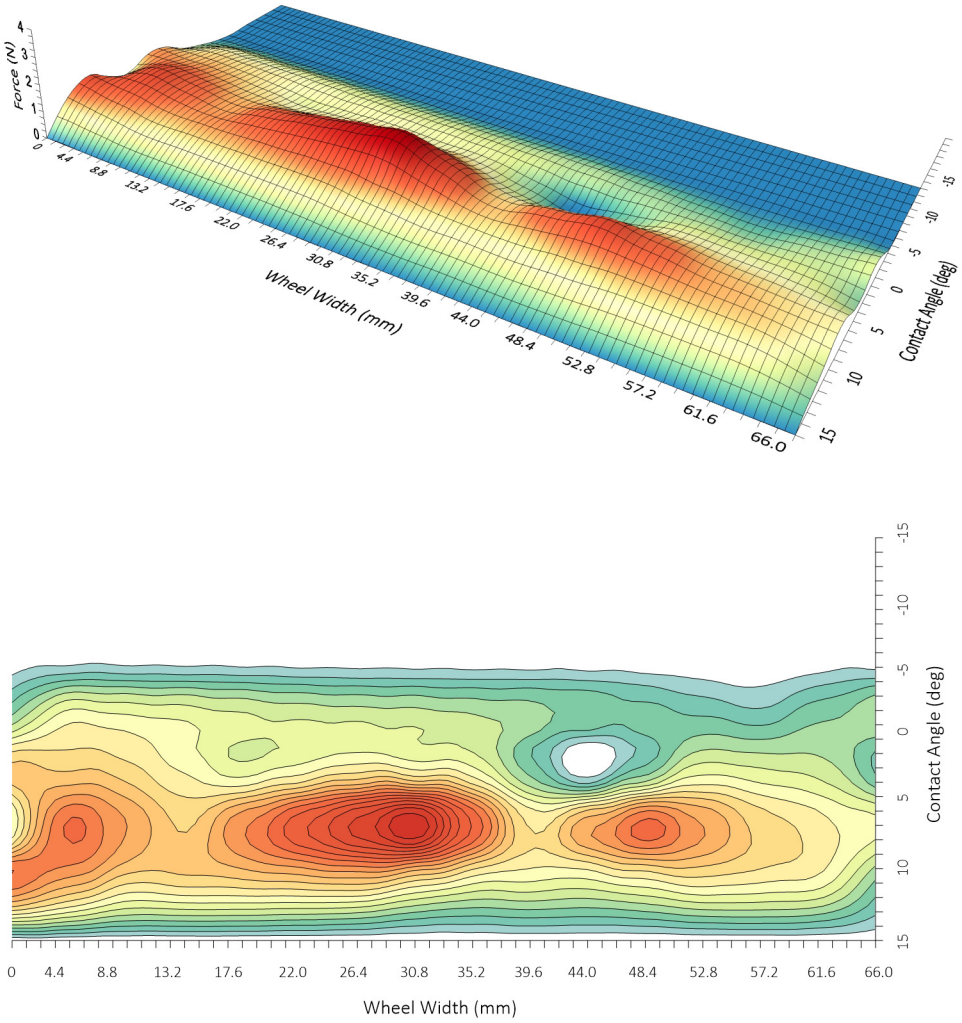

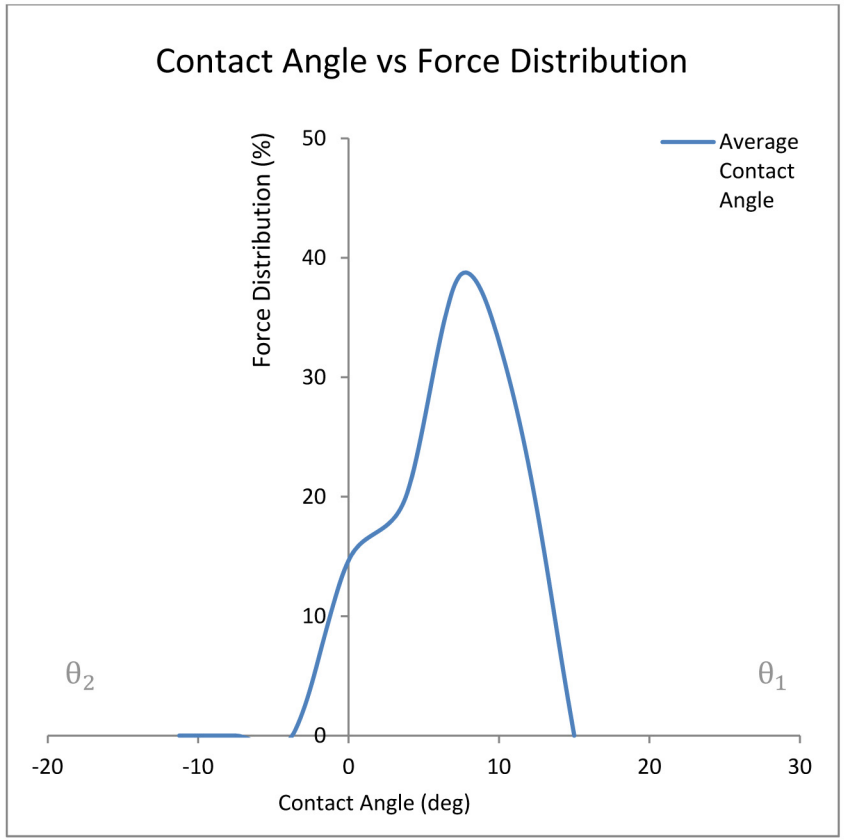

Appendix F

Datum Test		Lateral Wheel Width (mm)																Force (N)	Distribution (%)
No	Ave	0.0	4.4	8.8	13.2	17.6	22.0	26.4	30.8	35.2	39.6	44.0	48.4	52.8	57.2	61.6	66.0		
Longitudal Contact Angle (deg)	15.00	0.00	0.00	0.00	0.00	0.00	0.00	0.00	0.00	0.00	0.00	0.00	0.00	0.00	0.00	0.00	0.00	0.00	0.00
	11.25	0.64	0.56	0.46	0.46	0.48	0.54	0.60	0.53	0.45	0.42	0.41	0.39	0.38	0.47	0.58	0.33	7.69	10.11
	7.50	0.88	1.43	1.25	1.10	1.15	1.22	1.35	1.46	1.36	1.29	1.28	1.28	1.28	1.42	1.62	1.27	20.64	27.12
	3.75	1.77	1.79	1.52	1.40	1.40	1.45	1.53	1.63	1.69	1.70	1.58	1.46	1.81	2.23	2.12	1.27	26.35	34.62
	0.00	0.65	1.08	0.98	0.90	0.93	0.98	1.05	1.05	0.96	0.94	1.04	1.11	1.21	1.36	1.36	1.01	16.60	21.81
	-3.75	0.20	0.21	0.17	0.15	0.14	0.21	0.31	0.32	0.31	0.29	0.25	0.26	0.28	0.32	0.35	0.28	4.05	5.32
	-7.50	0.01	0.03	0.01	0.00	0.03	0.06	0.06	0.05	0.04	0.03	0.04	0.05	0.09	0.12	0.09	0.05	0.78	1.03
	-11.25	0.00	0.00	0.00	0.00	0.00	0.00	0.00	0.00	0.00	0.00	0.00	0.00	0.00	0.00	0.00	0.00	0.00	0.00
Force (N)		4.16	5.10	4.39	4.03	4.13	4.46	4.88	5.05	4.81	4.68	4.60	4.55	5.05	5.93	6.10	4.21	A (cm^2)	26.27
Distribution (%)		5.46	6.71	5.77	5.29	5.42	5.85	6.41	6.63	6.32	6.14	6.04	5.97	6.63	7.79	8.02	5.53	L_v (N)	0.75

Datum Test

Test Number: Averages

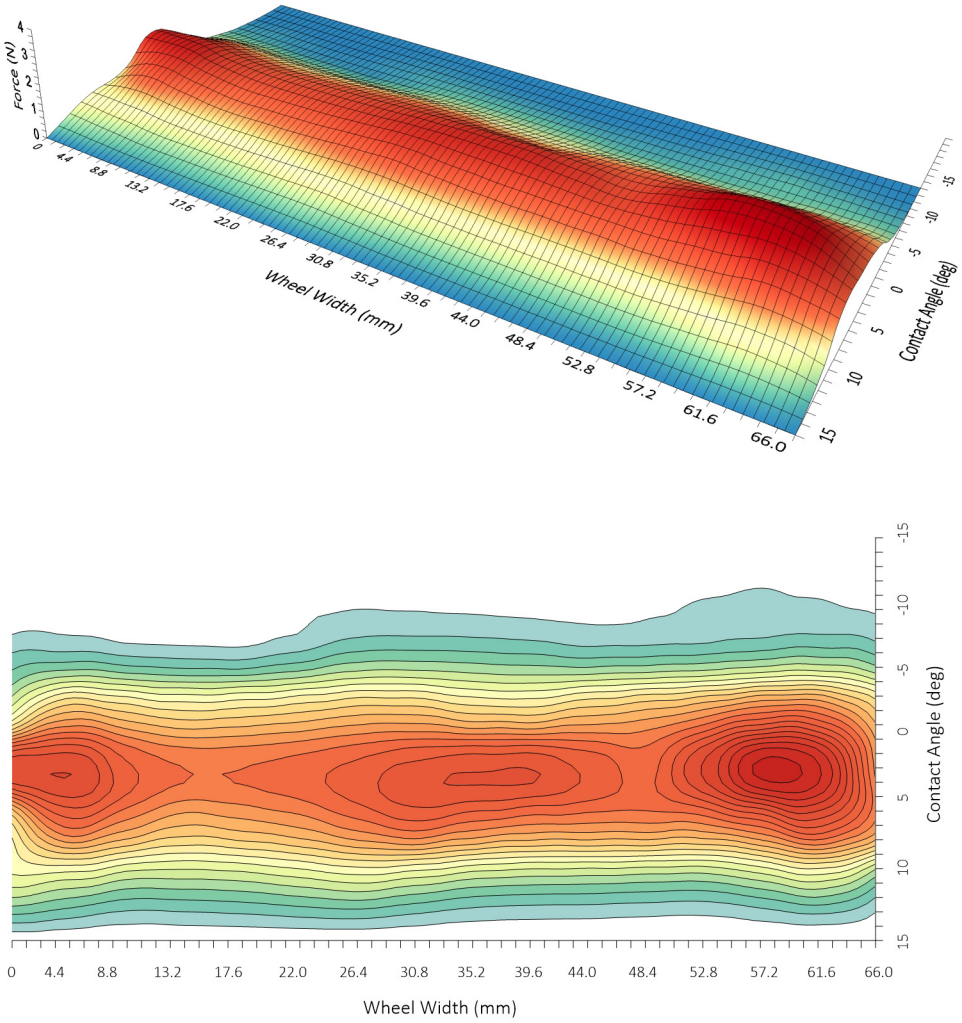

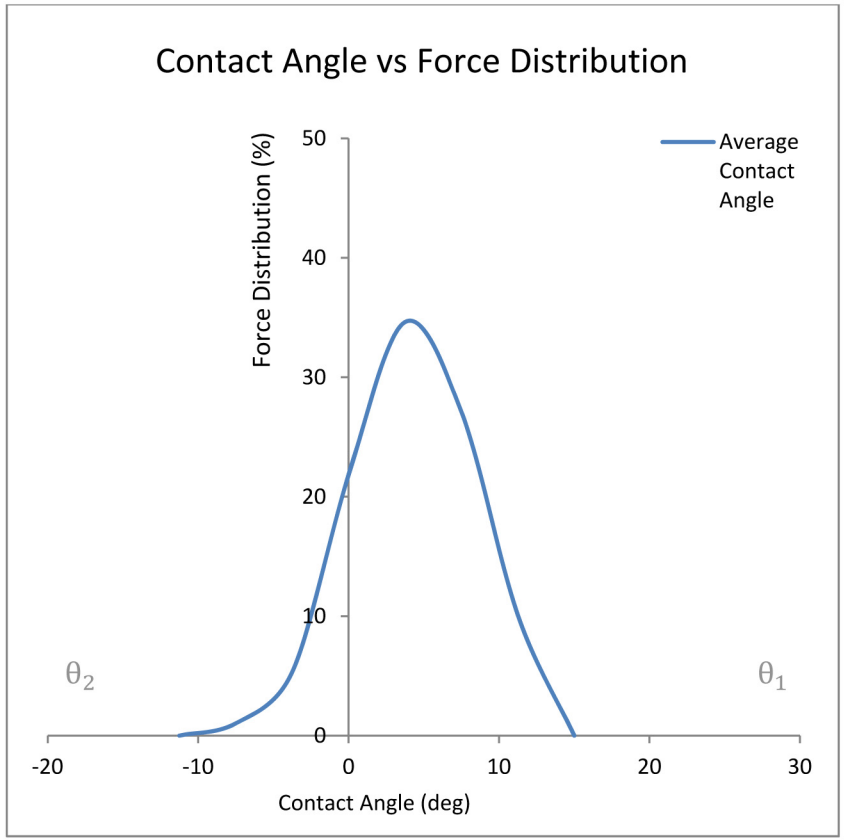

APPENDIX G

2-5mm Gravel Results

2-5mm Gravel		Lateral Wheel Width (mm)																Force (N)	Distribution (%)
No	1	0.0	4.4	8.8	13.2	17.6	22.0	26.4	30.8	35.2	39.6	44.0	48.4	52.8	57.2	61.6	66.0		
Longitudal Contact Angle (deg)	15.00	0.00	0.00	0.00	0.00	0.00	0.00	0.00	0.00	0.00	0.00	0.00	0.00	0.00	0.00	0.00	0.00	0.00	0.00
	11.25	0.08	0.09	0.09	0.05	0.00	0.00	0.00	0.00	0.00	0.00	0.00	0.00	0.00	0.00	0.00	0.00	0.30	1.23
	7.50	0.10	0.20	0.10	0.00	0.00	0.00	0.00	0.00	0.00	0.00	0.00	0.00	0.00	0.00	0.00	0.00	0.41	1.66
	3.75	2.12	1.06	0.00	0.00	0.00	0.00	0.00	0.00	0.00	0.00	0.00	0.40	0.80	0.40	0.00	0.00	4.78	19.46
	0.00	0.00	0.00	1.01	2.01	1.01	0.00	0.00	0.00	0.00	0.00	0.00	0.00	0.34	0.68	0.34	0.00	5.38	21.91
	-3.75	0.55	0.70	0.86	0.69	0.53	0.27	0.00	0.12	0.23	0.24	0.25	0.53	0.82	0.46	0.11	0.05	6.40	26.07
	-7.50	0.41	0.82	0.49	0.16	0.08	0.00	0.10	0.20	0.48	0.77	0.39	0.00	0.10	0.19	0.10	0.00	4.27	17.38
	-11.25	0.79	0.79	0.79	0.39	0.00	0.00	0.00	0.00	0.00	0.00	0.00	0.00	0.00	0.00	0.00	0.00	2.75	11.20
	-15.00	0.07	0.13	0.07	0.00	0.00	0.00	0.00	0.00	0.00	0.00	0.00	0.00	0.00	0.00	0.00	0.00	0.27	1.09
	-18.75	0.00	0.00	0.00	0.00	0.00	0.00	0.00	0.00	0.00	0.00	0.00	0.00	0.00	0.00	0.00	0.00	0.00	0.00
	-22.50	0.00	0.00	0.00	0.00	0.00	0.00	0.00	0.00	0.00	0.00	0.00	0.00	0.00	0.00	0.00	0.00	0.00	0.00
Force (N)		4.11	3.79	3.40	3.30	1.61	0.27	0.10	0.31	0.72	1.01	0.63	0.93	2.05	1.73	0.54	0.05	A (cm^2)	17.24
Distribution (%)		16.72	15.43	13.85	13.45	6.57	1.08	0.39	1.27	2.92	4.12	2.58	3.79	8.35	7.05	2.20	0.22	L_v (N)	2.09

2 - 5mm Test

Test Number: 01

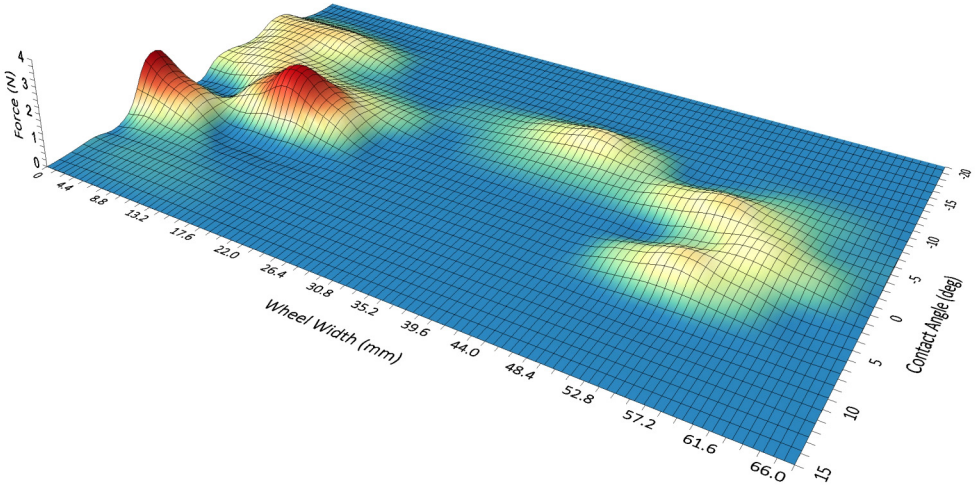

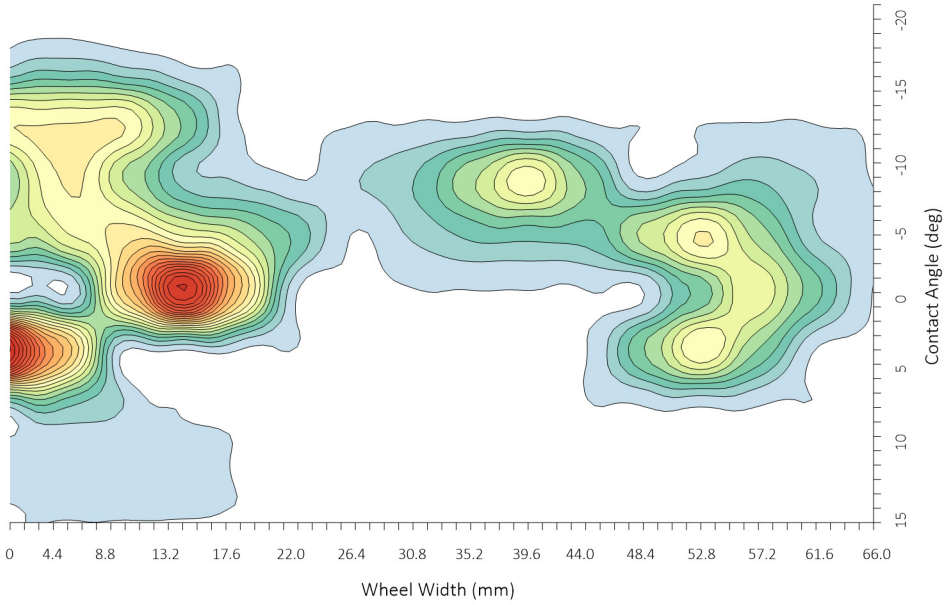

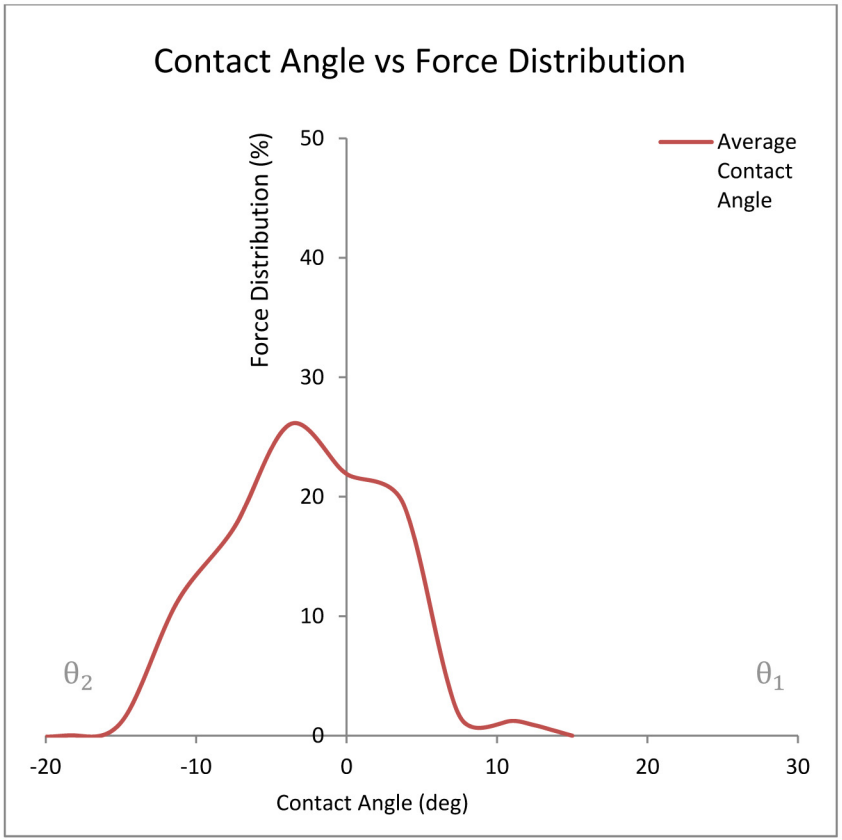

2-5mm Gravel		Lateral Wheel Width (mm)																Force (N)	Distribution (%)
No	2	0.0	4.4	8.8	13.2	17.6	22.0	26.4	30.8	35.2	39.6	44.0	48.4	52.8	57.2	61.6	66.0		
Longitudal Contact Angle (deg)	15.00	0.00	0.00	0.00	0.00	0.00	0.00	0.00	0.00	0.00	0.00	0.00	0.00	0.00	0.00	0.00	0.00	0.00	0.00
	11.25	0.88	1.76	0.88	0.00	0.00	0.00	0.69	1.37	1.24	1.10	0.84	0.57	0.96	1.34	0.67	0.00	12.28	19.73
	7.50	0.46	1.31	2.17	1.08	0.00	0.56	1.11	0.92	0.73	0.36	0.00	0.00	0.00	0.00	0.00	0.00	8.69	13.97
	3.75	2.69	5.37	4.54	3.70	2.32	0.94	1.25	1.57	1.48	1.38	0.69	0.00	1.25	2.50	1.25	0.00	30.91	49.66
	0.00	0.55	0.64	0.72	0.36	0.00	0.23	0.46	0.23	0.00	0.61	1.22	0.61	0.00	0.13	0.26	0.13	6.16	9.90
	-3.75	0.16	0.31	0.89	1.46	0.78	0.09	0.05	0.00	0.00	0.00	0.00	0.00	0.00	0.00	0.16	0.31	4.20	6.74
	-7.50	0.00	0.00	0.00	0.00	0.00	0.00	0.00	0.00	0.00	0.00	0.00	0.00	0.00	0.00	0.00	0.00	0.00	0.00
	-11.25	0.00	0.00	0.00	0.00	0.00	0.00	0.00	0.00	0.00	0.00	0.00	0.00	0.00	0.00	0.00	0.00	0.00	0.00
	-15.00	0.00	0.00	0.00	0.00	0.00	0.00	0.00	0.00	0.00	0.00	0.00	0.00	0.00	0.00	0.00	0.00	0.00	0.00
	-18.75	0.00	0.00	0.00	0.00	0.00	0.00	0.00	0.00	0.00	0.00	0.00	0.00	0.00	0.00	0.00	0.00	0.00	0.00
	-22.50	0.00	0.00	0.00	0.00	0.00	0.00	0.00	0.00	0.00	0.00	0.00	0.00	0.00	0.00	0.00	0.00	0.00	0.00
Force (N)		4.74	9.39	9.19	6.60	3.10	1.82	3.56	4.09	3.44	3.45	2.75	1.18	2.20	3.97	2.33	0.44	A (cm^2)	18.33
Distribution (%)		7.61	15.09	14.76	10.61	4.97	2.92	5.72	6.57	5.52	5.55	4.42	1.90	3.54	6.37	3.75	0.71	L_v (N)	3.35

2 - 5mm Test

Test Number: 02

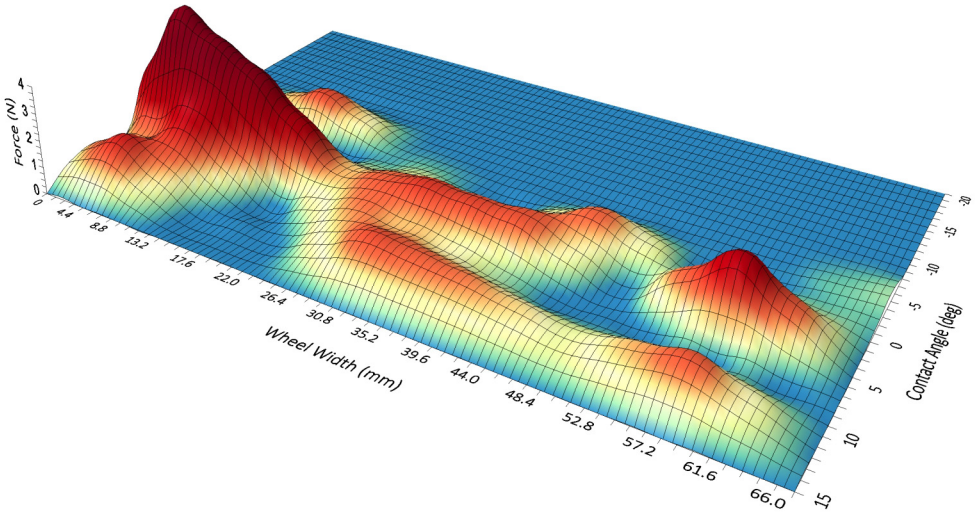

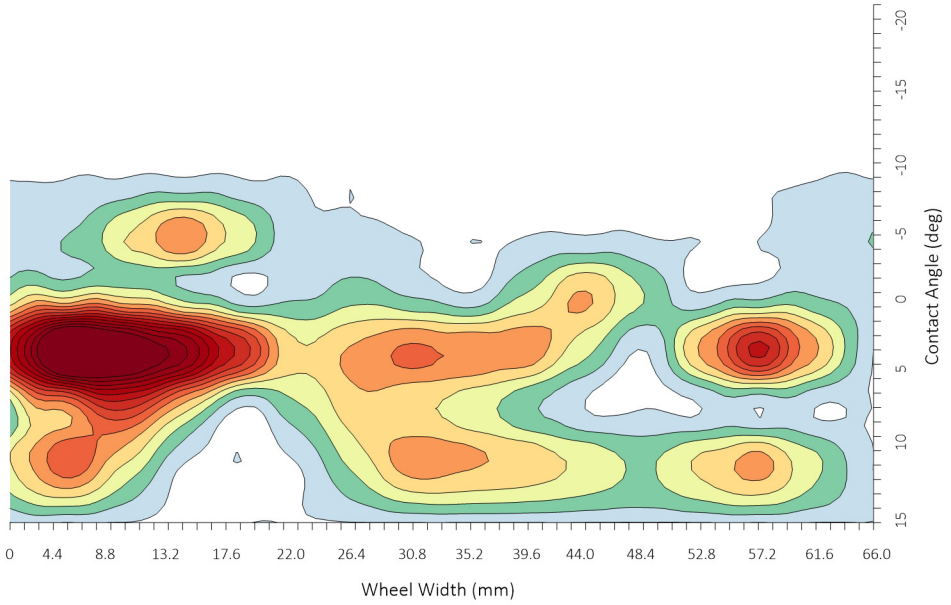

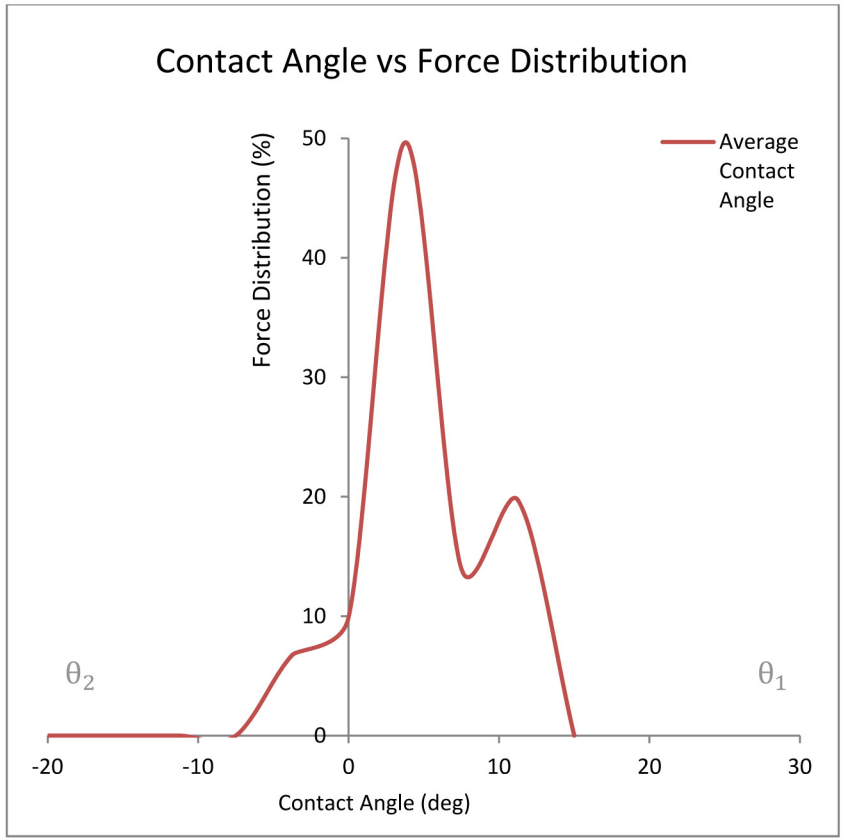

2-5mm Gravel		Lateral Wheel Width (mm)																Force (N)	Distribution (%)
No	3	0.0	4.4	8.8	13.2	17.6	22.0	26.4	30.8	35.2	39.6	44.0	48.4	52.8	57.2	61.6	66.0		
Longitudal Contact Angle (deg)	15.00	0.00	0.00	0.00	0.00	0.00	0.00	0.00	0.00	0.00	0.00	0.00	0.00	0.00	0.00	0.00	0.00	0.00	0.00
	11.25	0.00	0.13	0.26	0.13	0.00	0.00	0.00	0.00	0.00	0.00	0.00	0.00	0.00	0.00	0.00	0.00	0.51	1.22
	7.50	1.11	2.23	1.25	0.27	0.13	0.00	0.00	0.00	0.29	0.57	0.29	0.00	1.02	2.03	1.02	0.00	10.19	24.51
	3.75	0.42	0.85	1.28	0.84	0.40	0.20	0.00	0.24	0.47	0.42	0.37	0.51	0.65	0.56	0.47	0.24	7.93	19.06
	0.00	0.98	1.96	0.98	0.00	0.32	0.65	0.32	0.00	0.01	0.03	0.27	0.51	0.53	0.55	0.37	0.18	7.66	18.43
	-3.75	2.51	1.26	0.00	0.00	0.00	0.28	0.56	0.28	0.00	0.00	0.00	0.00	0.00	0.26	0.51	0.26	5.90	14.18
	-7.50	0.42	0.84	0.42	0.00	0.00	0.00	0.10	0.20	0.10	0.00	0.00	0.00	0.00	0.00	2.44	4.88	9.40	22.59
	-11.25	0.00	0.00	0.00	0.00	0.00	0.00	0.00	0.00	0.00	0.00	0.00	0.00	0.00	0.00	0.00	0.00	0.00	0.00
	-15.00	0.00	0.00	0.00	0.00	0.00	0.00	0.00	0.00	0.00	0.00	0.00	0.00	0.00	0.00	0.00	0.00	0.00	0.00
	-18.75	0.00	0.00	0.00	0.00	0.00	0.00	0.00	0.00	0.00	0.00	0.00	0.00	0.00	0.00	0.00	0.00	0.00	0.00
	-22.50	0.00	0.00	0.00	0.00	0.00	0.00	0.00	0.00	0.00	0.00	0.00	0.00	0.00	0.00	0.00	0.00	0.00	0.00
Force (N)		5.45	7.26	4.19	1.24	0.86	1.13	0.98	0.72	0.87	1.02	0.92	1.01	2.19	3.40	4.81	5.55	A (cm^2)	18.88
Distribution (%)		13.10	17.46	10.06	2.98	2.07	2.71	2.36	1.73	2.10	2.45	2.21	2.44	5.27	8.18	11.55	13.35	L_v (N)	3.46

2 - 5mm Test

Test Number: 03

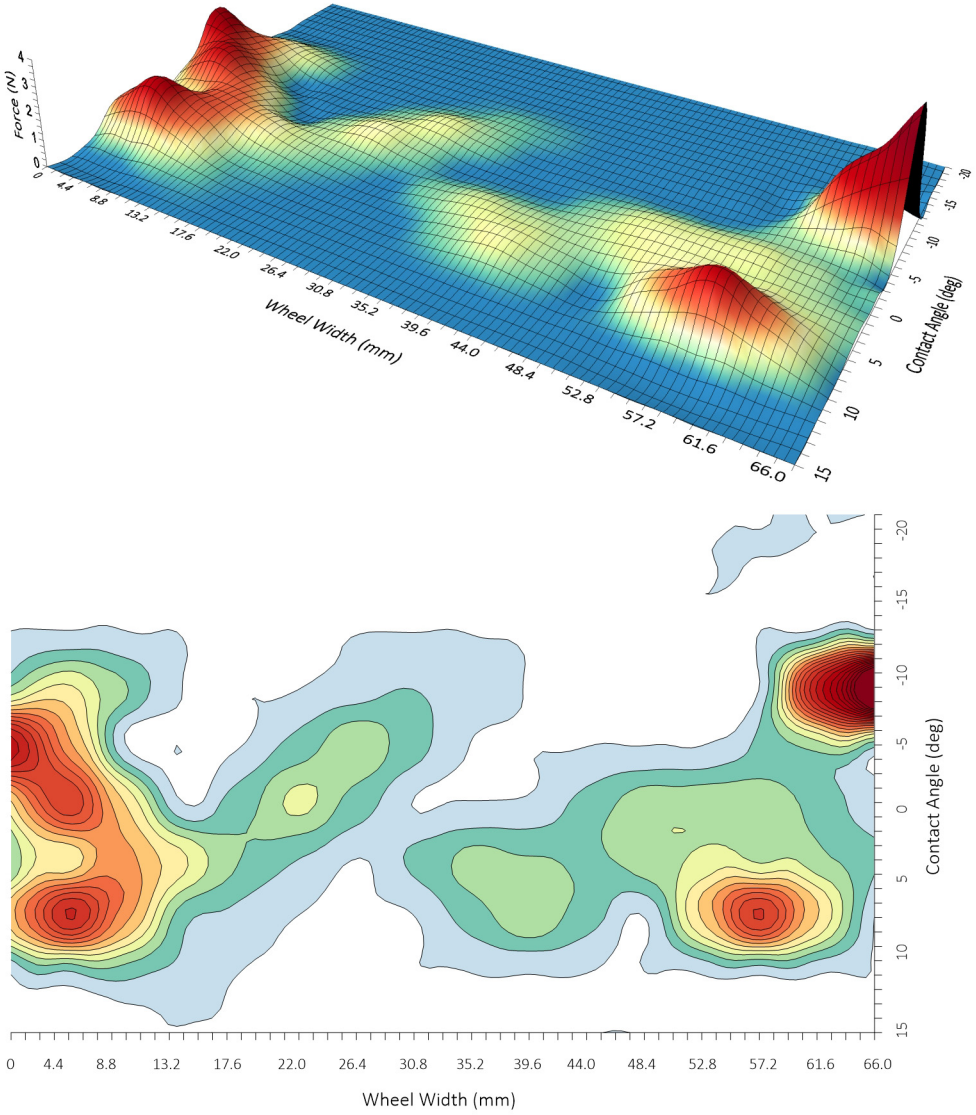

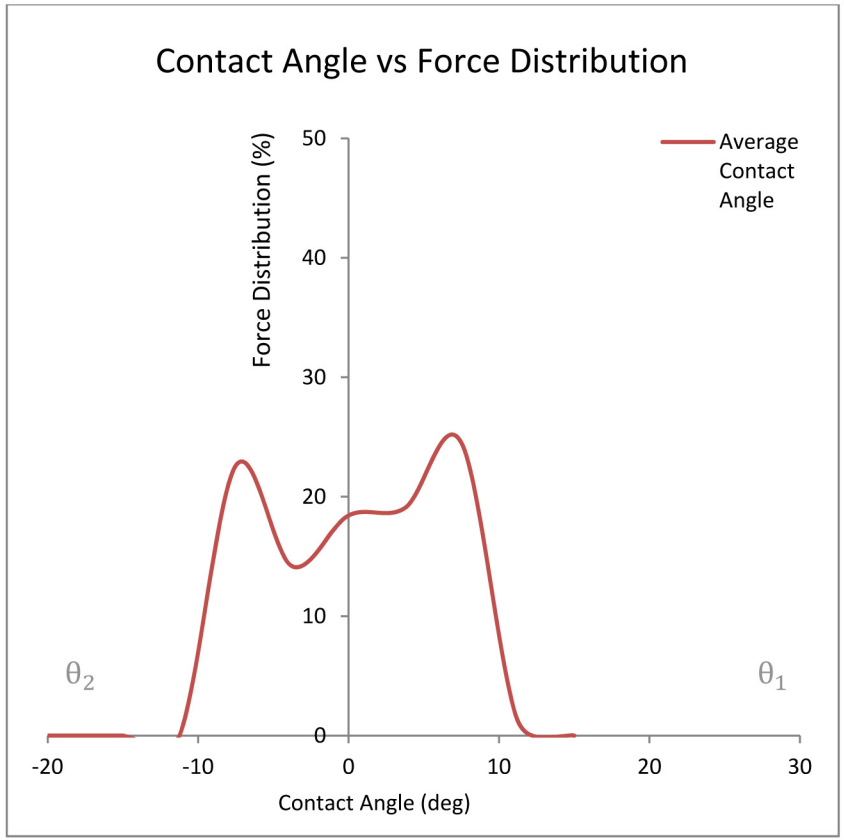

Appendix G

2-5mm Gravel		Lateral Wheel Width (mm)																Force (N)	Distribution (%)
No	4	0.0	4.4	8.8	13.2	17.6	22.0	26.4	30.8	35.2	39.6	44.0	48.4	52.8	57.2	61.6	66.0		
Longitudal Contact Angle (deg)	15.00	0.00	0.00	0.00	0.00	0.00	0.00	0.00	0.00	0.00	0.00	0.00	0.00	0.00	0.00	0.00	0.00	0.00	0.00
	11.25	0.00	0.00	0.00	0.00	0.62	1.25	0.92	0.60	0.30	0.00	0.00	0.00	0.00	0.00	0.06	0.13	3.88	11.34
	7.50	0.25	0.66	1.06	0.64	0.22	0.46	0.70	0.35	0.00	0.35	0.70	0.48	0.26	0.19	0.11	0.06	6.48	18.93
	3.75	0.40	0.80	0.78	0.75	0.64	0.53	0.33	0.13	0.35	0.56	0.64	0.72	0.36	0.00	0.15	0.29	7.42	21.65
	0.00	1.19	1.06	0.92	1.00	1.07	0.73	0.39	1.15	1.90	1.11	0.32	0.42	0.53	0.40	0.27	0.13	12.57	36.71
	-3.75	0.14	0.29	0.14	0.00	0.10	0.19	0.10	0.00	0.00	0.00	0.04	0.07	0.14	0.20	0.10	0.00	1.50	4.38
	-7.50	0.26	0.29	0.33	0.16	0.00	0.00	0.00	0.00	0.00	0.09	0.18	0.09	0.00	0.00	0.00	0.00	1.39	4.06
	-11.25	0.11	0.21	0.11	0.00	0.00	0.00	0.00	0.00	0.15	0.29	0.15	0.00	0.00	0.00	0.00	0.00	1.01	2.94
	-15.00	0.00	0.00	0.00	0.00	0.00	0.00	0.00	0.00	0.00	0.00	0.00	0.00	0.00	0.00	0.00	0.00	0.00	0.00
	-18.75	0.00	0.00	0.00	0.00	0.00	0.00	0.00	0.00	0.00	0.00	0.00	0.00	0.00	0.00	0.00	0.00	0.00	0.00
	-22.50	0.00	0.00	0.00	0.00	0.00	0.00	0.00	0.00	0.00	0.00	0.00	0.00	0.00	0.00	0.00	0.00	0.00	0.00
Force (N)		2.35	3.30	3.34	2.55	2.64	3.15	2.44	2.23	2.70	2.40	2.02	1.78	1.28	0.78	0.69	0.61	A (cm^2)	26.54
Distribution (%)		6.85	9.65	9.74	7.43	7.70	9.20	7.12	6.52	7.87	7.02	5.90	5.20	3.74	2.28	2.01	1.78	L_v (N)	1.64

2 - 5mm Test

Test Number: 04

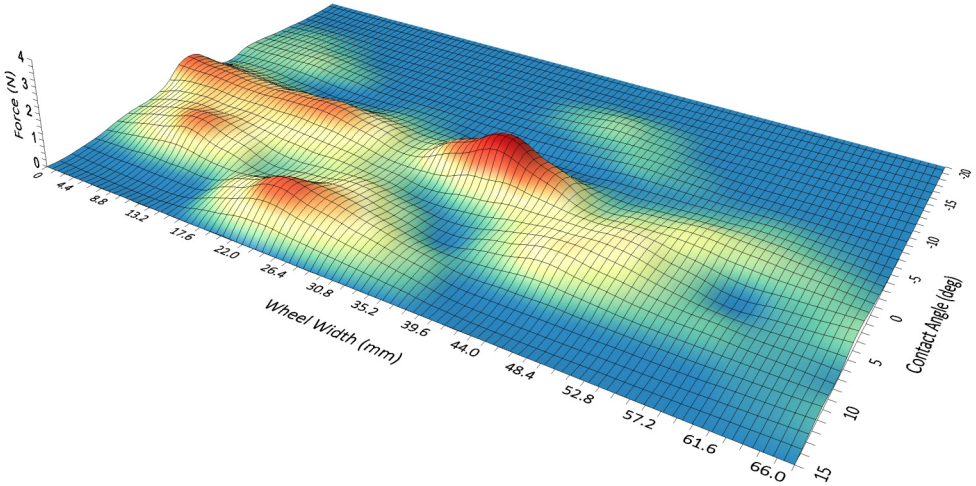

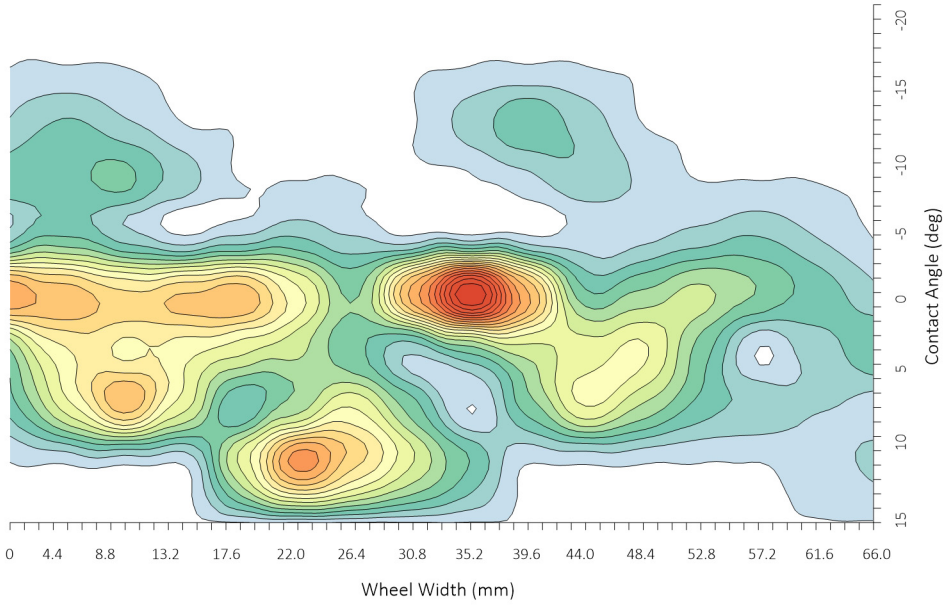

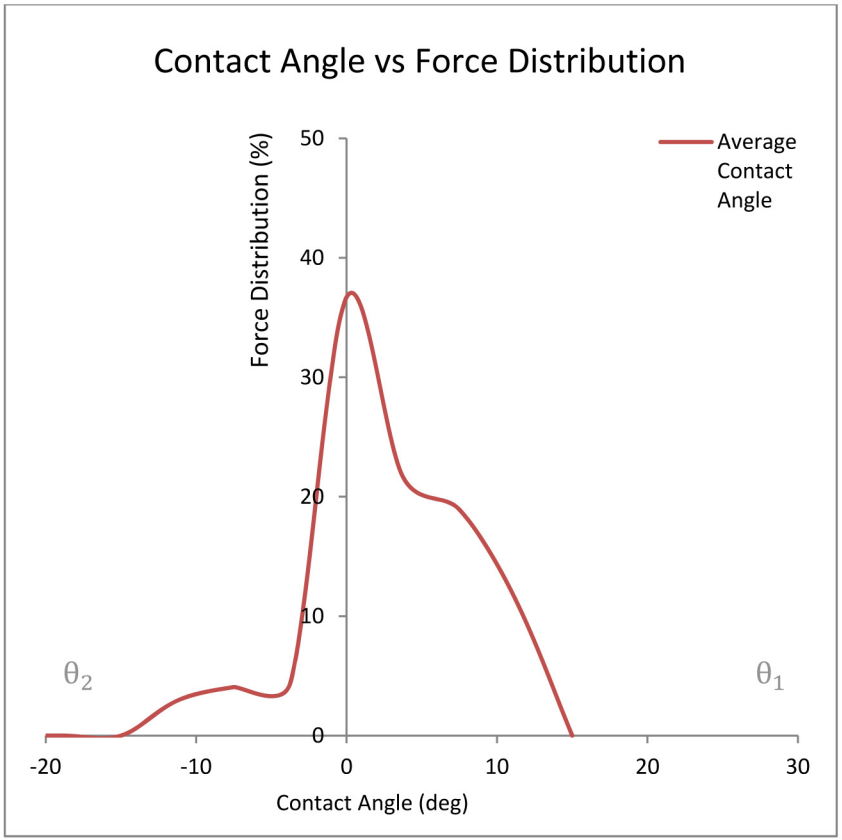

2-5mm Gravel		Lateral Wheel Width (mm)																Force (N)	Distribution (%)
No	5	0.0	4.4	8.8	13.2	17.6	22.0	26.4	30.8	35.2	39.6	44.0	48.4	52.8	57.2	61.6	66.0		
Longitudal Contact Angle (deg)	15.00	0.00	0.00	0.00	0.00	0.00	0.00	0.00	0.00	0.00	0.00	0.00	0.00	0.00	0.00	0.00	0.00	0.00	0.00
	11.25	0.00	0.51	1.03	0.51	0.00	0.90	1.80	0.90	0.00	0.40	0.81	2.58	4.35	2.40	0.45	0.23	16.85	28.50
	7.50	1.19	2.37	1.61	0.85	0.83	0.82	0.79	0.76	0.80	0.84	0.61	0.38	0.39	0.40	0.39	0.38	13.39	22.65
	3.75	1.76	0.88	0.00	0.27	0.55	0.27	0.00	0.15	0.31	0.40	0.50	0.40	0.29	1.91	3.53	1.76	12.99	21.98
	0.00	1.09	2.18	1.88	1.59	1.22	0.85	0.43	0.00	0.00	0.00	0.15	0.31	0.76	1.21	0.85	0.49	13.00	21.99
	-3.75	0.10	0.05	0.00	0.25	0.51	0.25	0.00	0.00	0.00	0.00	0.00	0.00	0.00	0.28	0.55	0.28	2.28	3.85
	-7.50	0.00	0.00	0.00	0.00	0.00	0.00	0.15	0.30	0.15	0.00	0.00	0.00	0.00	0.00	0.00	0.00	0.61	1.03
	-11.25	0.00	0.00	0.00	0.00	0.00	0.00	0.00	0.00	0.00	0.00	0.00	0.00	0.00	0.00	0.00	0.00	0.00	0.00
	-15.00	0.00	0.00	0.00	0.00	0.00	0.00	0.00	0.00	0.00	0.00	0.00	0.00	0.00	0.00	0.00	0.00	0.00	0.00
	-18.75	0.00	0.00	0.00	0.00	0.00	0.00	0.00	0.00	0.00	0.00	0.00	0.00	0.00	0.00	0.00	0.00	0.00	0.00
	-22.50	0.00	0.00	0.00	0.00	0.00	0.00	0.00	0.00	0.00	0.00	0.00	0.00	0.00	0.00	0.00	0.00	0.00	0.00
Force (N)		4.14	6.00	4.52	3.47	3.11	3.09	3.16	2.11	1.26	1.65	2.07	3.66	5.79	6.20	5.77	3.13	A (cm^2)	21.07
Distribution (%)		7.01	10.15	7.64	5.88	5.26	5.23	5.34	3.57	2.13	2.79	3.50	6.18	9.79	10.48	9.76	5.30	L_v (N)	3.51

2 - 5mm Test

Test Number: 05

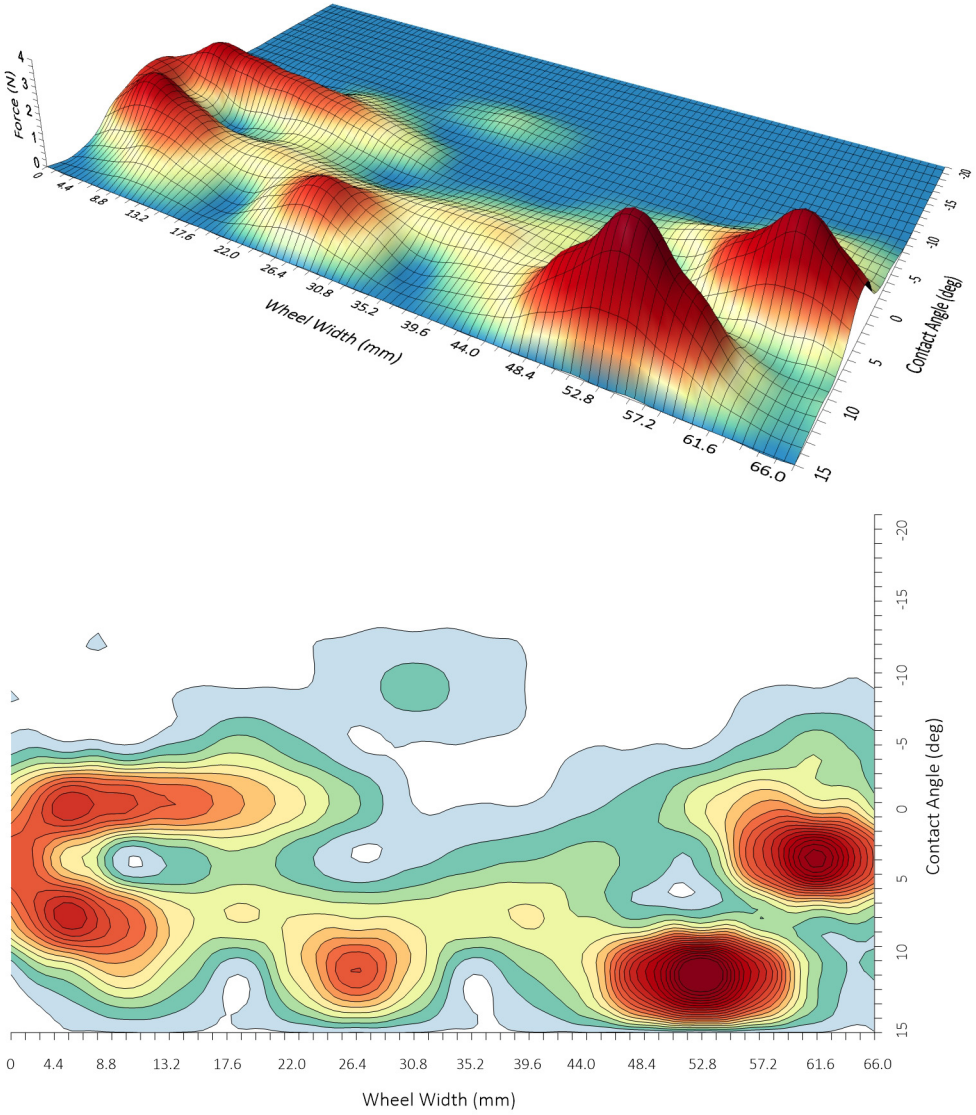

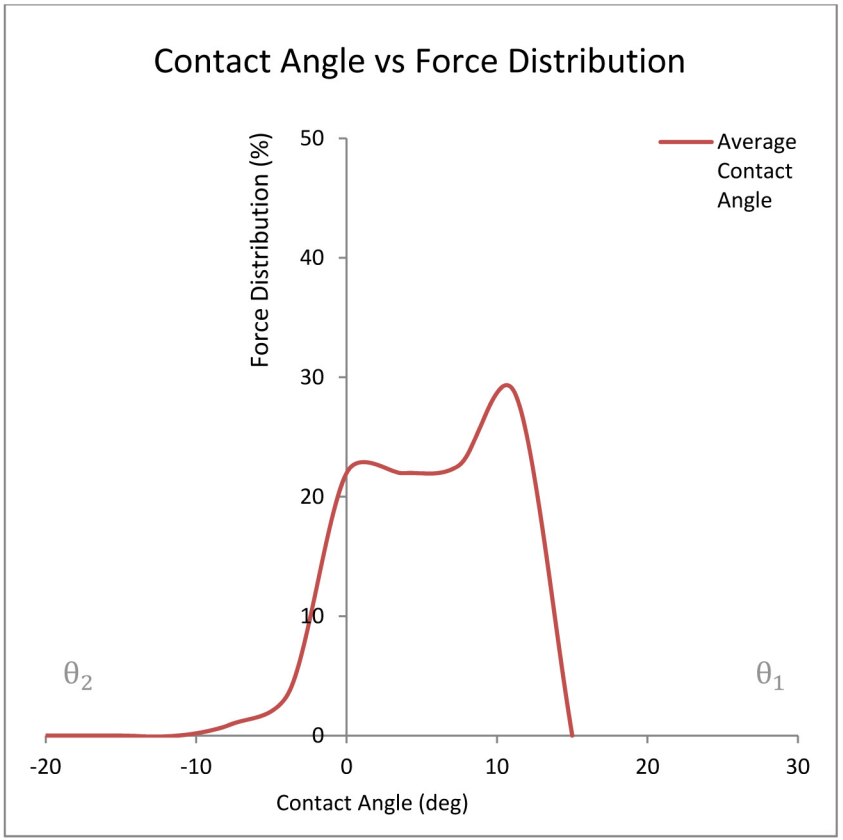

2-5mm Gravel		Lateral Wheel Width (mm)																Force (N)	Distribution (%)
No	Ave	0.0	4.4	8.8	13.2	17.6	22.0	26.4	30.8	35.2	39.6	44.0	48.4	52.8	57.2	61.6	66.0		
Longitudal Contact Angle (deg)	15.00	0.00	0.00	0.00	0.00	0.00	0.00	0.00	0.00	0.00	0.00	0.00	0.00	0.00	0.00	0.00	0.00	0.00	0.00
	11.25	0.10	0.24	0.25	0.12	0.07	0.15	0.25	0.21	0.12	0.11	0.11	0.21	0.35	0.29	0.17	0.08	2.83	6.43
	7.50	0.31	0.67	0.62	0.32	0.23	0.29	0.34	0.29	0.22	0.32	0.38	0.21	0.31	0.50	0.27	0.05	5.36	12.18
	3.75	0.88	1.04	0.95	0.93	1.04	1.37	1.25	0.76	0.50	0.40	0.33	0.31	0.39	0.53	0.62	0.40	11.67	26.55
	0.00	0.51	0.82	0.96	1.07	0.89	0.69	0.73	0.69	0.56	0.52	0.46	0.34	0.35	0.44	0.41	0.29	9.74	22.15
	-3.75	0.44	0.53	0.54	0.49	0.49	0.42	0.24	0.23	0.35	0.45	0.48	0.33	0.22	0.43	0.61	0.38	6.64	15.09
	-7.50	0.24	0.46	0.50	0.54	0.36	0.17	0.19	0.26	0.31	0.30	0.22	0.11	0.08	0.13	0.37	0.53	4.76	10.83
	-11.25	0.09	0.14	0.20	0.16	0.08	0.07	0.17	0.23	0.13	0.08	0.06	0.04	0.09	0.13	0.10	0.04	1.80	4.10
	-15.00	0.01	0.01	0.03	0.06	0.08	0.13	0.12	0.08	0.05	0.02	0.09	0.19	0.11	0.02	0.02	0.02	1.02	2.31
	-18.75	0.02	0.01	0.00	0.00	0.02	0.05	0.03	0.02	0.01	0.00	0.00	0.00	0.00	0.00	0.00	0.00	0.16	0.36
	-22.50	0.00	0.00	0.00	0.00	0.00	0.00	0.00	0.00	0.00	0.00	0.00	0.00	0.00	0.00	0.00	0.00	0.00	0.00
Force (N)		2.59	3.92	4.05	3.69	3.26	3.34	3.32	2.76	2.24	2.20	2.14	1.74	1.90	2.47	2.58	1.78	A (cm^2)	36.94
Distribution (%)		5.89	8.91	9.22	8.39	7.41	7.60	7.54	6.28	5.10	4.99	4.86	3.96	4.32	5.62	5.86	4.05	L_v (N)	1.17

2 - 5mm Test

Test Number: Averages

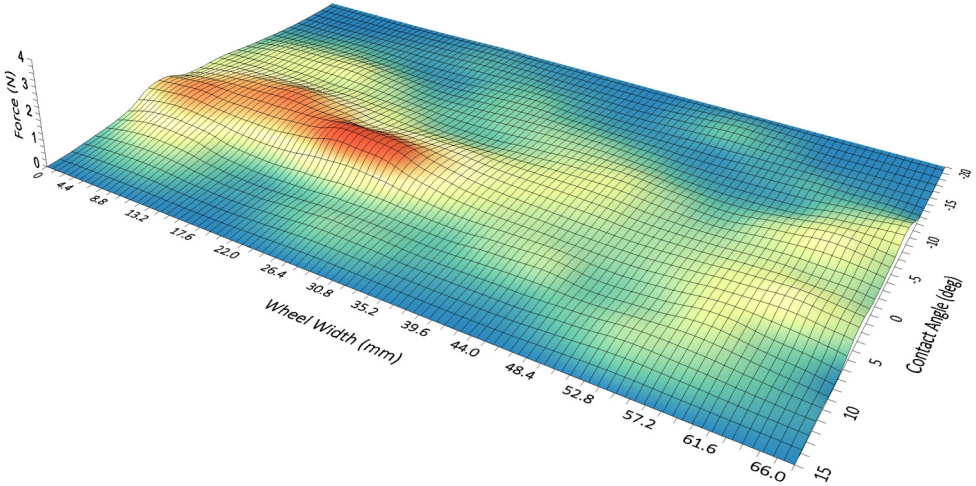

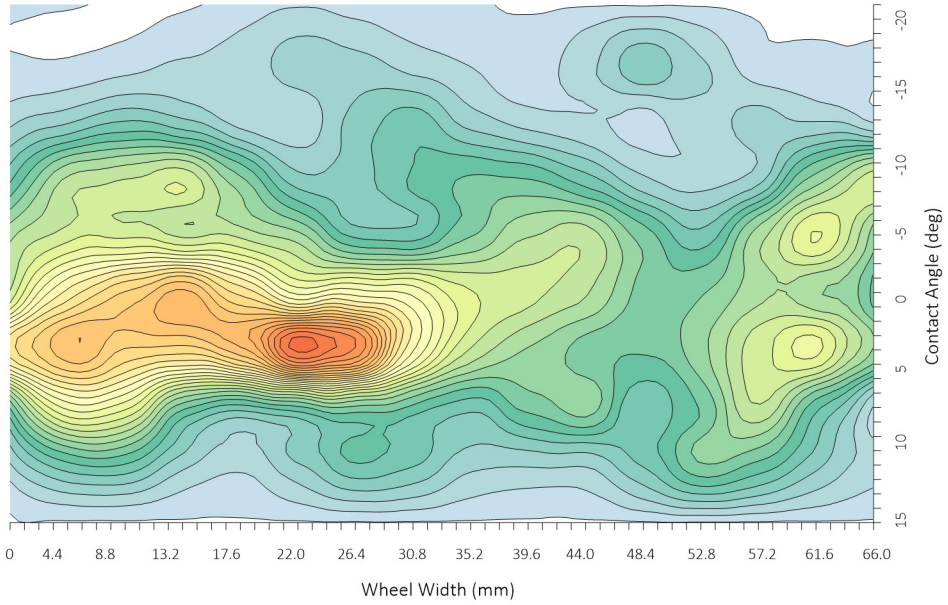

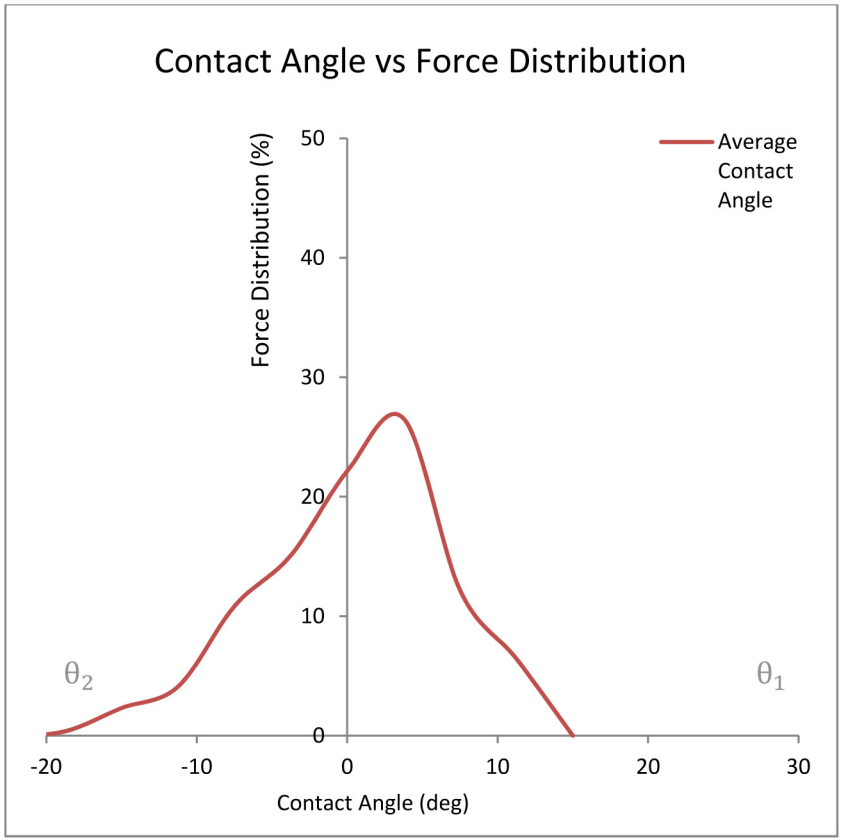

APPENDIX H

10-20mm Gravel Results

10-20mm Gravel		Lateral Wheel Width (mm)																Force (N)	Distribution (%)
No	1	0.0	4.4	8.8	13.2	17.6	22.0	26.4	30.8	35.2	39.6	44.0	48.4	52.8	57.2	61.6	66.0		
Longitudal Contact Angle (deg)	18.75	0.00	0.00	0.00	0.00	0.00	0.00	0.00	0.00	0.00	0.00	0.00	0.00	0.00	0.00	0.00	0.00	0.00	0.00
	15.00	0.00	0.00	0.00	0.02	0.04	0.02	0.00	0.00	0.00	0.15	0.29	0.28	0.27	0.31	0.35	0.17	1.90	5.00
	11.25	0.00	0.00	0.00	0.00	0.33	0.66	0.33	0.00	0.57	1.15	1.01	0.87	0.44	0.00	0.14	0.28	5.77	15.20
	7.50	0.72	0.85	0.98	0.49	0.00	0.34	0.68	0.34	0.00	0.00	0.00	0.46	0.92	0.69	0.46	0.23	7.16	18.88
	3.75	1.09	2.19	1.37	0.55	0.55	0.54	0.27	0.00	0.00	0.00	1.66	3.31	2.41	1.51	0.86	0.22	16.54	43.61
	0.00	0.30	0.15	0.00	0.00	0.00	0.00	0.00	0.34	0.67	0.52	0.38	0.19	0.00	0.34	0.69	0.34	3.92	10.34
	-3.75	0.08	0.17	0.08	0.00	0.32	0.65	0.41	0.18	0.25	0.33	0.16	0.00	0.00	0.00	0.00	0.00	2.64	6.97
	-7.50	0.00	0.00	0.00	0.00	0.00	0.00	0.00	0.00	0.00	0.00	0.00	0.00	0.00	0.00	0.00	0.00	0.00	0.00
	-11.25	0.00	0.00	0.00	0.00	0.00	0.00	0.00	0.00	0.00	0.00	0.00	0.00	0.00	0.00	0.00	0.00	0.00	0.00
Force (N)		2.20	3.36	2.44	1.06	1.24	2.21	1.69	0.86	1.50	2.14	3.49	5.11	4.04	2.85	2.49	1.24	A (cm^2)	18.60
Distribution (%)		5.80	8.86	6.42	2.81	3.27	5.82	4.46	2.26	3.95	5.64	9.21	13.48	10.65	7.52	6.57	3.27	L_v (N)	2.20

10 - 20mm Test

Test Number: 01

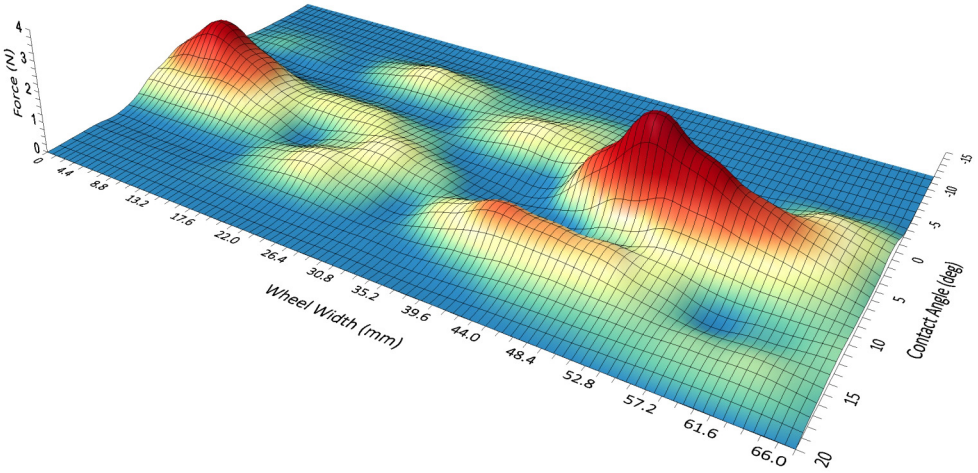

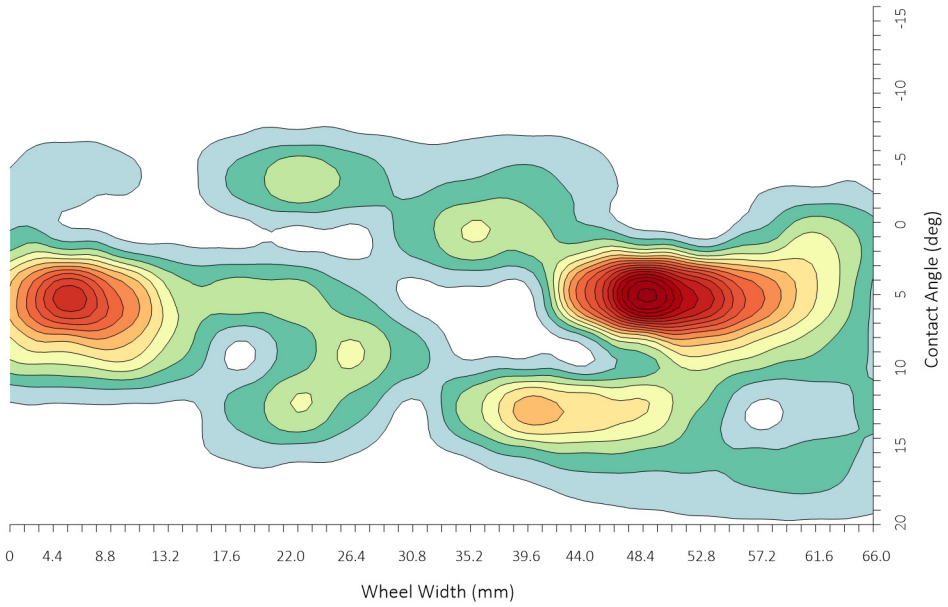

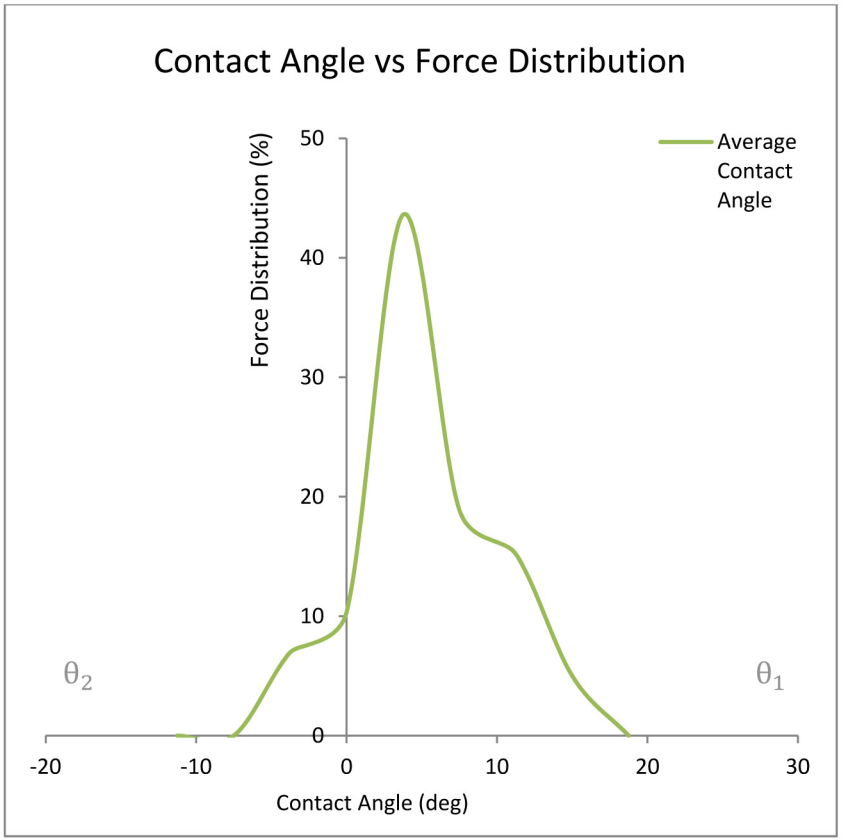

10-20mm Gravel		Lateral Wheel Width (mm)																Force (N)	Distribution (%)
No	2	0.0	4.4	8.8	13.2	17.6	22.0	26.4	30.8	35.2	39.6	44.0	48.4	52.8	57.2	61.6	66.0		
Longitudal Contact Angle (deg)	18.75	0.00	0.00	0.00	0.00	0.00	0.00	0.00	0.00	0.00	0.00	0.00	0.00	0.00	0.00	0.00	0.00	0.00	0.00
	15.00	0.00	0.00	0.00	0.00	0.00	0.00	0.00	0.00	0.00	0.00	0.07	0.14	0.07	0.00	0.00	0.00	0.29	0.96
	11.25	0.00	0.13	0.25	0.13	0.00	0.00	0.00	0.00	0.00	0.16	0.32	0.16	0.00	0.41	0.82	0.41	2.77	9.29
	7.50	0.09	0.17	0.22	0.27	3.23	6.20	3.33	0.45	0.68	0.91	0.46	0.00	0.00	0.00	0.67	1.34	18.01	60.37
	3.75	3.29	2.10	0.91	0.45	0.00	0.13	0.27	0.13	0.00	0.00	0.00	0.00	0.00	0.00	0.00	0.00	7.28	24.39
	0.00	0.00	0.00	0.06	0.12	0.12	0.11	0.06	0.00	0.00	0.00	0.00	0.00	0.00	0.00	0.34	0.68	1.49	4.99
	-3.75	0.00	0.00	0.00	0.00	0.00	0.00	0.00	0.00	0.00	0.00	0.00	0.00	0.00	0.00	0.00	0.00	0.00	0.00
	-7.50	0.00	0.00	0.00	0.00	0.00	0.00	0.00	0.00	0.00	0.00	0.00	0.00	0.00	0.00	0.00	0.00	0.00	0.00
	-11.25	0.00	0.00	0.00	0.00	0.00	0.00	0.00	0.00	0.00	0.00	0.00	0.00	0.00	0.00	0.00	0.00	0.00	0.00
Force (N)		3.37	2.39	1.44	0.97	3.35	6.45	3.65	0.58	0.68	1.07	0.84	0.30	0.07	0.41	1.83	2.43	A (cm^2)	10.40
Distribution (%)		11.30	8.02	4.82	3.25	11.23	21.61	12.23	1.95	2.28	3.59	2.82	1.01	0.24	1.37	6.13	8.15	L_v (N)	2.99

10 - 20mm Test

Test Number: 02

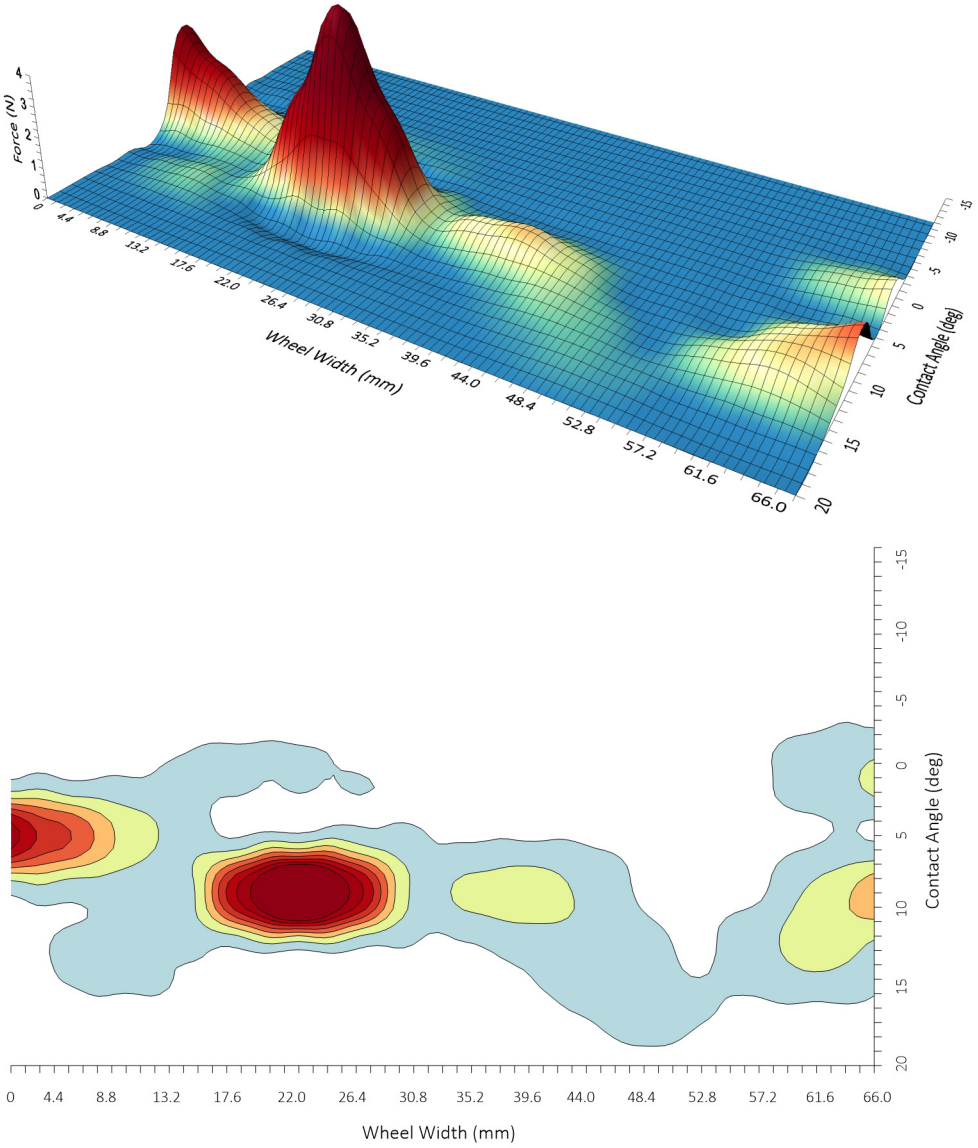

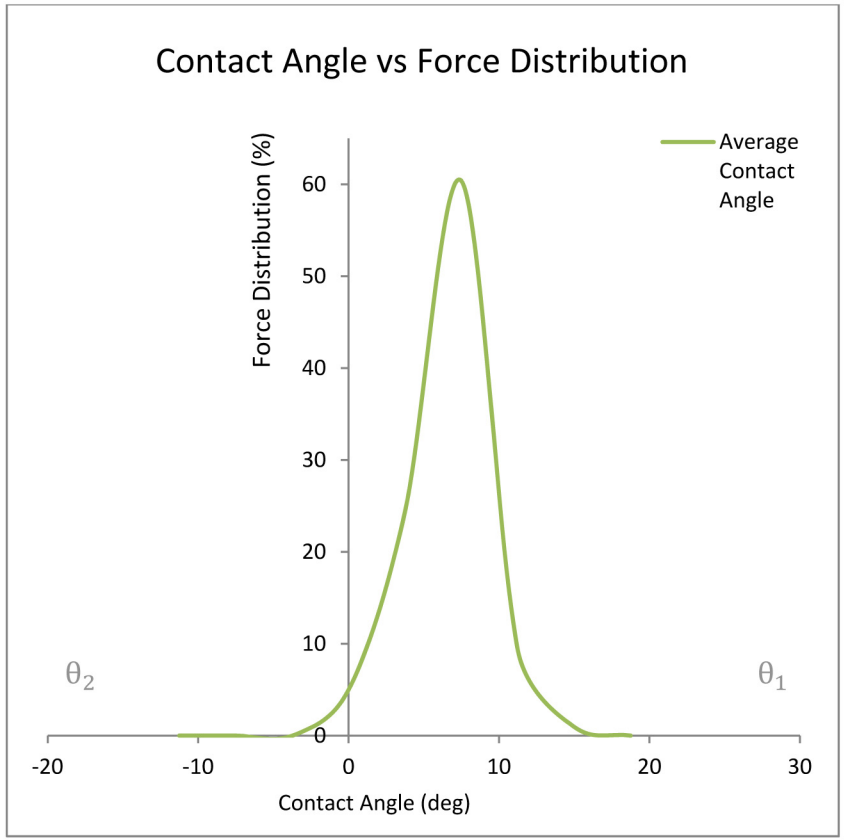

10-20mm Gravel		Lateral Wheel Width (mm)																Force (N)	Distribution (%)
No	3	0.0	4.4	8.8	13.2	17.6	22.0	26.4	30.8	35.2	39.6	44.0	48.4	52.8	57.2	61.6	66.0		
Longitudal Contact Angle (deg)	18.75	0.00	0.00	0.00	0.00	0.00	0.00	0.00	0.00	0.00	0.00	0.00	0.00	0.00	0.00	0.00	0.00	0.00	0.00
	15.00	0.00	0.00	0.00	0.34	0.68	0.93	1.18	0.59	0.00	0.14	0.27	0.18	0.08	0.18	0.28	0.14	4.97	22.22
	11.25	0.00	0.00	1.26	2.53	1.34	0.14	0.07	0.00	0.00	0.00	0.00	0.00	0.32	0.63	0.32	0.00	6.60	29.50
	7.50	0.24	0.12	0.00	0.38	0.76	0.71	0.65	0.67	0.68	0.34	0.00	0.48	0.95	0.48	0.00	0.00	6.45	28.80
	3.75	0.16	0.31	0.31	0.32	0.16	0.00	0.36	0.71	0.48	0.24	0.25	0.26	0.20	0.15	0.13	0.11	4.14	18.51
	0.00	0.00	0.05	0.11	0.05	0.00	0.00	0.00	0.00	0.00	0.00	0.00	0.00	0.00	0.00	0.00	0.00	0.22	0.97
	-3.75	0.00	0.00	0.00	0.00	0.00	0.00	0.00	0.00	0.00	0.00	0.00	0.00	0.00	0.00	0.00	0.00	0.00	0.00
	-7.50	0.00	0.00	0.00	0.00	0.00	0.00	0.00	0.00	0.00	0.00	0.00	0.00	0.00	0.00	0.00	0.00	0.00	0.00
	-11.25	0.00	0.00	0.00	0.00	0.00	0.00	0.00	0.00	0.00	0.00	0.00	0.00	0.00	0.00	0.00	0.00	0.00	0.00
Force (N)		0.39	0.48	1.69	3.61	2.93	1.78	2.26	1.97	1.16	0.72	0.52	0.91	1.55	1.44	0.73	0.25	A (cm^2)	13.41
Distribution (%)		1.76	2.16	7.53	16.15	13.10	7.95	10.11	8.81	5.16	3.19	2.32	4.06	6.93	6.42	3.24	1.12	L_v (N)	1.53

10 - 20mm Test

Test Number: 03

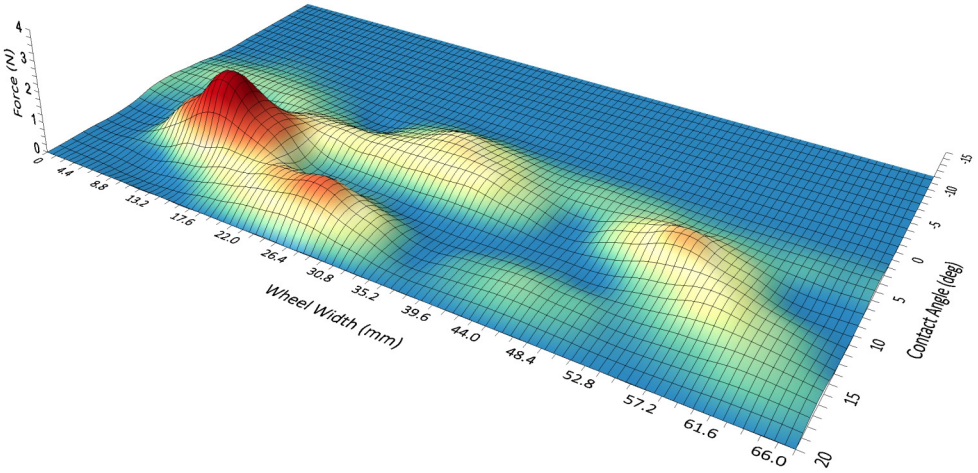

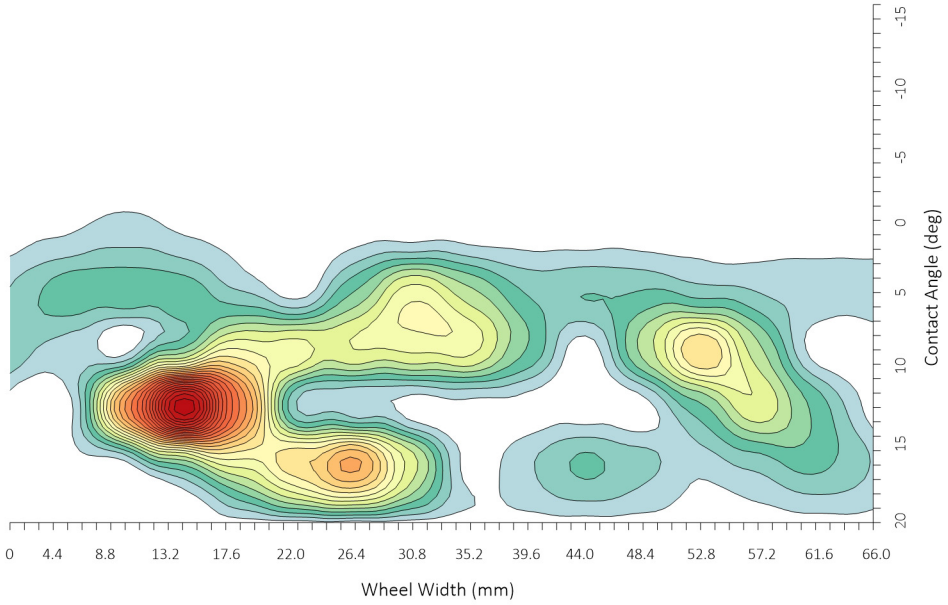

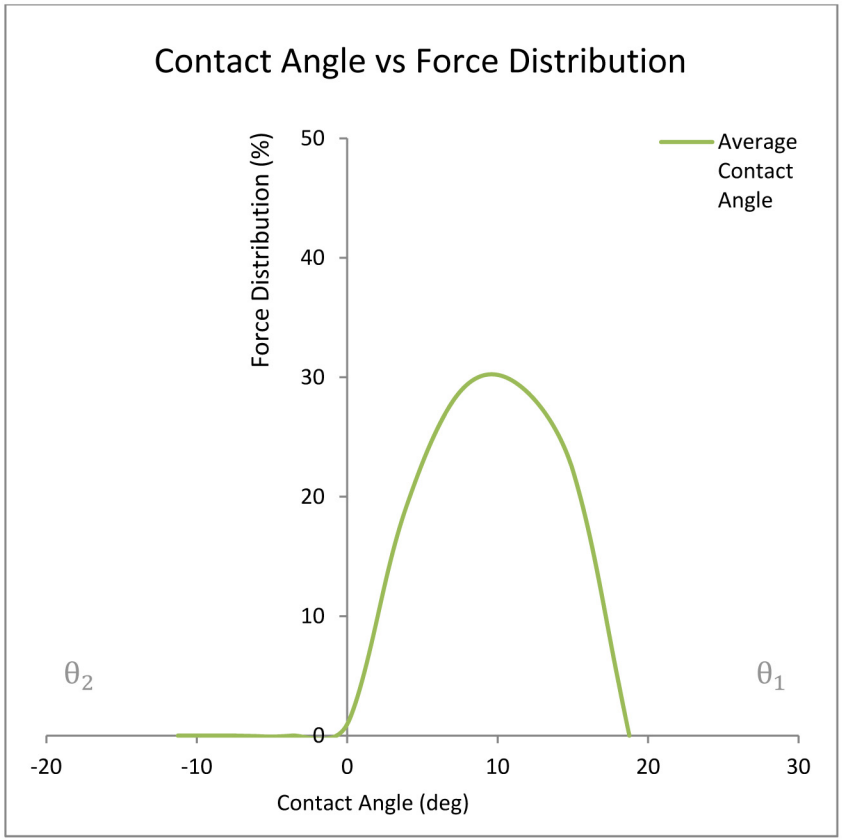

10-20mm Gravel		Lateral Wheel Width (mm)																Force (N)	Distribution (%)
No	4	0.0	4.4	8.8	13.2	17.6	22.0	26.4	30.8	35.2	39.6	44.0	48.4	52.8	57.2	61.6	66.0		
Longitudal Contact Angle (deg)	18.75	0.00	0.00	0.00	0.00	0.00	0.00	0.00	0.00	0.00	0.00	0.00	0.00	0.00	0.00	0.00	0.00	0.00	0.00
	15.00	0.05	0.24	0.43	0.22	0.00	0.00	0.00	0.00	0.00	0.59	1.17	0.59	0.00	0.08	0.16	0.08	3.60	7.65
	11.25	2.38	4.75	2.39	0.03	0.09	0.15	0.37	0.58	0.29	0.00	0.85	1.70	0.85	0.00	0.00	0.00	14.42	30.60
	7.50	1.65	0.83	0.00	0.00	0.00	1.76	3.51	1.76	0.00	0.00	0.00	0.00	0.00	0.00	0.00	0.00	9.50	20.16
	3.75	0.53	1.06	2.34	3.62	1.81	0.00	1.12	2.24	1.65	1.06	1.01	0.96	0.48	0.00	0.00	0.00	17.89	37.95
	0.00	0.00	0.00	0.00	0.00	0.00	0.00	0.00	0.00	0.00	0.00	0.00	0.43	0.86	0.43	0.00	0.00	1.72	3.64
	-3.75	0.00	0.00	0.00	0.00	0.00	0.00	0.00	0.00	0.00	0.00	0.00	0.00	0.00	0.00	0.00	0.00	0.00	0.00
	-7.50	0.00	0.00	0.00	0.00	0.00	0.00	0.00	0.00	0.00	0.00	0.00	0.00	0.00	0.00	0.00	0.00	0.00	0.00
	-11.25	0.00	0.00	0.00	0.00	0.00	0.00	0.00	0.00	0.00	0.00	0.00	0.00	0.00	0.00	0.00	0.00	0.00	0.00
Force (N)		4.61	6.89	5.16	3.86	1.90	1.91	5.00	4.58	1.94	1.65	3.03	3.67	2.19	0.51	0.16	0.08	A (cm^2)	11.49
Distribution (%)		9.79	14.61	10.95	8.19	4.03	4.05	10.61	9.72	4.12	3.49	6.43	7.79	4.64	1.08	0.34	0.17	L_v (N)	3.82

10 - 20mm Test

Test Number: 04

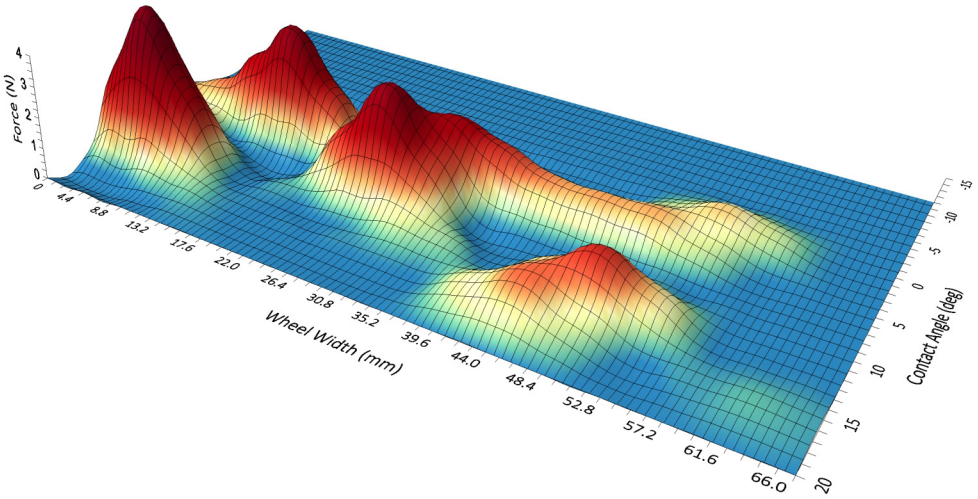

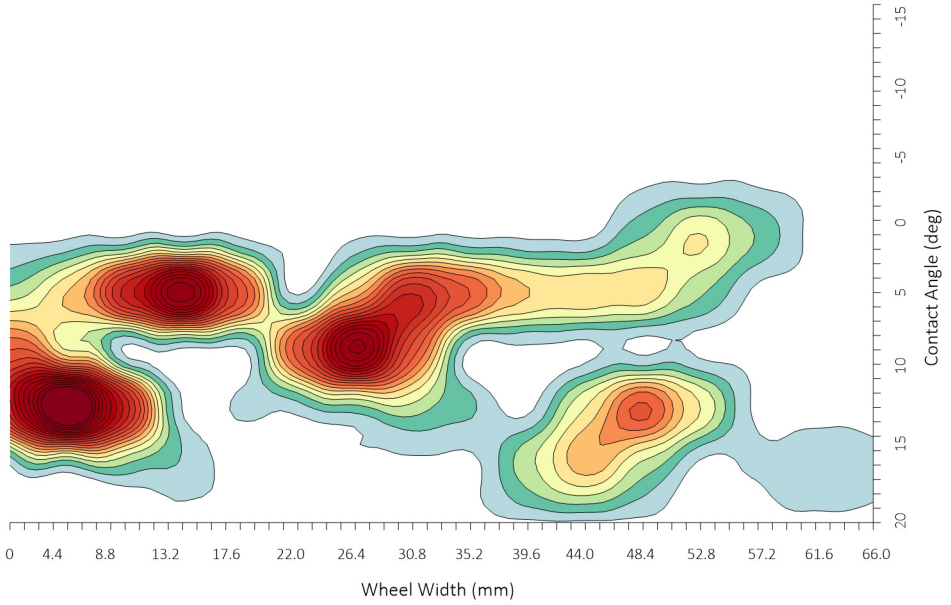

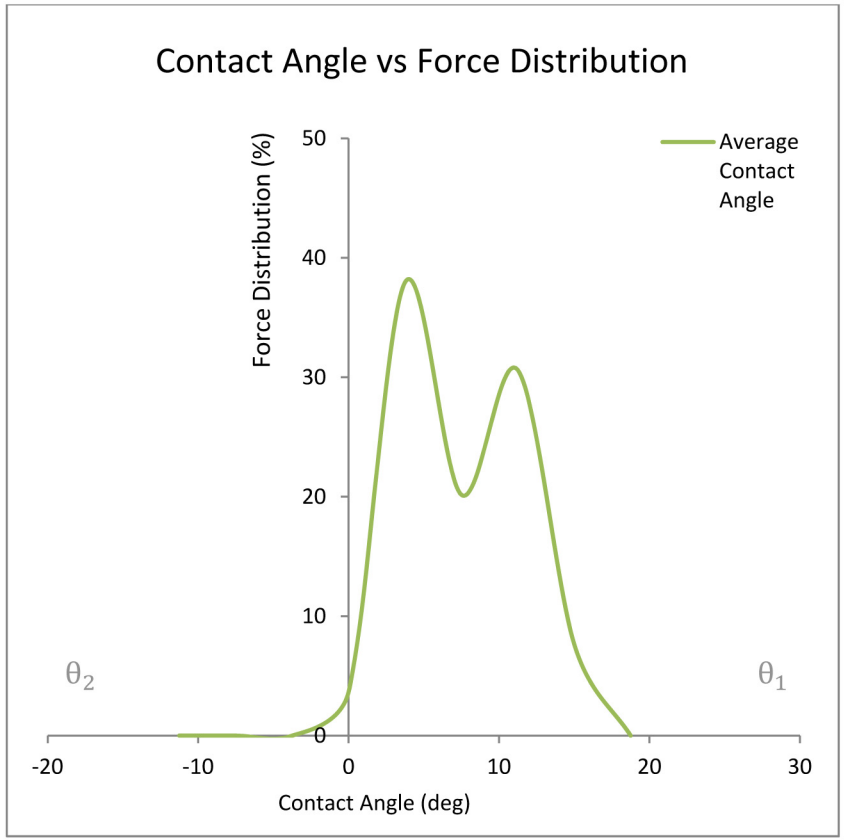

10-20mm Gravel		Lateral Wheel Width (mm)																Force (N)	Distribution (%)
No	5	0.0	4.4	8.8	13.2	17.6	22.0	26.4	30.8	35.2	39.6	44.0	48.4	52.8	57.2	61.6	66.0		
Longitudal Contact Angle (deg)	18.75	0.00	0.00	0.00	0.00	0.00	0.00	0.00	0.00	0.00	0.00	0.00	0.00	0.00	0.00	0.00	0.00	0.00	0.00
	15.00	0.00	0.00	0.00	0.00	0.00	0.00	0.00	0.00	0.00	0.00	0.00	0.00	0.00	0.02	0.05	0.02	0.09	0.22
	11.25	0.46	0.91	0.65	0.39	0.19	0.00	0.42	0.84	0.42	0.00	1.46	2.92	1.46	0.00	0.52	1.04	11.67	27.02
	7.50	0.96	0.82	0.67	0.61	0.55	0.41	0.26	0.52	0.78	0.48	0.18	1.63	3.08	1.54	0.00	0.00	12.48	28.90
	3.75	0.00	0.00	0.00	0.00	0.27	0.54	0.42	0.29	2.92	5.56	3.41	1.26	0.91	0.56	0.28	0.00	16.40	37.97
	0.00	0.95	0.48	0.00	0.00	0.00	0.00	0.00	0.00	0.00	0.00	0.00	0.00	0.00	0.28	0.56	0.28	2.55	5.90
	-3.75	0.00	0.00	0.00	0.00	0.00	0.00	0.00	0.00	0.00	0.00	0.00	0.00	0.00	0.00	0.00	0.00	0.00	0.00
	-7.50	0.00	0.00	0.00	0.00	0.00	0.00	0.00	0.00	0.00	0.00	0.00	0.00	0.00	0.00	0.00	0.00	0.00	0.00
	-11.25	0.00	0.00	0.00	0.00	0.00	0.00	0.00	0.00	0.00	0.00	0.00	0.00	0.00	0.00	0.00	0.00	0.00	0.00
Force (N)		2.37	2.20	1.32	1.00	1.01	0.95	1.10	1.66	4.13	6.04	5.05	5.81	5.44	2.40	1.40	1.34	A (cm^2)	12.59
Distribution (%)		5.48	5.10	3.05	2.30	2.34	2.19	2.55	3.83	9.55	13.98	11.69	13.44	12.60	5.55	3.25	3.10	L_v (N)	3.28

10 - 20mm Test

Test Number: 05

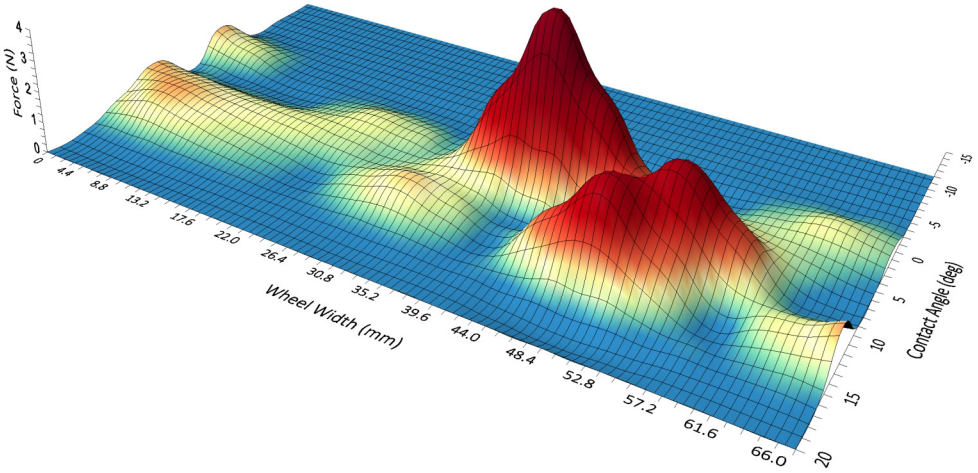

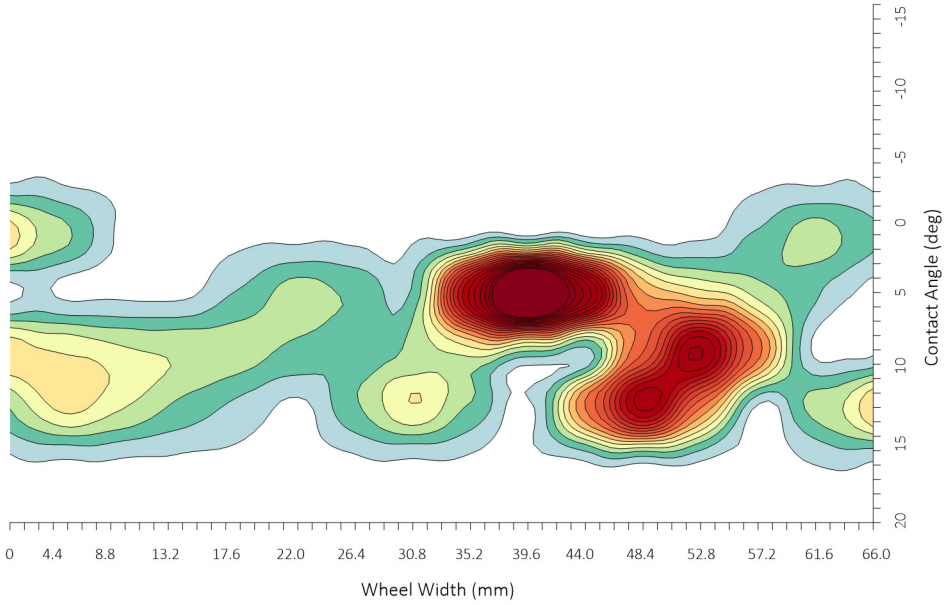

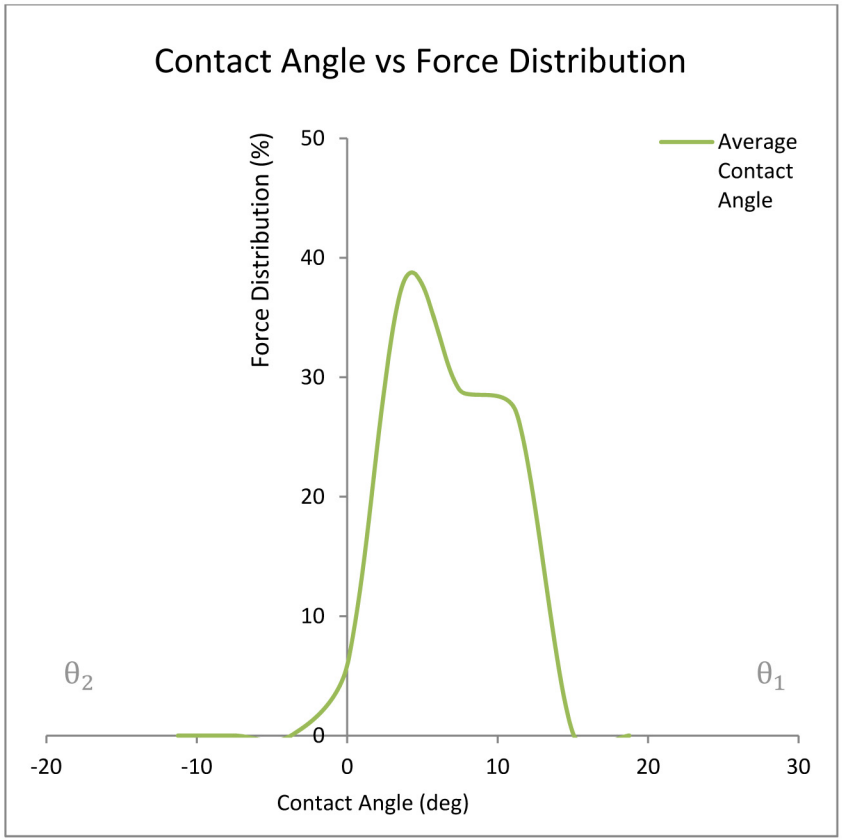

10-20mm Gravel		Lateral Wheel Width (mm)																Force (N)	Distribution (%)
No	Ave	0.0	4.4	8.8	13.2	17.6	22.0	26.4	30.8	35.2	39.6	44.0	48.4	52.8	57.2	61.6	66.0		
Longitudal Contact Angle (deg)	18.75	0.00	0.00	0.00	0.00	0.00	0.00	0.00	0.00	0.00	0.00	0.00	0.00	0.00	0.00	0.00	0.00	0.00	0.00
	15.00	0.22	0.17	0.12	0.24	0.37	0.28	0.17	0.20	0.24	0.20	0.18	0.18	0.20	0.30	0.43	0.36	3.84	9.99
	11.25	0.37	0.86	0.85	0.68	0.59	0.32	0.28	0.41	0.30	0.40	0.76	0.66	0.29	0.20	0.35	0.39	7.71	20.06
	7.50	0.31	0.35	0.84	1.40	1.31	1.33	1.44	0.99	0.56	0.51	0.59	0.68	0.70	0.52	0.32	0.23	12.08	31.42
	3.75	0.59	0.73	0.61	0.53	0.56	0.68	0.69	0.67	0.91	1.20	1.10	0.76	0.68	0.68	0.34	0.06	10.78	28.05
	0.00	0.26	0.22	0.10	0.10	0.11	0.10	0.08	0.09	0.18	0.20	0.13	0.10	0.26	0.47	0.37	0.13	2.90	7.55
	-3.75	0.04	0.08	0.06	0.04	0.09	0.14	0.11	0.06	0.04	0.03	0.05	0.09	0.06	0.01	0.01	0.02	0.92	2.40
	-7.50	0.00	0.00	0.05	0.10	0.05	0.00	0.00	0.00	0.00	0.00	0.00	0.00	0.00	0.00	0.00	0.00	0.20	0.53
	-11.25	0.00	0.00	0.00	0.00	0.00	0.00	0.00	0.00	0.00	0.00	0.00	0.00	0.00	0.00	0.00	0.00	0.00	0.00
Force (N)		1.78	2.43	2.62	3.07	3.07	2.85	2.77	2.41	2.22	2.55	2.81	2.47	2.18	2.18	1.82	1.20	A (cm^2)	27.09
Distribution (%)		4.64	6.31	6.82	7.99	7.99	7.41	7.21	6.28	5.78	6.64	7.32	6.43	5.67	5.66	4.74	3.11	L_v (N)	1.13

10 - 20mm Test

Test Number: Averages

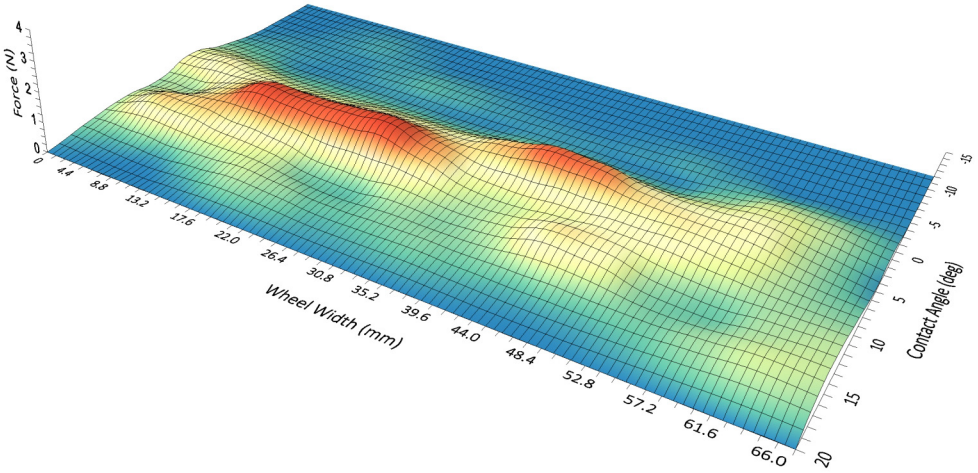

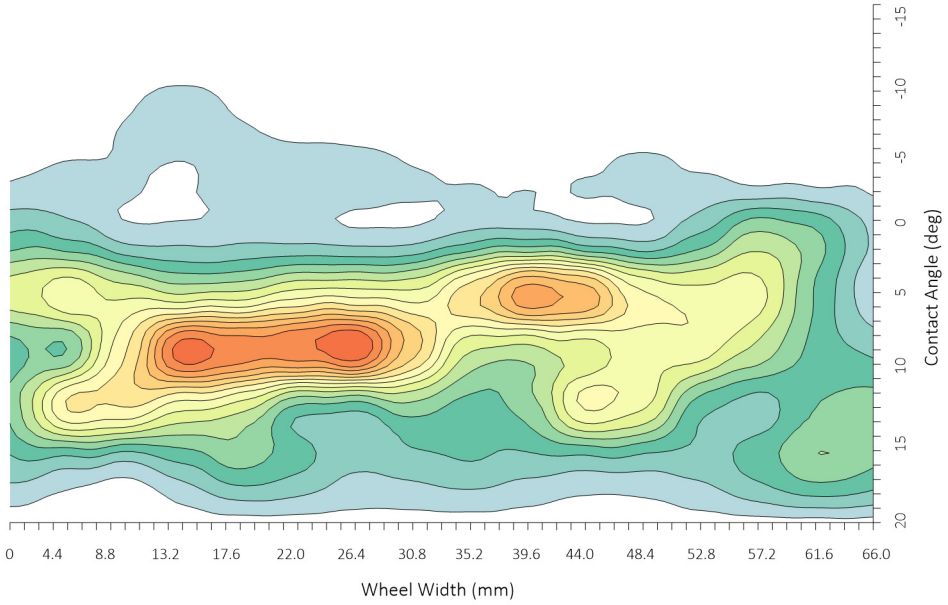

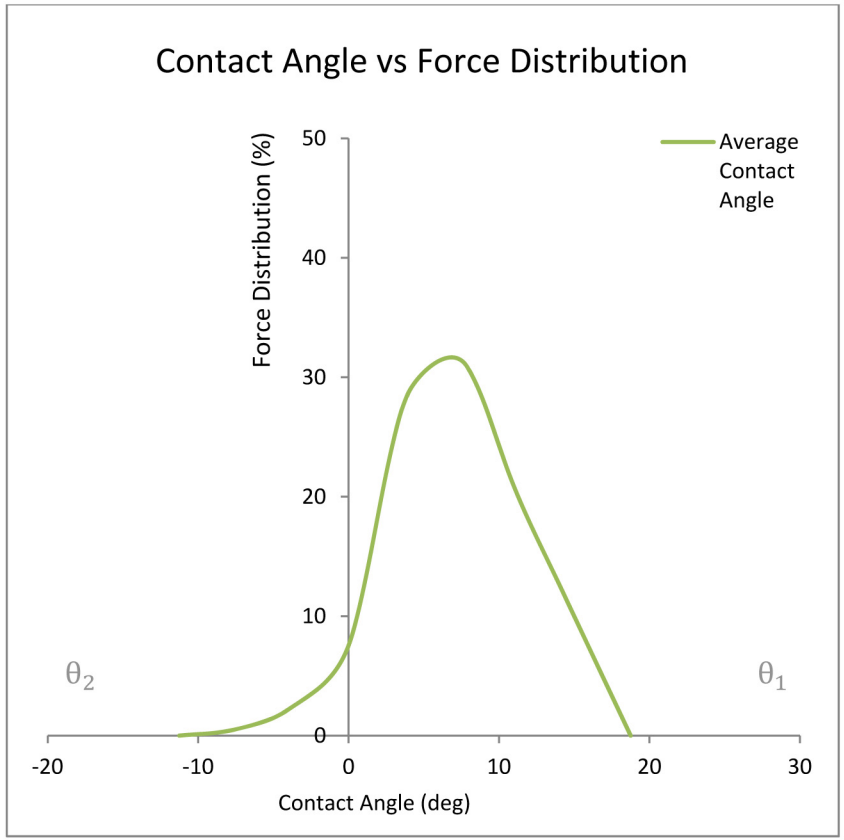

APPENDIX I

20-40mm Gravel Results

20-40mm Gravel		Lateral Wheel Width (mm)																Force (N)	Distribution (%)
No	1	0.0	4.4	8.8	13.2	17.6	22.0	26.4	30.8	35.2	39.6	44.0	48.4	52.8	57.2	61.6	66.0		
Longitudal Contact Angle (deg)	18.75	0.00	0.00	0.00	0.00	0.00	0.00	0.00	0.00	0.00	0.00	0.00	0.00	0.00	0.00	0.00	0.00	0.00	0.00
	15.00	0.00	0.00	0.00	1.47	2.94	1.47	0.00	0.00	0.00	0.00	0.00	0.00	0.00	0.00	0.00	0.00	5.88	9.88
	11.25	0.00	0.00	0.49	0.98	1.48	1.97	0.99	0.00	0.00	0.00	0.00	0.00	0.00	0.00	0.00	0.00	5.91	9.92
	7.50	7.37	3.69	0.00	2.35	4.70	2.35	0.00	0.00	0.00	0.00	0.00	0.29	0.58	3.48	6.38	3.19	34.37	57.73
	3.75	0.00	0.00	0.00	0.00	0.08	0.17	0.08	0.00	0.00	0.00	0.70	1.39	0.95	0.51	0.68	0.85	5.41	9.08
	0.00	0.00	0.00	0.00	0.00	0.00	0.00	0.00	1.52	3.04	1.52	0.00	0.00	0.00	0.00	0.00	0.00	6.08	10.22
	-3.75	0.00	0.00	0.00	0.00	0.00	0.00	0.47	0.94	0.47	0.00	0.00	0.00	0.00	0.00	0.00	0.00	1.88	3.16
	-7.50	0.00	0.00	0.00	0.00	0.00	0.00	0.00	0.00	0.00	0.00	0.00	0.00	0.00	0.00	0.00	0.00	0.00	0.00
	-11.25	0.00	0.00	0.00	0.00	0.00	0.00	0.00	0.00	0.00	0.00	0.00	0.00	0.00	0.00	0.00	0.00	0.00	0.00
Force (N)		7.37	3.69	0.49	4.80	9.20	5.96	1.54	2.46	3.51	1.52	0.70	1.69	1.53	3.99	7.05	4.04	A (cm^2)	9.03
Distribution (%)		12.39	6.19	0.82	8.06	15.45	10.01	2.59	4.14	5.90	2.55	1.17	2.83	2.57	6.69	11.85	6.78	L_v (N)	5.36

20 - 40mm Test

Test Number: 01

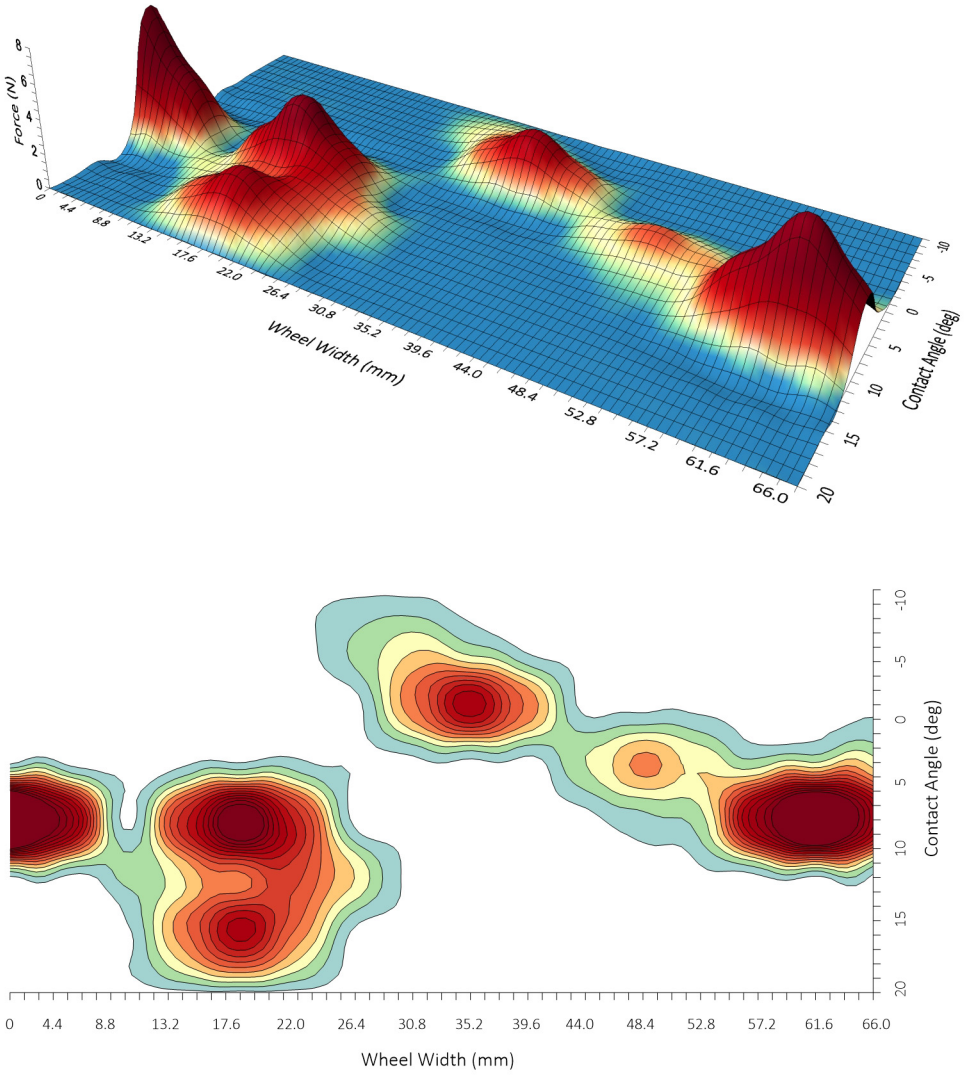

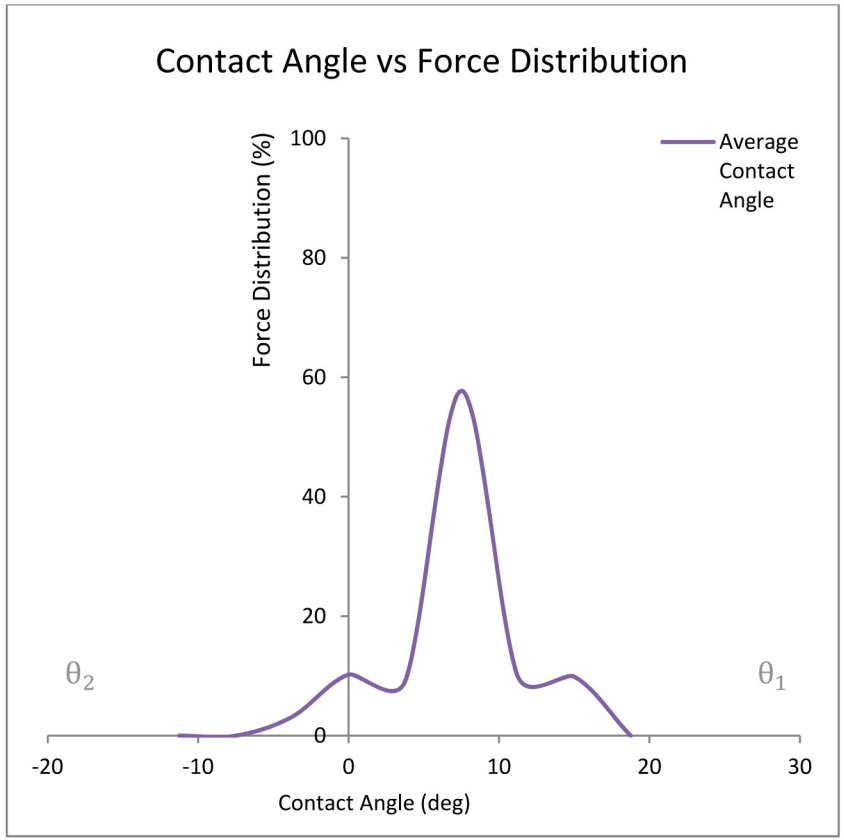

20-40mm Gravel		Lateral Wheel Width (mm)																Force (N)	Distribution (%)
No	2	0.0	4.4	8.8	13.2	17.6	22.0	26.4	30.8	35.2	39.6	44.0	48.4	52.8	57.2	61.6	66.0		
Longitudal Contact Angle (deg)	18.75	0.00	0.00	0.00	0.00	0.00	0.00	0.00	0.00	0.00	0.00	0.00	0.00	0.00	0.00	0.00	0.00	0.00	0.00
	15.00	0.65	1.30	0.65	0.00	0.00	0.00	0.00	0.00	0.00	0.00	0.00	0.00	0.90	1.81	0.90	0.00	6.20	7.53
	11.25	5.08	3.67	2.25	1.13	0.00	2.84	5.67	2.84	0.00	0.00	0.00	9.09	18.17	10.22	2.27	1.14	64.35	78.14
	7.50	2.41	4.81	2.41	0.00	0.00	0.00	0.17	0.34	0.17	0.00	0.00	0.00	0.38	0.75	0.38	0.00	11.80	14.32
	3.75	0.00	0.00	0.00	0.00	0.00	0.00	0.00	0.00	0.00	0.00	0.00	0.00	0.00	0.00	0.00	0.00	0.00	0.00
	0.00	0.00	0.00	0.00	0.00	0.00	0.00	0.00	0.00	0.00	0.00	0.00	0.00	0.00	0.00	0.00	0.00	0.00	0.00
	-3.75	0.00	0.00	0.00	0.00	0.00	0.00	0.00	0.00	0.00	0.00	0.00	0.00	0.00	0.00	0.00	0.00	0.00	0.00
	-7.50	0.00	0.00	0.00	0.00	0.00	0.00	0.00	0.00	0.00	0.00	0.00	0.00	0.00	0.00	0.00	0.00	0.00	0.00
	-11.25	0.00	0.00	0.00	0.00	0.00	0.00	0.00	0.00	0.00	0.00	0.00	0.00	0.00	0.00	0.00	0.00	0.00	0.00
Force (N)		8.13	9.77	5.31	1.13	0.00	2.84	5.84	3.17	0.17	0.00	0.00	9.09	19.45	12.77	3.55	1.14	A (cm^2)	7.39
Distribution (%)		9.88	11.87	6.44	1.37	0.00	3.44	7.09	3.85	0.21	0.00	0.00	11.03	23.62	15.51	4.31	1.38	L_v (N)	6.59

20 - 40mm Test

Test Number: 02

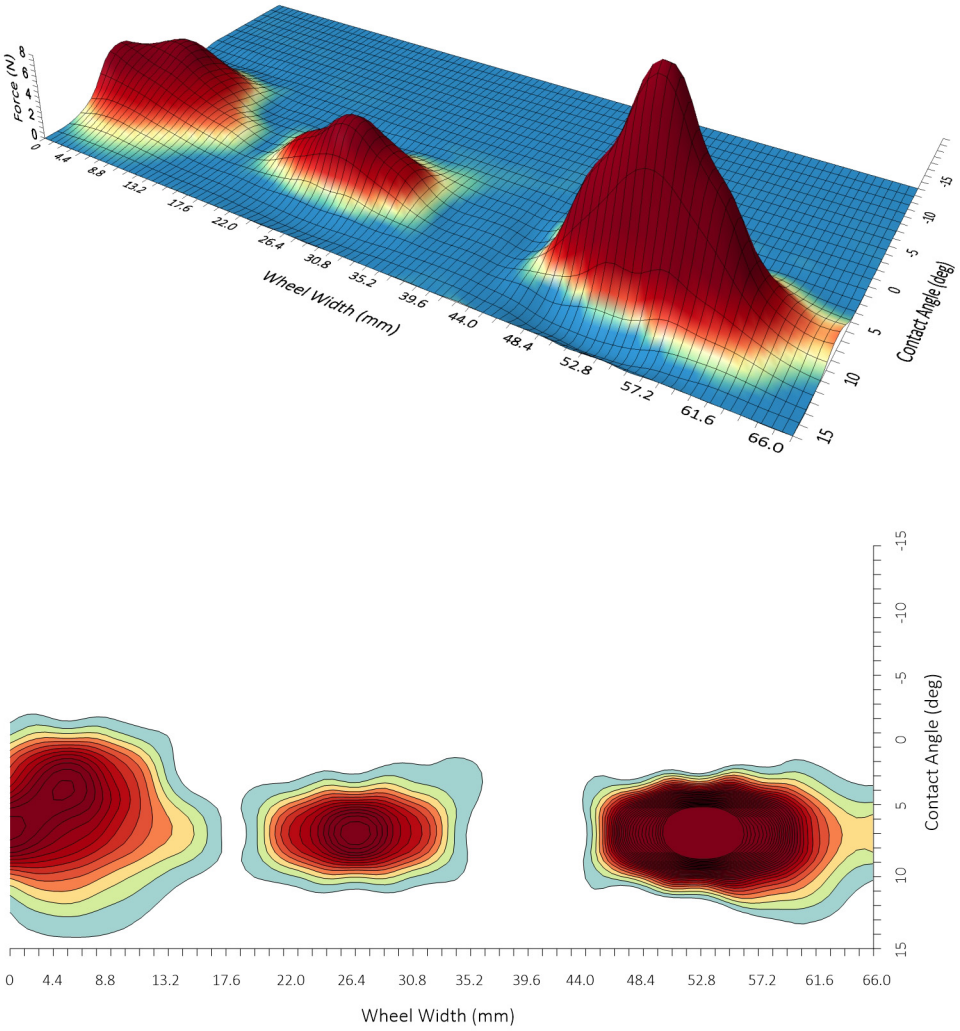

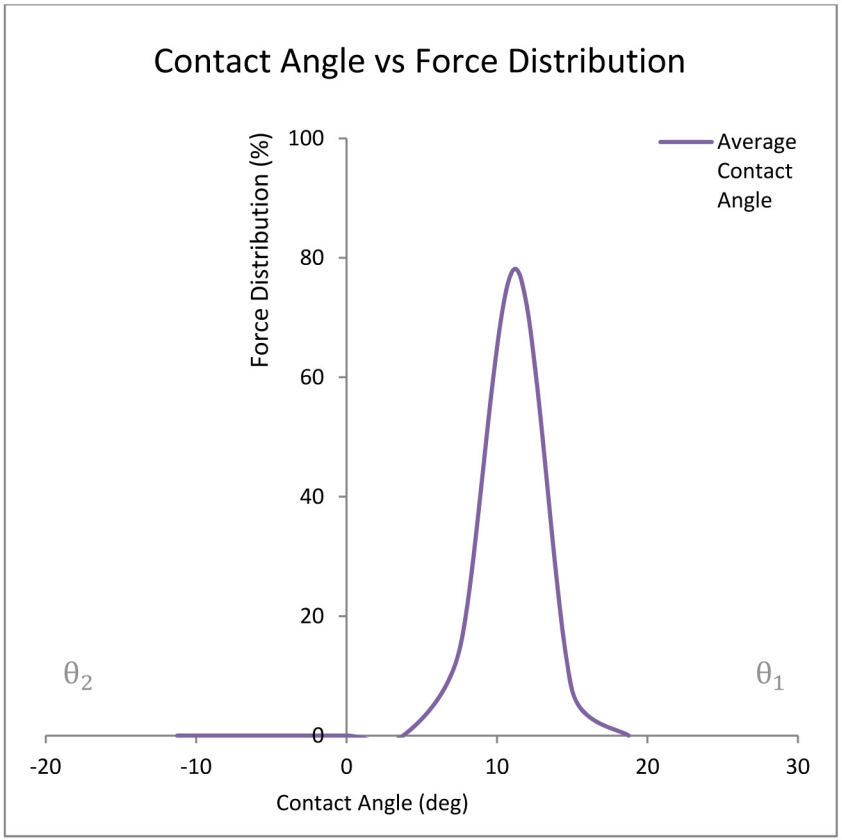

Appendix I

20-40mm Gravel		Lateral Wheel Width (mm)																Force (N)	Distribution (%)
No	3	0.0	4.4	8.8	13.2	17.6	22.0	26.4	30.8	35.2	39.6	44.0	48.4	52.8	57.2	61.6	66.0		
Longitudal Contact Angle (deg)	18.75	0.00	0.00	0.00	0.00	0.00	0.00	0.00	0.00	0.00	0.00	0.00	0.00	0.00	0.00	0.00	0.00	0.00	0.00
	15.00	0.26	0.52	0.26	0.00	0.00	0.00	0.00	0.00	0.00	0.00	0.00	0.00	0.00	0.00	0.00	0.00	1.03	3.37
	11.25	3.61	1.80	0.00	0.00	0.00	0.00	0.00	0.00	0.00	0.00	0.00	0.00	0.00	0.00	0.00	0.00	5.41	17.73
	7.50	0.00	0.00	0.09	0.18	0.51	0.84	0.42	0.00	0.00	0.00	0.00	0.00	0.00	0.00	0.00	0.00	2.02	6.64
	3.75	0.00	0.00	0.00	0.00	0.00	0.00	0.00	0.85	1.70	0.85	0.00	0.00	0.00	0.00	0.00	0.00	3.40	11.13
	0.00	0.00	0.00	0.00	0.00	0.00	0.00	0.00	0.00	0.97	1.93	0.97	0.00	0.00	0.00	0.21	0.41	4.48	14.68
	-3.75	0.42	0.21	0.00	0.00	0.00	0.88	1.75	1.01	0.27	1.63	2.99	1.50	0.00	0.00	0.00	0.00	10.66	34.96
	-7.50	0.00	0.00	0.34	0.68	0.34	0.00	0.01	0.02	0.19	0.37	0.53	0.69	0.35	0.00	0.00	0.00	3.51	11.49
	-11.25	0.00	0.00	0.00	0.00	0.00	0.00	0.00	0.00	0.00	0.00	0.00	0.00	0.00	0.00	0.00	0.00	0.00	0.00
Force (N)		4.29	2.53	0.68	0.85	0.84	1.71	2.18	1.88	3.13	4.78	4.49	2.19	0.35	0.00	0.21	0.41	A (cm^2)	10.12
Distribution (%)		14.05	8.29	2.24	2.80	2.77	5.61	7.14	6.15	10.25	15.67	14.71	7.17	1.13	0.00	0.68	1.35	L_v (N)	3.45

20 - 40mm Test

Test Number: 03

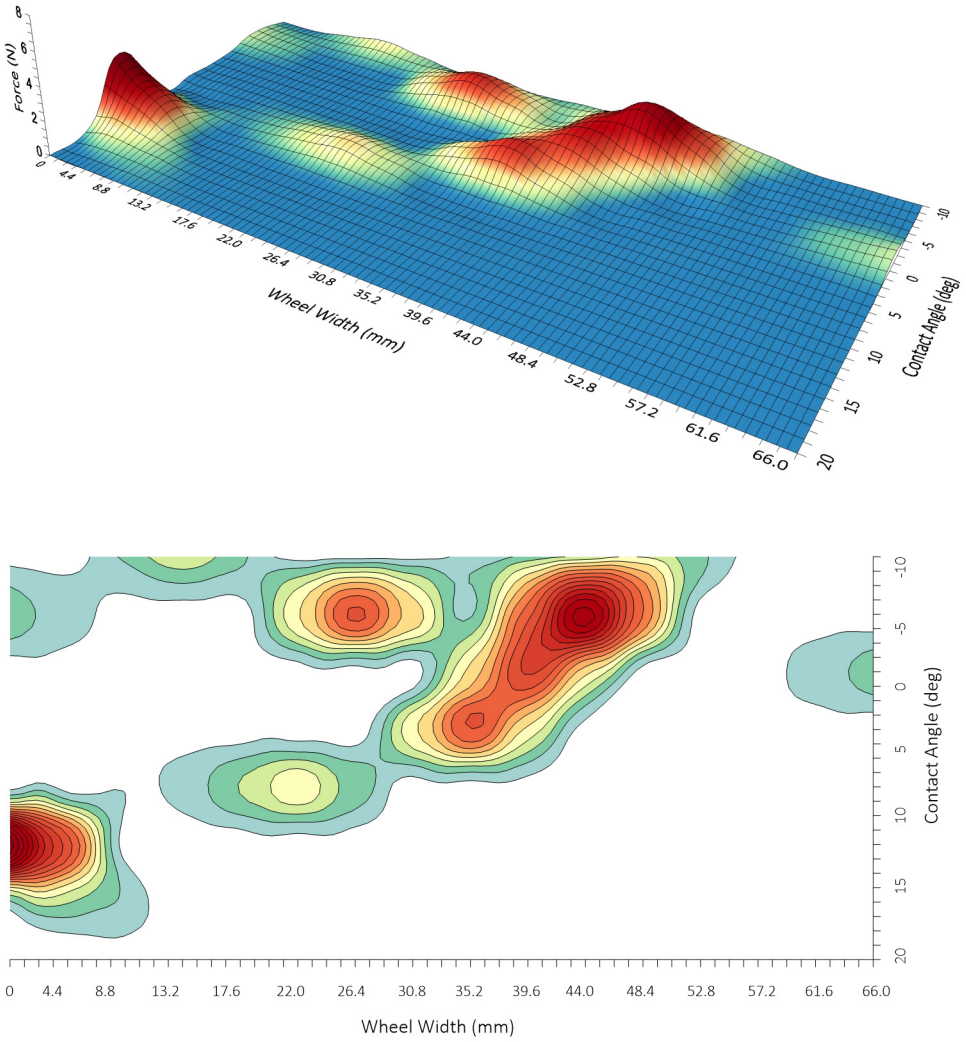

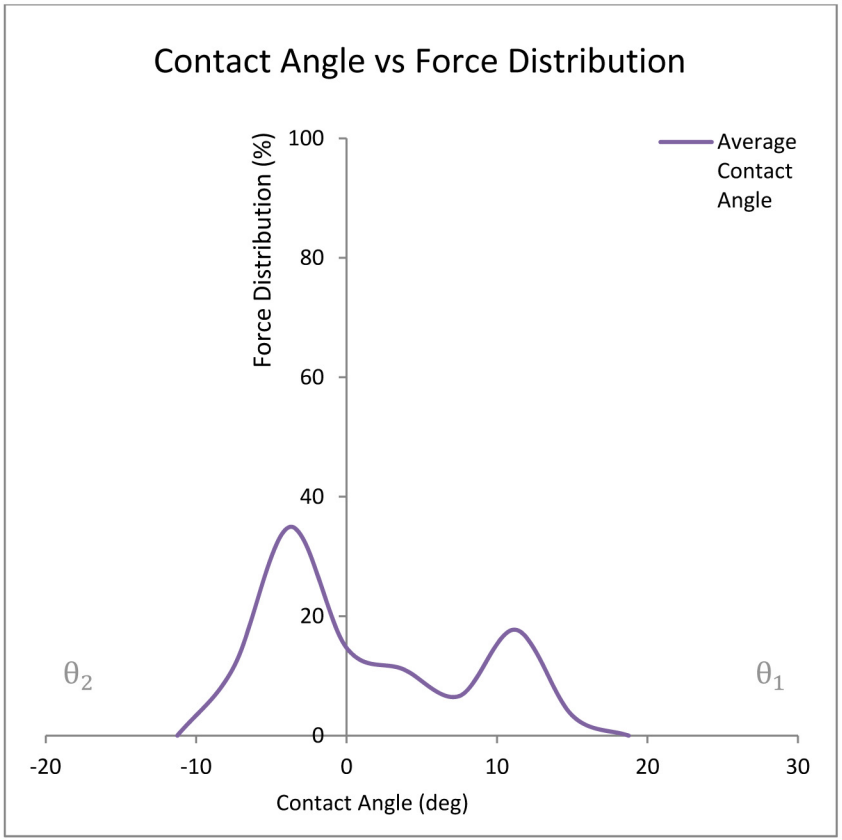

20-40mm Gravel		Lateral Wheel Width (mm)																Force (N)	Distribution (%)
No	4	0.0	4.4	8.8	13.2	17.6	22.0	26.4	30.8	35.2	39.6	44.0	48.4	52.8	57.2	61.6	66.0		
Longitudal Contact Angle (deg)	18.75	0.00	0.00	0.00	0.00	0.00	0.00	0.00	0.00	0.00	0.00	0.00	0.00	0.00	0.00	0.00	0.00	0.00	0.00
	15.00	0.00	0.00	0.00	0.00	0.00	0.00	0.00	0.00	0.00	0.15	0.29	0.15	0.00	0.00	0.00	0.00	0.59	1.15
	11.25	0.00	0.00	0.00	0.00	0.00	0.00	0.00	0.00	0.00	0.00	0.00	0.00	0.00	0.00	0.00	0.00	0.00	0.00
	7.50	8.74	8.32	7.90	3.95	0.00	0.00	0.00	0.00	0.00	0.00	0.00	0.10	0.21	2.50	4.78	2.39	38.89	76.51
	3.75	1.33	2.66	2.01	1.36	0.68	0.00	0.00	0.00	0.00	0.00	0.00	0.00	0.48	0.96	0.54	0.11	10.12	19.92
	0.00	0.00	0.00	0.00	0.00	0.00	0.00	0.00	0.31	0.62	0.31	0.00	0.00	0.00	0.00	0.00	0.00	1.23	2.42
	-3.75	0.00	0.00	0.00	0.00	0.00	0.00	0.00	0.00	0.00	0.00	0.00	0.00	0.00	0.00	0.00	0.00	0.00	0.00
	-7.50	0.00	0.00	0.00	0.00	0.00	0.00	0.00	0.00	0.00	0.00	0.00	0.00	0.00	0.00	0.00	0.00	0.00	0.00
	-11.25	0.00	0.00	0.00	0.00	0.00	0.00	0.00	0.00	0.00	0.00	0.00	0.00	0.00	0.00	0.00	0.00	0.00	0.00
Force (N)		10.07	10.98	9.91	5.31	0.68	0.00	0.00	0.31	0.62	0.46	0.29	0.25	0.69	3.46	5.32	2.51	A (cm^2)	6.57
Distribution (%)		19.81	21.60	19.49	10.44	1.34	0.00	0.00	0.61	1.21	0.90	0.58	0.49	1.35	6.80	10.47	4.93	L_v (N)	4.25

20 - 40mm Test

Test Number: 04

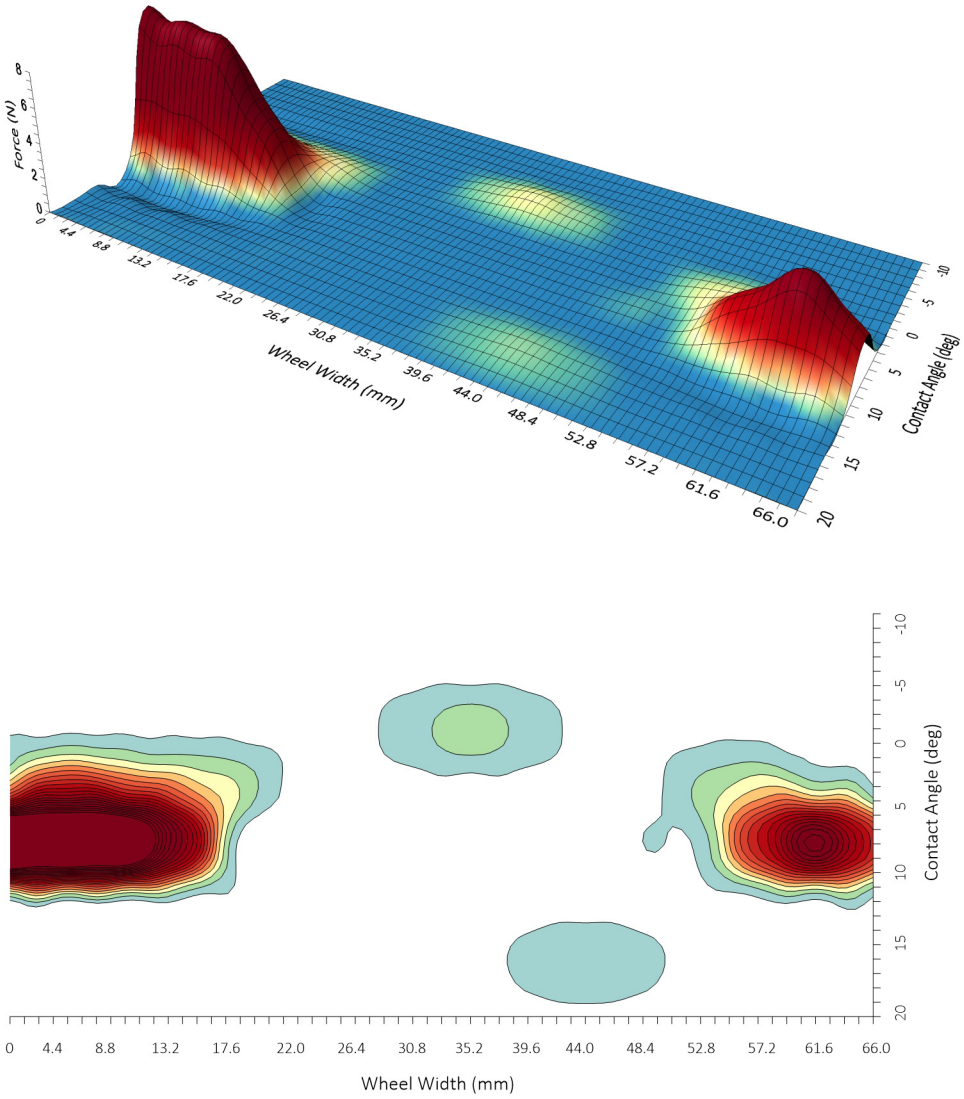

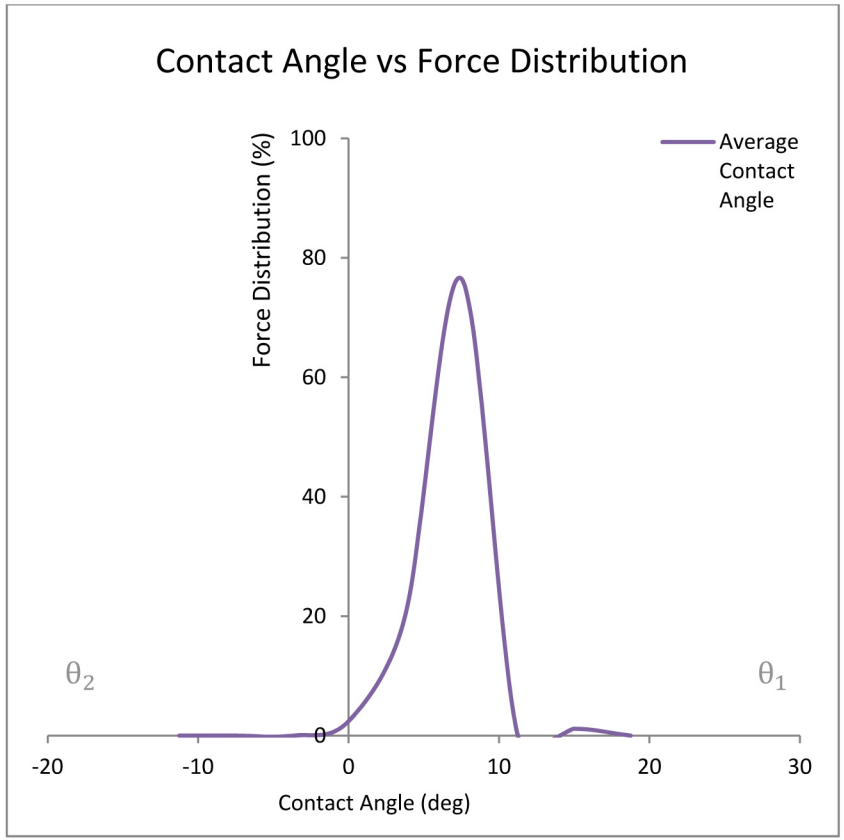

20-40mm Gravel		Lateral Wheel Width (mm)																Force (N)	Distribution (%)
No	5	0.0	4.4	8.8	13.2	17.6	22.0	26.4	30.8	35.2	39.6	44.0	48.4	52.8	57.2	61.6	66.0		
Longitudal Contact Angle (deg)	18.75	0.00	0.00	0.00	0.00	0.00	0.00	0.00	0.00	0.00	0.00	0.00	0.00	0.00	0.00	0.00	0.00	0.00	0.00
	15.00	0.00	0.00	0.00	0.00	0.00	0.00	0.00	0.00	0.00	0.00	0.00	0.00	0.00	1.33	2.67	1.33	5.33	4.40
	11.25	0.00	0.00	0.00	0.00	0.00	0.00	0.30	0.60	0.30	0.00	0.00	0.00	1.10	2.20	34.69	67.18	106.36	87.82
	7.50	0.00	0.39	0.78	0.39	0.00	0.00	0.00	0.00	0.00	0.00	0.00	0.00	0.00	0.00	0.00	0.00	1.56	1.28
	3.75	0.00	0.00	0.59	1.17	0.59	0.00	0.00	0.00	0.00	0.00	1.19	2.38	1.19	0.00	0.00	0.00	7.10	5.86
	0.00	0.00	0.00	0.00	0.00	0.00	0.00	0.00	0.00	0.00	0.10	0.20	0.19	0.18	0.09	0.00	0.00	0.77	0.63
	-3.75	0.00	0.00	0.00	0.00	0.00	0.00	0.00	0.00	0.00	0.00	0.00	0.00	0.00	0.00	0.00	0.00	0.00	0.00
	-7.50	0.00	0.00	0.00	0.00	0.00	0.00	0.00	0.00	0.00	0.00	0.00	0.00	0.00	0.00	0.00	0.00	0.00	0.00
	-11.25	0.00	0.00	0.00	0.00	0.00	0.00	0.00	0.00	0.00	0.00	0.00	0.00	0.00	0.00	0.00	0.00	0.00	0.00
Force (N)		0.00	0.39	1.36	1.56	0.59	0.00	0.30	0.60	0.30	0.10	1.39	2.57	2.47	3.62	37.35	68.51	A (cm^2)	6.29
Distribution (%)		0.00	0.32	1.13	1.29	0.48	0.00	0.25	0.49	0.25	0.08	1.15	2.12	2.04	2.99	30.84	56.57	L_v (N)	19.42

20 - 40mm Test

Test Number: 05

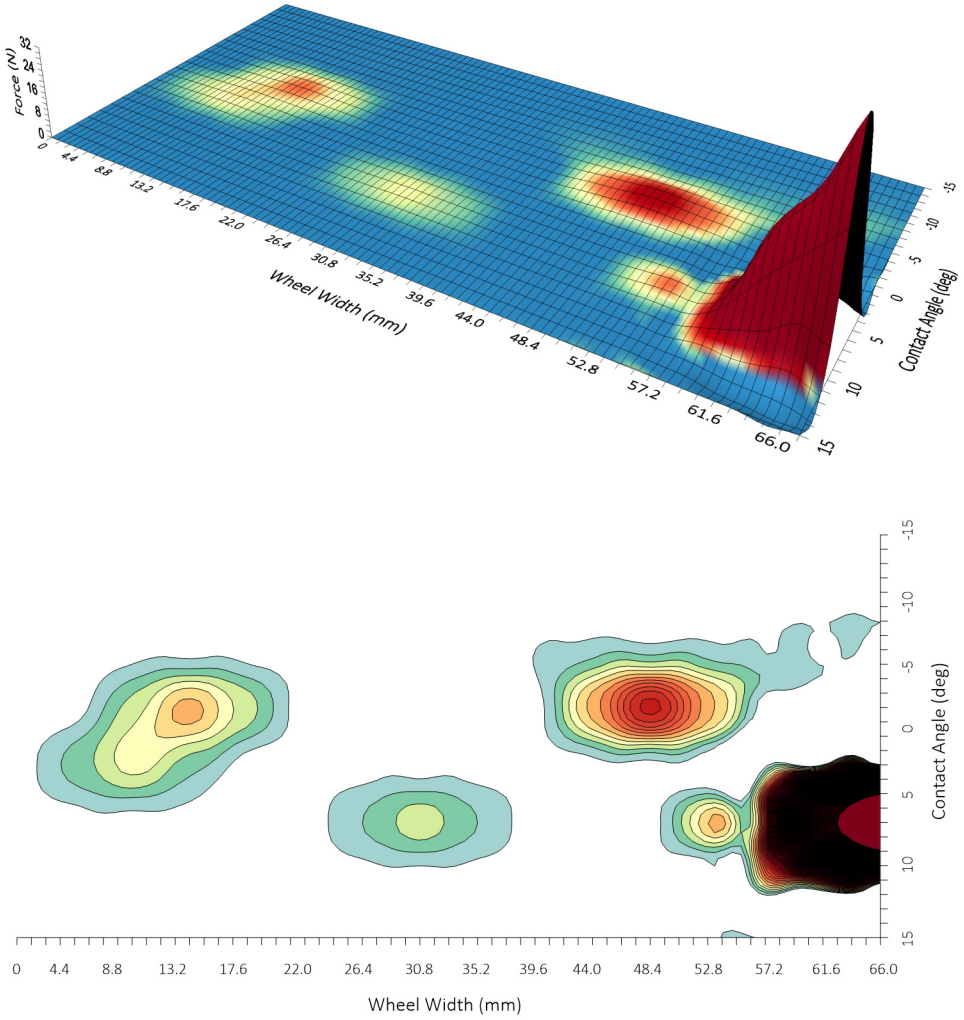

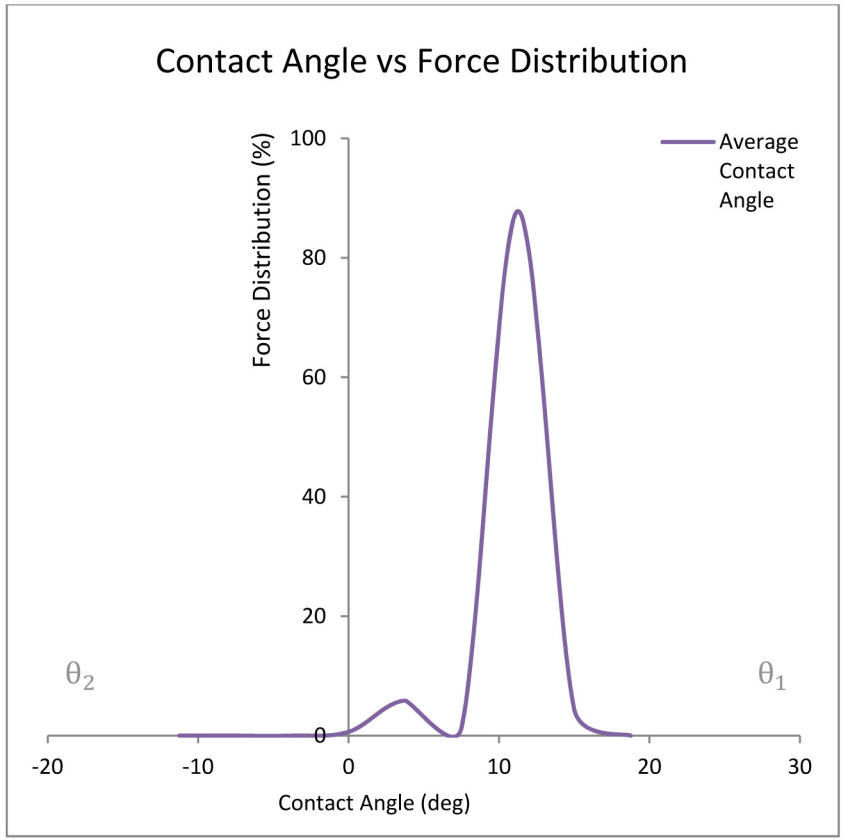

20-40mm Gravel		Lateral Wheel Width (mm)															Force (N)	Distribution (%)
No	Ave	0.0	4.4	8.8	13.2	17.6	22.0	26.4	30.8	35.2	39.6	44.0	48.4	52.8	57.2	61.6	66.0	
Longitudal Contact Angle (deg)	18.75	0.00	0.00	0.00	0.00	0.00	0.00	0.00	0.00	0.00	0.00	0.00	0.00	0.00	0.00	0.00	0.00	0.00
	15.00	0.06	0.12	0.15	0.35	0.42	0.26	0.23	0.37	0.48	0.29	0.06	0.10	0.25	0.46	0.59	0.32	4.50	9.74
	11.25	0.64	0.51	0.42	0.26	0.54	1.21	0.99	0.43	0.40	0.49	0.26	0.68	1.43	1.03	2.59	4.61	16.48	35.70
	7.50	1.36	1.23	1.06	1.24	1.05	0.43	0.15	0.37	0.61	1.31	1.79	1.03	0.40	0.86	1.23	0.57	14.67	31.79
	3.75	0.39	0.35	0.19	0.17	0.26	0.35	0.18	0.15	0.40	0.40	0.35	0.35	0.28	0.27	0.17	0.06	4.33	9.39
	0.00	0.23	0.14	0.05	0.22	0.39	0.22	0.07	0.18	0.36	0.30	0.09	0.32	0.63	0.41	0.20	0.12	3.92	8.50
	-3.75	0.09	0.14	0.15	0.18	0.09	0.06	0.15	0.13	0.17	0.35	0.33	0.13	0.02	0.01	0.01	0.00	2.00	4.34
	-7.50	0.00	0.00	0.02	0.05	0.02	0.00	0.00	0.00	0.01	0.03	0.04	0.05	0.02	0.00	0.00	0.00	0.25	0.54
	-11.25	0.00	0.00	0.00	0.00	0.00	0.00	0.00	0.00	0.00	0.00	0.00	0.00	0.00	0.00	0.00	0.00	0.00	0.00
Force (N)		2.77	2.49	2.04	2.45	2.77	2.53	1.75	1.64	2.44	3.15	2.92	2.66	3.04	3.05	4.78	5.68	A (cm^2)	28.18
Distribution (%)		5.99	5.39	4.41	5.32	6.00	5.48	3.79	3.56	5.28	6.83	6.33	5.77	6.58	6.60	10.36	12.31	L_v (N)	2.04

20 - 40mm Test

Test Number: Averages

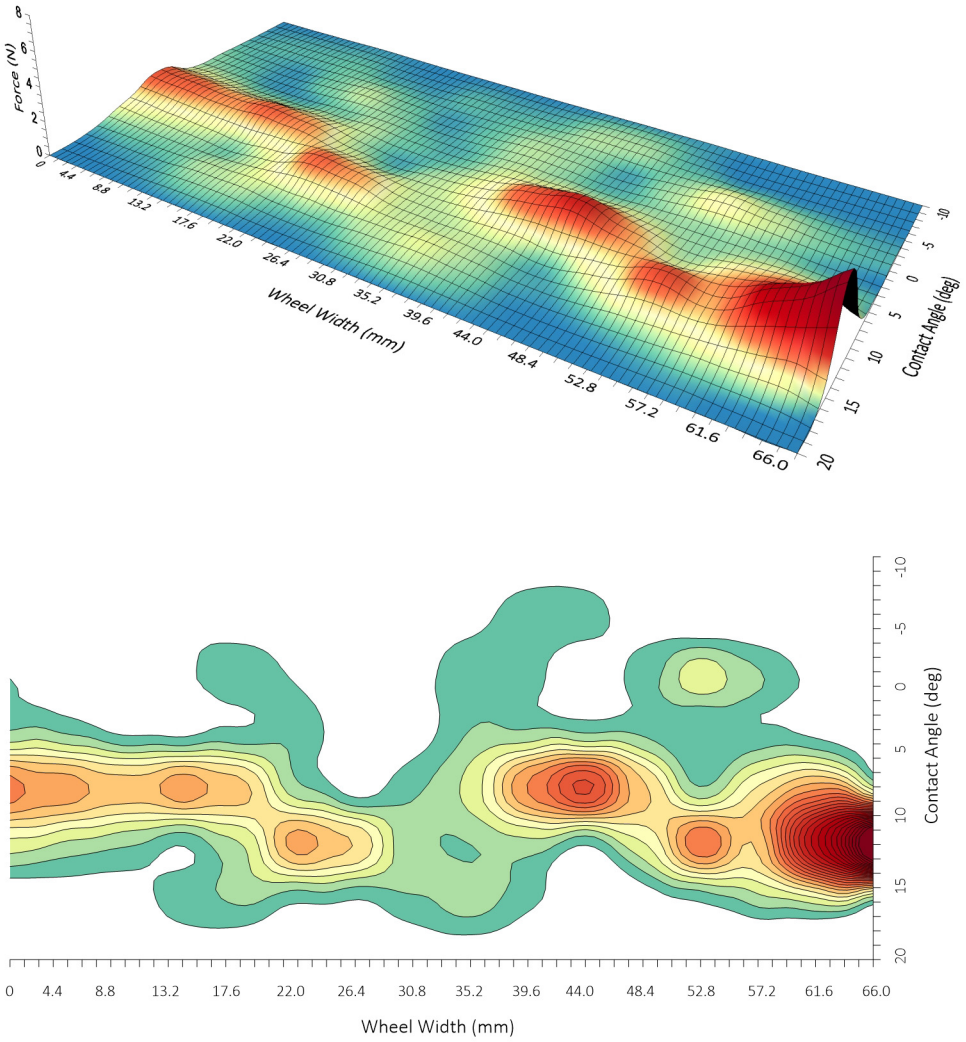

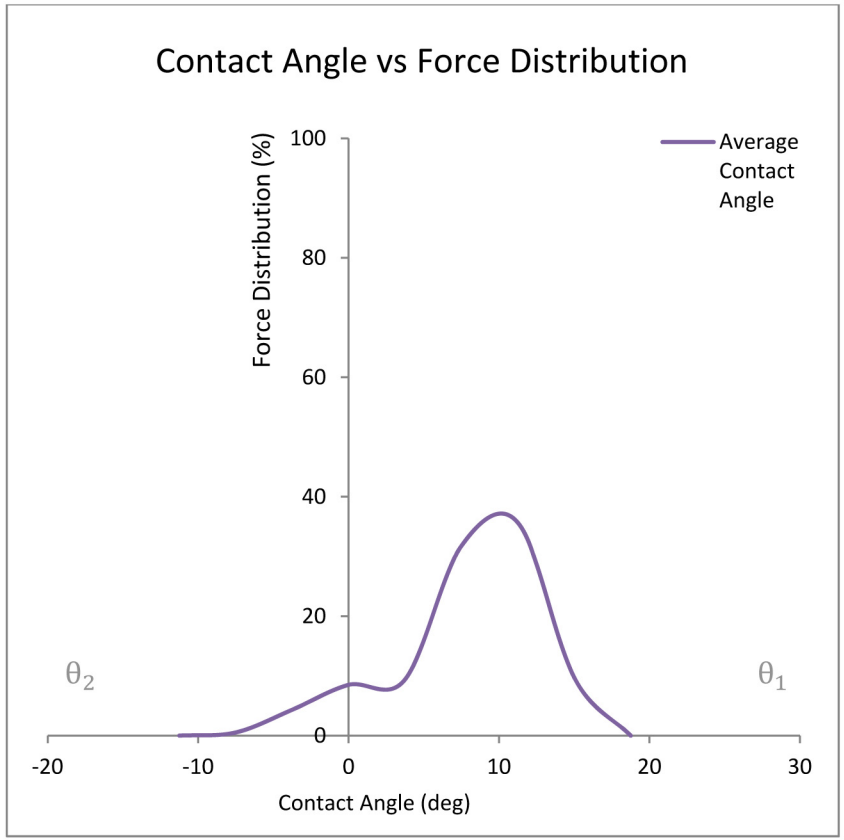

APPENDIX J

Classification Validation Results

Classification		Lateral Wheel Width (mm)																Force (N)	Distribution (%)
No		0.0	4.4	8.8	13.2	17.6	22.0	26.4	30.8	35.2	39.6	44.0	48.4	52.8	57.2	61.6	66.0		
Longitudal Contact Angle (deg)	15.00	0.00	0.00	0.00	0.00	0.00	0.00	0.00	0.00	0.00	0.00	0.00	0.00	0.00	0.00	0.00	0.00	0.00	0.00
	11.25	0.70	0.61	0.50	0.53	0.57	0.61	0.64	0.58	0.49	0.38	0.35	0.42	0.44	0.38	0.31	0.14	7.63	11.08
	7.50	1.42	2.39	1.77	1.01	1.05	1.22	1.25	1.45	1.50	1.21	1.03	1.04	0.94	0.86	0.82	0.59	19.55	28.42
	3.75	2.10	2.18	2.00	1.80	1.64	1.78	1.69	1.39	1.48	1.45	0.89	0.65	1.15	1.53	1.43	1.01	24.15	35.10
	0.00	0.68	1.15	1.13	1.15	1.14	1.10	1.21	1.25	1.11	1.07	0.86	0.63	0.57	0.48	0.53	0.55	14.62	21.25
	-3.75	0.27	0.31	0.19	0.15	0.13	0.12	0.14	0.20	0.23	0.19	0.16	0.16	0.13	0.10	0.16	0.21	2.86	4.15
	-7.50	0.00	0.00	0.00	0.00	0.00	0.00	0.00	0.00	0.00	0.00	0.00	0.00	0.00	0.00	0.00	0.00	0.00	0.00
	-11.25	0.00	0.00	0.00	0.00	0.00	0.00	0.00	0.00	0.00	0.00	0.00	0.00	0.00	0.00	0.00	0.00	0.00	0.00
Force (N)		5.17	6.64	5.59	4.64	4.53	4.83	4.93	4.87	4.81	4.29	3.29	2.89	3.23	3.36	3.26	2.50	A (cm^2)	17.97
Distribution (%)		7.51	9.65	8.12	6.74	6.58	7.02	7.16	7.08	6.99	6.24	4.78	4.20	4.70	4.89	4.73	3.63	L_v (N)	1.72

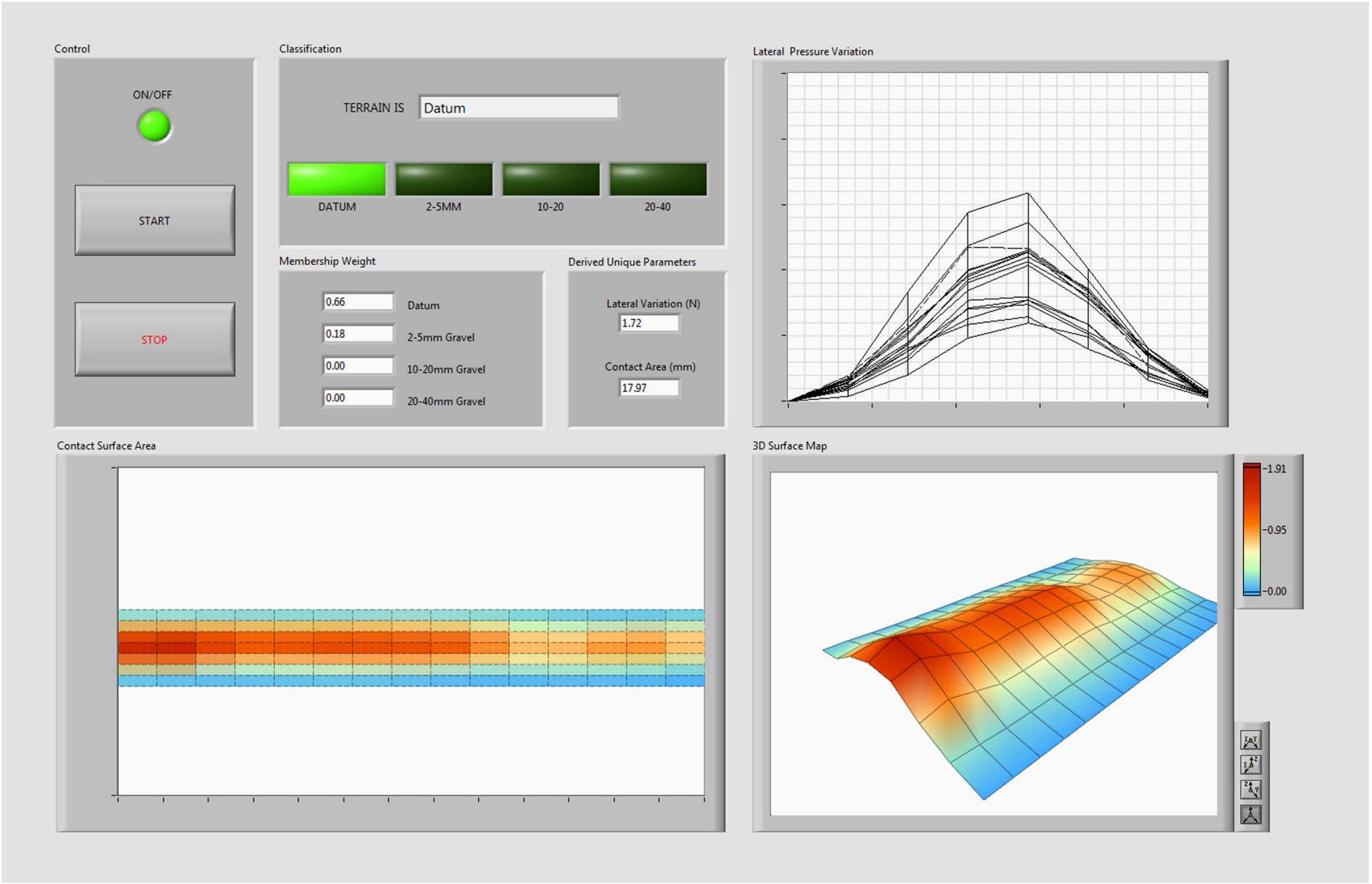
Control
ON/OFF
START
STOP
Classification
TERRAIN IS
Datum
DATUM
2-5MM
10-20
20-40
Membership Weight
0.66
Datum
0.18
2-5mm Gravel
0.00
10-20mm Gravel
0.00
20-40mm Gravel
Derived Unique Parameters
Lateral Variation (N)
1.72
Contact Area (mm)
17.97
Lateral Pressure Variation
Contact Surface Area
3D Surface Map
-1.91
-0.95
-0.00

Classification		Lateral Wheel Width (mm)																Force (N)	Distribution (%)
No		0.0	4.4	8.8	13.2	17.6	22.0	26.4	30.8	35.2	39.6	44.0	48.4	52.8	57.2	61.6	66.0		
Longitudal Contact Angle (deg)	15.00	0.00	0.00	0.00	0.00	0.00	0.00	0.00	0.00	0.00	0.00	0.00	0.00	0.00	0.00	0.00	0.00	0.00	0.00
	11.25	0.07	0.31	0.53	0.42	0.33	0.71	0.91	0.50	0.10	0.13	0.27	0.86	1.45	0.80	0.17	0.12	7.68	15.93
	7.50	0.66	1.44	1.57	1.06	0.79	0.73	0.66	0.54	0.45	1.06	1.57	0.85	0.22	0.22	0.21	0.16	12.18	25.27
	3.75	0.93	0.98	0.95	1.30	2.07	2.66	1.40	0.28	0.43	0.56	0.54	0.46	0.26	0.64	1.22	0.69	15.37	31.89
	0.00	0.76	1.19	1.15	0.97	0.76	0.60	0.41	0.45	0.63	0.40	0.23	0.28	0.43	0.64	0.58	0.31	9.79	20.31
	-3.75	0.08	0.11	0.05	0.08	0.26	0.26	0.09	0.00	0.18	0.35	0.19	0.02	0.05	0.16	0.22	0.09	2.18	4.52
	-7.50	0.09	0.10	0.11	0.05	0.00	0.00	0.05	0.10	0.05	0.03	0.06	0.03	0.00	0.00	0.00	0.00	0.67	1.38
	-11.25	0.04	0.07	0.04	0.00	0.00	0.00	0.00	0.00	0.05	0.10	0.05	0.00	0.00	0.00	0.00	0.00	0.34	0.70
	-15.00	0.00	0.00	0.00	0.00	0.00	0.00	0.00	0.00	0.00	0.00	0.00	0.00	0.00	0.00	0.00	0.00	0.00	0.00
	-18.75	0.00	0.00	0.00	0.00	0.00	0.00	0.00	0.00	0.00	0.00	0.00	0.00	0.00	0.00	0.00	0.00	0.00	0.00
	-22.50	0.00	0.00	0.00	0.00	0.00	0.00	0.00	0.00	0.00	0.00	0.00	0.00	0.00	0.00	0.00	0.00	0.00	0.00
Force (N)		2.62	4.19	4.39	3.88	4.21	4.96	3.52	1.88	1.89	2.63	2.90	2.50	2.40	2.45	2.40	1.37	A (cm^2)	21.52
Distribution (%)		5.44	8.69	9.11	8.06	8.74	10.29	7.30	3.90	3.92	5.46	6.02	5.19	4.98	5.08	4.98	2.84	L_v (N)	2.94

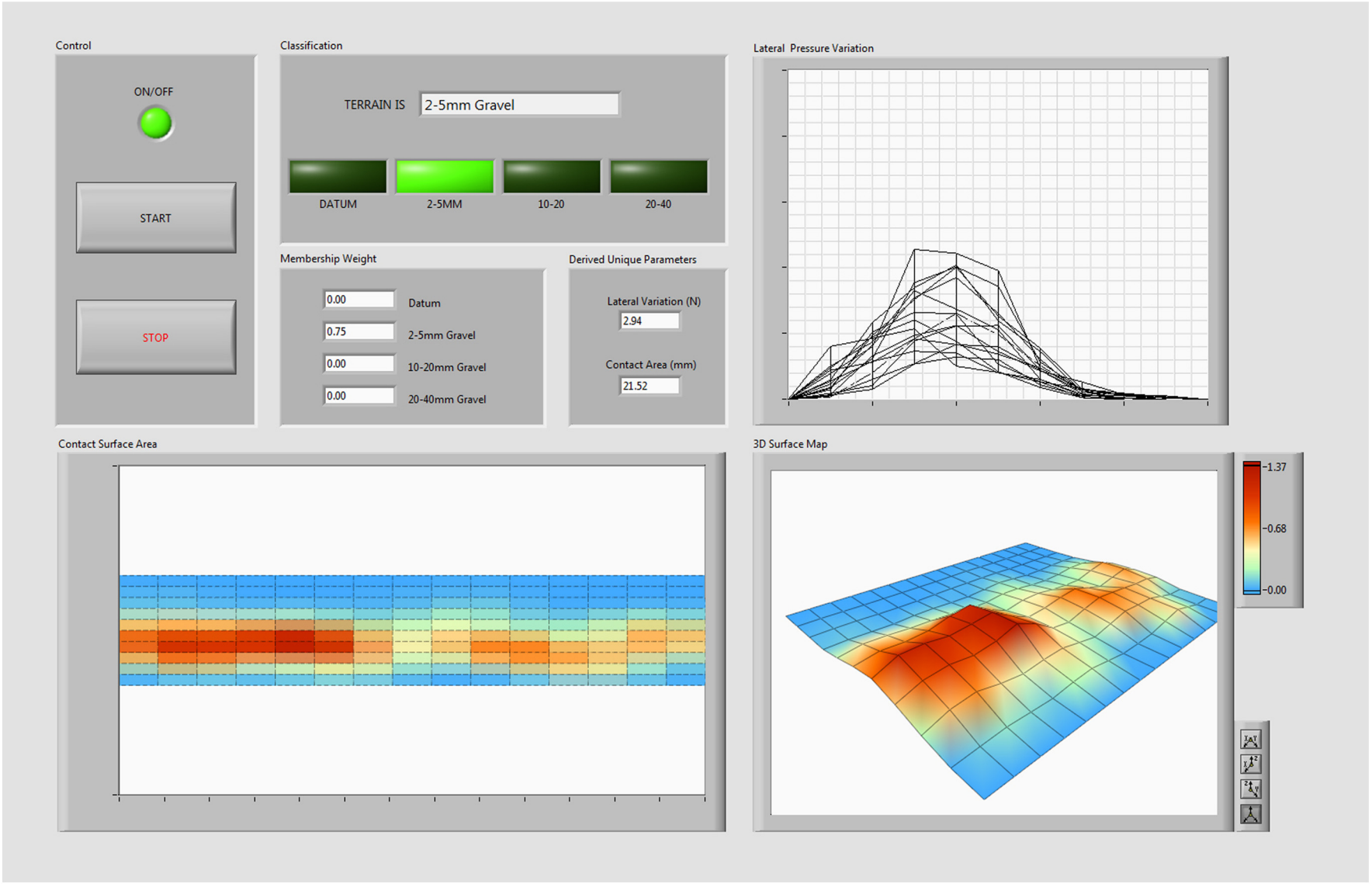
Control
ON/OFF
START
STOP
Classification
TERRAIN IS
2-5mm Gravel
DATUM
2-5MM
10-20
20-40
Membership Weight
0.00
Datum
0.75
2-5mm Gravel
0.00
10-20mm Gravel
0.00
20-40mm Gravel
Derived Unique Parameters
Lateral Variation (N)
2.94
Contact Area (mm)
21.52
Lateral Pressure Variation
Contact Surface Area
3D Surface Map
-1.37
-0.68
-0.00

Classification		Lateral Wheel Width (mm)																Force (N)	Distribution (%)
No		0.0	4.4	8.8	13.2	17.6	22.0	26.4	30.8	35.2	39.6	44.0	48.4	52.8	57.2	61.6	66.0		
Longitudal Contact Angle (deg)	18.75	0.00	0.00	0.00	0.00	0.00	0.00	0.00	0.00	0.00	0.00	0.00	0.00	0.00	0.00	0.00	0.00	0.00	0.00
	15.00	0.48	0.46	0.44	0.22	0.07	0.25	0.28	0.67	1.12	0.60	0.08	0.04	0.00	0.15	0.42	0.38	5.66	12.99
	11.25	0.35	0.41	0.27	0.31	0.26	0.12	0.54	0.93	0.53	0.45	0.73	0.53	0.21	0.20	0.57	0.69	7.09	16.28
	7.50	0.25	0.12	1.00	2.30	1.73	0.90	1.43	1.60	0.68	0.08	0.32	0.63	1.11	1.46	0.85	0.31	14.77	33.90
	3.75	0.07	0.20	0.40	0.41	0.26	0.30	0.43	0.72	1.02	1.47	1.93	1.19	0.82	0.97	0.38	0.01	10.58	24.30
	0.00	0.00	0.00	0.01	0.02	0.08	0.14	0.07	0.00	0.17	0.34	0.22	0.11	0.93	1.76	0.88	0.00	4.72	10.83
	-3.75	0.00	0.00	0.00	0.05	0.11	0.05	0.00	0.00	0.00	0.00	0.00	0.00	0.00	0.00	0.00	0.00	0.21	0.48
	-7.50	0.00	0.00	0.13	0.26	0.13	0.00	0.00	0.00	0.00	0.00	0.00	0.00	0.00	0.00	0.00	0.00	0.53	1.21
	-11.25	0.00	0.00	0.00	0.00	0.00	0.00	0.00	0.00	0.00	0.00	0.00	0.00	0.00	0.00	0.00	0.00	0.00	0.00
Force (N)		1.16	1.19	2.26	3.57	2.63	1.76	2.74	3.93	3.53	2.94	3.29	2.50	3.06	4.53	3.09	1.39	A (cm^2)	13.13
Distribution (%)		2.66	2.73	5.19	8.20	6.04	4.04	6.29	9.02	8.10	6.76	7.54	5.73	7.03	10.40	7.10	3.18	L_v (N)	3.02

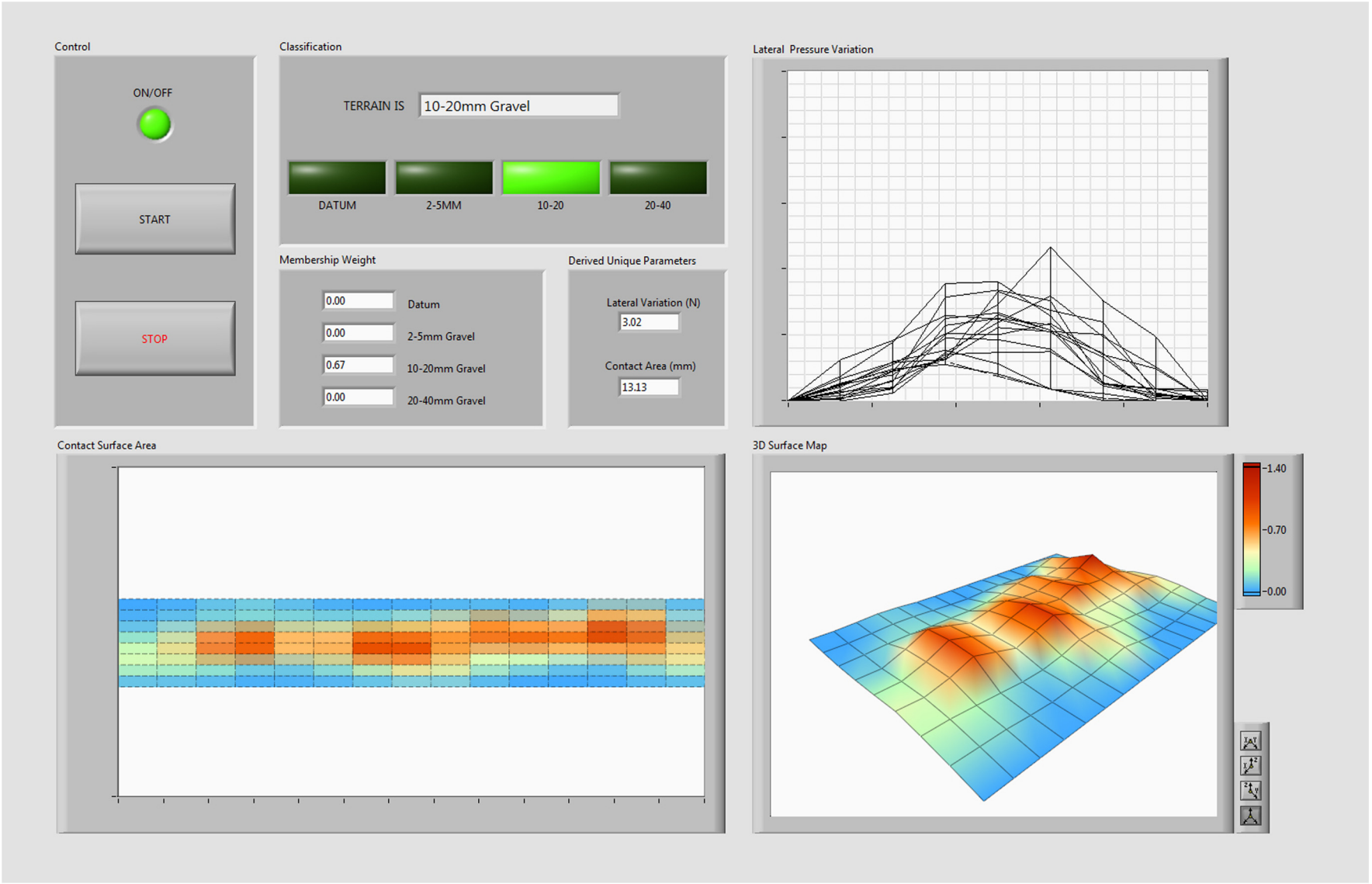
Control
ON/OFF
START
STOP
Classification
TERRAIN IS
10-20mm Gravel
DATUM
2-5MM
10-20
20-40
Membership Weight
0.00
Datum
0.00
2-5mm Gravel
0.67
10-20mm Gravel
0.00
20-40mm Gravel
Derived Unique Parameters
Lateral Variation (N)
3.02
Contact Area (mm)
13.13
Lateral Pressure Variation
Contact Surface Area
3D Surface Map
-1.40
-0.70
-0.00

Classification		Lateral Wheel Width (mm)																Force (N)	Distribution (%)
No		0.0	4.4	8.8	13.2	17.6	22.0	26.4	30.8	35.2	39.6	44.0	48.4	52.8	57.2	61.6	66.0		
Longitudal Contact Angle (deg)	18.75	0.00	0.00	0.00	0.00	0.00	0.00	0.00	0.00	0.00	0.00	0.00	0.00	0.00	0.00	0.00	0.00	0.00	0.00
	15.00	0.30	0.60	0.30	0.49	0.98	0.49	0.00	0.00	0.00	0.00	0.00	0.00	0.30	0.60	0.30	0.00	4.37	7.61
	11.25	2.89	1.82	0.91	0.70	0.49	1.60	2.22	0.95	0.00	0.00	0.00	3.03	6.06	3.41	0.76	0.38	25.22	43.89
	7.50	3.26	2.83	0.83	0.84	1.73	1.06	0.20	0.11	0.06	0.00	0.00	0.10	0.32	1.41	2.25	1.06	16.06	27.96
	3.75	0.00	0.00	0.00	0.00	0.03	0.06	0.03	0.28	0.57	0.28	0.23	0.46	0.32	0.17	0.23	0.28	2.93	5.11
	0.00	0.00	0.00	0.00	0.00	0.00	0.00	0.00	0.51	1.34	1.15	0.32	0.00	0.00	0.00	0.07	0.14	3.52	6.13
	-3.75	0.14	0.07	0.00	0.00	0.00	0.29	0.74	0.65	0.25	0.54	1.00	0.50	0.00	0.00	0.00	0.00	4.18	7.28
	-7.50	0.00	0.00	0.11	0.23	0.11	0.00	0.00	0.01	0.06	0.12	0.18	0.23	0.12	0.00	0.00	0.00	1.17	2.03
	-11.25	0.00	0.00	0.00	0.00	0.00	0.00	0.00	0.00	0.00	0.00	0.00	0.00	0.00	0.00	0.00	0.00	0.00	0.00
Force (N)		6.60	5.33	2.16	2.26	3.35	3.50	3.19	2.50	2.27	2.10	1.73	4.32	7.11	5.59	3.60	1.86	A (cm^2)	8.85
Distribution (%)		11.48	9.27	3.76	3.93	5.83	6.09	5.54	4.36	3.95	3.65	3.01	7.52	12.37	9.72	6.27	3.24	L_v (N)	5.13

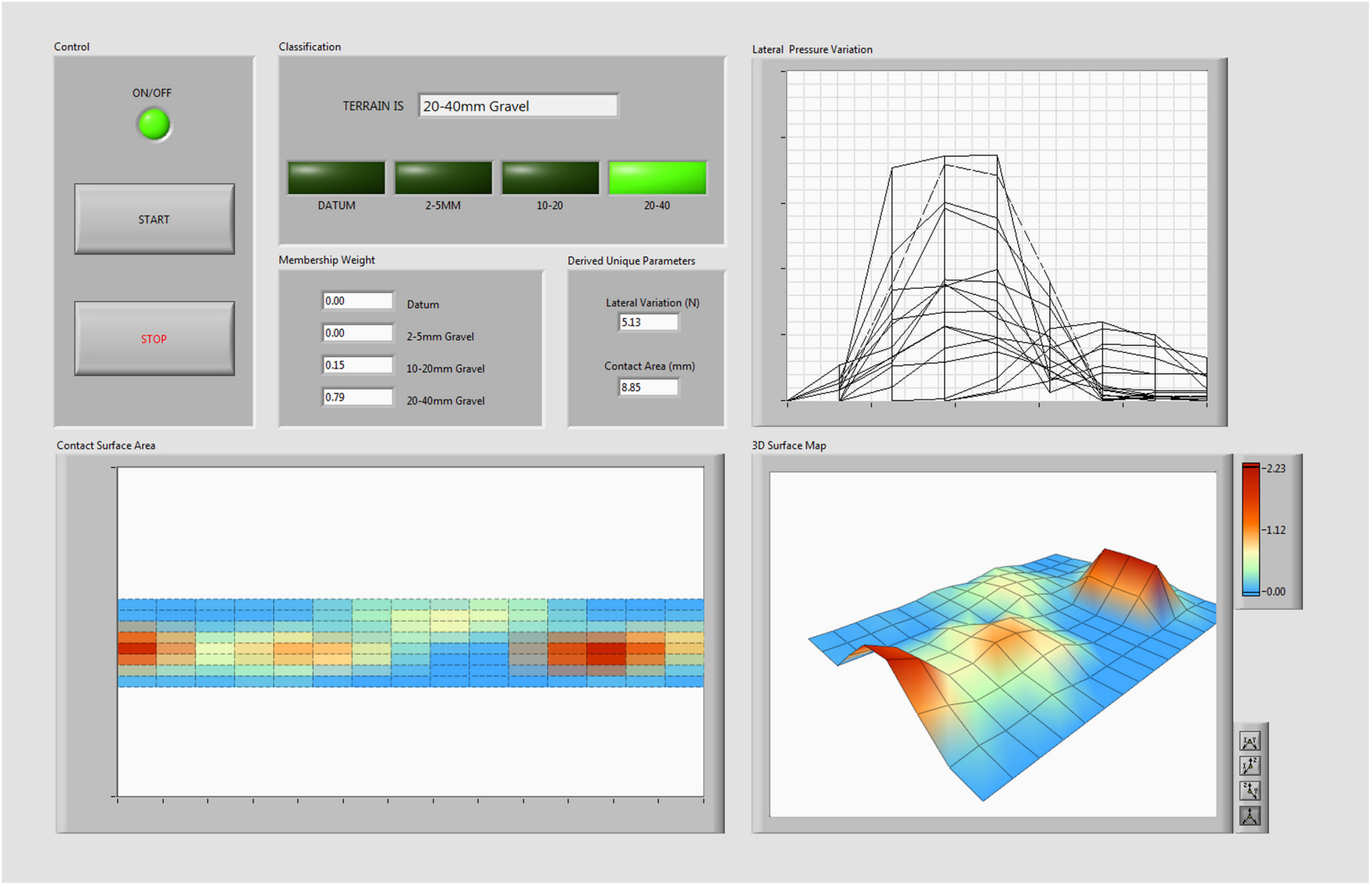
Control
ON/OFF
START
STOP
Classification
TERRAIN IS
20-40mm Gravel
DATUM
2-5MM
10-20
20-40
Membership Weight
0.00
Datum
0.00
2-5mm Gravel
0.15
10-20mm Gravel
0.79
20-40mm Gravel
Derived Unique Parameters
Lateral Variation (N)
5.13
Contact Area (mm)
8.85
Lateral Pressure Variation
Contact Surface Area
3D Surface Map
2.23
1.12
0.00